STRUCTURAL AND CATALYTIC INVESTIGATIONS ON VANADIUM OXIDE NANOPARTICLES SUPPORTED ON SILICA FILMS GROWN ON A Mo(112) SUBSTRATE

DISSERTATION

zur Erlangung des akademischen Grades
doctor rerum naturalium
(Dr. rer. nat.)
im Fach Chemie

eingereicht an der
Mathematisch-Naturwissenschaftlichen Fakultät I
der Humboldt-Universitat zu Berlin

von
Sarp Kaya
geboren am 15. September 1977
in Ankara-Turkey

Prasident der Humboldt-Universitat zu Berlin
Prof. Dr. C. Markschies

Dekan der Mathematisch-Naturwissenschaftlichen Fakultat I
Prof. Dr. C. Limberg

Gutacher:
1. Prof. Dr. H.-J. Freund
2. Prof. Dr. K. Rademann

Tag der mündlichen Prüfung: 13.07.2007

ACKNOWLEDGEMENTS

The acknowledgments are the best and most difficult part of this thesis to write. They are the best because it makes me happy to remember all the people who touched my life in a way that influenced the content of this thesis. They are the hardest because it's difficult for me to express in writing the great sense of gratitude I feel for all those mentioned here. I'll do my best to put my feelings into words.

I would like to begin by thanking my advisor, Prof. Dr. Hans- Joachim Freund for giving me the opportunity to perform this work in his fascinating research group and for his guidance and advices. In him I found not only an immense source of knowledge but also a source of guidance and encouragement so crucial in scientific research.

I gratefully acknowledge Dr. Shamil Shaikhutdinov for his advice, supervision, and crucial contribution, which made him a backbone of this research and so to this thesis. His involvement with his originality has triggered my intellectual maturity that I will benefit from, for a long time to come.

Many thanks go in particular to Dr. Boonchuan Immaraporn, Dr. Jonas Weissenrieder, and Dr. Dario Stacchiola. I learnt many things about UHV systems from Boohchuan. I am much indebted to wonderful friends Jonas and Dario for their valuable advice in science discussions.

I also thank to Junling Lu, Yingna Sun and Martin Baron for all of their invaluable assistance. I would never have made it through those long hours in the lab without their help.

The silica project was very much a collaborative work between experimentalist and theoreticians. Many special thanks go to the members of the research group of Prof. Dr. Joachim Sauer, Dr. Marek Sierka and Tanya K. Todorova without whom much of the scientific understanding in the thesis would not have been possible.

There are also a number of other people who do not work directly with me but have been friends for many years and I would also like to thank them for their support. Dr. David Starr, Alexander Uhl, Jani Sainio, my office mates Kerstin Jacobsen-Stefan Ulrich-Bjorn Brandt, Tobias Schalow, Sebastien Guimond, Mohammad Abu-Haija deserve my sincere gratitude.

Many thanks go to Matthias Naschhitzki, Klaus Peter Vogelgesang for their technical assistance and to Manuela Misch and Gabriele Mehnerd for their tireless support in administrative works.

Finally, I would like to extend my deepest gratitude to my family. They always have provided unwavering love and encouragement. Thank you for believing in me.

ABSTRACT

The widespread use of model systems for understanding the heterogeneous catalytic processes is based on bridging the structural complexity gap between present generation of supported metal and metal oxide technical catalysts and crystalline metal and planar metal/oxide systems, which are utilized to investigate structure-reactivity relationships by a large variety of surface science techniques. In this thesis, we focused on a concept of so-called 'monolayer' vanadium oxide catalysts, which have been introduced particularly for methanol oxidation reactions. Following a bottom-up approach, silica supported vanadium oxide model catalysts were investigated. Combining a number of experimental techniques, the surface of Mo(112) used as a substrate for the silica films was characterized in detail and the atomic structure of the silica film was determined. Adsorption of water and growth of vanadium oxide nanoparticles on the silica films, and finally the reactivity of vanadium oxide/silica systems towards methanol were studied. In contrast to the previously suggested models, an oxygen induced p(2×3) superstructure formed on a Mo(112) surface should be considered as one dimensional surface oxide where Mo=O groups are formed preferentially along the $[\bar{1}\bar{1}1]$ direction of the Mo(112) surface. Monolayer silica films grown on Mo(112) surfaces are composed of two-dimensional network of SiO_4 tetrahedra. Depending on the film preparation conditions, the structure can be altered by additional oxygen atoms adsorbed on the Mo substrate. The defect structure includes antiphase domain boundaries which form by a half-lattice shift along the $[\bar{1}10]$ direction and a low density of point defects, most probably silicon vacancies.

Water does not dissociate on the monolayer silica film. An ordered structure of water with respect to silica film was observed at 140 K owing to good lattice matching between the silica film and hexagonal ice. Amorphous solid water layers homogenously covering the surface at 100 K were used as reactive layers for vanadium oxide particles in order to mimic 'wet chemistry' used in preparation of technical catalysts. The results revealed that ice layer assisted the formation of hydrated vanadium oxide nanoparticles partially terminated by V=O and V-OH groups. The dehydration takes place above 500 K, thus exposing V-terminated surface. Methanol dissociates on dehydrated vanadium oxide particles and methoxy species are stable on the surface up to 500 K only in the presence of vanadium terminated surface sites. Formaldehyde production which takes place at ~550 K is strongly affected by the surface structure of the vanadium oxide particles and exhibits a maximum at specific ratio between V- and V=O sites on the surface.

The results presented may have a strong impact on our understanding of the catalytic reactions at the molecular level.

ZUSAMMENFASSUNG

Die breite Anwendung von Modellsystemen, um heterogene katalytische Prozesse zu verstehen, basiert darauf, die Lücke der strukturellen Komplexität zu überbrücken zwischen heutigen technischen Katalysatoren, bestehend aus einem Metalloxid sowie einem darauf geträgerten Metall, sowie kristallinen Metallen und planaren Metall/Oxid-Systemen, welche dazu benutzt werden, Struktur-Reaktivitäts-Beziehungen mittels einer Fülle von Surface Science-Methoden zu untersuchen. In der vorliegenden Arbeit liegt das Hauptaugenmerk auf so genannten Vanadiumoxid-‚Monolagen’-Katalysatoren, die insbesondere für Oxidationsreaktionen von Methanol eingeführt wurden. Mittels eines ‚bottom-up’-Ansatzes wurden Silica-geträgerte Vanadiumoxid-Modellkatalysatoren untersucht. Durch Kombination einer Reihe experimenteller Techniken wurde die Oberfläche von Mo(112), die als Substrat für den Silica-Film diente, im Detail untersucht und die atomare Struktur des Silica-Films wurde ermittelt. Adsorption von Wasser und das Wachstum von Vanadiumoxid-Nanopartikeln auf dem Silica-Film und schließlich die Reaktivität von Vanadiumoxid/Silica-Systemen gegenüber Methanol wurden untersucht. Im Gegensatz zu früher vorgeschlagenen Modellen sollte eine Sauerstoff-induzierte $p(2\times3)$-Überstruktur, die sich auf einer Mo(112)-Oberfläche ausbilded, angenommen werden als ein eindimensionales Oberflächenoxid, bei dem sich Mo=O-Gruppen bevorzugt entlang der $[\bar{1}\bar{1}1]$-Richtung der Mo(112)-Oberfläche ausbilden. Monolagen-Silica-Filme, die auf Mo(112) gewachsen wurden, bestehen aus einem zweidimensionalen Netz von SiO_4-Tetraedern. In Abhängigkeit der Bedingungen, unter denen der Film präpariert wurde, kann die Struktur durch zusätzlich auf dem Mo-Substrat adsorbierte Sauerstoff-Atome verändert werden. Die Defekt-Struktur schließt Antiphasen-Domänengrenzen ein, die durch eine Verschiebung um die halbe Gitterkonstante entlang der $[\bar{1}10]$-Richtung gebildet werden, und eine geringe Dichte von Punkt-Defekten, die höchstwahrscheinlich Silizium-Fehlstellen darstellen.

Wasser dissoziiert nicht auf dem Monolagen-Silica-Film. Eine Wasser-Struktur, die geordnet bezüglich des Silica-Films ist, wurde bei 140 K beobachtet, was der guten Übereinstimmung der Gitterkonstanten von Silica-Film und hexagonalem Eis geschuldet ist. Amorphe Lagen festen Wassers, die die Oberfläche bei 100 K homogen bedecken, wurden als reaktive Lagen für Vanadiumoxid-Partikel benutzt, um die ‚Nasschemie’ nachzubilden, wie sie in der Präparation technischer Katalysatoren zum Einsatz kommt. Die Ergebnisse verdeutlichen, dass die Eis-Lagen die Bildung von hydratisierten Vanadiumoxid-Nanopartikeln, welche teilweise von V=O und V-OH-Gruppen terminiert werden, begünstigen. Die Dehydratisierung geschieht oberhalb 500 K, wobei eine V-terminierte Oberfläche entsteht. Methanol dissoziiert auf dehydratisierten Vanadiumoxid-Partikeln, und Methoxy-Spezies sind auf der Oberfläche stabil bis 500 K, allerdings nur in der Gegenwart von V-Plätzen. Die Produktion von Formaldehyd, die bei etwa 550 K stattfindet, ist stark abhängig von der Struktur der Oberfläche der Vanadiumoxid-Partikel und weist ein Maximum bei einem spezifischen Verhältnis zwischen V- und V=O-Oberflächenplätzen auf.

Die hier vorgestellten Ergebnisse könnten unser Verständnis von katalytischen Reaktionen auf molekularer Ebene bedeutend vorantreiben.

CONTENTS

Acknowledgements i

Abstract iii

Zusammenfassung v

List of Figures xi

List of Tables xvii

CHAPTER 1 INTRODUCTION 1

CHAPTER 2 EXPERIMENTAL TECHNIQUES 5

2.1 Photoelectron Spectroscopy 5

2.1.1 Photoelectron Cross-section 7

2.1.2 Analyzing Photoemission Spectra 8

2.1.3 Core Level Chemical Shifts 10

2.2 Low Energy Electron Diffraction 10

2.3 Scanning Tunneling Microscopy 13

2.3.1 Theoretical Description of the Tunneling Process 14

2.4 Infrared Reflection Absorption Spectroscopy 17

2.5 Surface Processes 19

2.5.1 Adsorption Kinetics 20

2.5.2 Physisorption and Chemisorption 20

2.6 Temperature Programmed Desorption 22

2.6.1 Fundamental Aspects 22

2.6.2 Evaluation of the Desorption Activation Parameter E_a^{des}, n, and υ_n 22

CHAPTER 3 INTERACTION OF OXYGEN WITH Mo(112): FORMATION OF A SURFACE OXIDE 25

3.1 Oxygen Induced Structures on Mo(112) Surface: LEED 27

3.2 STM Investigations of Mo(112) p(2×3)-O Structure 29

3.3 Core Level Shifts Due To Oxide Formation 30

3.4 Probing the Surface Sites 32

3.5 Structural Model 35

CHAPTER 4 SILICA FILMS GROWN ON A Mo(112) SURFACE 37

4.1 Review of Bulk Silica Structures 37

4.1.1 Crystalline Silica 37

4.1.2 Amorphous Silica 38

4.2 Thin Films on Single Crystal Surfaces 39

4.3 Structural Characterization of One Monolayer Silica Film on Mo(112) 41

4.4 Electronic Properties 44

4.5 Vibrational Properties 48

4.6 Summary of the Results of DFT Calculations 53
4.7 Defect Structure 54
4.7.1 Line Defects: Antiphase Domain Boundaries 55
4.7.2 Point Defects 56

CHAPTER 5 INTERACTION OF WATER WITH SILICA FILM 59
5.1 The Water Molecule and Hydrogen Bonding 59
5.2 Ice 61
5.3 Interaction of Water with Surfaces 61
5.4 Adsorption of Water on Silica Surface and Formation of Ordered Water Overlayer 63
5.4.1 Desorption Kinetics of Amorphous and Crystalline Water 63
5.4.2 Monitoring Crystallization with Vibrational Spectroscopy 65
5.4.3 Photoelectron Spectroscopy 68
5.4.4 Formation of Ordered Water Layer 69
5.4.5 Determination of Coverage 71
5.5 The Nature of Water Bonding to Silica Film 72
5.5.1 Polar Ordering Probed by IRAS 72
5.5.2 Electronic Structure of Amorphous and Crystalline Water 75

CHAPTER 6 CHARACTERIZATION OF VANADIUM OXIDE NANOPARTICLES 79
6.1 Vanadium Oxide 79
6.2 Vanadium Oxide Catalysis 80
6.3 Morphologies of Vanadium Oxide Nanoparticles on Silica Film 82
6.4 Oxidation States 84
6.5 Surface Termination and Vibrational Properties 88
6.6 Effects of Dehydration and Thermal Stability 93
6.7 Probing Surface Sites by CO 94
6.8 Effect of Water Layer on the Morphology of Vanadium Oxide Particles 95

CHAPTER 7 METHANOL ADSORPTION AND OXIDATION ON SILICA SUPPORTED VANADIUM OXIDE NANOPARTICLES 99
7.1 Adsorption of Methanol on Vanadyl Terminated Particles 102
7.2 Adsorption of Methanol on Dehydrated Vanadium Oxide Particles 104
7.3 Influence of Surface Oxygen on Formaldehyde Formation 110

CHAPTER 8 SUMMARY AND OUTLOOK 113
APPENDIX A Symbols 117
APPENDIX B Abbreviations 119
APPENDIX C Sample preparation 121

Curriculum Vitae 125
Publications 127
Bibliography 129

LIST OF FIGURES

Figure 2.1 Schematic representation of the photoemission process. The circles represent the electrons in the core levels. 6

Figure 2.2 Schematic of a LEED optics for electron diffraction experiments. The integrated electron gun consist of heated filament (tungsten or LaB_6), a Wehnelt cylinder (W). 11

Figure 2.3 a_1 and a_2 correspond to the substrate unit cell vectors. b_1 and b_2 indicate the superstructure unit cell vectors. α is the enclosed angle between the substrate and γ is the enclosed angle between the superstructure unit cell vectors. The angle β accounts for a rotation of the superstructure with respect to the substrate. 12

Figure 2.4 STM instrumental apparatus. 13

Figure 2.5 Schematic Energy diagram in one dimension, in case of electrons tunneling from the tip to the sample. $E_F^{T/S}$ is the tip/sample Fermi energies, $E_V^{T/S}$ is the tip/sample vacuum levels, and $\varphi^{T/S}$ is the tip/sample work functions, respectively. V_{Tunnel} is the tunneling bias. 15

Figure 2.6 Schematic picture of tunnelling geometry in the Tersoff-Hamann model. The probe tip has arbitrary shape but is assumed locally spherical with a radius of curvature R, where it approaches nearest the surface. The distance of nearest approach is d. The centre of curvature of tip is r_0 [28]. 16

Figure 2.7 Infrared radiation impinging on a substrate can be resolved into two components. 18

Figure 2.8 A schematic representation of an infrared spectrometer (left) and dipole moment of CO adsorbed on a surface in two different orientations (right). 19

Figure 2.9 Schematic and simplified potential energy diagram for the interaction of a diatomic molecule, X_2, approaching and interacting with a surface. At first upon approaching, Van der Waals interactions may attract the molecule into a weakly bound, physisorbed, state. From this physisorbed state it may proceed into an associative (non-dissociated) chemisorbed state. If the activation barrier E_a^{diss} is overcome the molecule may dissociate into two chemisorbed atoms. The energy required to desorb these atoms again is E_a^{des}. Also shown are the corresponding adsorption energies, E_{ads} for the physisorbed and associatively chemisorbed states. 21

Figure 3.1 LEED patterns of (a) clean Mo(112), (b) p(1×2), (c) p(1×2)+ p(1×3), and (d) p(2×3) oxygen induced superstructures. (e) Schematic illustrations of the top layer of a Mo(112) surface and representative unit cells of the structures observed by LEED. Possible locations for adsorption sites for oxygen atoms are also indicated as black circles: (1) atop, (2) short bridge, (3) long bridge, and (4) quasi threefold hallow sites. 28

Figure 3.2 STM images of the Mo(112)-p(2×3)-O surfaces. In both images bright one-dimensional structures can be observed. Tunneling conditions are (a) 40×40 nm^2, V_s/I: +1.0 V/0.2 nA and (b) 9×8 nm^2, V_s/I: +1.2 V/0.61 nA. p(2×3) periodicity is indicated by white rectangular unit meshes. Dark and light spots highlight half lattice shifts due to domain boundaries. 29

Figure 3.3 Photoelectron spectra taken from clean Mo(112) and Mo(112)-p(2×3)-O surfaces. (a) O 1s spectra including p(2×1) and p(1×2) structures. Mo $3d_{5/2}$ surface states were measured at (b) normal and (c) grazing emission angles. For all deconvoluted Mo 3d spectra, circles represent the experimental data points and the black lines on top of them are fitted curves. The thick lines represent the metallic states (of the clean sample) and oxide components are indicated with thin lines. Light gray, gray and black thick lines are topmost, second and bulk $3d_{5/2}$ states of clean Mo(112) surface, respectively. Various coordinations of molybdenum atoms to oxygen atoms are also shown with color coded thin lines. Grazing angle measurements were performed at 75°. 31

Figure 3.4 IRA spectra of (a) Mo(112)-p(2×3)-^{16}O and (b) Mo(112)-p(2×3)-^{18}O surface oxides. 33

Figure 3.5 IRA spectra of CO (*upper panel*) and D_2O (*lower panel*) adsorbed on p(2×3) surface oxide at 100 K. Saturation CO coverage is obtained after adsorbing 0.2 L CO. Frequency shifts of Mo=O species were followed by adsorbing (a) 0.5 L, (b) 1.0 L, (c) 1.5 L, and (d) 2.0 L D_2O. 34

Figure 3.6 Structural model for on p(2×3) surface oxide Mo(112). Gray shaded balls represent molybdenum atoms and they become darker while going from the surface to the deeper atomic layers. Smaller solid balls are oxygen ions and oxygen ions of Mo=O groups are coordinated to the topmost (lightest) molybdenum atoms. p(2×3) unit cell is indicated by dotted lines. 36

Figure 4.1 Phase diagram of silica (adapted from [99]). 38

Figure 4.2 Large scale STM images showing well ordered 1 ML silica structure. (a) 100×100 nm^2, V_s/I=+2.0 V/0.20 nA, (b) 20×12.5 nm^2, V_s/I=+2.0 V/0.40 nA, (c) line profile showing the step height (taken from (b)). Inset: c(2×2) LEED pattern of silica superstructure (E_p = 60 eV). Rectangle represents unit cell of Mo(112) surface. Crystallographic orientations are also indicated. 42

Figure 4.3 STM topographic images taken at the different tunneling conditions and structural model of two dimensional silica film. The size of each STM image is 3.75×3.75 nm^2. Tunneling conditions (V_s/I) are (a) +1.2 V/0.35 nA, (b) -0.4 V/0.30 nA, (c) 0.65 V/0.75 nA, (d) -0.17 V/0.75 nA, (e) -0.72 V/0.45 nA, (f) -0.50 V/0.45 nA. Top view (g) and side views (h) of ball model of silica film on Mo(112) surface. Inter-atomic distances and crystallographic orientations were indicated. 43

Figure 4.4 O 1s and Mo $3d_{5/2}$ regions of high resolution photoemission spectra of silica film taken at two different electron emission angles. Take-off angles are 0° and 80° for spectrum (a) and (b), respectively. 45

Figure 4.5 XP spectra of O-poor and O-rich silica films. *Top left panel*: O 1s spectra of (a) as deposited, (b) well-ordered O-poor and (c) well-ordered O-rich silica film. Circles: experimental data, light gray: O1-O2, gray: O3, dark gray: O* components and black: fitted curve. *Bottom left panel*: Effect of additional oxygen atoms onto molybdenum surface in Mo 3d states. (a) black: O-poor film, gray: O-rich film. (b) Difference spectra obtained by subtracting Mo 3d spectrum of O-rich film from that of O-poor. *Top right panel*: 2D model of silica film with varying amount of oxygen atoms on molybdenum substrate. *Bottom right panel*: Si 2p region of (a) O-poor and (b) O-rich films. 46

Figure 4.6 Valence band spectra of O-poor and O-rich silica films taken at two different excitation energies. All spectra are aligned with respect to Fermi level of molybdenum substrate. *Left panel*: Valence band spectra of (a) O-poor and (b) O-rich silica film. *Right panel*: Valence band spectra of O-poor film measured at the take-off angles of (a) 0° and (b) 70°, respectively. Excitation energies are indicated. 48

Figure 4.7 Characterization of structural improvement of an as-deposited silica film. *Left*: STM image of an as-deposited film 100×100 nm^2, $V_s/I=3.0$ V/0.1 nA. *Right*: IRA spectra of (a) deposited at 900 K and the same film annealed to (b) 1000 K, (c) 1100 K, and (d) 1250 K. All spectra were taken at 300 K. 51

Figure 4.8 STM images and IRA spectra of silica particles formed on the well-ordered silica film by Si deposition in 5×10^{-8} mbar O_2 at 900 K. Spectrum (2) and (3) correspond to the STM images (c) and (a), respectively. The spectrum (1) is for the original well-ordered film. Image size and the tunneling parameters: (a) 100×100 nm^2, $V_s/I=+2.8$ V/0.20 nA; (c) 100 × 100 nm^2, $V_s/I=+3.5$ V/0.10 nA. 52

Figure 4.9 IRA spectra of O-poor (a) and O-rich (b) silica films on a Mo(112) substrate. 53

Figure 4.10 STM images of an antiphase domain boundary on silica surface. Image contrast is dependent on tunneling conditions. Left STM image showing Si ions and right image showing O1 and O2 ions were obtained by adjusting the tunneling parameters to $V_s/I=+1.2$ V/0.35 nA and $V_s/I=-0.72$ V/0.45 nA, respectively. A structural model for the O-poor film including an APDB is placed in between for clarity. 56

Figure 4.11 STM images (3.3×2.2 nm^2) of point defects on silica film. Tunneling conditions are $V_s/I=$ (a) -1.0 V/0.40 nA, (b) 0.5 V/0.4 nA, (c) 1.0 V/0.6 nA. (d) Structural representation of a Si vacancy. (e) IRA spectra of CO adsorbed on silica film at 100 K. 57

Figure 5.1 Molecular orbital energy level diagram of H_2O (adapted from [185]). 60

Figure 5.2 The phase diagram of water/ice. Inset: The medium pressure range showing the melting curves of metastable ices IV and XII. 61

Figure 5.3 TPD spectra of H_2O adsorbed on a silica film at (a) 100 K and (b) 140 K. (c) TPD spectra of ~1 BLE D_2O adsorbed at 100 and 150 K. Heating rate was 3 Ks^{-1} for each spectrum. (d) Arrhenius plot of the amorphous H_2O desorption. The black line is a linear fit to the experimental data and corresponding slope (activation energy) is shown in the figure. 64

Figure 5.4 IRA spectra of H_2O adsorbed on a silica film at 100 K at increasing coverage as indicated. 65

Figure 5.5 IRA spectra of 6 BLE of H_2O adsorbed on the silica film at 100 K and slowly heated up to complete desorption. 67

Figure 5.6 Consecutive PE-spectra of the silica film, exposed to 6 L of water at 100 K, on slow heating to 170 K. The states at 532.5 and 531.3 eV are assigned to the surface and interfacial O species in the silica film. The spectra were recorded with low acquisition time in order to prevent any photon-induced effects on the water overlayer. The spectra are off-set for clarity. 69

Figure 5.7 LEED pattern (negative contrast) (a) and its schematic presentation (b) developed at around 145 K during heating of the 6 BLE water, initially adsorbed at 100 K. (c) Structural model of the ice layer formed on the silica film, which exhibits a c(6×2)-Mo(112) or c(2×2)-Silica superstructure as indicated by a rhomb. A and B indicate the second- and first-layer water molecules, respectively. 70

Figure 5.8 Quantitative analysis of infrared spectra. (a) Deconvoluted OD stretching region. (b) Coverage dependent frequency shift of main silica phonon. (c) Deconvoluted divided Si−O−Mo vibrational band due to crystallization of water. 72

Figure 5.9 Comparison of vibrational bands of amorphous and crystalline H_2O and D_2O. 74

Figure 5.10 UP spectra of water adsorbed on silica film. Left panel: Growth of ASW at 100 K. Difference spectra was collected while dosing D_2O and plotted by subtracting the spectrum of clean silica surface. Each spectrum indicates 0.1 BLE water coverage increase. Right panel: Change of valence band structure of silica film due to water crystallization. Valence bands of (a) clean silica film (O-poor), (b) ~0.8 BLE AS H_2O at 100 K, (c) ~0.8 BLE AS D_2O at 100 K, (d) crystallized form of (b) at 140 K, (e) crystallized form of (c) at 150 K. 76

Figure 6.1 Possible structures of supported vanadium oxide species. 81

Figure 6.2 STM images (100×100 nm^2) of a model supported vanadium oxide catalyst prepared by depositing vanadium in 2×10^{-7} mbar O_2 on a pristine silica surface. The images are taken at 300 K with a tunnel current of 0.2 nA and a sample bias of 3.0 V. Silica surface is covered by (a) 0.12 ML and (b) 0.4 ML vanadium oxide. 82

Figure 6.3 STM images (100×100 nm^2) of a model supported vanadium oxide catalyst prepared by depositing vanadium in 2×10^{-7} mbar O_2 on 3-5 ML solid water covered pristine silica surface. Many particles are nucleated at the steps on the silica surface, but many are also located on the terraces. Deposited vanadium amounts are (a) 0.035 ML, (b) 0.15 ML, (c) 0.5 ML. Tunneling parameters: V_s/I = (a) +4.0 V/0.2 nA, (b) +4.0 V/0.2 nA, (c) +3.0 V/0.2 nA. Inset (a) 10×4 nm^2 - V_s/I = +1.2 V/0.3 nA, (b) 12×8 nm^2 – Vs/I = +1.0 V/0.18 nA. 83

Figure 6.4 The O 1s and V 2p photoemission spectra of clean and vanadium oxide deposited Silica/Mo(112) surface. All spectra were referenced to the Fermi level of the molybdenum substrate. Deposited vanadium amounts are (a) 0, (b) 0.1, (c) 0.3, (d) 0.6, and (e) 1.0 ML. All spectra were taken at 300 K. 84

Figure 6.5 O 1s and V 2p photoemission spectra of vanadium oxide deposited on solid water covered Silica/Mo(112) surface. Deposited vanadium amounts are (a) 0.1, (b) 0.2, (c) 0.4, (d) 0.6, and (e) 1.0 ML. All measurements were performed at 100 K. 86

Figure 6.6 XPS and ARXPS analysis of 1 ML vanadium oxide particles on silica. *Top panel*: Deconvoluted V $2p_{3/2}$ region of the XP spectra taken at (a) hydrated particles at 100 K (b) hydrated particles at 300 K, (c) totally dehydrated particles at 600 K (d) reoxidized particles by oxygen exposure at 600 K. *Bottom left panel*: Deconvoluted O1s region of the XP spectra taken at (a-b) hydrated and (c-d) dehydrated particles at two different electron emission angles. *Bottom right panel*: Deconvoluted V $2p_{3/2}$ region of the XP spectra taken at (a-b) partially hydrated and (c-d) dehydrated particles. Dehydration was done at 550 K. Take-off angles are indicated. Shirley background was subtracted from all spectra. 87

Figure 6.7 IRA spectra of vanadium oxide particles deposited on pristine silica surface at 300 K. (a) 0, (b) 0.1, (c) 0.3, (d) 0.6, and (e) 1.0 ML vanadium is deposited in 2×10^{-7} mbar O_2. 89

Figure 6.8 IRA spectra from hydrated and dehydtated vanadium oxide particles grown on amorphous solid water layer by layer fashion. *Left panel*: IRA spectra of OH stretch vibrational bands of (a) 5 ML amorphous solid water film on silica at 100 K, (b) after deposition of 0.4 ML vanadium in 2×10^{-7} O_2 ambient at 100 K and (c) after sublimating unreacted solid water by annealing the sample to 300 K. *Right panel*: IRA spectra of (a) 0, (b) 0.1, (c) 0.2, (d) 0.4, (e) 0.6 ML vanadium oxide layers grown on 3-5 ML solid water films each. Spectra were recorded at 100 K. 0.6 ML vanadium oxide particles were annealed to 300 K (f) and to 600 K (g) in UHV. Spectra (h) and (i) were recorded after oxidizing the particles in 1×10^{-7} mbar O_2 at 300 K and at 600 K, respectively. 90

Figure 6.9 IRA spectra of hydrated vanadium oxide particles on isotopically labeled silica films. (a) silica film labeled with ^{16}O, (b) silica film labeled with ^{18}O, (c) 0.5 ML particles deposited on silica film prepared by using ^{18}O, (d) 0.8 ML particles deposited on silica film prepared by using ^{16}O, (e) 2 ML particles deposited on silica film prepared by using ^{16}O, (f) after dehydrating the sample (e). 92

Figure 6.10 Morphologies of vanadium oxide particles at two different dehydration states. (a) STM image of hydrated vanadium oxide particles 100×100 nm^2 - V_s/I = 3.0 V/0.1 nA, (b) TPD spectra of desorbing species during dehydration process. Heating rate is 3 Ks^{-1}. (c) STM image of totally dehydrated vanadium oxide particles 100×100 nm^2 - V_s/I = 3.0 V/0.2 nA. 94

Figure 6.11 (a) CO TPD spectra taken during stepwise dehydration treatments. 1 L CO was adsorbed each time after dehydrating the vanadium oxide particles at 225, 250, 300, 400, 500 and 600 K (from bottom to top). (b) Comparison of CO TPD behaviors of dehydrated and vanadyl terminated particles. 95

Figure 6.12 STM images of vanadium oxide prepared by varying thickness of ASW layers. (a) 200×200 nm^2 - V_s/I = 2.0 V/0.1 nA, (b) 40×40 nm^2 - V_s/I = 2.0 V/0.2 nA, (c) 400×400 nm^2 - V_s/I = 1.8 V/0.1 nA, (d) 50×50 nm^2 - V_s/I = 2.0 V/0.3 nA, (e) 400×400 nm^2 - V_s/I = 5.0 V/0.1 nA, (f) 30×30 nm^2 - V_s/I = -1.0 V/0.1 nA and (g) sketches of sample preparation methods (see also Appendix C). 96

Figure 6.13 IRA spectra of OH stretching region of 100 % CI (black) and amorphous water buffer layer (gray). 2 ML vanadium oxide was deposited onto 50 BLE ASW at 100 K in 2×10^{-7} mbar O_2. The sample was then slowly heated (in 45 min) until no unreacted water remained on the surface. 97

Figure 7.1 Decomposition routed of methoxy on oxide surfaces. 101

Figure 7.2 IRA spectra of methanol multilayer adsorbed on vanadyl terminated particles (0.8 MLV) at 100 K. Each spectrum represents the increase in methanol coverage by 0.4 L. 102

Figure 7.3 TPD data for 0.8 MLV vanadyl terminated particles exposed to 2 L CH_3OH at 100 K. Heating rate was 3 Ks^{-1}. Spectra have been offset for clarity. 104
Figure 7.4 IRA spectra as a function of annealing temperature following a 2 L methanol exposure to dehydrated vanadium oxide nanoparticles supported by silica film. 105
Figure 7.5 (a) TPD spectra following adsorption of methanol (1 L) at 100 K on 1 MLV dehydrated vanadium oxide nanoparticles (solid lines). Dotted line represents a TPD spectrum of water following dosing 100 L of H_2O at 160 K (above multilayer desorption temperature) (b) Formaldehyde desorption following successive adsorption of methanol at 100 K. Initial coverages are indicated in the figure. Heating rate was 3 Ks^{-1}. 108
Figure 7.6 TPD spectra of H_2O, CO, CH_2O and CH_3OH following 0.5 L methanol adsorption on 0.1, 0.3 and 0.8 MLV dehydrated particles at 100 K. Heating rate was 3 Ks^{-1}. 109
Figure 7.7 Effect of predosed oxygen on formaldehyde formation. *Left panel*: TPD spectra of formaldehyde following 0.5 L methanol adsorption on 0.6 MLV (a) dehydrated, (b) oxygen predosed (25 L at 300 K) and (c) oxygen predosed (25 L at 500 K) vanadium oxide particles. *Right panel*: TPD spectra of formaldehyde following 0.5 L methanol adsorption on 0.6 MLV dehydrated (top) and 5, 25, 50 and 300 L oxygen predosed (from second from the top to bottom) vanadium oxide particles at 500 K. Heating rate was 3 Ks^{-1}. 111
Figure C.1 Schematic illustration of the UHV system (MEGA machine). 123

LIST OF TABLES

Table 3.1 Binding energies and fractions of the Mo $3d_{5/2}$ components (normal emission). 32
Table 4.1 Structural properties of various crystalline forms of silica. 39
Table 4.2 Selected structural parameters (Å, deg) for the SiO_2/Mo(112) films: 1 ML O-poor model (0O) and 1 ML *A*/*n*O atoms up to O-rich (4O). 53
Table 7.1 IR frequencies and mode assignments of methanol adsorbed on silica supported vanadyl terminated particles. 103

CHAPTER 1

INTRODUCTION

A catalyst is a compound, which increases the rate of a chemical reaction, but which is not consumed by the reaction. The catalyst speeds up the reaction by assisting the bond breaking of the reactant molecules and the formation of new bonds to create the reaction product, usually by opening some alternative pathway for the reaction. A good catalyst keeps the balance between the interaction with the reactant molecules being sufficiently strong to break their bonds, and the interaction being sufficiently weak not to prevent the reaction and the subsequent release of the product molecules. Catalysts are widely used in chemical technology for reactions like oil refining and the production of chemicals by hydrogenation, dehydrogenation, partial oxidation, and organic molecular rearrangements (isomerization, cyclization), ammonia synthesis, and reduction of the emission in exhaust gas, to name a few [1, 2]. Often, the catalyst is in another phase than the reactants, e.g. a solid catalyst such as a metal or an oxide and gaseous reactants, a situation which is referred to as heterogeneous catalysis [3]. Since the gas phase reactants only come in contact with the surface of the solid catalyst, the properties of this surface are very important. For this purpose, the active species are often dispersed as small particles on a support material. This makes it a so-called supported catalyst. The support material is usually not catalytically active itself, although it may be in some cases, and it should be relatively stable at elevated temperatures under reaction conditions. In order to maximize the active surface area to volume ratio the support material is often highly porous. Frequently used support materials are Al_2O_3, SiO_2, activated carbon, zeolites, and sometimes also TiO_2 [1, 2]. Since the reactants and the products need to be transported to and from the active sites, different processes are important on different scales. On a large scale, the reactor beds are filled with the catalyst. The reactants have to diffuse and flow through the bed. An important parameter from an engineering point of view is the amount of pressure over such a bed that is needed to sustain a sufficient flow. On a smaller scale both the reactant and the product molecules need to diffuse through the pores of the catalyst particles. On this level the pore size distribution is an important parameter. Finally, on the smallest scale, the reactant molecules adsorb on the active species and they react. After this reaction the product molecules can desorb and will try to find their way out of the catalyst bed.

Clearly, an investigation of a catalyst is an investigation of many simultaneous processes in a complex system. Needless to say, it may be very difficult to extract the desired information from such an investigation. For example, if one attempts to study the rates of adsorption or desorption of products and reactants at the surface of the active species one can easily end up in a situation where the rate is limited by the transport properties instead of the adsorption and desorption at the active surface. The lack of information about processes on a local scale in such a catalyst seriously hinders research aimed at fundamentally understanding and systematically improving the fabrication of catalysts in a controlled way.

In order to improve our understanding about the processes taking place on a catalyst on a microscopic scale, one is forced to investigate these processes in a simplified system [4]. In such a model system, one can isolate and investigate specific phenomena without being overwhelmed by other processes taking place at the same time. The knowledge gained by these model investigations can then be combined to interpret experiments done on more complex systems.

In principle, there are two possible strategies to model a supported catalyst. One can start with an industrial catalyst and leave out certain components in order to simplify it, or one can start with the simplest model system and add features in order to make it more realistic. The simplest model catalyst is probably a single crystal surface of an active metal. Although the study of surfaces was initiated in the 19th century, most of our present understanding is based on research of the last 25 years. Ultra-high vacuum (UHV) systems have been developed in which surfaces can be kept clean for a sufficient period of time and an impressive collection of surface sensitive techniques has been invented. In the mean time, fundamental studies of adsorption, desorption and surface reactions performed on many single crystal metal surfaces have revealed many intriguing phenomena. Adsorption of molecules on a single crystal surface for example leads in many cases to a reconstruction of the surface [5]. Even a simple reaction, such as the oxidation of CO can lead to a very complicated process with oscillatory behavior in which patterns are formed on the surface with regions covered mainly by oxygen and regions covered mainly by CO.

Studies of single crystals have contributed a great deal to the understanding of the processes that play a role on the microscopic scale in a catalyst. Nevertheless, their practical value is often limited. In modeling the surface of a catalyst by a single crystal surface many aspects have been neglected. The most obvious simplification is the complete absence of a support material. This implies that processes in which for example a reactant adsorbs on the support and diffuses to a supported metal particle where it reacts, as well as processes in which molecules adsorb on a metal particle and spill over to the support, are completely absent on the single crystal model surface. In practical catalysis; however, these processes may be very important. Also, the properties of the surface of a small metal particle are not always properly represented by the single crystal counterpart. On a small particle different kinds of facets are present, and the density of edge and corner sites is much higher than on a low index single crystal surface. Finally, the electronic structure of small particles might differ from the electronic structure of large crystals [6]. The transition from metallic to insulating behavior for very small clusters may significantly influence the catalytic properties [7]. Small particles supported on a flat substrate may be the ideal compromise between reality and simplicity. Such a system can be made in several ways. For the flat support one can think of a single crystal oxide surface. However, many oxides have a very poor electrical conductivity, which limits the range of experimental techniques that can be applied. Furthermore, the surfaces of these oxides are often much harder to prepare at a high quality than are metal single crystal surfaces [8].

Alternatives can be graphite, which is sufficiently conductive, single crystal oxides like TiO_2 [8], MgO [9] and ZnO [10], which are prepared by cleavage and made relatively conductive by doping, or very thin films of oxides on top of a conducting substrate. Thin films of alumina and silica have been grown on proper metal substrates, and they have been used as a support material for small metal clusters [11, 12]. However, growing high quality oxide films can be a complex problem in itself, and the properties of thin films may only partly resemble the properties of a bulk oxide, just like the properties of small particles can be different from bulk material.

Thin films on metal substrates and depositing metal and metal oxide particles on these supports can be achieved by several means. Molecular beam epitaxy (MBE), chemical and physical vapor deposition (CVD and PVD) of materials are very well controlled ways of depositing material [13]. One can either first make small particles and deposit those particles on a substrate, or one can deposit an amount of material, and have the deposit aggregate into particles on the support. In cluster beams one can select clusters with a specific mass and soft-land these particles on a surface. A rather clean (contaminant free) materials can be deposited while employing PVD techniques in UHV conditions.

The aim of this thesis was to investigate the activities of so-called monolayer vanadium oxide catalysts towards methanol oxidation reaction. When supported on another oxide material, monolayer vanadium oxide catalysts have been classified as a good candidate for this reaction owing to their enhanced selectivity towards formaldehyde. The model systems which provide the possibility to study the catalytic processes at the molecular level are thus worthwhile in order to envisage their functionalities. The thin silica films grown on a Mo(112) substrates were the support of choice. Even though a single crystal silica film had been grown on this substrate, its structure, thickness, surface termination, etc. were unknown. PVD technique was employed in order to deposit vanadium oxide catalysts on silica film; however a method was required to prepare hydrated and dehydrated catalysts. Hydrated/dehydrated states of vanadium oxide play an important role in catalytic performances so detail understanding of their activities in methanol oxidation reaction was crucial.

The present thesis has been structured as follows. The detailed knowledge of the surface structure of the silica films is the crucial first step in obtaining information about their interaction with vanadium oxide particles. This was accomplished by using a number of experimental tools and their theoretical working principles are described in Chapter 2. Film preparation and metal deposition methods both involve oxygen treatment and thus it is worth taking a closer look at the interaction of oxygen with a clean Mo(112) surface in the first place. Chapter 3 deals with a concept, one dimensional oxide formation, and covers the fundamental findings related the type of a surface oxide layer forming on Mo(112). Then, the geometric structure and properties of silica films grown on this surface are discussed in Chapter 4. Electronic and vibrational properties, thickness, growth strategies and defect structures are well-documented. Chapter 5 explains the interaction of water with the silica film and discuses the results in the light of the information provided in Chapter 4. Similar methodology is followed in Chapter 6, which mainly deals with the deposited vanadium oxide particles. Chapter 7 addresses the importance of surface termination of there vanadium oxide particles taking methanol adsorption as a case study. Finally, Chapter 8 summarizes the thesis.

CHAPTER 2

EXPERIMENTAL TECHNIQUES

The work was performed by employing a combination of experimental techniques including x-ray photoelectron spectroscopy (XPS), ultraviolet photoelectron spectroscopy (UPS), infrared reflection absorption spectroscopy (IRAS), scanning tunneling microscopy (STM), low energy diffraction (LEED), and temperature programmed desorption (TPD). The following sections were devoted to describe the fundamentals of these techniques.

2.1 Photoelectron Spectroscopy

Photoelectron spectroscopy has attracted a lot of attention for its unique properties and has been used in many fields like the study of heterogeneous catalysis, corrosion prevention, and tribology as well as to new materials development and semiconductor technology. One of the most striking properties of this technique is its chemical sensitivity. The electrons that are photo-emitted in the photoemission process have a particular binding energy which is a fingerprint of the elements present in the sample. Moreover, also different types of bonds affect these binding energies creating the so called chemical shifts which are useful to distinguish between atoms or molecules in different chemical or structural environments. The other important property is the surface sensitivity of this technique. In fact, one of the main reasons to use electrons in surface science is the inelastic mean free path of the electrons in matter. The mean free path of electrons with kinetic energy between 50 and 100 eV is less than 10 Å (1 nm) [14]. This means that the photo-electrons detected without energy loss originate from the first few layers of the solid. This renders photoemission spectroscopy suitable to identify the chemical elements present on a surface and to gain insight on the actual electronic structure of the surface itself.

The photoemission event from a solid takes place when electromagnetic radiations, i.e.; the photons of a proper source hit the solid and kick out electrons that are detected outside. Obviously, the energy of the photons, hν, has to be high enough in order to remove the electron from the proper core level and lets it overcome the work function φ of the solid. The energy distribution of the electrons detected outside reflects in this way the density of states inside the solid. This is schematically shown in Figure 2.1. If the binding energies are referred to the Fermi level E_F, E_b^F, a quantity that can be easily measured in the photoemission spectrum from a metal, then the energy with respect to the vacuum level E_b becomes [15]:

$$E_b = E_b^F + \varphi \tag{2.1}$$

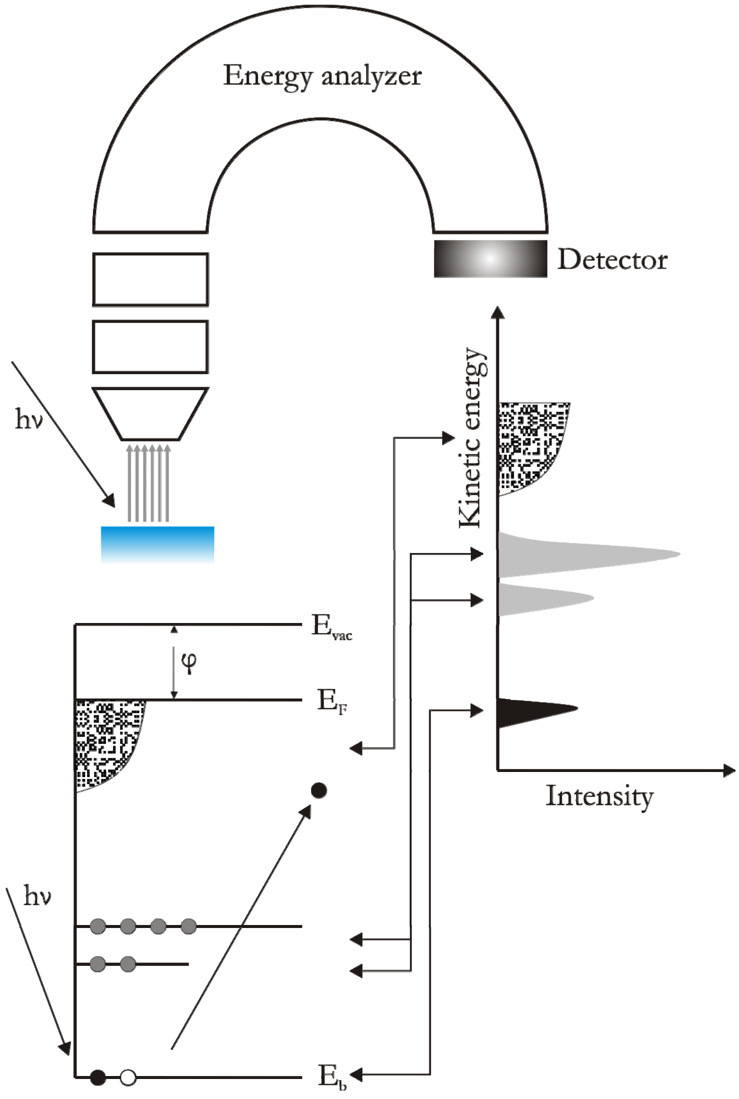

Figure 2.1 Schematic representation of the photoemission process. The circles represent the electrons in the core levels.

The kinetic energy of the electrons in the vacuum level is given by

$$E_{kin} = h\nu - E_b^F - \varphi \qquad 2.2$$

Once the electron is in the vacuum level, in order to enter in the analyzer, its energy is changed by the difference in the work function between the electron energy $\varphi_{analyser}$ and the sample.

$$E_{kin}^{meas} = E_{kin} - \varphi_{analyzer} = h\nu - E_b^F - \varphi - \varphi_{analyzer} = h\nu - E_b^F - \Delta\varphi \qquad 2.3$$

Depending on the energy of the photons used to ionize the sample, the photoemission technique can be divided into two main branches, namely UPS and XPS. The UPS, performed with low photon energies, deals mainly with the valence levels while in XPS the higher energy of the photons allows to ionize deeper electronic core levels.

In the ionization event, the ionized electron leaves a system on a time-scale dependent on the kinetic energy. For photon energies well above the ionization potential (~10 eV above ionization potential), the ionization event can be considered to be an instant (sudden approximation) process, taking place in the order of 10^{-17} s (0.01 fs). In the sudden approximation the electrons do not have time to change their distribution according to the new final states. Thus, the final states are thought to be populated according to the overlap with the initial state distribution. Since the overlap between the unrelaxed and relaxed orbitals is not perfect; a part of the energy is deposited into low-energy excitations, giving rise to satellite (shake-up) structures in the photoelectron spectrum, in addition to the highest kinetic energy "main" line corresponding to the relaxed case.

The excited electron on the other hand is either trapped in a bound state or leaves slowly (if close to the IP). Here, at so called adiabatic limit, the process is sufficiently slow that the system adjusts to the effective potential in an instantaneous, self-consistent way [16]. The adiabatic limit is a theoretical construct based on the experimental fact that no satellites are found for energies below or close to IP, and the IP is the same as the "main" line measured in the sudden limit of XPS. To understand the energetics of the relaxed electronic states in the presence of a core hole, one often makes use of the equivalent core approximation. In fact, since the remaining electrons do feel the ionization, they reorganize themselves to the new potential. This effect depends on the kinetic energy of the emitted electron. In the case of low kinetic energy, we are in the adiabatic limit in which the N-1 electrons system is left fully relaxed, i.e. in the ionic state with the lowest energy. In this case the ejected electron picks up the full relaxation energy thus increasing its kinetic energy. Large relaxation energy implies that the initial and final state wave functions are very different. The adiabatic approximation is valid in the time regime of 1-0.1 fs.

The fast electronic excitation in XPS can be accompanied by the population of vibrationally excited states. This is due to the Franck-Condon principle which states that the inter-nuclear distance can be assumed to be constant during the fast electronic excitation process. During each absorption event the atoms can thus be assumed to be structurally frozen. If the ground and the core excited state electronic potentials differ, the overlap of the vibrational wave functions is non-zero for not only the lowest vibrational state. In addition to the main line there are vibrational satellites created, with amplitudes related to the corresponding FC factors. Both discrete vibrational excitations and quasi-continuous phonon bands must be considered (e.g. larger molecules and solids).

In a metal, the valence electrons available in the conduction band are very mobile and therefore can flow to the site of the core-hole, screening in this way its positive charge. This means that the core ionized atom is a neutral atom with a core hole, compared to the free atom case whose final state is an ionic state. In the adiabatic limit, the full energy coming from the valence electrons is transferred to the emitted electron. Thus, its kinetic energy is higher than from the atom in its free state, by an amount called inter-atomic relaxation energy.

In the sudden approximation it is expected to see well separated shakeup and shake-off related features in the spectrum as explained before for the free atom case. This does not happen for the atom in the solid because its excited states now form a continuum in the valence band. In this case electron-hole pairs around the Fermi level are excited. These low energy excitations give rise to a low kinetic energy tail to the observed photoemission peak [17]. The most important conclusion of these studies was that the transition metals exhibit larger asymmetry than noble metals. The reason of this is that the transition metals have higher density of states at the Fermi level which results in higher probability of core-hole creation.

2.1.1 Photoelectron Cross-section

The total relative intensity of a spectroscopic line is partly dependant on the transition probability, i.e. the photoelectron cross-section, σ. A starting point for the discussion is Fermi's golden rule. The phenomenon that some spectroscopic lines have more relative intensity than others can be explained by the overlap between quantum mechanical wave functions. In general conceptual terms, a transition rate depends upon the strength of the coupling between the initial and final state of a system and upon the number of ways the transition can happen (i.e. the density of the final states). If it is assumed that the wavelength of the radiation is large compared to the dimensions of the excitation volume (i.e. the dipole approximation) the dipole operator, r, can be used yielding Eq. 2.4.

$$\sigma \propto \left|\langle \psi_f | r | \psi_i \rangle\right|^2 \delta\left(E_f^{N-1} + E_k - E_i^N - h\nu\right) \tag{2.4}$$

In Eq. 2.4 ψ_i is the total initial wave function of the system and ψ_f is the total final wave function of the system. As the equation is written, the total initial wave function includes N electrons in ground state and the total final state wave function includes N-1 electrons in a core excited orbital system plus one photoelectron. Depending on the definition of the spectroscopic core line intensity, the right hand side of Eq. 2.4 should be multiplied by the appropriate density of states. Atomic subshell ionization cross sections have been calculated for the pure elements with reasonable accuracy using the dipole approximation. Theory and experiments show that the ionization cross-section is very different between orbitals and depends on the energy of the incoming photon.

2.1.2 Analyzing Photoemission Spectra

Line shape of photoemission spectra can be decomposed into several contributions, the most important being the natural lifetime and the Gaussian broadening.

Life time broadening

A photoemission peak has an intrinsic width which is due to the finite lifetime of the core hole. Its decay can be either radiative or non-radiative [18]. These processes involve some of the orbitals that have a lower binding energy than the excited core level. The influence of the chemical surrounding on the decay rate is usually quite small and therefore the intrinsic width is essentially an atomic property. Lifetime of the core hole (τ) is of the order of some femto seconds, the peak will have a natural width of 100-200 meV. This broadening, always present in any photoemission spectrum, is described with a Lorentzian distribution (Eq. 2.5), whose full width at half maximum (FWHM) is denoted with Γ and E_0 is the position for the maximum intensity I_0

$$I_{Lor}(E_{kin}) = I_0 \frac{\frac{\Gamma}{2\pi}}{(E_{kin} - E_0)^2 + \frac{\Gamma^2}{2\pi}} \tag{2.5}$$

Gaussian broadening

The Gaussian broadening of a core level photoemission peak is mainly given by three contributions namely, the experimental energy resolution, the vibrational and inhomogeneous broadening. The experimental energy resolution is due to the fact that the photon source has a finite line width and the electron energy analyzer has a certain resolving power. The increased energy resolution allows distinguishing very fine structures in the spectra. The vibrational broadening, in molecules or solids, is given by the excitation of low energy vibrational modes in the final state. For solids, while multiple phononic losses end up in the low kinetic energy region of the so-called true secondary electrons, the intrinsic phonons induce a broadening of the photoemission peaks which can, in most cases, be described by a Gaussian distribution [19]. The inhomogeneous broadening is due to the presence in the spectrum of unresolved chemical or structural shifted components. These three effects are represented by a Gaussian distribution with FWHM, σ_{Gaus},

$$I_{Gaus}(E_{kin}) = I_0 \exp\left(-\frac{\ln 2 (E_{kin} - E_0)^2}{\frac{\sigma_{Gaus}}{2\pi}} \right) \qquad 2.6$$

Doniach-Ŝunjić (DS) line-shape

In the case of a metal, the shape of the peak is the convolution of a Lorentzian life time broadening, of a Gaussian broadening plus an asymmetry due to the creation of electron-hole pairs at the Fermi level. The most commonly used line shape in analyzing photoemission spectra from metals is the DS line shape calculated by Doniach and Ŝunjić [20]. It is obtained by taking the convolution of a singularity function

$$f(E) \propto \frac{1}{(E_0 - E)^{1-\alpha}} \qquad 2.7$$

representing the core-hole excitation in metals for a constant density of states around the Fermi level at T=0 K, with the Lorentzian broadening of Eq. 2.5. The calculated intensity is:

$$I_{DS}(E_{kin}) = I_0 \frac{\Gamma_E(1-\alpha)}{\left((E_0 - E_{kin})^2 + \frac{\Gamma^2}{4} \right)^{\frac{(1-\alpha)}{2}}} \xi(E_{kin}) \qquad 2.8$$

$$\xi(E_{kin}) = \cos\left[\frac{1}{2}\pi\alpha + (1-\alpha)\tan^{-1}\left(2\frac{(E_0 - E_{kin})}{\Gamma} \right) \right] \qquad 2.9$$

where Γ_E is the so-called Γ function defined as

$$\Gamma_E(x) = \int_0^\infty t^{x-1} e^{-t} dt \qquad 2.10$$

Here, α is the asymmetry parameter. The T=0 K approximation implies that there are no electron-hole pair excitations in the neutral ground state. At finite temperature the core level should exhibit additional broadening due to thermal excitations of the conduction electrons. However, this effect is quite small compared to the phonon or lifetime broadening and is well approximated with an additional Gaussian broadening. In all the core level lines described in this thesis, dealing with metals like Mo, and oxides like silica and vanadium oxide, the deconvolution of the spectra have been performed using the DS line shape, convoluted with a combined Lorenzian-Gaussian broadening.

Background subtraction

Extrinsic inelastic scattering occurs when the photoelectron on its way out of the material is scattered by non-localized electrons or electrons localized at other atoms. If the kinetic energy of the photoelectron is high the probability of forward inelastic scattering is high. This implies that a detected photoelectron can have been scattered one or several times, with some kinetic energy loss for each event. The amount of energy loss for each inelastic scattering event can be viewed as a continuous probability function depending on the kinetic energy of the photoelectron and the type of material. As a result of the inelastic scattering the core level photoemission spectra have a seemingly featureless rising background. Calculation of the background profile under a peak shape that have a width of only a few electron volts can however be performed without significant information loss by using Shirley's method [21]. In Shirley's method the spectrum is viewed as a series of discrete intensity measurements called channels. Each channel represents a constant spectroscopic binding energy interval. Start and end binding energies for the fit are chosen from “featureless” parts of the spectrum on each side of the peak. If the signal in the ith channel, s_i, is the sum of a background, b_i, and peak, p_i, Shirley’s method gives:

$$\left\{ \begin{array}{l} b_i = k\sum_{j=i+1}^{N} p_j \\ s_i = b_i + p_i \end{array} \right\} \qquad 2.11$$

In the above Eq. 2.11, k is a fitting parameter and N is the number of channels. The numbering of the channels is such that the channel representing the highest binding energy gets the lowest number. Thus, the background rises on the high binding energy side of the peak. The equation system 2.11 is iterated to find the value of k and the background intensity vector, b_i (i = 0-N).

2.1.3 Core Level Chemical Shifts

The ability to observe chemical shifts makes core level photoelectron spectroscopy a very powerful technique. From the ground state orbital energy point of view the chemical shifts originate from different bonding structures. For example, an oxidized atom obtains higher core level binding energies compared to the pure element due to the nature of the bonding. An oxidized atom donates one or more valence electrons completely or partly to more electronegative elements. The core level orbitals for the oxidized atom experiences reduced screening from valence orbitals and will therefore be more strongly attracted by the core. This is a quite general behavior that can be observed on many metal atoms where changes in the oxidation state of the metal are usually accompanied by binding energy shifts towards higher binding energies. The chemical shifts span an energy range from a few meV to several eV [22], thus enabling an identification of binding partners and a distinction of single or double covalent bonds.

The chemical shift is given by:

$$\Delta E_b = E^f_{tot,A}(N-1) - E^i_{tot,A}(N) - E^f_{tot,B}(N-1) - E^i_{tot,B}(N) = \Delta^f_{A,B} - \Delta^i_{A,B} \qquad 2.12$$

where A and B denote the system A and system B respectively and A, B the total energy difference between the two systems. It is clear then that the chemical shift is not just an initial state effect but one has to take into account also the system with the core-hole, i.e. the final state effects to achieve a good description of such shifts.

2.2 Low Energy Electron Diffraction

The wavelength of an electron due to the wave-particle duality nature of matter is given by the de Broglie relation:

$$\lambda = \frac{h}{2m_e E} \qquad 2.13$$

where λ is the wavelength of the electron wave, h is the Planck constant, m_e is the electron mass and E is the kinetic energy. Similar to photoelectron spectroscopy, an electron with a wavelength on the order of interatomic spacing (~0.1 nm) has a kinetic energy of approximately 150 eV and the resulting high surface sensitivity forms the basis for LEED from solid surfaces. A second feature that contributes to surface sensitivity in LEED is the fact that backscattering probability of electrons is higher than that of forward scattering in the low kinetic energy regime. Electrons with energies in the range 20−400 eV that are elastically backscattered will form a diffraction pattern. The electron beam used at above 50 eV has typically a beam diameter of around 1 mm with a coherence width of approximately

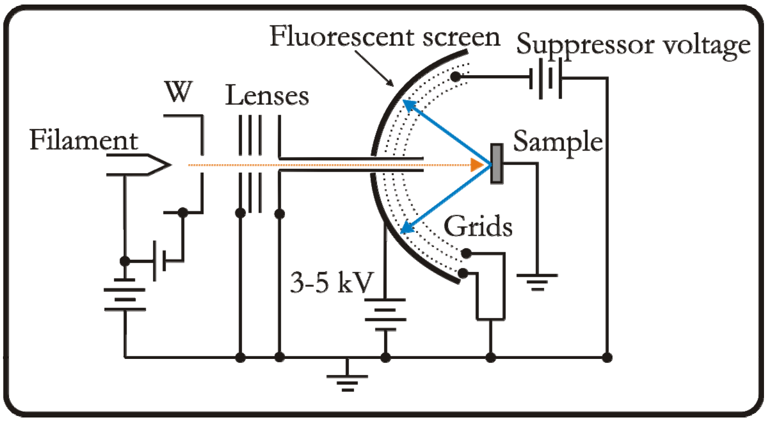

Figure 2.2 Schematic of a LEED optics for electron diffraction experiments. The integrated electron gun consist of heated filament (tungsten or LaB_6), a Wehnelt cylinder (W).

5−10 nm. The coherence width of the beam sets the limit for constructive interference and structural domains with a smaller diameter than the coherence width will not constructively add to the diffraction pattern but add diffuse background intensity. The observed diffraction pattern is therefore an ensemble average of structural domains (larger than the incident electron beam coherence width) within the electron beam. With this in mind, it is imperative to realize that the symmetry of the surface atom arrangement is at most the symmetry indicated by the LEED pattern.

A typical LEED arrangement is depicted in Figure 2.2. The electrons pass a lens system which collimates the electron beam. Afterwards the electrons hit the sample surface where they are coherently scattered by the regular arrangement of surface atoms. The diffracted electrons are detected on a fluorescent screen on which the diffraction pattern becomes visible. Electrons are not only elastically scattered but the majority amount looses energy via plasmon, phonon excitation. These electrons contribute to the diffraction pattern by a diffuse background. In order to avoid them the scattered electrons have to pass a retarding field which is applied to the grid. Only elastically scattered electrons pass and are accelerated towards the screen.

In order to be able to interpret the diffraction pattern it is good to recall the concept of reciprocal space which is well known from X-ray diffraction [23]. Here, methods for giving a geometric interpretation of the pattern are presented. This interpretation of the pattern allows finding the surface unit mesh. No information concerning the arrangement of the atoms in the unit mesh can be derived from this simple interpretation. In 2D space the 2D reciprocal space is spanned by the two unit vectors of the reciprocal unit mesh:

$$\vec{a}_1^* = 2\pi \frac{\vec{a}_2 \times \vec{n}}{\vec{a}_1(\vec{a}_2 \times \vec{n})}, \quad \vec{a}_2^* = 2\pi \frac{\vec{a}_1 \times \vec{n}}{\vec{a}_2(\vec{a}_1 \times \vec{n})}, \quad \vec{G} = h\vec{a}_1^* + k\vec{a}_2^* \tag{2.14}$$

where $\vec{a}_1$, $\vec{a}_2$, $\vec{b}_1$, and $\vec{b}_2$ are first and second real and reciprocal space unit vectors, respectively. $\vec{n}$ is the vector normal to the surface. This also means:

$$a_i^* \bullet a_j^* = 2\pi\delta_{ij} \tag{2.15}$$

$$\left|a_1^*\right| = 2\pi \frac{1}{\left|\vec{a}_1\right| \sin\gamma} \text{ and } \left|a_2^*\right| = 2\pi \frac{1}{\left|\vec{a}_2\right| \sin\gamma} \tag{2.16}$$

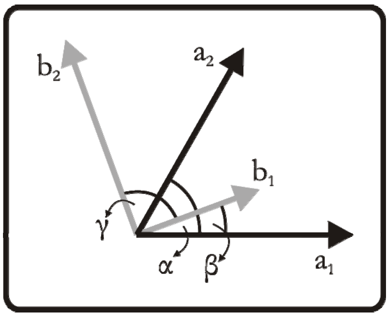

Figure 2.3 a_1 and a_2 correspond to the substrate unit cell vectors. b_1 and b_2 indicate the superstructure unit cell vectors. α is the enclosed angle between the substrate and γ is the enclosed angle between the superstructure unit cell vectors. The angle β accounts for a rotation of the superstructure with respect to the substrate.

where γ is the enclosed angle between $\vec{a}_1$ and $\vec{a}_2$. This construction is very useful upon considering the two dimensional Laue conditions which state:

$$\vec{a}\Delta\vec{k} = 2\pi h \text{ and } \vec{b}\Delta\vec{k} = 2\pi k \qquad 2.17$$

with $\Delta\vec{k} = \vec{k}' - \vec{k}$. They principally represent the conservation of energy and momentum between the incident wave vector $\vec{k}$ and the emerging wave vector $\vec{k}'$. These equations can be fulfilled whenever $\Delta\vec{k}$ equals a reciprocal lattice vector $\vec{G}$. In other words: Every point in the diffraction pattern corresponds to a reciprocal lattice vector or more theoretically: The diffraction pattern is the Fourier transformation of the surface structure in real space. By back transforming the reciprocal lattice via Eq. 2.14, 2.15, and 2.16, it is possible to analyze the surface structure.

Looking at clean non-reconstructed surfaces without any adsorbates gives a rather simple diffraction pattern. An overlayer structure with a rather large unit mesh and various domains may generate a complicated pattern. Domains are a form of long range imperfection in which distinct patches of the surface coexist. These different patches have mutually identical structures but they do not mesh together without breaks in the periodicity. Thus, domain boundaries occur over which the periodicity is broken. Here, it is time to introduce the matrix presentation of superstructures. If $\vec{b}_1$ and $\vec{b}_2$ are the overlayer unit cell vectors they can be built up by the substrate unit cell vectors $\vec{a}_1$, $\vec{a}_2$:

$$\vec{b}_1 = m_{11}\vec{a}_1 + m_{12}\vec{a}_2, \quad \vec{b}_2 = m_{21}\vec{a}_1 + m_{22}\vec{a}_2 \qquad 2.18$$

$$M = \begin{pmatrix} m_{11} & m_{12} \\ m_{21} & m_{22} \end{pmatrix} \qquad 2.19$$

The matrix M determines the superstructure of the unit cell in the most general form. The indices m_{ij} can be drives by simple trigonometric considerations:

$$M = \begin{pmatrix} \frac{|b_1|}{|a_1|}\left[\cos\beta - \sin\beta\cot\alpha\right] & \frac{|b_1|}{|a_2|}\frac{\sin\beta}{\sin\alpha} \\ \frac{|b_2|}{|a_1|}\left[\cos(\beta+\gamma) - \sin(\beta+\delta)\cot\alpha\right] & \frac{|b_2|}{|a_2|}\frac{\sin(\beta+\gamma)}{\sin\alpha} \end{pmatrix} \qquad 2.20$$

The meaning of the variables in Eq. 2.20 is illustrated in Figure 2.3.

Irradiation of surface structures and especially adsorbates by low energetic electrons may destroy the structures or lead to electron stimulated desorption. Therefore care must be taken when investigating delicate samples, i.e. low beam currents and short exposure

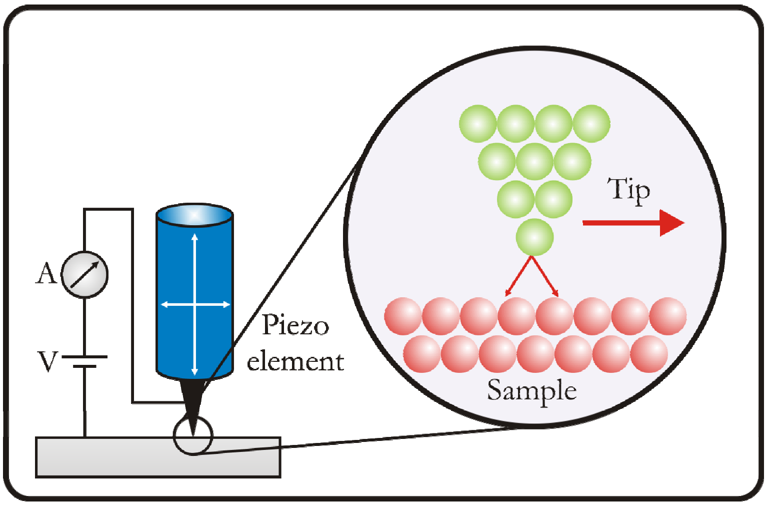

Figure 2.4 STM instrumental apparatus.

times. No information about exact atomic positions (e.g. adsorption sites) can be retrieved from the observed LEED pattern in itself. This is so because it is translationally invariant to the origin of the surface net. However, due to the very strong electron-matter interactions at low kinetic energies, which are the foundation for the surface sensitivity in the first place, multiple scattering events are highly probable and lead to intensity modulations of observed LEED spots as a function of kinetic energy of diffracting electrons. From the energy dependence of LEED spot intensities structural information can be obtained utilizing multiple scattering reconstructions of the energy dependence. For a more in-depth discussion on this topic, see ref. [24].

2.3 Scanning Tunneling Microscopy

The Scanning tunneling microscope was invented in 1981 by G. Binnig and H. Rohrer [25, 26] and within a few years it emerged to one of the most widely used tools in surface science. The STM makes use of the quantum mechanical tunnel effect: A sharp metallic tip is positioned a few Angstrom over a conductive surface and a voltage in the order of 1 V is applied. The potential barrier between tip and surface is larger than the electrons energy, thus forbidding a current flow in the classical picture. Nevertheless, the electronic wave functions of tip and surface, decaying into the junction gap, overlap each other, leading to a finite probability of tunneling for the electrons. The tunnel current is usually in the order of pico to nano Ampere (pA to nA) and depends exponentially on the distance between tip and sample, changing about one order of magnitude with 0.1 nm change in the tip-sample distance.

As shown in Figure 2.4, the instrument essentially consists of two electrodes: a sample and a tip, which can be scanned over the sample. In the typical working mode (called constant-current-mode) the tip is scanned line wise over a region of the surface and the tunneling current is kept constant by regulating the tip height (z) through a feedback loop. A map of the surface is obtained by assigning to each lateral x/y-position of the scanned region the tip height z(x,y). In this mode the tip follows roughly the corrugation of the surface, creating a nearly topological map. However, the STM image is also influenced by electronic effects. More precisely the tip moves on a surface of constant local density of states (LDOS) close to the Fermi energy. In general it is not trivial to distinguish between topologic and electronic effects.

In order to achieve high spatial resolution, the demands on stability and precision of the tip movement are extreme. For the tip positioning, piezoelectric crystals, called piezos in the following, are employed. These are materials which deform in dependence on the applied voltage. Microscope used to study surfaces in this thesis hangs at springs and is damped by an eddy current break. Furthermore, the whole STM chamber rests on pneumatically damped feet. Typically the lateral resolution is in the order of 1 Å and the vertical resolution is in the order of 1 pm.

2.3.1 Theoretical Description of the Tunneling Process

A variety of theories have been developed to describe the tunneling process taking place in STM. The fundamental works will be briefly reviewed in the following. In a first schematic approach, the tunnel-effect is treated one dimensionally and time-independent. In this approximation, the problem can be solved analytically. The elastic tunneling of an electron of energy E through a constant potential barrier V_0 can be described by a stationary Schrödinger equation:

$$\left[\frac{1}{2m}\left(\frac{\hbar}{i}\frac{\partial}{\partial x}\right)^2 + V(x)\right]\Psi(x) = E\Psi(x) \qquad 2.21$$

Inside the metal, the electron is treated as a free particle, while in the tunneling region (barrier of length s) the potential is higher than the energy of the electron:

$V(x) = 0$ for $x \notin [0,s]$ (inside the metal),

$V(x) = V0$ for $x \in [0,s]$ (inside the barrier).

The solutions have the form:

$$\Psi(x) = \exp(\pm ikx) \text{ with } k = \sqrt{\frac{2m(E)}{\hbar^2}} \text{ for } x \notin [0,s] \text{ and} \qquad 2.22$$

$$\Psi(x) = \exp(\pm \varkappa x) \text{ with } \varkappa = \sqrt{\frac{2m(V_0 - E)}{\hbar^2}} \; x \in [0,s] \qquad 2.23$$

An incident wave is partly reflected and partly transmitted by the barrier and the transmission coefficient T can be determined by wave-matching of the amplitude and the first derivative. Energy diagram and wave functions are shown schematically in Figure 2.5. For the transmission coefficient one obtains:

$$T = \frac{1}{1 + \frac{(k^2+\varkappa^2)^2 \sinh^2(ks)}{4k^2\varkappa^2}} \qquad 2.24$$

For a large barrier ($s\varkappa >> 1$), T can be approximated [27] as:

$$T \approx \frac{16k^2\varkappa^2}{(k^2+\varkappa^2)^2}\exp(-2\varkappa s) \qquad 2.25$$

This result shows the exponential relation between transmission coefficient and tunneling distance s and yields to the exponential dependence of the tunneling current, which is proportional to the transmission coefficient, on the tip-sample distance. This exponential dependence is the fundament for the high spatial resolution of the scanning tunneling microscope.

The solution can be expanded to a non-constant potential V(x), yielding the transmission coefficient

$$T \cong \exp\left[-\frac{2}{\hbar}\int_0^s \sqrt{2m[V(x) - E]}dx\right] \qquad 2.26$$

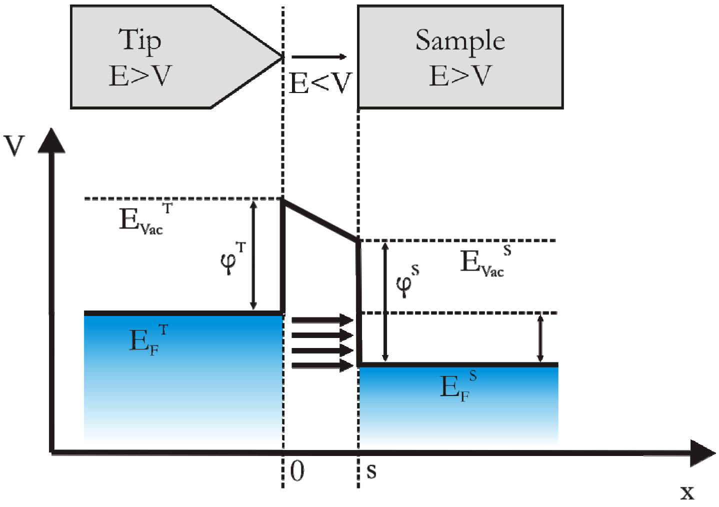

Figure 2.5 Schematic energy diagram in one dimension, in case of electrons tunneling from the tip to the sample. $E_F^{T/S}$ is the tip/sample Fermi energies, $E_V^{T/S}$ is the tip/sample vacuum levels, and $\varphi^{T/S}$is the tip/sample work functions, respectively. V_{Tunnel} is the tunneling bias.

However, a three-dimensional treatment is required to describe the tunneling geometry to treat the problem as a time-dependent perturbation. The transmission probability from an unperturbed state on one side of the barrier to an unperturbed state on the other side, considering the tunneling region as a perturbation, is calculated in analogy to Fermi's Golden rule. The transition probability from the tip state ψ_t to the sample state ψ_s is called the tunneling matrix element M_{ts}:

$$M_{ts} = \frac{-\hbar^2}{2m}\int dS(\psi_t^*\nabla\psi_s - \psi_s\nabla\psi_t^*) \tag{2.27}$$

The integration is done over a surface S between tip and sample, through which the entire tunneling current flows. The transition rate is $|M_{ts}|^2$. For the tunneling current one obtains:

$$I = \frac{2\pi e}{\hbar}\sum_{t,s}\left[f(E_t)(1-f(E_s+eV)) - f(E_s+eV)(1-f(E_t))\right]\times|M_{ts}|^2\delta(E_t-(E_s-eV)) \tag{2.28}$$

where f(E) are the Fermi functions and E_t and E_s are the energies of the unperturbed wave functions of tip and sample, respectively. The Fermi functions enter here because only tunneling from an occupied to an unoccupied state is allowed. As electrons can tunnel in both directions, from tip to sample and from sample to tip, partly compensating each other, the tunneling matrix element has to be summed over all possible tip and sample states. The delta function is expression of energy conservation during the tunneling process.

Tersoff and Hamann [28] calculated the tunneling current in case of STM and allowed the theoretical interpretation of STM images. They assumed the relatively simple geometry of a spherical tip and a plane substrate (Figure 2.6), therefore using s-like wave-functions (angular momentum quantum number $l = 0$) for the tip.

In the limit of small voltage ($V \rightarrow 0$) and low temperature ($T \rightarrow 0$) Eq. 2.28 reduces to:

$$I = \frac{2\pi e^2}{\hbar}V\sum_{t,s}|M_{ts}|^2\delta(E_s-E_F)\delta(E_t-E_F) \tag{2.29}$$

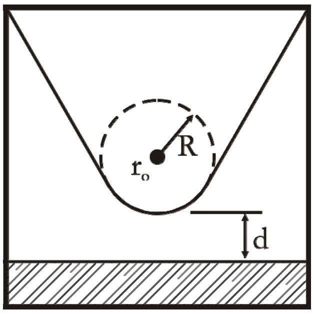

Figure 2.6 Schematic picture of tunneling geometry in the Tersoff-Hamann model. The probe tip has arbitrary shape but is assumed locally spherical with a radius of curvature R, where it approaches nearest the surface. The distance of nearest approach is d. The centre of curvature of tip is r_0 [28].

However, to calculate the tunneling matrix element, the wave-functions of sample and tip have to be defined. The sample wave-function is assumed to decay exponentially outside the metal and to propagate freely parallel to the surface. The decay rate κ outside the metal depends on the work function of the metal φ. Assuming the s-like wave function of the spherical tip with radius R at position r_0, the matrix element can be calculated:

$$M_{ts} = \frac{2\pi\hbar^2}{m}\Omega_t^{-1/2} R\exp(\varkappa R)\sum_s \left|\psi_s((\vec{r_0})^2\right|\delta(E_s - E_t) \text{ with } \varkappa = \frac{\sqrt{2m\varphi}}{\hbar} \qquad 2.30$$

where Ω is the volume of the sample. Using Eq. 2.29 the tunneling current is evaluated. One obtains:

$$I = \frac{32\pi^3 e^2 V\Phi^2 R^2 \exp(2\varkappa R)}{\hbar\varkappa^4} D_t(E_F)\sum_s \left|\psi_s((\vec{r_0})^2\right|\delta(E_s - E_t) \qquad 2.31$$

where $D_t(E_F)$ is the density of states per unit volume of the tip at the Fermi energy E_F. The sum in Eq. 2.31 is identified as the local density of states at E_F of the sample at the position of the tip. This is often referred to as local density of states (LDOS):

$$\varrho(\vec{r_0}, E_F) = \sum_s \left|\psi_s((\vec{r_0})^2\right|\delta(E_s - E_t). \qquad 2.32$$

Substituting typical values in Eq. 2.31 one obtains

$$I = 0.1R^2 V\exp(2\varkappa R)\varrho(\vec{r_0}, E_F) \qquad 2.33$$

where the distance is in a.u. and energy in eV. This result means that the STM is measuring the contour of constant LDOS of the sample. Since

$$\psi_s(\vec{r_0})^2 \propto \exp\bigl(-2\varkappa(R+s)\bigr) \qquad 2.34$$

One obtains once again the exponential distance dependence for the tunneling conductance σ_T, i.e.

$$\sigma_T \propto \exp(-2\varkappa s) \qquad 2.35$$

Substituting a typical metal work function of φ = 4.5 eV, one can estimate the tunneling resistance as

$$R \propto \exp(As) \qquad 2.36$$

With A = 2.18 and s in Å, showing that R increases approximately one order in magnitude, when s increases 1 Å. In combination with the contact resistance R_0 (corresponding to s = 0), which can be experimentally measured, the tip height can be approximately estimated for a given tunneling resistance, obtaining

$$s \approx \log(\frac{R}{R_0}), \qquad 2.37$$

With s in Å, where the contact resistance on the metal surfaces is typically $R_0 \approx 10k\Omega$ [29].

2.4 Infrared Reflection Absorption Spectroscopy

The use of vibrational spectroscopy to study surface bound species, as well as interfacial reactions, is well established [30-32]. The well-ordered model surfaces are prepared on metal substrates and thus, the reflective nature of the metal interface permits reflectance methods to be utilized in the analysis of surface bound species. The molecular geometry and chemical environment, as well as identity, of adsorbates on surfaces can be determined from this powerful spectroscopic technique. For the thin films on metal substrates, the method involves an incident IR beam penetrating the thin film, followed by reflection at a metal surface and the subsequent retransmission through the film, before the beam enters the detector. An analysis of the reflected beam provides information on the molecular vibrations in the surface film and can be used to identify the surface species.

The IR process is governed by a direct absorption of a photon (usually from the vibrational ground level) to an excited state. The transition moment for a transition between lower and upper vibrational wave functions ψ''_v and ψ'_v can be given by

$$R_v = \int \psi'_v \mu \psi''_v dx \qquad 2.38$$

where x is (r-r_e), the displacement of the internuclear distance from equilibrium. For example, the dipole moment μ is zero for a homomolecular diatomic in the gas phase, resulting in R_v=0 and all vibrational transition being forbidden. For a heteronuclear diatomic molecule dipole moment is nonzero and varies with x. This variation can be expressed as a Taylor series expansion

$$\mu = \mu_e + \left(\frac{d\mu}{dx}\right)_e x + \frac{1}{2!}\left(\frac{d^2\mu}{dx^2}\right)_e x^2 + \ldots \qquad 2.39$$

where the subscript 'e' refers to the equilibrium configuration. The transition moment of Eq. 2.38 now becomes

$$R_v = \mu_e \int \psi'_v \psi''_v dx + \left(\frac{d\mu}{dx}\right)_e \int \psi'_v x \psi''_v dx + \cdots \qquad 2.40$$

Since ψ''_v and ψ'_v are eigenfunctions of the same Hamiltonian, when $v' \neq v''$,

$$\int \psi'_v \psi''_v dx = 0 \qquad 2.41$$

Then Eq. 2.40 becomes,

$$R_v = \left(\frac{d\mu}{dx}\right)_e \int \psi'_v x \psi''_v dx + \cdots \qquad 2.42$$

In the case of $\Delta v = \pm 1$, a selection rule applies in IR spectroscopy that the dipole moment μ must alter with respect to the normal coordinate x during a vibration, which is formalized in Eq. 2.43,

$$\frac{d\mu}{dx} \neq 0 \qquad 2.43$$

Needless to say, the frequency of the incident light has to match a vibrational transition frequency to induce IR absorption. In the specific case of IRAS, an additional requirement denoted as the "metal surface selection rule" (MSSR) also applies [31]. This

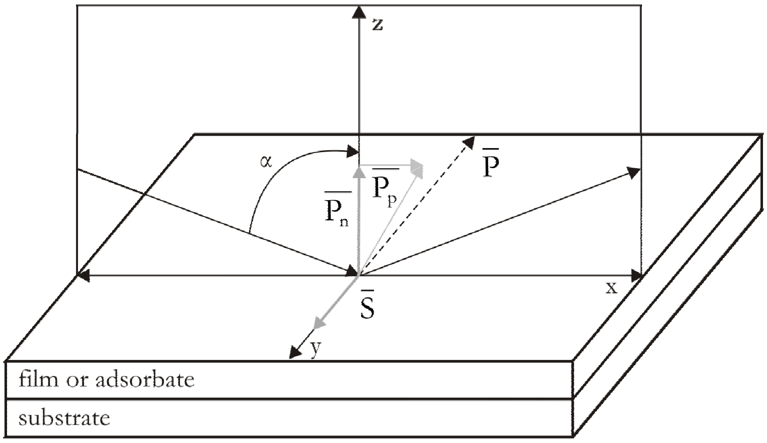

Figure 2.7 Infrared radiation impinging on a substrate can be resolved into two components.

rule stresses that a component of the dipole derivative is required to be along the surface normal in order to activate a molecular vibration. The origin of this selection rule stems from the fact that radiation polarized perpendicular to the plane of incidence (s-polarized) undergoes a phase shift of approximately 180° upon reflection from a metal surface, with the concomitant cancellation of an s-polarized electric field in the surface region. Therefore vibrations aligned along the surface plane will not give rise to any signal in an IRA spectrum. The interaction of p-polarized light with the metal surface is markedly different, since the phase shift is dependent on the angle of incidence, with a constructive interference prevalent for high angles of incidence, measured from the surface normal [31]. Figure 2.7 summarizes components of polarized light on a planar surface. The s-polarized light only has a component parallel to the surface in the y direction (S), but the p-polarized radiation has components that are parallel (Pp) and perpendicular (Pn) to the substrate. The electric field vector of the impinging IR beam, that is normal to the surface, excites dipole-active vibrational modes of surface bound molecules. The perpendicularly polarized radiation, when reflected from the surface, results in a net doubling of the electric field vector amplitude. Therefore, only surface bound molecules with active IR modes that have a portion of their transition dipole moment perpendicular to the surface will be observed in IRA spectra. In addition to this surface selection rule, Greenler [31], using Maxwell's equations, determined that the p-polarized component of electromagnetic radiation that is perpendicular to the surface reaches a maximum at grazing angles of incidence (α). Therefore, IRAS experiments are performed using IR radiation at or near an incident angle of 84°. By employing the surface selection rule, the orientation of the adsorbed molecules can be deduced [33].

Fourier transform techniques are used to generate spectra. In the course of spectral generation, an interferogram of sample signal is collected using a Michelson interferometer, which measures all of the infrared frequencies simultaneously by dividing a beam of radiation into two paths and then recombining the two beams after a path difference has been introduced. A condition is thereby created under which interference between the beams can occur. A sample form of the Michelson interferometer is shown in Figure 2.8. It consists of two mutual perpendicular plane mirrors, one of which can move along an axis that is perpendicular to its plane. The movable mirror is moved at a constant velocity. Between the fixed mirror and movable mirror is a beam-splitter, where beam of a radiation from an external source (a SiC glowbar) can be partially reflected to the fixed mirror and partially transmitted to the movable mirror. After the beams return to the beam splitter, they interfere and are again partially reflected and partially transmitted. Because of the

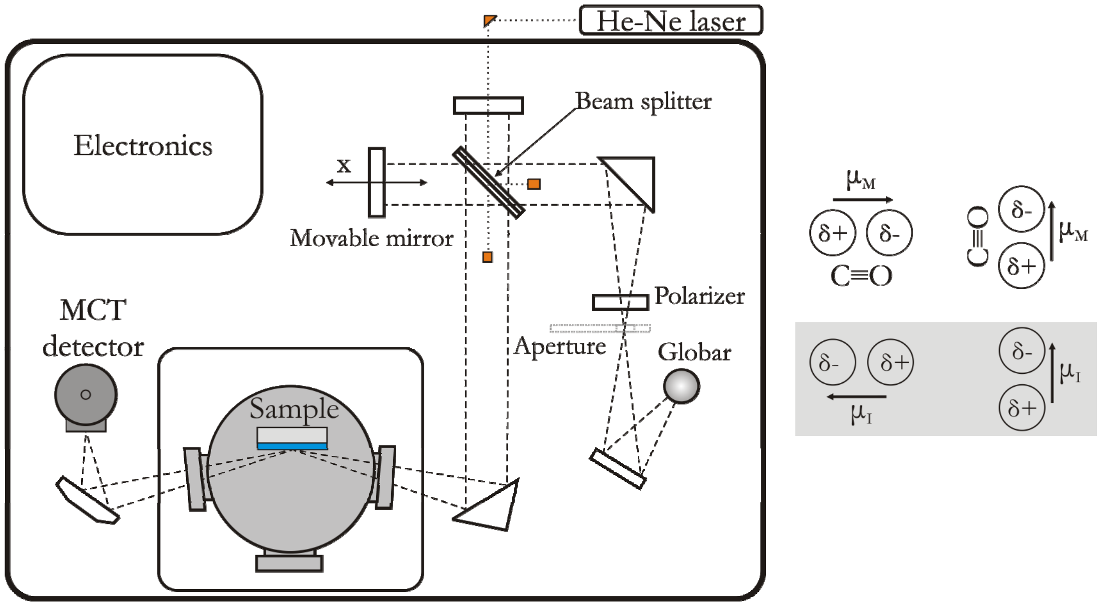

Figure 2.8 A schematic representation of an infrared spectrometer (left) and dipole moment of CO adsorbed on a surface in two different orientations (right).

effect of interference, the intensity of each beam passing to the detector and returning to the source as a function of the path difference ultimately yields a spectral information. Then, the spectrometer acquires and digitizes the interferogram and performs a mathematical function known as a Fourier transform. This function deconvolutes all individual cosine waves that contribute to the interferogram. The result of the transformation is a plot of intensity versus wavelength or frequency.

2.5 Surface Processes

As the atom/molecule approaches the solid surface from gas-phase the interaction with the surface starts becoming non-negligible. Depending on the nature of the interaction-potential there is a certain probability that the atom/molecule is not immediately scattered back into the gas-phase but comes to reside at the surface. The probability of this event is referred to as the sticking coefficient (S) and takes a value from 0 to 1 where the value of 1 means that all atoms/molecules impinging the surface spend significantly longer time at the surface compared to in the direct scattering process. Once adsorbed a wealth of surface phenomena can occur such as:

- diffusion at the surface
- surface reaction, e.g. association with another adsorbate (or entity of the solid surface) or
dissociation
- desorption of the original molecule or product of surface reaction

In this section only the very basics of adsorption, desorption and surface reaction kinetics will be covered. For a more thorough and proper treatment see e.g. textbooks by Chorkendorff-Niemantsverdriet [34] and Masel [35].

2.5.1 Adsorption Kinetics

The rate of adsorption is governed by the rate of impingement of molecules at the surface and the sticking coefficient. The impingement rate or flux (F) of molecules striking the surface per unit area is given by the Hertz-Knudsen equation:

$$F = 3.51 \mathrm{x} 10^{22} \frac{T}{\sqrt{MT}} \tag{2.44}$$

where M is the average molar weight of the impinging species and T is the absolute temperature. The rate of adsorption (R_{ads}) is simply

$$R_{ads} = F \times S \tag{2.45}$$

It is essential here to mention that S has dependence on the temperature of the substrate as well as on the temperature of the incoming molecule, but more importantly it strongly depends on the number of available adsorption sites at the surface, decreasing with decreasing number of available adsorption sites. In the case of high availability of surface adsorption sites, and low temperatures at which adsorbate can form condensed multilayers, one can assume S to be essentially constant.

2.5.2 Physisorption and Chemisorption

There are two principal modes of adsorption and they are physisorption and chemisorption. Physisorption is a weak bonding, typically around 0.2 eV and below, characterized by the lack of a true chemical bond between adsorbate and surface, i.e. no electrons are shared, not saying that there can not be significant electron rearrangement in the molecule upon adsorption. The energetic contributions to this mode of adsorption is the van der Waals interaction (attractive but the weakest form of bonding) and a repulsive part originating from the kinetic energy increase of electrons in atoms at short distances from each other as a result of the Pauli exclusion principle. The repulsive part is generally referred to as “Pauli repulsion”. Chemisorption includes also all other types of interactions resulting in a stronger net chemical bonding to the surface compared to physisorption.

Activation barriers

So far we have not considered the energetics of different possible surface processes. The dynamics involved in changing from one state to another is determined by the potential energy landscape in which the system evolves. The trajectory (time evolution) of e.g. a diatomic molecule in the potential energy landscape at the solid surface is referred to as the reaction coordinate.

In Figure 2.9 very simplified potential energy curves for a generic diatomic molecule approaching and interacting with a solid surface are shown. Initially upon approaching the surface from the gas-phase the weak Van der Waals interaction sets in. If the molecule can loose kinetic energy upon interacting with the surface, it may be trapped in the weak attractive potential and become physisorbed at the surface. The energy of adsorption, E_{ads}^{phys}, is here the energy change upon adsorption. It is a negative value since it follows from a net attractive interaction.

Through substantial charge rearrangement in the molecule and the surface, the molecule may form a proper chemical bond to the surface and become chemisorbed with adsorption energy E_{ads}^{chem}. Following the minimum energy path, shown as the thicker solid line in Figure 2.9, from the bottom of the well of the physisorbed state to the associatively (not dissociatively) chemisorbed state we note there to be a small energy barrier to be overcome. The barrier between the physisorbed state and the chemisorbed state is usually

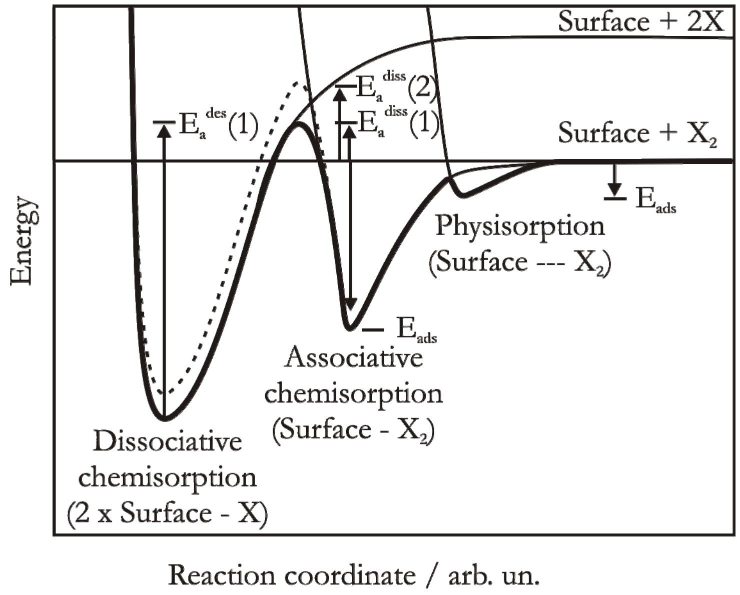

Figure 2.9 Schematic and simplified potential energy diagram for the interaction of a diatomic molecule, X_2, approaching and interacting with a surface. At first upon approaching, Van der Waals interactions may attract the molecule into a weakly bound, physisorbed, state. From this physisorbed state it may proceed into an associative (non-dissociated) chemisorbed state. If the activation barrier E_a^{diss} is overcome the molecule may dissociate into two chemisorbed atoms. The energy required to desorb these atoms again is E_a^{des}. Also shown are the corresponding adsorption energies, E_{ads} for the physisorbed and associatively chemisorbed states.

small but system-dependent. Molecular chemisorption may occur directly from gas-phase without passing through a physisorbed precursor-state.

Breaking the intra-atomic bond in the molecule requires a supply of energy allowing for the substantial charge rearrangement necessary. Approaching from gas-phase towards the dissociated state the molecule encounters a larger energy barrier, E_a^{diss}, which needs to be overcome. As shown in Figure 2.9, the curve crossing between the potential energy curves here is above the "zero energy" of the system which means that there is a direct "activation barrier" towards dissociative adsorption and dissociation can therefore not proceed barrierlessly from gas-phase. As shown in Figure 2.9, depending on the adsorption strength of the two adsorbed atoms to the surface (E_{ads}^{diss}), i.e. the depth of the dissociative chemisorption potential well (solid and dashed lines), there will be differences in the magnitude of the activation barrier (E_a^{diss} (1) or E_a^{diss} (2)) as the position of the curve-crossing shifts. The dissociation process may even proceed barrierlessly if the potential energy curve-crossing occurs near or below the "zero energy" of the system.

One can also draw conclusions about desorption phenomena. The energy required, i.e. the activation barrier, for desorbing the two atoms, E_a^{diss}, generated from the dissociation process depends on the depth of the potential-well and the position of the curve-crossing. For the case of the physisorbed and associatively chemisorbed molecule we see that the activation barrier to desorb from the surface E_a^{des} is equivalent to $-E_{ads}$. In some cases there is an activation barrier from physisorption to associative chemisorption but this barrier is often very small compared to the chemisorption energy so the relationship

$$E_a^{des} \sim -E_{ads} \tag{2.46}$$

is very often a good approximation.

In the end, we realize that what determines the potential energy landscape in which adsorbates move on a surface is the nature of interaction between the electronic structure of the adsorbate and solid surface, i.e. the chemical bonding.

2.6 Temperature Programmed Desorption

2.6.1 Fundamental Aspects

Temperature programmed desorption, also named thermal desorption spectroscopy (TDS) named, was introduced by Langmuir [36] and is an extensively used since experimentally relatively simple technique in surface science and catalysis [37-40]. TPD is often employed for determining coverages and for evaluating activation energies and frequency factors of desorption. After appropriate calibration, it is also possible to measure absolute coverages and sticking coefficients with high accuracy. Within the framework of suitable models, adsorbate-substrate binding energies and entropies can be calculated.

In a TPD experiment, adsorbate-covered sample is heated with a defined heating rate, $\beta = dT/dt$, from a temperature below to a temperature above the expected desorption temperature of the adsorbate, and simultaneously detect the partial pressures, p_i, of the desorbing species with a mass spectrometer. In a pumped recipient, we obtain curves $p_i = p_i(t,T)$ with one or more maxima, the thermal desorption spectra.

A frequently used basis for the evaluation of kinetic parameters from thermal desorption spectra is the Polanyi-Wigner equation 2.47 [35]:

$$R_{des} = -\frac{d\theta}{dt} = -\frac{d\theta}{dT}\frac{dT}{dt} = -\frac{d\theta}{dT}\beta = \nu_n \theta^n \exp\left(-\frac{E_a^{des}}{RT}\right) \tag{2.47}$$

with the coverage θ, the frequency factor ν_n, the desorption order n, and the desorption activation energy E_a^{des}.

The parameters E_a^{des}, n, and ν_n should generally be considered as functions of coverage and may in cases of complex kinetics (e.g., a phase equilibrium on the surface) also depend on desorption temperature, which is a function of the heating rate. That means that desorption parameters can depend on the conditions of the TPD experiment.

Within the general limitation of kinetic measurements, proposed mechanisms can only be excluded, not be proven, TPD is also a method suitable for investigating desorption mechanisms. The desorption order, if interpreted as the molecularity of an elementary reaction, allows insight into the nature of the rate-limiting step of the desorption process, which is, from the kinetic point of view, in general a consecutive reaction. From the molecularity of the desorption process one can often draw conclusions about the state of the adsorbate itself. To give an example, a desorption order of two suggests a bimolecular bimolecular reaction as rate-limiting step, e.g., the combination of two fragments. If the desorbing molecule is of the type X_2, than a species X(ad) is likely to exist on the surface. In contrast, in the case of an adsorbate species X_2(ad) we expect a first-order desorption kinetics.

2.6.2 Evaluation of the Desorption Activation Parameter E_a^{des}, n, and υ_n

In the literature, several methods for evaluating the desorption activation parameters E_a^{des}, n, and ν_n have been described [41]. These methods can be arranged according to the fraction of each spectrum employed for the data evaluation: a single point, a small part of the curve, or the whole curve. In the same order, the methods become increasingly sensitive towards errors and inconsistencies of the measurement, e.g., erroneous over-crossing of the curves, background intensity, temperature errors, variations of the heating rate, etc.

Heating rate variation and Redhead's formula

The temperature of maximum desorption, T_{max}, measured as a function of the heating rate, allows the determination of E_{des} and ν_n, if the desorption order n is known. Using only one point of each peak, this method is not economical in respect of the data material, but it easily manages overlapping peaks. Therefore, it is particularly attractive for studies in which the substrate provides several desorption states which are saturated, for example in supported catalysts. The method requires a number of spectra taken for the same initial coverage, but at different heating rates. In the following, we derive a relation between T_{max}, β, and the activation parameters E_a^{des}, n, and ν_n under the assumption that the latter are independent of coverage or temperature.

Differentiation of 2.47 with respect to temperature and setting the result equal to zero yields the following equation containing the temperature at maximum desorption T_{max}:

$$\frac{E_a^{des}}{RT_{max}^2} = \frac{\nu_n}{\beta} n\theta_{max}^{n-1} \exp\left(-\frac{E_a^{des}}{RT_{max}}\right) \qquad 2.48$$

with $\theta_{max} = \theta(T_{max})$. This equation can be arranged as follows:

$$\ln\frac{\tilde{T}_{max}^2}{\tilde{\beta}} = \frac{E_a^{des}}{RT_{max}} + \ln\frac{\tilde{E}_a^{des}}{\tilde{\nu}_n \tilde{R} n} + (1-n)\ln\theta_{max} \qquad 2.49$$

The tilde denotes division by an appropriate unit. According to Eq. 2.49, plots of $\ln(\tilde{T}_{max}^2 / \tilde{\beta})$ vs. $1/T_{max}$ are linear if the desorption behavior is consistent with Eq. 2.47 and if the activation parameters are constant. From the slope and intercept of the best fit, the desorption energies E_a^{des} and the frequency factors ν_n can be determined. This method is particular convenient for first-order desorption, since the coverage-dependent term on the right hand side of Eq. 2.49 vanishes for n=1. Redhead [42] proposed a relation for estimating desorption energies from a single thermal desorption trace. The formula simply converts T_{max} into E_a^{des} for first-order desorption. The only requirement – and the main source of error – is a reasonable estimate for the frequency factor ν_1. Rearranging Eq. 2.48 for n=1 one can obtain:

$$E_a^{des} = RT_{max}\left[\ln\frac{\nu_1 T_{max}}{\beta} - \ln\frac{E_a^{des}}{RT_{max}}\right] \qquad 2.50$$

The second term in the brackets is small compared to the first one and is approximated by $\ln(E_a^{des}/RT_{max}) = 3.64$, leading to an error < 1.5% for $10^8 < \nu_1/\beta < 10^{13}$ K^{-1}.

Sometimes, zeroth order processes occur. This is the case whenever the concentration of the adsorbed particles is not rate-limiting for the desorption reaction, for example, if the condensed multilayers of adsorbate grown on a substrate are removed. We then have from Eq. 2.47, by letting n = 0, the simple exponential relation for the rate of desorption.

$$-\frac{d\theta}{dT}\beta = \nu_0 \exp\left(-\frac{E_a^{des}}{RT}\right) \qquad 2.51$$

which states that regardless of the initial coverage there is a single exponential function, which describes all desorption curves. Once he surface particle reservoir is exhausted, the rate simply returns to zero, which is seen experimentally as a cut-off the high temperature site of the spectra. In Chapter 5, kinetics of water desorption from the surface of silica thin films will be discussed in detail.

Leading edge analysis

The leading edge analysis, as suggested by Habenschaden and Küppers [43], allows to evaluate coverage-dependent (and even temperature-dependent) activation parameters. In order to fix θ and T at the same time, the analysis is carried out for a small section on the low-temperature side of each spectrum. For this section, $\ln(\vec{R}_{des})$ is plotted vs. 1/T. According to Eq. 2.47, rearranged to

$$\ln \vec{R}_{des} = -\frac{E_a^{des}}{RT_{max}} + \ln \tilde{\nu}_n + n \ln \vec{\theta} \qquad 2.52$$

this procedure should result in a straight line with the slope E_a^{des}/RT_{max} and an intercept that depends on ν_n. The analyzed section was limited by the condition that only ≤ 5 % of the initial coverage were allowed to desorb.

CHAPTER 3

INTERACTION OF OXYGEN WITH Mo(112): FORMATION OF A SURFACE OXIDE

Understanding the oxidation pathways of metallic surfaces remains one of the challenges of today's surface science. The oxidation process to a higher or lower extent occurs for all metals, significantly changing the properties from those of the original material. This important but complicated process proceeds in several stages, beginning with the dissociation of the oxygen molecule above or at the surface and ending with the restructured bulk oxide. Obtaining a detailed understanding of the atomic-scale processes involved as well as of the detailed atomic geometry of the oxide layers formed is therefore a very important task.

The interplay between chemisorption, subsurface diffusion and oxidation is certainly one of the key issues in interaction of oxygen with metal surfaces. The general trend of oxygen interacting with the surface sites follows a delicate balance of reaching the optimum electron density offered by the metal surface and minimizing the Pauli repulsion between the metal and the oxygen atom charge density [44]. If oxygen is coordinated to many metal atoms the optimum electron density is provided at a larger bond lengths which in turn minimizes the Pauli repulsion making this adsorption site favorable. Obviously, each metal (or more specifically transition metal) has different affinity towards oxygen. Depending on the adsorption energy of oxygen and the surface free energy of the metal substrate, non-reconstructive or reconstructive adsorption may take place. Oxygen adsorption on the hexagonal fcc(111) and hcp(0001) surfaces are accompanied by substantial displacements of metal atoms in the top two layers [45], which is indicative of a quite strong bonding and which demonstrates that the substrate surface participates actively in the chemisorption process in order to optimize the electronic environment for the oxygen atom, however these close-packed surfaces of metals do not experience severe reconstruction [46-50]. The fcc(110) surfaces, which are more open as compared to fcc(111) and contain furrows propagating in one dimension, are well known for their strong tendency to reconstruct. For example, upon exposure to oxygen, Ni(110) [51], Cu(110) [52, 53], Ag(110) [54], and Fe(211)[1] [55] undergo missing-row type of reconstructions. Depending on the lateral interactions between adatoms, surface reconstructions parallel or perpendicular to the direction of furrows may occur.

---

[1] Structures of fcc(110) metal surfaces are similar to that of (211) surfaces of bcc metals.

The initial stage of the surface oxidation is generally assumed to proceed via the formation of a chemisorbed oxygen monolayer, followed by the nucleation, growth, and coalescence of two-dimensional oxide islands. The growth of the oxide phase is governed by kinetic limitations since the dissociation tendency of transition metal surfaces decreases steeply on approaching the saturation coverage of chemisorbed oxygen. The binding energy per O atom decreases with increasing oxygen uptake beyond the saturation coverage [56], so that incorporation into the subsurface region may become energetically favorable. On many surfaces, an intermediate surface oxide phase precedes the formation of the two-dimensional oxide film. the examples include structures on the (111) surfaces of silver, copper, and palladium, and the oxygen-induced missing-row reconstructions of the (110) surfaces of copper, nickel, and silver [57-59]. Other surfaces such as Ni(001) and Al(111) oxidize directly from the chemisorbed state [60]. Pd_5O_4 has been suggested as the phase of the two dimensional surface oxide forming on Pd(111) prior to formation of bulk PdO which is the stable phase observed at oxygen pressures close to ambient [61]. Similar trends have been observed on Rh(111) [62], Pd(100) [63], Ru(0001) [64], and Ag(111) [65] surfaces where oxygen incorporation into the sub-surface region starts at essentially the same coverage as formation of the surface oxide. In these examples, the role of subsurface oxygen has been considered as a metastable precursor in the oxidation process of the surface. The formation of an aligned O-TM-O trilayered structure (TM=Ru, Rh, Pd, Ag) together with an efficient coupling to the underlying substrate has been suggested to be key ingredients in this surface oxide formation phenomena [66].

Early transition metals like tungsten and molybdenum interact with oxygen more strongly. The most of the previous works has been concentrated on tungsten, in particular O-W(110) [67] and O-W(100) [68] systems. Similarly, (111), (110) and (100) terminations of molybdenum metal have received more attention than (112) termination in terms of their reactivity towards oxygen. A massive surface reconstruction has been the common observation for oxygen covered Mo(110) and Mo(100) surfaces, the extent of which indeed strongly depends on the oxygen coverage [69, 70]. On more open Mo(112) surfaces, various surface structures induced by oxygen adsorption have been observed depending on the experimental conditions. The examples include p(3×9) [71], p(6×12) [71], p(1×2) [72, 73], p(1×3) [73], p(2×1) [74], c(4×2) [74] and p(2×3) [75] structures. The oxygen-induced p(1×3) structure has been postulated as a precursor for the epitaxial formation of MoO_2(100) [73]. Even for the simplest p(1×2) phase, several models have been proposed based either on experimental data [72, 73] or theoretical calculations [76] involving both unreconstructed and reconstructed surface structures. Similarly, for p(1×3)- and p(2×3)-Mo(112) structures, oxygen induced reconstructions have been postulated. As compared to the behaviors observed on the surfaces of late transition metals, the situation is further complicated due to the fact that the formation of surface oxide at relatively lower temperatures may occur through intermediate phases, and bulk oxide layers may grow rapidly. Thin oxide films of MoO_2 on Mo(112) [77] and MoO_3 on Au(111) [78, 79] have been studied in detail, but; any sort of surface oxide forming on topmost atomic layer of molybdenum metals has not been reported.

A few reports have appeared in the literature concerning about the formation of low dimensional oxide layers on the surfaces of transition metals, including mostly vicinal surfaces of Rh(553) and Pt(332) [80, 81]. These examples are in agreement with the general consensus that low-dimensional structures may form on uncoordinated atoms at steps. Growth of the oxide phase is usually considered as auto-catalytic triggering of those defective sites by impinging oxygen molecules. It has also been argued that the surface oxidation facilitates the deep growth of oxide phase since surface oxide phase enhances oxygen dissolution capacity of the parent metal. Subsurface oxygen and its role have been critically discussed especially on late transition metal surfaces. Energy gained by expansion of the surface atoms from their equilibrium positions upon oxygen adsorption leads to the relaxation of neighboring atomic layers and missing-row type of reconstructions can be seen for the open surfaces. Depending on the formation energies, severe step bunching can indeed be observed on vicinal surfaces of late transition metals or surface long range order can even be truncated with the formation of facets. Lattice misfits between the parent metal and oxide overlayer plays a decisive role in faceting especially for early transition metal oxides which may be in the forms of several structures.

This chapter covers the determination of the p(2×3) superstructure on Mo(112) after reaction with oxygen, which is proposed as a model for the low dimensional oxide systems. The interest in this system also stems from the necessity of detailed knowledge regarding the oxygen uptake capacity of Mo(112) surface, which will be critical for the preparations of well ordered silica films on the same substrate.

3.1 Oxygen Induced Structures on Mo(112) Surface: LEED

The clean Mo(112) surface showing a ridge-and-trough structure with the top layer Mo atoms forming close-packed rows along the $[\bar{1}\bar{1}1]$ direction separated from each other by 0.445 nm in $[\bar{1}10]$ direction has mainly four adsorption sites, namely; atop, short bridge, long bridge and 'quasi' three-fold hollow sites. LEED pattern of a clean Mo(112) surface can be seen in Figure 3.1 (a). Quasi term is used for the threefold hollow sites because furrowed surface layer enables those sites to be composed of two first layer molybdenum atoms and one second layer atom or the other way around. Similarly, long bridge sites are defined for the sites between first and second layer molybdenum atoms, whereas; short bridge sites are located in between two surface molybdenum atoms along $[\bar{1}10]$ direction. These sites are shown schematically in Figure 3.1 (e). Of all the adsorption sites available on unreconstructed Mo(112) surfaces, short-bridge sites have recently been estimated to be the most favorable for oxygen adsorption below one monolayer and quasi threefold hollow sites have been found more favorable above one monolayer of oxygen [76]. It is worth noting that the bridge and threefold hollow sites are not very different from each other energetically, however; the models [74, 82] suggesting threefold hollow sites as most favorable sites for low oxygen coverage have not been verified by DFT calculations [83].

A well-ordered p(2×1) structure can be formed after annealing the molybdenum surface covered by 1 L of O_2 to ≥600 K. The p(2×1) LEED pattern gradually vanishes at increasing oxygen exposure, but the p(1×1) pattern remains. A diffuse p(1×2) pattern appears after further adsorption of 4 L of oxygen, and the spots gain more intensity after annealing to 800 K. The same structure can also be fully developed, as shown in Figure 3.1 (b), by dosing 6 L of O_2 at 850 K. In LEED experiments one initially observes (1×1) patterns, and p(1×2) pattern is formed only after annealing to the temperatures above 600 K. These findings confirm that this structure can be reached only during activated adsorption process. Increasing the oxygen exposure time (amount) and/or temperature (i.e. 30 L, 900 K) results in LEED patterns (see Figure 3.1 (c)), which can be interpreted as a combination of p(1×2) and p(1×3) phases. Attempts to form a pure p(1×3) structure always result in the formation of a p(2×3) phase shown in Figure 3.1 (d). The former can also be developed exposing the clean surface to 500 L O_2 at 900 K, above which severe surface faceting takes place and the surface oxide layer gets thicker [77]. Even though very sharp LEED spots along $[\bar{1}10]$ direction separate reciprocal unit cell into three, the spots at the half of the reciprocal unit cell along $[\bar{1}\bar{1}1]$ direction are not well-separated. The formation of streaks instead of spots indicates the presence of a high density of antiphase

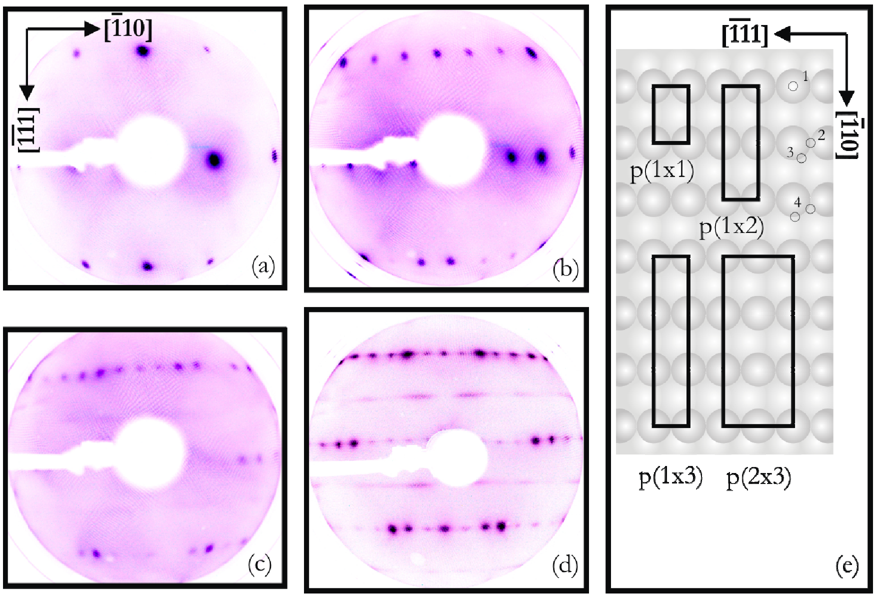

Figure 3.1 LEED patterns of (a) clean Mo(112), (b) p(1×2), (c) p(1×2)+ p(1×3), and (d) p(2×3) oxygen induced superstructures. (e) Schematic illustrations of the top layer of a Mo(112) surface and representative unit cells of the structures observed by LEED. Possible locations for adsorption sites for oxygen atoms are also indicated as black circles: (1) atop, (2) short bridge, (3) long bridge, and (4) quasi threefold hallow sites.

domain boundaries as previously pointed out by Schroeder et al. [75]. Surface symmetry is broken in the direction perpendicular to the direction of those domain boundaries (along $[\bar{1}\bar{1}1]$ direction). Attempts to produce the pure p(1×3) surface structure as described by Santra et al. [73] (270 L oxygen exposure at 1100 K) give a LEED pattern which at first glance could be assigned to a pure p(1×3) structure. However, a close inspection of this pattern at different electron energies shows less intense but streaky spots corresponding to the initial formation of the p(2×3) structure. The LEED results show that the p(1×3) structure is basically metastable under the conditions applied and often co-exist with either p(1×2) or p(2×3) phases. A very recent DFT calculations have shown that oxygen adsorption on this surface induces a missing-row type reconstruction independent of periodicity [83]. Moreover, coexistence of the p(1×2) and p(1×3) structures have also been predicted. The relative stability of these reconstructed structures can be explained by effective screening ability of the repulsive interaction between oxygen atoms along the rows. Structural details of p(1×2) and p(1×3) will not be introduced here, however; these observations help us to realize that the diffusivity of the adsorbed species on this surface is expected to be greater along the troughs than across them in the $[\bar{1}10]$ direction. Molecular oxygen can diffuse along the troughs in the $[\bar{1}\bar{1}1]$ direction and undergo dissociation at the edge of the growing p(1×2) domain. Buckled molybdenum surface generates additional sites for oxygen and thus p(1×3) structure obtained at higher oxygen coverages grows in the same fashion. The ordering of the oxygen atoms above 600 K indicates that oxygen diffusion along $[\bar{1}10]$ direction becomes significant as confirmed by identical p(1×2) or p(2×3) LEED patterns obtained after oxygen adsorption experiments at 850 L. This surface thus has a certain one dimensional character as far as the adsorption mechanisms at especially elevated temperatures are concerned.

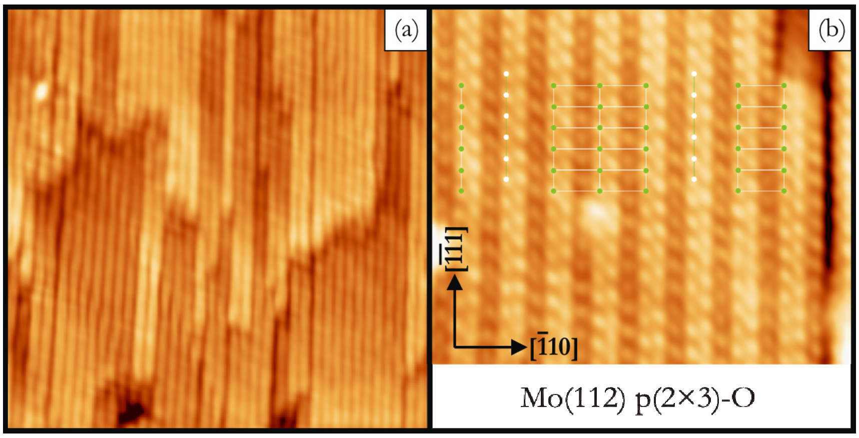

Figure 3.2 STM images of the Mo(112)-p(2×3)-O surfaces. In both images bright one-dimensional structures can be observed. Tunneling conditions are (a) 40×40 nm^2, V_s/I: +1.0 V/0.2 nA and (b) 9×8 nm^2, V_s/I: +1.2 V/0.61 nA. p(2×3) periodicity is indicated by white rectangular unit meshes. Dark and light spots highlight half lattice shifts due to domain boundaries.

3.2 STM Investigations of Mo(112) p(2×3)-O Structure

The morphology of the p(2×3) surface depends strongly on the preparation conditions, e.g. oxygen deposition temperature and coverage. Especially the degree of surface faceting is an important factor. The preparation method used in the measurements described previously results in a surface with relatively large terraces and a reasonable step density, but also facetted areas on a small fraction of the surface are observed. STM image seen in Figure 3.2 (a) verifies preferential growth. Missing single and double rows and high step density indicate very intense molybdenum mass transport upon interaction with oxygen. A statistical analysis made by collecting several STM images allow us conclude that p(2×3) is the dominating structure over 90 % of the whole surface and rest is composed of small facets. The structure of these facets has also been reported previously by Schroeder et al. [77]. The atomically resolved STM image presented in Figure 3.2 (b) shows bright protrusions separated from each other by ~0.54 nm along $[\bar{1}\bar{1}1]$ direction, which is twice the interatomic Mo-Mo distance along the same direction. The unit cell can easily be visualized with the aid of rectangular unit mesh plotted at the center of this STM image. The rows are separated by 1.335 nm along $[\bar{1}10]$ direction, which is three times the Mo-Mo inter-atomic distance between trenches. The p(2×3) periodicity observed by LEED is indicated by the black dots located on the rectangular unit mesh. However, along the $[\bar{1}10]$ direction, the unit cell next to the one indicated at the center can not be identified since the periodic structure is broken due to the domain boundaries, whose presence is also determined by LEED. As pointed out with white dots, the unit cell is half lattice shifted along $[\bar{1}\bar{1}1]$ direction (one lattice shifted with respect to Mo(112)). This gives streaky spots in reciprocal space along $[\bar{1}10]$ due to their high density throughout the surface. Based on a line profile analysis, the features located in between double rows can tentatively be attributed to missing-row type of reconstructions.

3.3 Core Level Shifts Due To Oxide Formation

MoO_3 and MoO_2 are the most commonly seen bulk oxide phases of molybdenum. On molybdenum single crystal surfaces, the formation of polycrystalline molybdenum oxide thin films of several tens of layers have already been identified by STM and XPS investigations [84]. However, to date, characterization of very thin oxide layers on molybdenum has not been done with the help of high resolution core level spectroscopy.

Figure 3.3 shows a high resolution photoelectron spectra of Mo 3d states of a clean Mo(112) and p(2×3)-O surfaces together with O 1s states taken from various oxygen induced surface structures. The broad O 1s spectra hinder us from resolving any fine structure, but the pronounced asymmetry of the peak suggests that oxygen atoms in different chemical environments as shown in Figure 3.3 (a). The intensity of the O 1s (top spectrum) as measured with Mg Kα radiation provides a quantitative measure of the oxygen concentration on the surface. A comparison with the intensity of the well known “oxygen poor” c(2×2)-SiO_2 structure (see Chapter 4 for details) yields 0.15 atoms/$Å^2$ in the p(2×3) surface structure, or at least 11 oxygen atoms per p(2×3) unit cell. This is comparable with the 12 Mo atoms on the unreconstructed Mo(112) surface (6 in the rows and 6 in the furrows) and indicate a high oxygen coverage structure. A Similar quantification can be made by comparing the oxygen amounts in different oxygen induced surface structures. The spectra at the bottom of Figure 3.3 (a) were collected from p(2×1)+ p(1×2) and p(1×2) structures, respectively. Based on the models proposed for p(1×2) [72] and p(1×3) [73, 83] structures, one can deduce that the amount of oxygen per unit cell is much more than the amount previously proposed for p(2×3) structure [75].

The binding energy shifts of core electrons arising between surface and bulk atoms, so-called surface core level shifts (SCLS’s), of bare and adsorbate covered metal surfaces are a rich source of chemical and structural information. On most metals only the first layer of atoms gives rise to an observable surface core level shift. This is due to the nature of the metallic bonding: in the second layer the atoms are highly coordinated and embedded in a charge density very similar to the bulk. There are, however, exceptions to this general trend, surfaces where second layer shifts have been found [85]. Besides, there is a clear dependence of the SCLS on the number of nearest neighbor atoms. The SCLS’s are smaller as compared to the chemical shifts occurring in compounds, since the electronic modifications are not as strong, and therefore the detection of these shifts becomes possible only by using high energy resolution photoelectron spectroscopy.

Figure 3.3 (b) and (c) show Mo $3d_{5/2}$ surface and bulk states of clean Mo(112) surface collected at normal and grazing electron emission angles, respectively. Excitation energy chosen (E_{kin}≈100 eV) ensures that escape depth of photoelectrons is not deeper than 3-4 atomic layers, however; the term 'bulk' will be used for the peak located at 228 eV for comparison. As seen more clearly in the spectrum taken at grazing emission angles, there are two more peaks which are found 0.15 and 0.4 eV below the main Mo $3d_{5/2}$ bulk component. These additional components are attributed to surface states of molybdenum substrate. The openness of the surface structure explains why there is more than one surface state. As compared to the third layer, second layer atoms of (112) surface are less coordinated. Comparing normal and grazing emission spectra, it is straightforward to conclude the SCLS such that the component with the largest shift originates in the first layer, the component with the second largest shift in the second layer, respectively. This assignment is not only based on intuition but also supported by the relative intensity of the lines: the SCLS lines from the deeper layers are lower in intensity, consistent with the expectation that the electrons from these layers are more likely to suffer inelastic scattering processes. However, the opposite behavior observed at grazing electron emission indicates

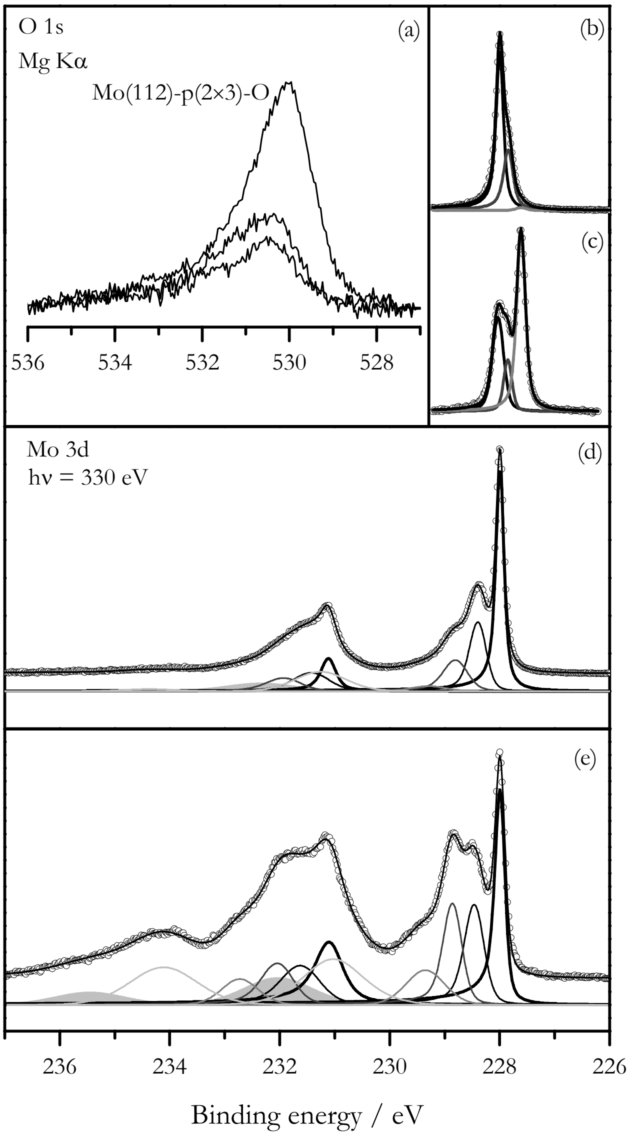

Figure 3.3 Photoelectron spectra taken from clean Mo(112) and Mo(112)-p(2×3)-O surfaces. (a) O 1s spectra including p(2×1) and p(1×2) structures. Mo $3d_{5/2}$ surface states were measured at (b) normal and (c) grazing emission angles. For all deconvoluted Mo 3d spectra, circles represent the experimental data points and the black lines on top of them are fitted curves. The thick lines represent the metallic states (of the clean sample) and oxide components are indicated with thin lines. Light gray, gray and black thick lines are topmost, second and bulk $3d_{5/2}$ states of clean Mo(112) surface, respectively. Various coordinations of molybdenum atoms to oxygen atoms are also shown with color coded thin lines. Grazing angle measurements were performed at 75°.

there might be some diffraction effects involved which influence intensities due to forward scattering process.

The formation of p(2×3) structure leads to appearance of several new features other than metallic Mo 3d states. In Figure 3.3 (d) and (e) high resolution Mo 3d spectra at normal and grazing emission angles are shown. The absence of the surface peak observed on the clean surface is a strong indication that no surface molybdenum atoms remain low-coordinated after oxidation. In the grazing emission spectrum, a fine structure with at least 5 different clearly resolved peaks is detected. This suggests a complicated surface structure with Mo atoms in different chemical states, from metallic up to binding energies reported for bulk MoO_2 [22]. Comparison of the grazing and normal emission spectra gives some information on how the different Mo atoms are positioned with respect to the surface. Not surprisingly, the component attributed to bulk Mo $3d_{5/2}$ at 228.0 eV diminishes at grazing emission and hence can be considered to be subsurface. The same seems to be the case for the component at around 228.4 eV, which consequently can be assigned to Mo atoms in contact with an O atom at a position slightly below the surface. The other two $3d_{5/2}$ components at higher energies (228.8 eV and 229.4 eV) all increase in intensity in the grazing emission spectra and can be considered to occupy positions closer to the surface. The two highest binding energy components of the Mo $3d_{5/2}$ overlap with the $3d_{3/2}$, therefore its core level shift is preferably extracted from the low and high binding energy sides of the $3d_{3/2}$ where two broad peaks around 231.1 eV and 232.0 eV are observed. The low energy peak is in good agreement with previously reported core level position for MoO_2 with an adiabatic peak at 229.5 eV for Mo $3d_{5/2}$ and a $3d_{3/2}$ satellite at 234.2 eV [86]. Table 3.1 shows the binding energies of Mo $3d_{5/2}$ components and their fractions obtained after deconvolution of the normal emission spectrum.

Table 3.1 Binding energies and fractions of the Mo $3d_{5/2}$ components (normal emission).

Mo $3d_{5/2}$ BE /eV	228	228.4	228.8	229.4	231.1	232.0
Intensity / %	35.1	23.8	15.5	2.6	14.8	8.2

In the grazing emission spectra, a shoulder around 235.4 eV is detected. Since the peak and shoulder are broad the exact binding energy positions are somewhat uncertain. Nevertheless, an analysis with proper peak fitting based on metallic spin orbit split peaks indicates that the oxide related peak at around 232 eV (light gray shaded component) is covering 10-15 % of whole surface. A previous study combining XPS and Raman spectroscopy has assigned this component to polymeric Mo(VI)O_6 surface units, similar to those in polymolybdates [87]. Here, it must again be noted that this fraction determined by spectroscopic analysis might be linked to the small facets covering the same fraction of the surface as measured by STM. Structural differences as well as the close proximity of the screening electron cloud in the metallic molybdenum crystal make direct comparison between the surface oxide and corresponding bulk oxides precarious, and observation of higher oxidation states at lower energies can not be ruled out. Screening in the metallic MoO_2 shifts the adiabatic peak roughly 1.6 eV to lower binding energies than expected from a linear interpolation between the insulating MoO_3 and elemental Mo. An enhanced core hole screening is also reported in metallic $K_{0.3}MoO_3$ bronze [88]. Since the surface oxide is ultra thin and dominated by metallic MoO_2, it may well be that Mo^{6+} units are present on the surface; which experience an efficient screening from the molybdenum substrate underneath.

3.4 Probing the Surface Sites

IRAS and HREELS techniques have extensively been utilized to study the oxygen chemisorption on various molybdenum surfaces [89]. The HREEL spectrum [72] of the p(1×2) surface structure shows three main vibrational features at 220, 460, 620 cm^{-1}, with a shoulder at 670 cm^{-1}. Oxygen exposure (less than a monolayer) and annealing to 1000 K yields two additional peaks at 779 and 970 cm^{-1}. The peak at 220 cm^{-1} is typical for a clean Mo(112) surface and has been assigned to a dipole active surface resonance [90]. The modes at 460 and 620 cm^{-1} have been assigned to pseudo threefold coordinated oxygen atoms, whereas the shoulder at 770 cm^{-1} has been associated with the loss of surface order

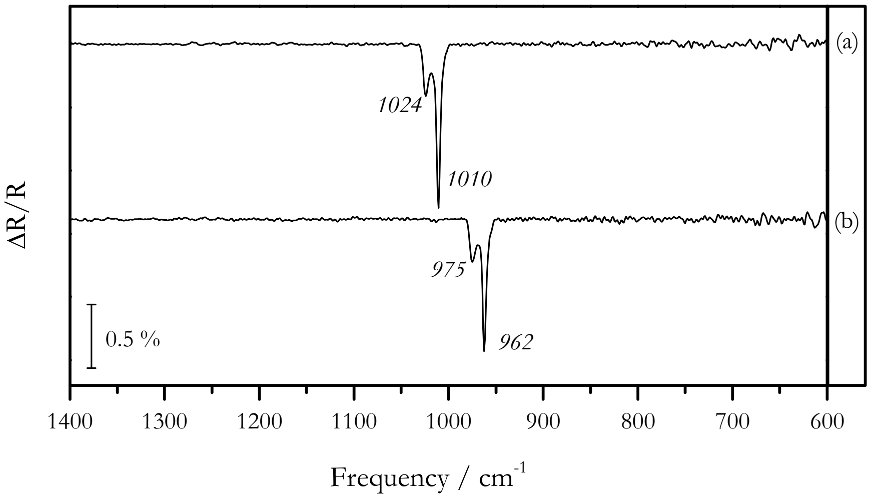

Figure 3.4 IRA spectra of (a) Mo(112)-p(2×3)-^{16}O and (b) Mo(112)-p(2×3)-^{18}O surface oxides.

and formation of three-dimensional Mo_xO_y phases. A similar vibration at 725 cm^{-1} has been attributed to the surface oxide MoO_2 formed after oxygen adsorption on the Mo(111) surface [91]. The 670 cm^{-1} mode was assigned to molecularly adsorbed oxygen and in particular to bridged peroxo species [72]. Figure 3.4 shows IRA spectra of oxygen induced p(2×3) structure which contain none of these modes[2] reported for O/Mo systems. Instead, the spectra show two vibrational modes centered at 1010 and 1024 cm^{-1} for surface oxide prepared by $^{32}O_2$ and at 962 and 975 cm^{-1} for the oxide prepared by $^{36}O_2$. This double peak feature has also been detected on Mo(110) surfaces and has been attributed to Mo=O moieties on terraces and steps, respectively [84]. Those terminal Mo=O species (molybdenyl groups) also dominate vibrational spectra of supported MoO_3 catalysts and their frequency is dependent on degree of polymerization of $[MoO_6]$ isolated species and degree of hydration [89]. The intensity ratio of these peaks depends on the details of the oxidation conditions, confirming that there is more than one type of Mo=O species. Increasing oxidation temperature by 100 K results in increase in the intensity of the peak at 1024 cm^{-1}, or in other words, relative intensities change at the expense of higher frequency component. STM images obtained on the samples prepared at oxidation temperatures higher than 1000 K show high degree of faceting. As mentioned before, surface oxidation at 900 K is a suitable condition for the formation of facets which cover 10-15 % of the surface. Same fraction can also be obtained from the relative intensities of double peak features and thus it can be concluded that the peak at 1024 cm^{-1} is Mo=O stretching confined on facetted regions. Isotopically labeled surface oxides show the same double peak feature with the same frequency difference. This finding rules out the possibility of presence of O=Mo=O type of surface species. Because, the peaks in IRA spectra can also be interpreted as symmetric an asymmetric Mo=O stretching of O=Mo=O species and an isotope effect is expected. The dominant low frequency component can then be ascribed to the terminal oxygen species formed on terraces in the p(2×3) surface oxide.

Molecules like CO, NO, and H_2O are frequently used as probe molecules to determine the nature of the oxide surfaces because vibrational frequencies of those probe molecules can be specific to the sites on which they adsorb. On clean Mo(112) surfaces, CO adsorbs dissociatively leaving carbon and oxygen as contaminants. Fukui et al. [74]

---

[2] It must be noted that vibrational modes below 600 cm^{-1} can not be detected because of medium band MCT detector cut-off.

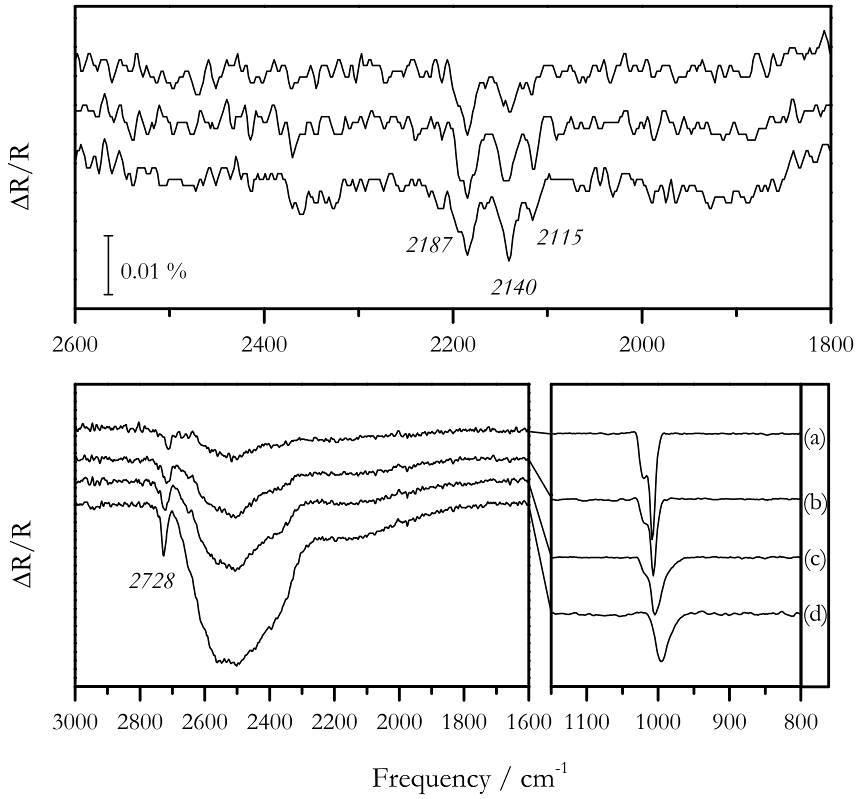

Figure 3.5 IRA spectra of CO (u*pper panel*) and D_2O (l*ower panel*) adsorbed on p(2×3) surface oxide at 100 K. Saturation CO coverage is obtained after adsorbing 0.2 L CO. Frequency shifts of Mo=O species were followed by adsorbing (a) 0.5 L, (b) 1.0 L, (c) 1.5 L, and (d) 2.0 L D_2O.

have shown that dissociated CO desorbs following recombination routes above 800 K, and those routes can be manipulated by changing local coordination of CO by predosing oxygen. An important factor influencing adsorption characteristics of CO on oxygen covered metal surfaces and metal oxides is the steric interaction between CO and O sitting in the next neighboring site. On the surfaces of metal oxides CO adsorbs on cationic sites.

Top panel of Figure 3.5 shows IRA spectra of saturation coverage of CO adsorbed on p(2×3) surface oxide. Reaching saturation coverage at very low CO dose at 100 K (<0.2 L) indicates that number of cationic sites available for adsorption of CO is quite low. Comparing CO uptake capacity of clean Mo(112) surface with the uptakes obtained on oxygen terminated p(2×3) structure, it is reasonable to conclude that CO adsorbs only on defective sites (oxygen vacancies). The frequency of the peak centered at 2187 cm^{-1} is higher than the stretching frequency of CO in the gas phase (2143 cm^{-1}). The main effects which describe the frequency shift of an adsorbed molecule are the wall effect, the self-image shift and the chemical shift [92]. Considering an isolated adsorbed CO molecule, the wall effect leads to a blue-shift [92]. This results form the Pauli repulsion between the carbon lone-pair electrons and the surface charge distribution. The self-image shift, on the other hand, leads to a red-shift due to the interaction between the dipole moment of the adsorbed CO and its image. As a result of the chemical bonding of CO to the substrate, a red shift is observed depending on the extent of the charge transferred (back-donation) from the substrate to the unoccupied $2\pi^*$ molecular orbital of the adsorbed CO. Intermolecular interactions such as dipole-dipole interactions between neighboring molecules, which result from the vibrational coupling of the molecule's dipole with its own image dipole in addition to the coupling with dipoles of neighboring molecules and their image dipoles are reflected to the spectra as a blue-shift. Colaianni et al. [93] have reported vibrational spectra of CO on oxygen modified Mo(110) surface. In their detailed work, of all surface pretreatments with oxygen no bands higher than 2030 cm^{-1}, attributed to CO on atop molybdenum site stabilized by neighboring oxygen atoms, have been observed. On p(2×3) structure, the peak at 2187 cm^{-1} can be attributed to Mo^{4+} sites, however the origin of the other peaks is not clear. Adsorbed CO equally influences both Mo=O stretching bands suggesting adsorption site for CO is close proximity to those terminal oxygen sites [94]. Annealing to 200 K results in total CO desorption leaving no carbon contaminants as evidenced by XPS.

Same scenario also holds for the interaction of water with molybdenyl terminated p(2×3) surface oxide. Water molecularly adsorbs and at 100 K condensed multilayers can be formed as shown in lower panel of Figure 3.5. Appearance of free OD stretching centered at 2728 cm^{-1} at the early state of adsorption indicates that there could be some monomeric D_2O species and with increasing coverage deuterium bonded water clusters may form (Chapter 5 is dedicated to the interpretation of clustering of water condensed layers on silica thin films based on methods including IRAS, here only relevant issues will be discussed). Upon adsorption, the response of double Mo=O groups is different. The high frequency band attenuates gradually with coverage, whereas only small attenuation and red-shift are observed for low frequency band. This can be explained as follows: on regular p(2×3) surface sites, water may diffuse fast and be bound to facetted regions. Then, three dimensional clusters start to nucleate on regular sites and weakens the low frequency Mo=O groups. Double peak spectrum fully recovers after desorption of molecular water overlayer. Combining total disappearance molybdenum surface states after forming p(2×3) structure with weak defective interactions of molecules, it can be concluded that the surface of Mo(112) is fully covered by oxygen and terminated (partially) with Mo=O groups.

3.5 Structural Model

High resolution photoelectron spectroscopy clearly indicates that there are at least five different molybdenum atoms on the Mo(112) surface coordinated to oxygen ions. Besides, the surface states completely vanish after formation of p(2×3) surface oxide. Clean Mo(112) surface has four sites available to adsorbed O, and quasi threefold hollow sites have been suggested as the most favorable one for oxygen amounts more than 0.5 ML [74]. In addition, DFT calculations estimate that the most stable p(1×2) and p(1×3) structures involve buckling of the top molybdenum layers [83]. Quantitative analysis of O 1s XP spectrum and presence of the component considered as Mo^{4+} state in the Mo 3d spectra let us suggest that the topmost molybdenum atoms can be oxidized by incorporation of subsurface oxygen ultimately pushing molybdenum atoms towards the vacuum. In general, there are two possibilities how a place exchange process can proceed depending on which atom initiates this process. First, an oxygen atom may penetrate into interstitial position between the first and second surface layers, pushes the nearest surface atom from its lattice site, and then simultaneously occupies this site and bonds with the substrate atom being pushed [95]. This mechanism has been suggested to be responsible for initial nickel oxidation [96]. Another possibility is a similar mechanism proposed above but substrate atom movement (vacancy formation) is the first step of oxide formation. A substrate atom left its place during vacancy formation is then bound with an oxygen atom captured into vacancy; this results in oxide molecule formation. Although this formalism has been developed for different conditions, in both mechanisms, interactions with oxygen adatoms play dominant roles.

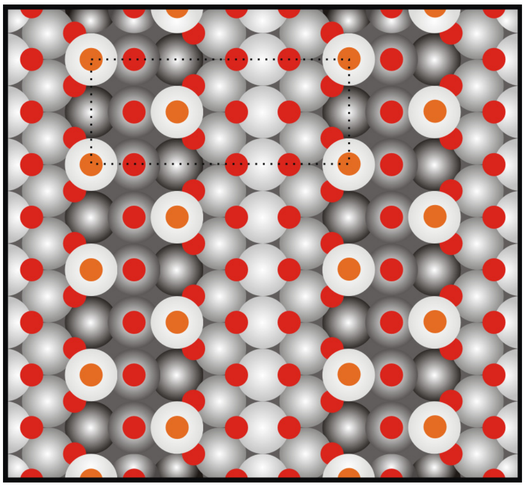

Figure 3.6 Structural model for on p(2×3) surface oxide Mo(112). Gray shaded balls represent molybdenum atoms and they become darker while going from the surface to the deeper atomic layers. Smaller solid balls are oxygen ions and oxygen ions of Mo=O groups are coordinated to the topmost (lightest) molybdenum atoms. p(2×3) unit cell is indicated by dotted lines.

Assigning the bright protrusions observed in STM images to Mo=O groups identified by IRAS, a tentative structure can be proposed for one dimensional surface oxide forming on Mo(112) with p(2×3) periodicity. Figure 3.6 shows the ball model of the proposed structure. The coordination of each molybdenum atom (color-coded by four different grades of gray) to oxygen ions provides a suitable picture matching with the number of peaks observed in the photoelectron spectra. Oxygen atoms adsorbed on quasi-threefold hollow sites enhances the relaxation of the topmost layers. The vertical shifts of the topmost molybdenum atoms by the incorporation of subsurface oxygen can thus be expected. $O=Mo-O_3$ topmost layer might appear in the PE spectra as the component with the highest oxidation state. The remaining three components are less coordinated to oxygen and therefore their oxidation state is lower due to reduced charge distributions. Moreover, there is no open molybdenum atom that can be accessed by adsorbed molecules. It is however required to do theoretical calculations to optimize the final structure.

To sum up, p(2×3) is the periodicity of an one dimensional surface oxide forming on the Mo(112) surface. The surface is partially terminated by Mo=O groups and no open metallic site is available at the surface. The surface symmetry is broken by antiphase domain boundaries and frequent lattice shifts along $[\bar{1}\bar{1}1]$ direction are observed. The structure is stable up to 900 K, above which the degree of faceting increases and oxide layer begins to grow into bulk molybdenum layers.

CHAPTER 4

SILICA FILMS GROWN ON A Mo(112) SURFACE

Silicon dioxide (silica) has been one of the most intensively studied materials in materials science and condensed matter physics. The main driver for this intense effort is its critical role in the metal-oxide-semiconductor field effect transistor (MOSFET), which dominates contemporary integrated circuit (IC) technology. Amorphous silica is also a material of choice for, e.g., catalyst supports, optical fibers and solar cells, making its role in modern technology even more important.

4.1 Review of Bulk Silica Structures

4.1.1 Crystalline Silica

X-ray diffraction experiments [97, 98] reveal that amorphous silica preserves much of the ordering present in the crystalline forms on a short or intermediate length scale. For example, the coordination of atoms and the first and second nearest neighbor distances is very similar in the amorphous and crystalline forms, suggesting that both materials have similar building blocks. It is therefore instructive to start our review with the various crystalline forms.

The pertinent forms of silica are α- and β-quartz, tridymite, coesite and stishovite; their thermodynamic stability ranges are indicated in Figure 4.1 and the structural properties are listed on Table 4.1 [99].

The basic bonding unit for all these forms of silica except stishovite is the SiO_4 tetrahedron. Each silicon atom is surrounded by four oxygen atoms with the Si−O distance ranging from 0.152 nm to 0.169 nm; the tetrahedral O−Si−O bond angle is 109.18°. Each oxygen atom is bonded to two silicon atoms, with the Si−O−Si bond angle varying from 120° to 180°, depending on the material. All forms of silica are constructed from the corner-sharing tetrahedra, such as the SiO_4 building block. High-temperature cristobalite and tridymite possess the largest bond angles, and have the most open structures of the crystalline forms of silica. The smaller the bond angle, the denser is the possible packing, reflected in measured density variations. Another important factor is the effective charge on each atom in SiO_2. For completely covalent bonding, the net excess charge on each atom would be zero, corresponding to four valence electrons on each silicon atom and six valence electrons (including the s electrons) on each oxygen atom. For completely ionic

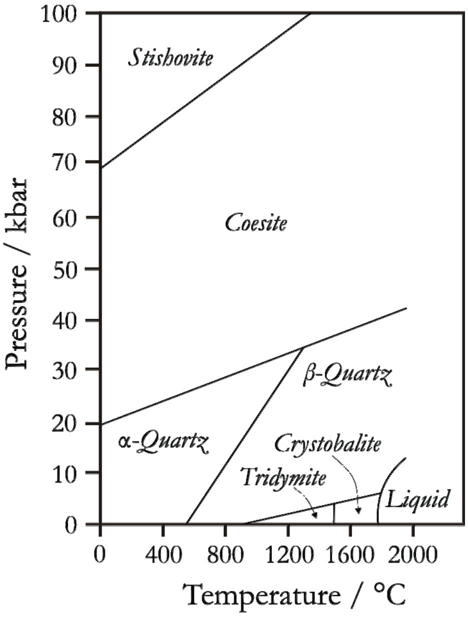

Figure 4.1 Phase diagram of silica (adapted from [99]).

silica, the net excess charge on each oxygen would be -2, and on each silicon, +4. The actual situation is somewhere between. Numerous calculations have been performed to determine the net charge transfer from Si to O in the various silica structures, and they are in agreement that the effective excess charge on O is about one electron per oxygen atom [100-102]. Moreover, these calculations indicate that this excess charge (i.e., the ionicity) increases as the Si−O−Si bond angle increases.

The temperature- and pressure-stability of the various forms of silica determine which might be present -as microcrystallites- in thermally grown oxide films or silica glass. Figure 4.1 shows that the most likely form is tridymite, which is stable at low pressure up to 1470 °C. High-temperature quartz might not be expected in a typical thermal oxide, as it transforms to tridymite at 870 °C. However, due to the large stresses possible during oxidation, the high-temperature quartz form and its associated bonding configuration should not be ruled out entirely. Similarly, both low-temperature quartz and coesite should be considered.

4.1.2 Amorphous Silica

Two models exist to describe the structure of amorphous silica, the continuous random network model first proposed by Zachariasen [103] and the microcrystalline model of Randall [104]. In the continuous random network model, the local structural unit (SiO_4 tetrahedron) remains unchanged, with each tetrahedron corner shared with another tetrahedron, as in the crystalline forms. However, the Si−O−Si bond angle will vary from one tetrahedron corner to another, yielding a continuous random network. In the microcrystalline model, the silica is constructed from microcrystallites of the various allotropic forms of crystalline silica or alternatively, sub-unit-cell-sized crystallites of one form of silica. In the limit of small crystallites, the two models converge. The local structure of bulk vitreous silica has been determined by both x-ray and neutron diffraction [97, 98, 105]. These studies are consistent with both the above models, giving Si−O to be 0.16 nm; O−O 0.262 nm; and Si−Si 0.313 nm; all are distances quite close to what is expected for crystalline silica. The difference from the crystalline forms is due primarily to the range in Si−O−Si bond angles present in the vitreous form. Based on the bond angle distribution of high-temperature structures tridymite and cristobalite obtained by x-ray, it has been reported that the latter has two reported bond angles 180° and 137°; tridymite has a distribution from 130° to 175° because of its large unit cell that contains 330 SiO_2 units [97, 106, 107]. In vitreous silica, the bond angles vary from 120° to 180°, with a mean of 152° [98].

Table 4.1 Structural properties of various crystalline forms of silica.

Phase	Symmetry	Cell params. (nm)	Si-O dist (nm)	O-O dist. (nm)	Bond angle (deg)	Ring size
Low-T quartz	Hexagonal	a = 0.49 c=0.540	0.161	0.260-0.267	144	6
High-T quartz	Hexagonal	a = 0.501 c=0.547	0.162	0.260	144	6
High-T tridymite		a=0.932 b=0.172 c=8.19 $\alpha,\beta,\gamma=90°$	0.158-0.162	0.263	140-173	6
High-T cristolbalite	Cubic	a=0.176	0.158-0.169	0.263	142-180	6
Ceosite	Monoclinic	a,b=0.717 c=1.238 $\gamma=120°$	0.160-0.163	0.260-0.267	120	4

4.2 Thin Films on Single Crystal Surfaces

Epitaxially grown thin films of oxides on metals or on different oxide substrates are used as supports with atomically ordered surface structure for the controlled deposition of metal and metal oxide particles, thus creating excellent model systems for supported metal and metal oxide catalysts [11, 108]. The general usage of the term 'thin film' refers to a layer of material with a thickness that is orders of magnitude smaller than its lateral dimensions. Depending on the application, the type of the thin film can range from a single layer to a multilayered structure. The stability and function of thin film materials depends dramatically on the levels of stress in the film, which in turn depends on the preparation conditions as well as the choice of the film and substrate materials.

Oxide thin films may be prepared by very different routes, such as oxidation of single crystal surfaces and physical vapor deposition and oxidation of metals on single crystal surfaces. A few model oxide surfaces have been selected both by theoreticians and by experimentalists, either because of their simplicity or because of their availability as large single crystals. Among them, $\gamma\text{-A1}_2\text{O}_3$, MgO, TiO_2, ZnO and $SrTiO_3$ surfaces are the most studied. Other oxides have also been studied to a less extent, such as: CaO, CeO_2, ZrO_2, Cr_20_3, Fe_2O_3, Fe_3O_4, CuO, etc. Most of the recent studies have been performed by oxidation of surfaces of binary intermetallic alloys like NiAl [109-111], FeAl [112] and CoGa [113] as substrates. The oxide layers grow after adsorption of oxygen and the preferential segregation of one of the metallic components (Al, Ga) at the surface. Details of these processes have been covered in detail by Franchy [114].

The second preparation route of an oxide film is based on the growth of the films on a dissimilar metallic substrate. The crystallographic structure of the substrate then determines to a large extent the structure of the oxide film [109]. The structural quality of the oxide film depends strongly on the epitaxial relation between the lattice constants of the metallic substrate and the oxide film. The lattice constant of the substrate has to be chosen properly in order to prepare a less strained layer with long-range order. In general, room temperature growth of oxide films leads to the formation of amorphous layers. Subsequent annealing to elevated temperatures usually orders the oxide films and the growth of thin, well-ordered (crystalline) films is obtained. If there is a large mismatch between the substrate surface and the oxide lattice constants, the film may be defect rich. Despite of the fact that there have been a numerous well ordered oxide thin films which have been grown on metallic substrates in the last decade; including V_2O_5 and V_2O_3 on Rh(111) [115, 116] and on Au(111) [117], MgO on Ag(001) [118] and on Mo(001) [119], FeO-Fe_3O_4-Fe_2O_3 on Pt(111) [120], not much is known about their surface structures. The structure of one of the most studied thin film, aluminum oxide (alumina) on NiAl(110), has recently been discovered [121] and it has been shown that the structure of the alumina film is a little different than the any bulk structures of aluminum oxide. The stabilities of thin films have been shown to be dependent of partial pressure of oxygen and it has been claimed that thin oxide films can be thermodynamically more stable as compared to their bulk phases [122].

The growth of ultra thin oxide films on silicon single crystal surfaces is the straightforward way of approaching to the silica film concept. The discovery that thermal oxidation of silicon passivates its surface is a crucial step in semiconductor device technology [123]. The development of integrated circuits, and thus today's computer industry, is based largely on the excellent properties of passivating silica film, including its interface with the silicon substrate. Although the passivating silica films on silicon wafers and single crystals are usually prepared at elevated temperatures (700±1200 °C) and can be significantly thicker than a few angstroms, they exhibit structural similarities to thin oxide films prepared at lower temperatures. Even though thinner films can be prepared by several means, thermally grown silica films are amorphous. Amorphous films can play an important role in the passivation of metals [124, 125]; however, they are not an ideal template for the systems where characterization at the atomic level is necessary.

The first attempts to grow crystalline silica films can be traced back to early 90's. Thin silica films have been grown on a Mo(100) substrate by evaporating silicon into an oxygen background. A Mo(100) single crystal was the substrate of choice because of its relative ease of cleaning and the ability to thermally desorb the thin films of silica from the surface [126, 127]. Even though the film was thin enough to be characterized by surface science techniques, it was amorphous in nature. The preparation of *well-ordered* thin silica films was achieved by Schroeder et al. [128] who suggested Mo(112) surface to use as a substrate since interatomic distances of molybdenum surface are quite close to crystalline forms of silica structures. Basically, a recipe originally applied to the Mo(100) was used to grow well ordered film. Even though the film exhibited a diffraction pattern with respect to Mo(112) substrate, thickness, structure, and the surface termination of the film remained unclear. The thickness of the film was initially estimated as 0.7 nm, but later it was suggested that the film is only a monolayer thick. Based on STM and vibrational spectroscopy, a structural model was proposed by Chen et al. claiming that isolated SiO_4 clusters were the building blocks of one monolayer (ML) silica film on Mo(112) substrate [129]. Besides, based on assumption that the film is three layers thick, Ricci and Pacchioni [130] proposed a β-cristobalite derived structure as thermodynamically the most stable one.

The rest of this chapter is devoted to characterization of silica thin film grown on Mo(112). The crystal structure, electronic and vibrational properties, and line and point defects will be discussed in following sections.

4.3 Structural Characterization of One Monolayer Silica Film on Mo(112)

In this section, important processes which are a part of silica film growth and which will be drawn upon in subsequent sections will be discussed. Understanding of these individual steps related to film structure is crucial, but it must be emphasized that what really counts is how different probing techniques helps us to identify the whole picture.

For silica films grown on the Mo(112) substrate, the so-called reactive evaporation technique has been used, i.e. the silicon has been evaporated in an oxygen background pressure onto the molybdenum substrate at elevated temperatures. All the details of the silica film preparation are given in Appendix C. Annealing temperature to make the film well-ordered and oxygen partial pressure during the silicon deposition are both critical parameters which certainly have influences on the electronic and vibrational structure of the film. Initially, cycles of room temperature silicon deposition and high temperature post oxidation (900 K) followed by successive annealing steps have been suggested to prepare well-ordered silica films [131, 132]. Films of the same quality as judged by LEED patterns have been prepared by single deposition of monolayer amount of silicon at room temperature and post oxidation at 850 K. It is worth noting here that the silicon deposition at room temperature results in the formation of three dimensional particles after oxidation, and those begin to wet the molybdenum substrate at the temperatures higher than 1100 K.

As was introduced in the previous chapter, dosing oxygen at 900 K on a clean Mo(112) surface leads to a formation of a surface oxide with p(2×3) superstructure. During film preparation, this surface on which silicon atoms are impinging might be a template for the silica film growth. Formation of silica stripes [133] along $[\bar{1}\bar{1}1]$ direction (the same direction along which Mo=O groups propagate) has been observed under the conditions where the amount of silicon is less than a monolayer indicating that the silicon atoms may preferentially get oxidized by molybdenyl groups. Silicon deposition and oxidation at 900 K is advantageous since the film growth kinetics does not play a major role. The sticking and oxidation probability of silicon atoms on molybdenum surface oxide is quite high up to 900 K, but a dramatic drop is observed at higher deposition temperatures. High diffusivity of silicon atoms on the areas covered by silica is the reason of the formation of a two dimensional wetting silica layer at elevated temperatures. Another advantage is the passivation molybdenum surface by a thin oxide layer which prevents the formation of molybdenum silicide [134].

As-deposited silica films exhibit a considerable degree of irregularity in their morphology. In addition, as the first silica layer is formed, the three dimensional particles start to nucleate. This growth behavior is similar to Stranski-Krastanov type where 3D nucleation begins to evolve after the first layer is complete [135]. Annealing film to a temperature which is close to decomposition point is required in order to obtain very well-ordered surface free of clusters. At 1250 K film becomes quite viscous and thermodynamically the most stable configuration is achieved. Increasing the annealing temperature causes partial and ultimately total evaporation of the film leaving behind oxygen induced superstructures on molybdenum surface. Mo(112)-p(1×2)-O structure can be obtained if monolayer thin silica film is annealed in UHV to 1300 K and above. However, structural analysis of ideal, well-ordered silica film without any imperfections will be made henceforth.

Large-scale STM images of the silica film are presented in Figure 4.2. It must be noted that all topographic STM images presented here were acquired in the constant current mode. After annealing to 1250 K, a highly ordered, cluster and hole free single layer silica surface is obtained. The surface shows terraces typically 20–50 nm in width with 1.2

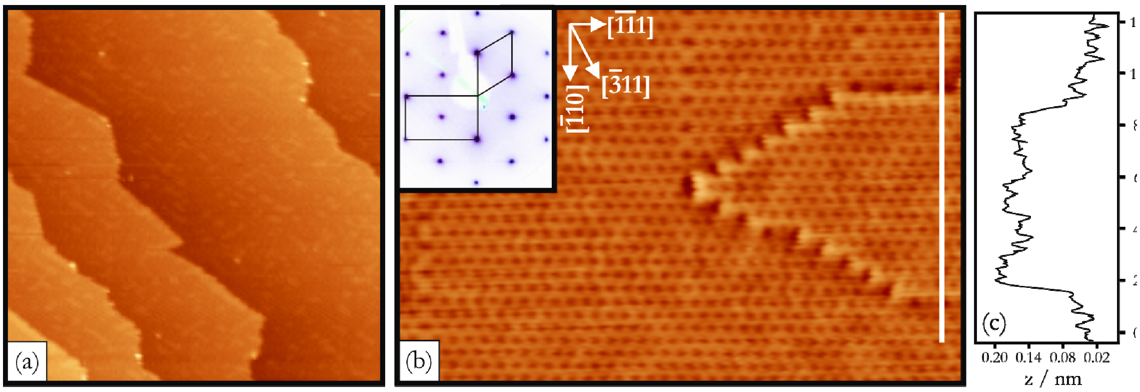

Figure 4.2 Large scale STM images showing well ordered 1 ML silica structure. (a) 100×100 nm^2, $V_s/I=+2.0$ V/0.20 nA, (b) 20×12.5 nm^2, $V_s/I=+2.0$ V/0.40 nA, (c) line profile showing the step height (taken from (b)). Inset: c(2×2) LEED pattern of silica superstructure (E_p = 60 eV). Rectangle represents unit cell of Mo(112) surface. Crystallographic orientations are also indicated.

nm step heights, corresponding to monatomic steps of the Mo substrate underneath the film, as illustrated in Figure 4.2 (a) and (c), respectively. The high resolution STM image (see Figure 4.2 (b)) reveals a honeycomb-like structure with a periodicity of ~0.52 nm in the $[\bar{3}11]$ direction and ~0.55 nm in the $[\bar{1}\bar{1}1]$ direction in agreement with c(2×2) structure observed by LEED (see inset of Figure 4.2 (b)). Absence of any other spots related to surface oxide or chemisorbed oxygen structures on molybdenum [74] is the evidence that as the film uniformly cover the surface of molybdenum substrate. As deposited films exhibit faint superstructure spots due to the lack of long range order. Annealing increases the intensity of spots suggesting the formation of well ordered structure. Even though no detailed spot profile analysis of the LEED patterns was performed, well ordered films quality of which are assured by STM do not show anisotropic spots.

Atomically resolved STM images presented in Figure 4.3 provide significant insights into the detailed structure of the silica films. In Figure 4.3 (a), a zigzag propagation of protrusions along the $[\bar{1}\bar{1}1]$ direction can be recognized. It is also observed that the protrusions are directly connected to each other along the $[\bar{1}10]$ direction. However, the protrusions seen in Figure 4.3 (c) do not propagate along the $[\bar{1}\bar{1}1]$ direction making zigzags. In addition, they are diagonally connected each other along the $[\bar{1}10]$ direction. Topographic differences seen in these two STM images suggest that two different surface ions can be imaged as protrusions. At specific tunneling conditions either the silicon or the oxygen ions could be imaged and by this means their relative positions of the surface ions within the unit cell of the film could be determined. The schematic illustration of the structure of the silica film[3] presented in Figure 4.3 (g) and (h) can help us to compare the STM images presented in Figure 4.3 (a) and (c). At large tip-sample distances silicon ions can be imaged as protrusions (Figure 4.3 (a)) whereas at closer tip-sample distances (higher tunneling current) it turns out that same is true for oxygen ions (Figure 4.3 (c)). Measured distances between two oxygen ions (O2) in $[\bar{1}\bar{1}1]$ and $[\bar{1}10]$ directions are 0.28 nm and

---

[3] Based on the experimental finding the structure of the silica film is determined by DFT calculations. The structural model presented here is based on the optimized structure and the details can be found in Chapter 4.6.

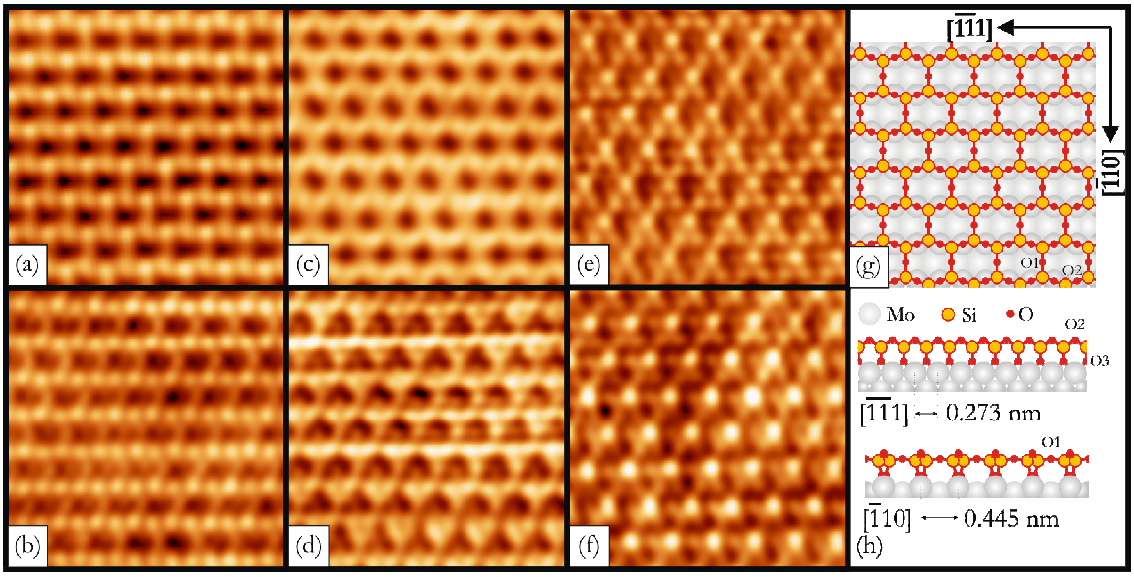

Figure 4.3 STM topographic images taken at the different tunneling conditions and structural model of two dimensional silica film. The size of each STM image is 3.75×3.75 nm^2. Tunneling conditions (V_s/I) are (a) +1.2 V/0.35 nA, (b) -0.4 V/0.30 nA, (c) 0.65 V/0.75 nA, (d) -0.17 V/0.75 nA, (e) -0.72 V/0.45 nA, (f) -0.50 V/0.45 nA. Top view (g) and side views (h) of ball model of silica film on Mo(112) surface. Inter-atomic distances and crystallographic orientations were indicated.

0.45 nm, respectively. In agreement with LEED, the structure shows a c(2×2) periodicity with respect to the Mo(112) substrate. Depending on the tunneling conditions, especially bias voltages below 1 eV, O1 and O2 surface oxygen ions can be imaged together or individually. As shown in Figure 4.3 (b), O2 ions can clearly be seen with a small contribution of O1 ions. O1 and O2 ions bridging silicon ions along $[\bar{1}10]$ and $[\bar{1}\bar{1}1]$ directions can be both seen in Figure 4.3 (e). Tunneling from the filled states of the sample at small tip-sample distances might lead to enhanced brightness. O1 ions which are the brightest protrusions in Figure 4.3 (f) can barely be seen in Figure 4.3 (b).

Contrast in STM images of thin films does not necessarily reflect the film morphology. It is influenced by a variety of effects, including the electronic structure of the substrate, film, and/or interface between them. Band-bending effects induced by the electric field between tip and sample, field resonances, image potential states, and the local work function can also be included into the list [136]. Depending on the energy of the tunneling electrons, especially in the vicinity of a band edge, oxide film and metallic substrate contributions to the current vary greatly. A constant current topograph of an oxide surface depends, thus, on the voltage applied between tip and sample [137, 138]. Such a variation with voltage of the apparent height of oxide islands on a metallic substrate gives access to the conduction- and valence-band edges of the oxide [139]. Once valence or conduction-band states of the oxide are accessible, anionic or cationic sites of the film contribute to the tunneling current.

Calculated density of the states of the silica film [140] shows that the occupied and unoccupied states around Fermi level are dominated by molybdenum d-states. As UP spectra indicate (see Chapter 4.4) that the valance band structure of the silica film is similar to that of the bulk. The valence band maximum is at about 5.0 eV below Fermi edge, so it is concluded that the tunneling current is most likely predominantly due to emission from Mo states through the silica layer. The lateral contrast, showing protrusions at either the

Si^{4+} or the O^{2-} positions, is due to a perturbation and interaction of the Mo wave functions by the silica layer causing a lateral variation of the tunneling barrier. There might be a very small contribution from the silica film to the density of states at the Fermi level due to the O atoms at direct contact with Mo. This is indicative of the strong hybridization at the interface. Interestingly, atomic resolution can be obtained on silica film surfaces over a wide range of electron energies, both in the oxide gap and above its band edges. Even while tunneling into the oxide band gap, the atomic structure of the oxide, especially the topography of its outer atoms, can be probed by STM using strong tip-surface interactions. The tip has indeed to be approached closer to the surface in order to probe the tail of a state localized at the metal/oxide interface.

4.4 Electronic Properties

The core-level binding energy shift of Si 2p upon the formation of SiO_2 is explained in terms of a charge transfer between Si and O atoms and mostly determined by the first-nearest-neighbor O atoms. Himpsel et al. [141] performed a photoelectron spectroscopy study on Si surface atoms with various adsorbates and showed a certain correlation between energy shift of Si 2p per adsorbate atom and the electronegativity difference between the adsorbate atom and the Si atom. Energy shift of Si 2p upon the formation of silica was given by four times the energy shift of Si 2p per O atom, since the Si atoms in silica are surrounded by four O atoms. Core level spectra of crystalline polymorphs of silica are quite similar to each other because the building block of all crystalline silica phases is SiO_4 units. In the case of SiO_2/Si systems, suboxides (SiO_x) localized at the interface of SiO_2 and Si make the spectra more complicated. From the charge transfer formalism, stoichiometry of the silicon suboxides can be estimated.

The left panel of Figure 4.4 shows O 1s region of high resolution PE spectra of one monolayer silica film. At least two different O species with binding energies of ~531.2 and ~532.5 eV can be distinguished. The latter BE value falls into the region reported for the bulk silica or thick silica films [142] and the former has a different origin. No asymmetry in the O 1s core level spectra that would indicate the presence of additional chemically shifted components is observed. This is consistent with the expectation that surface oxygen atoms experience the same local electronic environment. Further XPS studies done by using Mg Kα radiation as excitation energy nicely reproduced the formation of two different O species, which fits well to the 2D network model where two clearly different environments exist for the oxygen anions, i.e. Si−O−Mo and Si−O−Si, as indicated in Figure 4.3 (g) and (h). O3 represents oxygen anion binding Si cation in each tetrahedron to the bridge sites of Mo(112) surface. O1 and O2 represent surface oxygen anions bridging neighboring Si cations along $[\bar{1}10]$ and $[\bar{1}\bar{1}1]$ directions, respectively. The ratio of the integrated intensity of surface oxygen (O1+O2) to interface oxygen (O3) anions is 3:2. When measured at grazing emission angle (80° with respect to the surface normal), the low BE signal is strongly attenuated assuring that O3 species are located below the surface. Right panel of the Figure 4.4 shows the chemical state of the molybdenum substrate when its surface is covered by silica film. Apparently, relative intensity of the peak at 228 eV, which is Mo $3d_{3/2}$ state of bulk molybdenum, to the one at 228.2 is dropping as more surface sensitive measurement is carried out. Even though photon energy was tuned so that kinetic energy of the electrons to be around 100 eV, bulk molybdenum states are still accessible. The higher binding energy component is the molybdenum states coordinated to the interface oxygen atoms (O3) of the silica network. Surface states of molybdenum presented in previous chapter are not observed here, suggesting that all topmost molybdenum atoms are coordinated to the silica network.

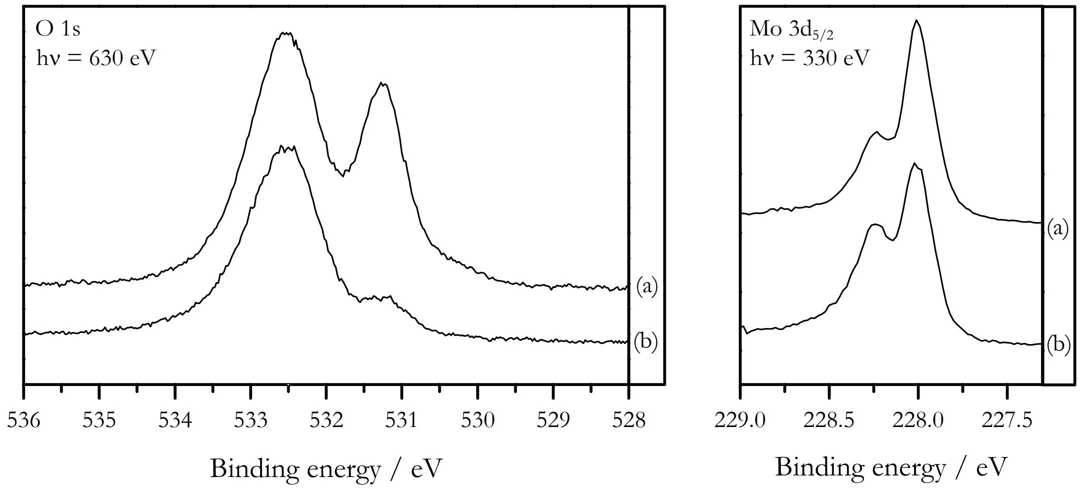

Figure 4.4 O 1s and Mo $3d_{5/2}$ regions of high resolution photoemission spectra of silica film taken at two different electron emission angles. Take-off angles are 0° and 80° for spectrum (a) and (b), respectively.

XPS measurements performed starting from the reactive silicon deposition step to the establishment of a well-ordered film do not show any indication of silicon suboxide formation. The films during each steps of the growth show a single peak in the Si 2p region with a binding energy of 103.2 eV (bottom right panel of Figure 4.5), which is characteristic for Si^{4+} oxidation state [143]. The line width (FWHM) of Si 2p levels is 1.5 eV; however, spin-orbit splitting could not be resolved neither by synchrotron radiation nor by conventional X-ray source. Because of the problem of charging induced line broadening, there has been very few line widths reported in the literature which are smaller than 2 eV (the Si $2p_{3/2,\,1/2}$ line widths for quartz are at 1.6 eV [142]). Excellent screening probability due to the metallic substrate and unique coordination of silicon to oxygen ions strongly influence of the width of the Si 2p spectra.

The presence of particles, which can be removed after annealing the film to 1250 K, can be identified by XP, UP and IRA spectroscopy. Besides, oxygen partial pressure during film growth and annealing is also important due to the fact that the affinity of molybdenum towards oxygen is quite high. The amount of oxygen on molybdenum surface can be varied by dosing it in controlled conditions. Annealing the as deposited silica film in UHV conditions or in oxygen ambient to 1250 K can lead to the formation of oxygen-poor and oxygen-rich silica films. The number of oxygen atoms on different sites of the molybdenum surface can be varied by manipulating oxygen dosing amount during annealing.

Oxygen enrichment of the unit cell of silica film induces appearance of additional components in O 1s and Mo 3d regions on XP spectra (see top and bottom left panels of Figure 4.5). Similar to the high resolution O 1s spectra presented in Figure 4.4, integral intensity ratio of surface oxygen (O1+O2) to interface oxygen (O3) is 3:2 for well ordered O-poor film (see O 1s spectrum (b) in Figure 4.5). Limits of the conventional X-ray source hinder us to resolve spectral components clearly. Nevertheless, fraction of oxygen ions could reasonably be calculated by peak fitting. The relative intensity of the surface oxygen component becomes larger in the existence of silica particles on the surface. Annealing the film in an oxygen ambient (1×10^{-6} mbar O_2) to 1250 K leads to incorporation of oxygen onto topmost molybdenum surface, which appears as a low binding energy component in O 1s spectrum. For the O-rich film (spectrum (c)) the presence of a third component

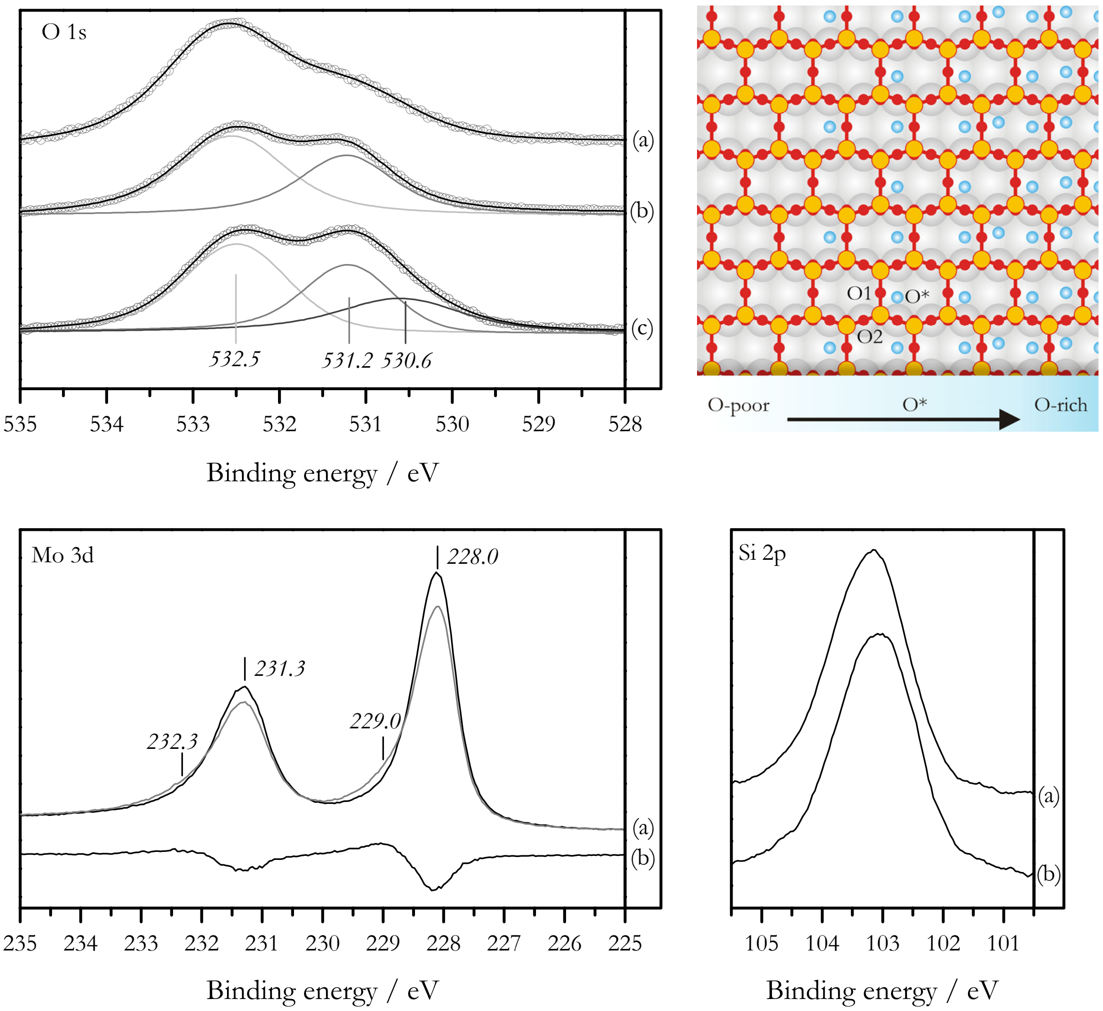

Figure 4.5 XP spectra of O-poor and O-rich silica films. *Top left panel*: O 1s spectra of (a) as deposited, (b) well-ordered O-poor and (c) well-ordered O-rich silica film. Circles: experimental data, light gray: O1-O2, gray: O3, dark gray: O* components and black: fitted curve. *Bottom left panel*: Effect of additional oxygen atoms onto molybdenum surface in Mo 3d states. (a) black: O-poor film, gray: O-rich film. (b) Difference spectra obtained by subtracting Mo 3d spectrum of O-rich film from that of O-poor. *Top right panel*: 2D model of silica film with varying amount of oxygen atoms on molybdenum substrate. *Bottom right panel*: Si 2p region of (a) O-poor and (b) O-rich films.

centered 530.6 eV is clearly visible. Those oxygen species chemisorbed on the Mo(112) surface are marked as O* in the top right panel of Figure 4.5 and they have virtually very small influence on the BE of the oxygen atoms within the silica layer. However, they partially oxidize the surface Mo atoms, leading to the prominent shoulder at high binding energy side of the Mo 3d spectra, which is even better resolved in the difference spectrum (see bottom left panel of Figure 4.5).

The number of surface O* atoms per unit cell can be up to 4. It must be noted that annealing the film in higher oxygen partial pressures gives rise to formation of deeper molybdenum oxide layers. Once prepared, the O-rich film cannot be converted back to the O-poor state without destroying the film structure. This is the consequence of a high binding energy of O* species to the Mo(112) surface. However, post-annealing of the O-poor film in oxygen ambient readily leads to the O-rich film. Binding energy of the Si 2p peaks shifts from 103.2 eV by about 0.15 eV to 103.05 eV as O-poor film is converted to

O-rich. The rather sharp O 2p valence peaks undergoes the same shift (details of the valence band structure will be discussed later). Therefore, the shift of the Si 2p core level can be attributed to shift of the Fermi level due to band banding.

It has been shown originally that the valence band electronic structure of silica could be understood simply in terms of the electronic levels of a small bonding unit containing an oxygen atom and one sp^3 hybrid from each adjacent silicon atom [100]. The three 2p orbitals on the oxygen interact with the hybrids to form five bond orbitals. The oxygen p state perpendicular to the bonding plane becomes the lone pair bond orbital at the O 2p level. The remaining nonbonding oxygen p interacts with the symmetric combination of hybrids to form weak-bonding and weak-antibonding bond orbitals. As this interaction reduces to zero when the Si−O−Si angle is increased to 180°, the amount of mixing is fairly small. The oxygen p pointing along the bond interacts with the antisymmetric combination of hybrids to form the strong-bonding and strong-antibonding bond orbitals. The six electrons available for bonding then fill the system up to the lone pairs, which thus form the upper valence bands. The gap lies between the lone pair and weak antibonding energies, which is approximately the difference between O 2p and Si hybrid levels.

In Figure 4.6, the valence-band (VB) spectra of O-poor and O-rich silica films are presented. The spectral features can be best understood by referring to the valence band structure of the bulk silicon dioxide crystals, which is well established through the photoemission studies of Fischer et al. [143] and of DiStefano [142]. Depending on the local bonding structure, small differences in VB spectra can be observed. The O 2p lone-pair orbital is perpendicular to the Si−O−Si bonding plane in the a-quartz and a-SiO compounds [100, 102]; however, angular deviations giving rise to modifications in the bonding structure are expected for other silica polymorphs. For instance, a splitting in nonbonding orbitals has been observed [142] and attributed to deviation of Si−O−Si bonds from linearity. He I results for the silica thin film shown might typify that structure. It consists of basically two regions, namely bonding and non bonding O 2p orbitals. Referring to the local symmetry of SiO_4 tetrahedra, the peak located at approximately 7.8 eV corresponds to the O 2p nonbonding states with $5t_2$ symmetry. The double peak between 5 and 6 eV is associated with $1t_1$ nonbonding orbital. However, it must be noted that O 1s spectra clearly show that O-poor films contain two different oxygen species and those might have slightly different electronic properties. The peaks above 11 eV are associated with the $5a_1$ and $4t_2$ orbitals, which are σ–bonding orbitals both resulting from O 2p and (Si 3p, Si 3s) mixed orbitals. Bonding state with mainly O 2p character is due to the strong polarity of the Si−O bond. Large Si 3p contribution spreading over about 2 eV can be the reason of the large dispersion on the bands above 10 eV [144].

Fine VB structure is closely related to the structural well-order, in other words regular Si−O bonding network. Therefore, VB spectra of the silica film are better resolved as compared to the valence structures of other silica polymorphs where bond angles and bond lengths may differ. Above 10 eV, one additional component centered at 10.7 eV can be identified in VB spectra of O-poor and O-rich films. The origin of this peak has been studied by slightly oxidizing molybdenum substrate [145]. A good correlation has been found between the intensity of the peak at 10.7 eV and the thickness of the oxide layer. This observation has been concluded by assigning this feature to Si−O−Mo bonds. However, the presence Si−O σ-bonding orbitals obscured under the wide band have been eliminated due to lack of resolution. Here, both of them in addition to Si−O−Mo band are clearly visible.

For O-poor films, the VB maximum is defined by the onset of the O 2p nonbonding states which are located 5 eV below Fermi level of molybdenum substrate. Assuming that Fermi level of the silica film lies at the center of the band gap, one can

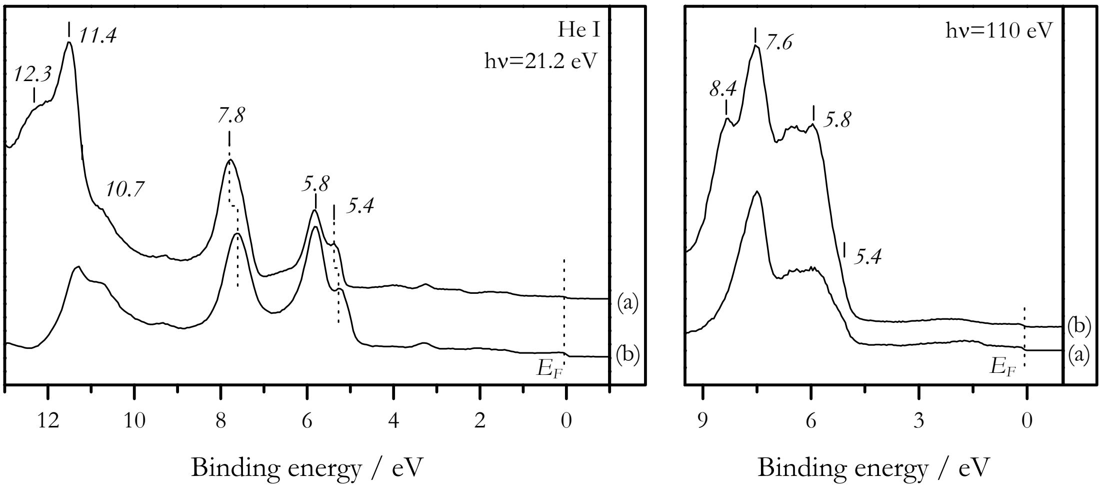

Figure 4.6 Valence band spectra of O-poor and O-rich silica films taken at two different excitation energies. All spectra are aligned with respect to Fermi level of molybdenum substrate. *Left panel*: Valence band spectra of (a) O-poor and (b) O-rich silica film. *Right panel*: Valence band spectra of O-poor film measured at the take-off angles of (a) 0° and (b) 70°, respectively. Excitation energies are indicated.

simply find that the band gap of the O-poor film is around 10 eV, which is in the range of the band gap of bulk silica [146]. The onset of the valence band slightly shifts to the lower binding energies with increasing oxygen concentration of the unit cell. In addition, the width of the peaks between 5 and 6 eV gets broaden due to contribution of additional oxygen atoms to the neighboring lone-pair orbitals. The binding energies of all peaks in valence spectrum of oxygen rich silica film shift to lower energies by 0.2 eV, except the one at 5.8 eV. This binding energy change agrees with the observation in which the binding energy of the Si 2p states is reduced due to band bending.

Even though the interpretation of the VB structure is not as straightforward as that of core levels, the surface sensitive measurements may shed light on fine details of the VB of silica film. The right panel of Figure 4.6 shows VB spectra of an O-poor film measured at two different electron emission angles. The differences in the relative intensities of the bonding and nonbonding O 2p states are due to differences in photoemission cross sections. The same reason makes the spectral analysis above 10 eV quite difficult since intensities of these bonding states are almost zero. Nevertheless, for nonbonding O 2p states, the qualitative picture is quite similar to UP spectra apart from the fact that a good spectral resolution is not achieved. Taking the spectra at grazing emission mode gives rise to appearances of additional peaks. Reduction in the relative intensity of the peak at 7.6 eV with respect to the one at 5.8 eV and appearance of a high binding energy peak at 8.4 eV suggest that energy of nonbonding states of surface oxygen atoms is obscured under the high binding energy shoulder. At grazing angles, the contribution of lone pair electrons localized perpendicular to the Si−O1−Si and Si−O2−Si planes is highly expected.

4.5 Vibrational Properties

Generally speaking, IR spectral measurements of ultrathin films are undertaken to determine (i) the chemical identity of adsorbed species (including dissociation fragments); (ii) the geometric or structural arrangement (orientation) of these species and their positions with respect to the surface atoms of the film; (iii) their vibrational, frustrated rotational, and frustrated translational motion on the surface; and (iv) the effects of external perturbations, such as the electric and magnetic fields, photons, electrons, and heating [147]. However, such information cannot be extracted directly from the IR spectra of ultrathin films due to the strong dependence of the shape and relative intensity of the bands on the geometry of the experiment, the optical properties of the substrate, the surroundings, the gradient of the optical properties at the film–substrate interface and in the film itself, as well as on the film thickness. One common problem when examining ultrathin films on various surfaces and at various interfaces by IR spectroscopy is that of comparing the spectra taken at different mode and experimental geometry.

When silica film is the material of choice, there are several complications which make the analysis of vibrational spectra difficult. The vibrational bands are influenced by the stoichiometry of the material and by the presence of the strain within the material (tensile or compressive) which distorts the average Si−O−Si bond angle [148]. The FWHM of the vibrational bands depends also on the degree of structural disorder and decreases with enhanced structural uniformity. Of course the FTIR measurement is not always conclusive by itself and the structural quality must be cross-checked with other tools. In fact, the main focus is usually given to the bending-stretching region between 800 cm^{-1} and 1400 cm^{-1} because it is the most sensitive to perturbations in the material [148].

It is known that the IR spectra of ultrathin films taken with different polarizations exhibit quite different excitations. The most rigorous interpretation of this phenomenon is given by the polariton theory [149, 150]. According to this theory, which is based conceptually on Maxwell's macroscopic electrodynamics, the eigenstates of the wave in a crystal are the coupled photon–polarization excitation modes. The latter arise from lattice vibrations (phonons), oscillations of free carriers (plasmons), and electron–hole excitations (excitons). Different optical modes of the system studied can contribute to the spectrum depending on the polarization of infrared light and angle of incidence. A qualitative understanding of the appearance of the absorption band near longitudinal optical mode (ν_{LO}) in p-polarized spectra can be reached by considering the electric polarization of a cubic ionic crystal. If the external electric field is perpendicular to the ionic system, the positive ions are displaced to one side and the negative ions to the other. The excess charge on the surfaces results in a polarization perpendicular to the surface plane. It follows that the polarization and the internal electric field show resonance behavior at the frequency of the LO mode of the film, ν_{LO}. When the external electric field is parallel to the film surface (s-polarization), the additional polarization due to the surface charges is absent and the absorption resonance position coincides with the frequency of the transverse optical mode.

The origin of the absorption bands in the IR spectra of ultrathin films can be clarified by considering a plane wave impinging on a film whose thickness is small compared to the wavelength but significantly larger than the value of the lattice constant of the ionic material constituting it. If the vibrations in an infinite crystal result in the appearance of the electric polarization, these vibrations represent the elastic waves, called the normal polarization waves, or normal polarization modes. The polarization and the electric field arising from them change periodically with space and time, obeying the law of the atom displacements. Those polarization waves can be either longitudinal or transverse in their form, but only the latter type can interact with transverse waves of the external electromagnetic radiation.

If a transverse polarization wave with its wave vector parallel to the film surface propagates along this film, positive ions will be displaced to one surface of the film and negative ions to the other by the electric field of this wave. The excess charge arising on the surfaces creates an electric field perpendicular to the film plane and virtually uniform at a distance exceeding the lattice constant. This field will vary with the wave frequency and at each instant will act on the lattice ions in the direction opposite to the direction of their displacement from the equilibrium position, thus contributing to the restoring force. This force is similar to that acting perpendicular to the front of a longitudinal wave propagating in an infinite crystal. Therefore, the frequency of the transverse wave in the film considered here will be close to the frequency of the longitudinal wave in the infinite crystal. As the film thickness increases (and the ratio of surface to volume decreases), the influence of the surface charge density on the internal field decreases, and the frequency of the transverse vibrations with the wave vector parallel to the surface will decrease, approaching ν_{TO}. When the transverse polarization wave propagates normal to the film surface (and thus the electric field is parallel to the surface), an additional field does not arise because the film is regarded as an infinite plane, and the frequency of the wave coincides with that of the transverse vibration, ν_{TO} in the infinite crystal. Such a wave interacts only with the tangential components of the electric field. Therefore, the s-spectrum of the film will consist of the single band near ν_{TO}, independent of the angle of incidence. Since the p-polarized radiation has tangential and normal electric field components, these components will interact with those dipoles within the film that are oriented parallel and perpendicular to the surface, respectively, according to the selection rule. Furthermore, under action of the external electric field normal to the surface, the dipoles experience an additional electric field induced by the polarized chemical bonds within the layer. It follows that in the p-polarized spectra, the band near the longitudinal optical mode ν_{LO} will be observed, in addition to the band near ν_{TO} resulting from the dipoles parallel to the film. It is evident that the dipole oscillations responsible for the ν_{TO} band are directed along the surface, these oscillations will be quenched by a metal surface and, hence, be absent in p-polarized spectra of films on metal substrates.

Figure 4.7 shows series of IRA spectra of one monolayer silica film taken as a function of annealing temperature. As-deposited films exhibit a main absorption band centered at ~1045 cm^{-1} with a broad feature extended up to 1250 cm^{-1}. These bands gradually attenuate upon annealing, while the peaks at 1059, 771, and 675 cm^{-1} gain intensity. The main signal at 1059 cm^{-1} becomes very sharp such that the full width half maximum is only 12 cm^{-1}, suggesting a high ordering of the film and a single phonon excitation. Spectrum (b) and (c) in Figure 4.7 are basically formed by superposition of spectra of as-deposited and well ordered film, which implies a structural transformation at intermediate annealing temperature.

As already mentioned, once the first silica layer is formed 3D silica clusters begin to nucleate. Keeping this in mind, a relatively thick silica film covered by clusters with diameters of approximately 3-5 nm was prepared (Figure 4.8 (a)). The clusters on the terraces cause a dramatic decrease in the intensity of main phonon (1059 cm^{-1}). A broad feature appears around 1025 cm^{-1} as well as two additional features at 1240 cm^{-1} and 860 cm^{-1}, as illustrated in Figure 4.8 (b). The feature at 1240 cm^{-1} is within the range of asymmetric Si−O stretching reported for silica films grown on silicon substrates and the feature at 860 cm^{-1} is its symmetric counterpart [151]. In order to unravel the origin of the band around 1025 cm^{-1}, silicon is deposited at elevated temperature (T=900 K) in oxygen atmosphere ($P=5\times10^{-8}$ mbar) on an already highly ordered silica film. According to STM observations (Figure 4.8 (c)), the silica clusters decorate mainly the step edges. In the corresponding IR spectrum a broad peak attributed to Si−O asymmetric stretching mode is observed, but the peak at 1025 cm^{-1} appearing as a shoulder to the main phonon as the clusters cover the terraces is absent, thus it is interpreted as the result of the interaction of the clusters with the single layer silica film on the terraces.

These experiments clearly show that IRAS features beyond those at 1059, 771 and 675 cm^{-1} originate from three-dimensional silica particles. Turning back to Figure 4.7, the enhancement of the IRAS spectra with annealing can be rationalized on the basis of wetting behavior of the silica film on molybdenum substrate. Annealing in UHV to 1250 K

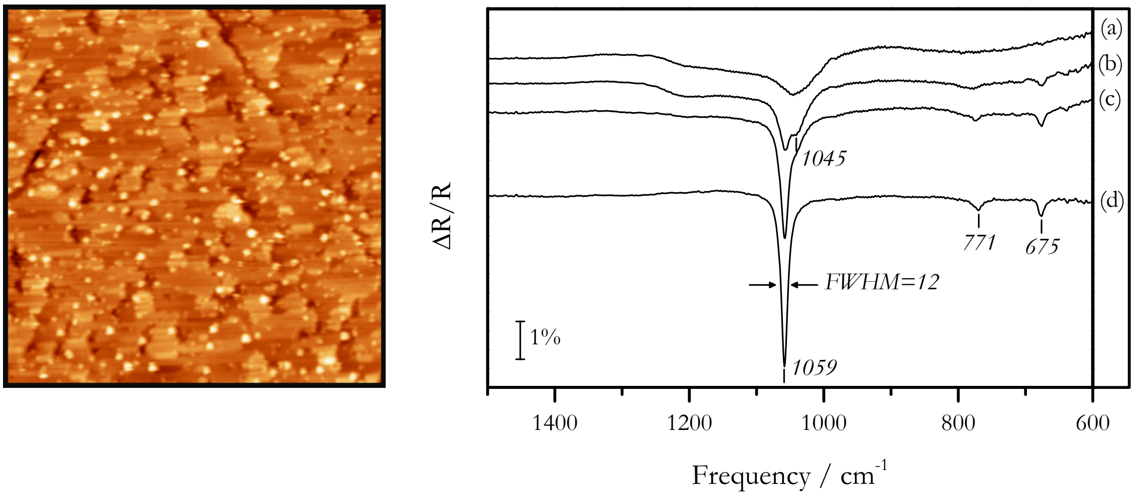

Figure 4.7 Characterization of structural improvement of an as-deposited silica film. *Left*: STM image of an as-deposited film 100×100 nm^2, V_s/I=3.0 V/0.1 nA. *Right*: IRA spectra of (a) deposited at 900 K and the same film annealed to (b) 1000 K, (c) 1100 K, and (d) 1250 K. All spectra were taken at 300 K.

reduces the Si 2p intensity together with the O 1s intensity (O1-O2 component only) simultaneously, which can also be explained by desorption of silica clusters. Gradual attenuation of the intensity of the peak at 1045 cm^{-1} and corresponding intensity gaining of the peak at 1059 cm^{-1} can then be attributed to structural transformation due to the stabilization of the interface bond and desoption of silica particles from the surface. DFT calculations reveal that energetically the most favorable silica film structure is the one which interface oxygen ions binds to the bridge site of the Mo(112) surface (complete results of DFT calculations will be given in the next section). The width of the terraces of the well-ordered films influences the low frequency shoulder of the peak at 1059 cm^{-1}. Deposition of silicon in higher oxygen pressures (>5×10^{-8} mbar) at 900 K might cause faceting of the substrate therefore the width of the terraces dramatically changes. Narrow, randomly oriented terraces apparently perturb long range order, leading to a shoulder in the vibrational spectrum of the silica film. High density of silica particles makes the film almost amorphous. All these findings point out that a well-ordered silica film is only one layer thick, any attempt to grow thicker layers results in formation of 3D particles.

Based on the experimental observations several structural models for one-, two-, and three-layer thick silica films have been proposed [129, 130]. First, the small peak at 675 cm^{-1} has been assigned to the Si−O−Mo interface modes [128]. The calculated vibrational energies [130] support the assignment of the low-frequency band to Si−O−Mo stretching, since the vibrations of various intensity have been found in this region. In particular, the calculations considering dehydroxylated β-cristobalite as the structure of the three layer silica film show one intense vibrational band at 677 cm^{-1}, justifying the experimental observations. Similar values have been calculated for the β-tridymite structure. The DFT calculations estimate the formation of 2-memebered Si−O rings at the surface of the reconstructed cristobalite and tridymite. The second small band at 771 cm^{-1} has been interpreted as ν_{LO} mode of the surface 2-membered rings of β-cristobalite. It has also been proposed that there can only be a sharp band between 1000 and 1050 cm^{-1} in case the film is thinner than two layers [152]. Comparing the calculated vibrational frequencies of two layer quartz, cristobalite and tridymite structures, the sharp band above 1000 cm^{-1} has been assigned to the normal vibration of the Si−O−Si bridges connecting the top and the interface layers. Origin of this sharp band has also been question by Chen and Goodman

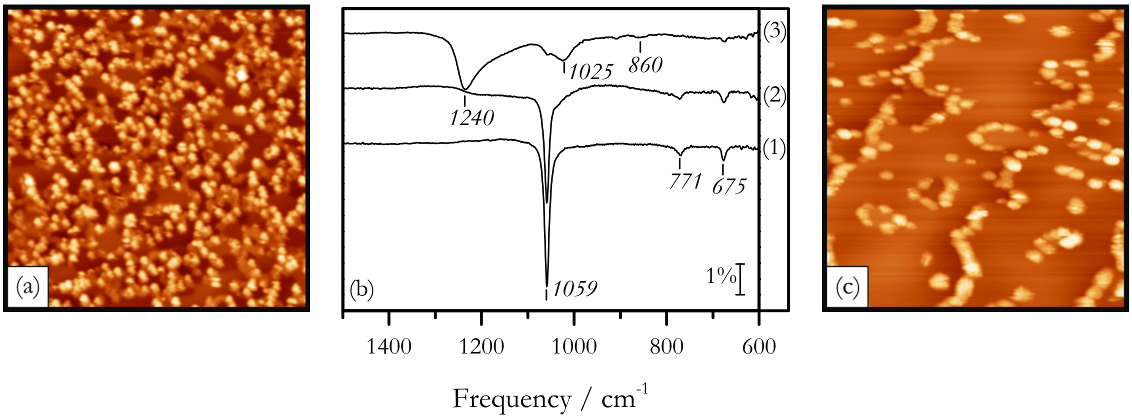

Figure 4.8 STM images and IRA spectra of silica particles formed on the well-ordered silica film by Si deposition in 5×10^{-8} mbar O_2 at 900 K. Spectrum (2) and (3) correspond to the STM images (c) and (a), respectively. The spectrum (1) is for the original well-ordered film. Image size and the tunneling parameters: (a) 100×100 nm^2, $V_s/I=+2.8$ V/0.20 nA; (c) 100 × 100 nm^2, $V_s/I=+3.5$ V/0.10 nA.

[129]. Proposing the isolated SiO_4 clusters fully coordinated to molybdenum substrate as the structural building block of the single layer film, they have concluded that this band can only be related to Si−O−Mo stretching vibration with strong dipole component perpendicular to the surface.

The combined experimental results suggest that there are two oxygen species residing in different chemical environments, one of which can reasonably be assigned to oxygen binding to the substrate. In addition, there is a very strong vibration of a bond with a dipole moment perpendicular to the surface. The asymmetric stretching vibration of Si−O−Mo species is a good candidate for such a mode, as suggested by Chen and Goodman. Concomitantly, the weaker bands at 771 and 675 cm^{-1} correspond to the vibrational modes with a small net dipole moment normal to the surface. DFT calculations employed to examine structural stability of silica films of various thickness estimate that the most stable ones are single-layer structures which form a network of corner sharing SiO_4 tetrahedra (see Figure 4.3 (g) and (h)). One corner of each tetrahedron is bonded to bridge site of the underlying Mo substrate thus forming a Si−O−Mo bond. The remaining oxygen anions (surface oxygen species) bridge neighboring Si cations and form 2D network. The most intense mode is observed for the asymmetric Si−O−Mo stretching at 1059 cm^{-1} originating from the Si−O bond pointing downwards to the Mo substrate. The second mode at 771 cm^{-1} is the Si−O−Si symmetric stretching coupled with Si−O−Si bending and the third mode at 675 cm^{-1} is a coupling of Si−O−Si bending modes.

One may expect that additional oxygen atoms (O*) may influence the vibrational properties of the silica films. Figure 4.9 clearly illustrates the differences in the vibrational spectra of O-poor and O-rich silica films. The additional oxygen atoms on molybdenum surface leads to a red-shift in the Si−O−Mo stretching mode from 1059 cm^{-1} to 1050 cm^{-1} and a broadening in its FWHM by 8 cm^{-1}. The peaks related to surface Si−O vibrational modes centered at 771 cm^{-1} and 675 cm^{-1} do not experience any shift justifying the assignments of the surface and interface relates vibrations. In addition, the most intense peak gives information about how collective motion of Si−O bond towards molybdenum substrate can be perturbed. Incorporation of oxygen into the unit cell in a controlled fashion results in a gradual red-shift in Si−O−Mo stretching frequency. It is reasonable to consider that the frequency and FWHM of Si−O−Mo mode is related to how additional oxygen atoms modify the molybdenum substrate. The structural optimizations done by

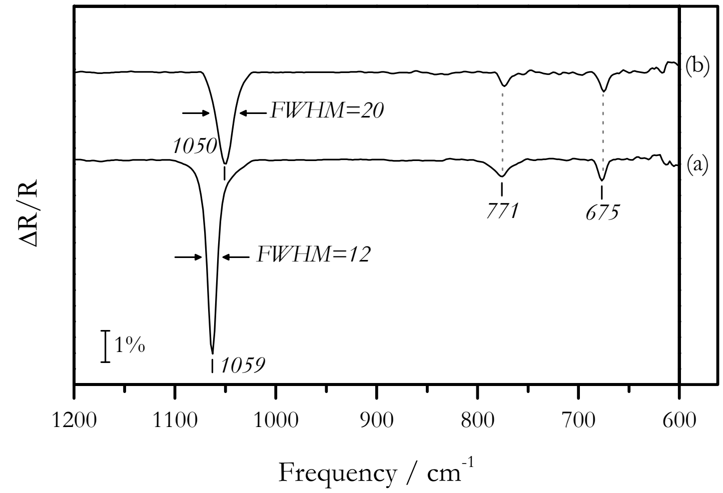

Figure 4.9 IRA spectra of O-poor (a) and O-rich (b) silica films on a Mo(112) substrate.

DFT calculations reveal also that surface molybdenum atoms slightly reconstruct when they are in contract with O*.

4.6 Summary of the Results of DFT Calculations

The atomic structure of the thin crystalline silica film on a Mo(112) substrate has been determined based on the excellent agreement between the results of DFT calculations and the high-quality experimental data. Inspired by the structures of layered silicates [153], more than 15 models consisting of single and double layers of SiO_4 tetrahedra, which do not have dangling Si-O bonds or edge-shared SiO_4 tetrahedra strained (two-member silica rings) at the film surface have been constructed. It has turned out that the most stable ones are single-layer structures with a surface unit cell composition of Si_4O_{10}, which form a network of corner sharing SiO_4 tetrahedra. One corner of each tetrahedron is pointing to the underlying Mo substrate thus forming a Si-O-Mo bond. The other three oxygen atoms form Si−O−Si bonds with the neighboring tetrahedra. There are three possible molybdenum surface sites (bridge, atop, and pseudo three-fold hollow) for the SiO_4 network to bind. The results of the calculations show that the structure with oxygen ions in bridge positions is energetically the most favorable one [154]. At elevated oxygen pressures (chemical potentials) the calculations also predict formation of O-rich silica films. Structural parameters of the O-poor, O-rich and intermediate phases for silica films are shown in Table 4.2.

Table 4.2 Selected structural parameters (Å, deg) for the SiO_2/Mo(112) films: 1 ML O-poor model (0O) and 1 ML *A*/*n*O atoms up to O-rich (4O).

Model	Si-O1	Si-O2	Si-O3	Mo-O3	Si-O1-Si	Si-O2-Si	Si-O-Mo
0O*	1.622	1.640	1.646	2.105-2.114	163.2	132.9	139.2-139.6
1O*	1.622(3)	1.640(1)	1.645-1.649	2.073-2.125	163.3-166.7	132.9	137.6-140.4
2O*	1.623(5)	1.640(1)	1.648-1.653	2.069-2.129	163.8-167.9	133.4	135.4-140.3
3O*	1.623-1.625(6)	1.640(1)	1.649-1.653	2.081-2.107	163.7-169.1	132.4	135.2-136.5
4O*	1.624	1.641(2)	1.649-1.650	2.080-2.100	166.8	130.8	135.8-137.3

Calculated vibrational spectra, O 1s core-level shifts, and simulated STM images of the silica film are all in excellent agreement with the experimental findings. Frequencies and relative intensities of vibrational bands of O-poor and O-rich silica films have been calculated and it has been shown that within those which are infrared active IRA spectra of silica films have only three bands as observed experimentally. Other 2D-network models and cluster model [129] suggesting SiO_4 isolated units as the building block of the silica films have been discarded since their calculated vibrational frequencies do not fit the experimental ones [155]. The same difference in binding energies of O 1s core levels, between surface (O1 and O2), interface (O3) and extra (O*) oxygen ions, has also been found in calculations. Experimentally observed core level shift between surface and interface oxygen ions (1.3 eV) has been proposed as another proof to discriminate isolated SiO_4 cluster model [129, 156] where there is no big difference in calculated binding energies. Finally, based on calculated density of states, STM images of the most stable structure have been simulated by following the Tersoff-Hamann approach [28]. The protrusions imaged by STM have been attributed to the Si atoms at a large tip-surface distance or to the bridging oxygen atoms at a smaller distance. In both cases, the simulated images match well with the experimental ones, providing further evidence concerning the precision of 2D structural model.

4.7 Defect Structure

Silica films grown on Mo(112) surfaces exhibit a high degree of order and very low surface roughness. However, the microscopic defect structures of the film have not been fully solved to date. Presence of antiphase domain boundaries has been predicted by Schroeder et al. [157] on the basis of LEED analysis. From the broadening of the LEED spots, antiphase domain boundaries propagating in both crystallographic directions of the molybdenum substrate have been found. Those boundaries have first been imaged by Min et al. [158]; however, atomic structure and their chemical activities have not been determined. Preparation of highly defective silica films has also been reported and their nature has been discussed by UPS analysis [159]. Annealing the silica film to a temperature lower than 1200 K has been proposed as a method to create high density defects. However, IRAS and STM results clearly indicate that there might be silica clusters at the surface of the wetting silica layer if the film is annealed at lower temperatures.

Defects that are associated with a deviation from the normal Si and O coordination involve atoms with broken or dangling bonds. These defects usually introduce dangling orbitals populated by only one (unpaired) electron. Using electron spin resonance (ESR) as the tool for studying defect sites, there have been reported an impressive array of paramagnetic point defects in the bulk silica structure, most of which are closely related to various defects in quartz or vitreous silica [160, 161]. A number of these defects have significant electrical properties; indeed, about half of the electrical defects in the Si/SiO_2 system have been shown to be paramagnetic in one state or another.

The excess-oxygen center, called non-bridging-oxygen (NBO) center, i.e., $O_3{\equiv}Si{-}O\cdot$, and the peroxy radical ($O_3{\equiv}Si{-}O{-}O\cdot$) are important centers, occurring frequently in bulk fused silica. They do not occur in quartz, since they would require a severe local distortion of the lattice. They have been observed in thin thermal oxides, and seem to behave more or less like those in fused silica. The essential element of the very important E' center is the moiety $O_3{\equiv}Si\cdot$ [161], i.e., a dangling Si sp^3 orbital with an unpaired electron in it. The E' center is usually associated with an oxygen vacancy which gives reason for the dangling Si bond. Altogether, more than ten E'-like centers have been differentiated in crystalline quartz, in amorphous fused silica, and in thin film silica. A major subdivision is the presence or absence of a complementary adjacent moiety $O_3{\equiv}Si+$. Other possibilities include the presence of atoms, mainly O or H but they will not be discussed here.

Among the various kinds of the E' centers in a-SiO_2, the E'_γ center appears to be the most common high-energy radiation-induced oxygen vacancy center generated in oxides prepared under a variety of conditions. The center also exists in crystalline silica, where it is denoted by E'_1. Extensive experimental [162] and theoretical studies [163, 164] have identified this center as a pair of silicon atoms, one bearing an unpaired electron spin and the other bearing a positive charge, adjoining an oxygen vacancy site (Si↑−Si+). The unpaired electron is localized primarily on an sp^3 bonding orbital of a tetrahedral Si. The positively charged Si atom is far removed from its tetrahedral counterpart and believed to be bonded to a triply coordinated O atom or a five-fold coordinated silicon atom in the oxide network. From the point of view of the ESR experiment, the important feature of this center is that the unpaired electron spin is localized on a single Si atom. The precursor defect is an oxygen vacancy or a Si−Si bond. The E'_δ center has the same precursor, but a slightly different ESR signature. These differences result from its different microscopic structure: the positively charged Si is not relaxed back to another network O or Si atom, but stays close to its nearest neighbor Si. As a result, this center is less stable and can be neutralized more easily [164]. The E'_d center comprises a Si atom containing the unpaired spin and an adjacent NBO center. It is assumed that the defect is created from rupturing strained Si−O−Si bonds [165, 166]. The E'_s center is observed on the surface of silica. Contrary to the previous E' centers it is neutral in the ESR active state and invisible for ESR if positively charged [167]. The E'_α center is believed to be a normal $O_3\equiv Si-O-Si\equiv O_3$ moiety in silica, from which the central oxygen is displaced by a radiation event, leaving behind $O_3\equiv Si\cdots Si\equiv O_3$.

4.7.1 Line Defects: Antiphase Domain Boundaries

The properties of epitaxial films grown on metal substrates depend on their composition, structure, lattice matching between film and substrate, and defect structure. In addition to the superstructure domains, a well distinct crystal defects usually form. These crystal defects are called antiphase domain boundaries and owing to the ordering phenomenon, these are characterized by a phase shift vector which describes the displacement of the lattice vector at the boundary. Therefore, the APDs subdivide the superstructure into domains. The origin of antiphase domain boundaries is closely connected to the strain caused by the action of stress. It is well-known that the thickness of the ordered domains and thus the distance between APDs depends on the growth conditions such as temperature, substrate misorientation etc.

Figure 4.10 shows STM images of an antiphase domain boundary taken in two different tunneling conditions, where surface silicon (left) and surface oxygen (right) ions appear as protrusions. When one considers the regular surface structure in the form of 6-membered rings, an APDB is a repetition of 8- and 4-membered rings along $[\bar{1}10]$ direction of the Mo(112) substrate, which is defined by a half lattice shift between regular domains. No other line defects propagating along $[\bar{1}\bar{1}1]$ have been observed as proposed by LEED spot profile analysis. Coordination number of Si ions to oxygen ions is still four, similar to coordination of those on regular sites. The domain boundaries propagate along the terraces and terminate at edge of the terraces. Within hundreds of STM images, no domain boundary that continues to propagate along the neighboring terrace has been observed. 4-member rings are composed of four silicon and four surface oxygen ions. Si ions placed at the corners of rectangular unit mesh can clearly be distinguished in the STM image (Figure 4.10, left). Si-Si interatomic distance along $[\bar{1}10]$ is 10 % shorter than the distance in 6-membered rings. Therefore, neighboring oxygen ions are pushed towards vacuum and appear somewhat brighter, as seen in the right STM image.

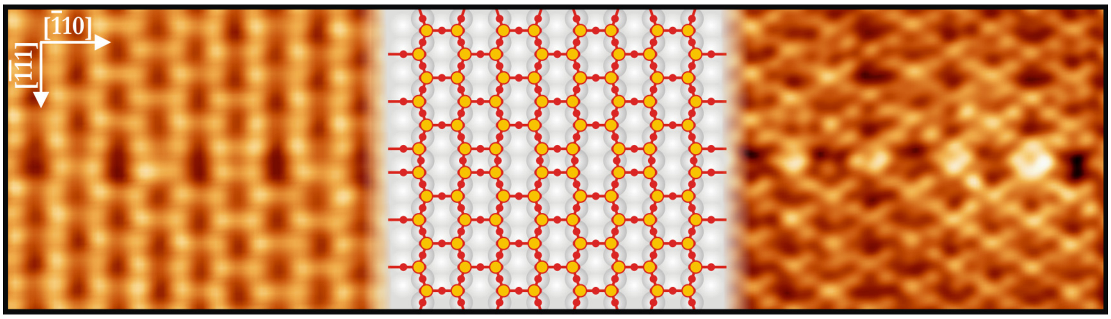

Figure 4.10 STM images of an antiphase domain boundary on silica surface. Image contrast is dependent on tunneling conditions. Left STM image showing Si ions and right image showing O1 and O2 ions were obtained by adjusting the tunneling parameters to $V_s/I=+1.2$ V/0.35 nA and $V_s/I=-0.72$ V/0.45 nA, respectively. A structural model for the O-poor film including an APDB is placed in between for clarity.

High density of APDBs increases the free energy of the thin films. The epitaxial films thus possess a large driving force for APDB removal. The situation can be compared to a polycrystalline film with grain boundaries. Density of the APDB in submonolayer silica films is much higher since the stress created is the driving force of the formation of domain boundaries. Annealing these films might cause the boundaries to migrate so that a local equilibrium at the boundaries can be achieved. The equilibrium at a boundary junction depends on the surface energy of the boundaries, the number of boundaries intersecting at a junction, the angle between the boundaries, and the curvature of the boundaries. DFT calculations predicted that energy cost to form two domain boundaries propagating right next to each other is not too different than the isolated ones suggesting that the free energy difference is not too drastic. As mentioned before, terrace sizes depend on the oxygen flux during silicon deposition at 900 K. The fact that the domain size is independent of the silicon flux but decreases with increasing oxygen amount is not surprising since this can be explained using general nucleation and growth arguments. During the initial stage of the growth, silica stripes are formed on molybdenum surface oxide and silicon atoms between those silica stripes react rapidly, leading to an increase in the island density. At certain coverage, the average separation between the islands becomes so small that most adatoms are captured by a defect site located on the island instead of forming new nuclei. At this stage, the maximum island density is reached. Finally, when two phases come together, they form an APDB. The average size of the islands is thus determined by the delicate balance between the deposition rate and amount of oxygen on the molybdenum surface to be reacted with Si adatoms.

4.7.2 Point Defects

The point defects influences nucleation and growth of the deposited particles on silica model systems therefore the nature of those has been questioned both experimentally and theoretically [146, 168]. Very recently, Martinez et al. [140] have calculated structures and properties of four different point defects possibly present at the surface of one monolayer silica film. The calculations have been restricted to the O-poor silica film structures and only $O_3{\equiv}Si{-}O\cdot$ (NBO), $O_3{\equiv}Si\cdot$ (E' center), $O_3{\equiv}Si{\cdots}Si{\equiv}O_3$ (oxygen vacancy), and $O_3{\equiv}Si{-}O{-}O{-}Si{\equiv}O_3$ (peroxo group) defect sites have been considered. Within those defect structures only NBO and oxygen vacancies have been found likely to be formed on silica surface. All defects introduce a state in the band gap and for NBO case; it is possible that dangling oxygen might capture one electron from the substrate.

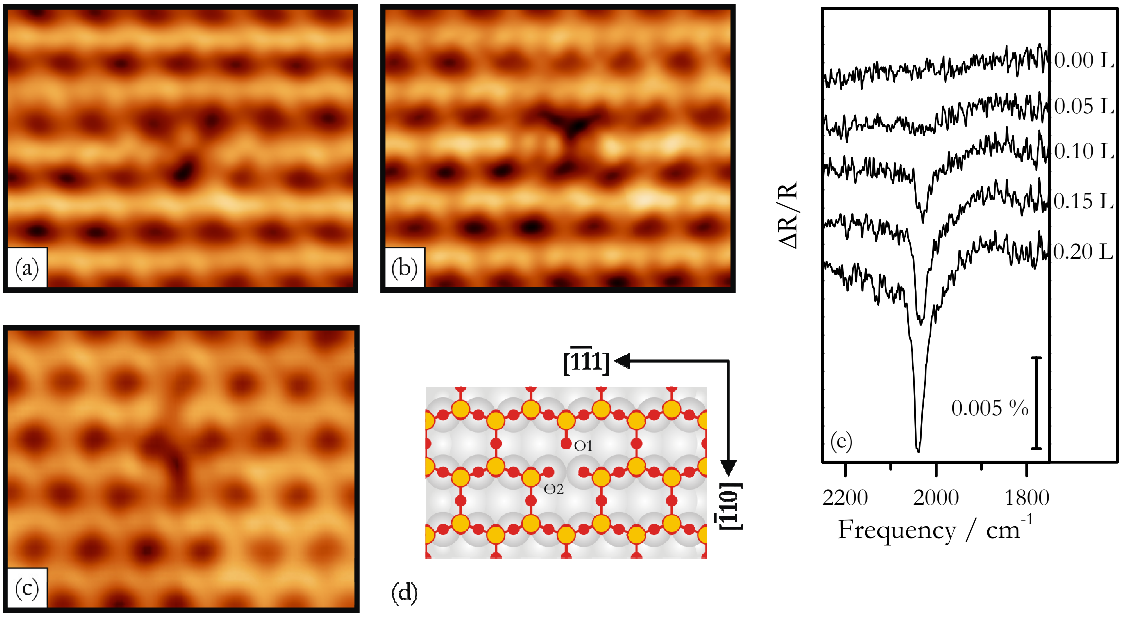

Figure 4.11 STM images ($3.3\times2.2\ \mathrm{nm}^2$) of point defects on silica film. Tunneling conditions are $V_s/I=$ (a) -1.0 V/0.40 nA, (b) 0.5 V/0.4 nA, (c) 1.0 V/0.6 nA. (d) Structural representation of a Si vacancy. (e) IRA spectra of CO adsorbed on silica film at 100 K.

Recent investigations performed by scanning probe techniques have improved the understanding of the structure of point defects on surfaces [169]. Since the local charge density dramatically changes on defect sites, it is very likely that pronounced contrast differences can be seen in topographic STM images. Figure 4.11 (a) and (b) show one type of point defect seldom observed on silica surfaces. The images of the same area were taken with negative and positive sample bias in order to differentiate the identity of the defect and its neighborhood. A registry analysis based on the known silica film structure reveals that the point defects are Si vacancies. One possibility in the presence of Si vacancy is the formation of peroxo groups. When the tunneling parameters fulfill the condition where only surface oxygen ions appear as bright protrusions, once might expect to see peroxo moieties if they exist. Since in 2D silica network there are two surface oxygen ions (O1 and O2), there are two geometrical possibilities that peroxo linkages might form. Difference in Si-Si interatomic distances in the presence of a Si vacancy makes $O_3{\equiv}Si{-}O1{-}O2{-}Si{\equiv}O_3$ along $[\bar{1}10]$ direction more probable than the alternative $O_3{\equiv}Si{-}O2{-}O2{-}Si{\equiv}O_3$ along $[\bar{1}\bar{1}1]$ direction. In addition, both possibilities leave one NBO in the next coordination neighborhood. STM image seen in Figure 4.11 (a) might favor the former because of the bright protrusion between molybdenum troughs. Reversing the sample bias also reverses the contrast at the defect site (Figure 4.11 (b)). Another possibility is the formation of three NBO dangling bonds due to Si vacancy. Two of them along $[\bar{1}\bar{1}1]$ will be identical ($O_3{\equiv}Si{-}O2\cdot$) and the third one ($O_3{\equiv}Si{-}O1\cdot$) would be coordinated to two O2 ions. Due to the low number density of there vacancies ($<10^{14}$ per cm^2), it is not possible to see a signature of these in the band gap of silica film. However, probe molecules might help us to distinguish the nature of those defects.

In general, dissociation of water on a defect site results in formation of two silanol (Si-OH) groups. Therefore, it is reasonable to assume that oxygen vacancies on silica film are hydroxylated and the other dissociation product, hydrogen, either recombines with another hydrogen and desorbs molecularly or form Si-OH group by reacting with $O_3{\equiv}Si{-}O\cdot$ dangling bonds. $O_3{\equiv}Si{-}O{\cdots}H$ vibration has a distinct stretching frequency and can be characterized by IRAS. In addition, if they exist, σ and π bonding states of hydroxyl groups can be distinguished in UP spectra. Adsorption of water at 100 K, 300 K and elevated temperatures under vapor pressures up to 1×10^{-4} mbar did not give any sign of the formation of hydroxyl groups (for details, see Chapter 5). CO is another potential molecule to probe defect sites on silica [170]. As IRA spectrum of CO adsorbed on silica film at 100 K show in Figure 4.11 (e), adsorbing 0.2 L CO is enough to saturate all the accessible defect sites. Since the valence state of Si is 4+, it is expected that stretching frequency of CO to be around 2200 cm^{-1}. However, the lower frequency of CO (2187 cm^{-1}) suggests that there might be another site where CO adsorbs. Since CO adsorbed on molybdenum surface oxide had the same stretching frequency, it reasonable to think that some molybdenum surface under Si vacancies can be exposed to CO. It is also likely that dangling NBO groups might form a bond with the substrate since affinity of molybdenum toward oxygen makes it quite favorable. This could also be the reason why dissociation of water does not take place on defect site. Nevertheless, those vacancies may certainly be nucleation sites for deposited particles and be still influence their coordination and reactivity.

CHAPTER 5

INTERACTION OF WATER WITH SILICA FILM

The importance of water in chemical and biological processes can hardly be exaggerated. However, it is not the only reason why water attracts so much attention in the scientific world [171, 172]. Being relatively simple, in the form of a single, isolated molecule, it demonstrates an impressive range of unusual properties in the condensed phase [173]. The best known ones are: a negative volume of melting, a density maximum at 4°C, and anomalously high melting and boiling points for such a low-molecular weight substance. In addition, an isothermal compressibility minimum at 46°C, a high value of the dielectric constant, an increase of the liquid fluidity with pressure, the existence of several distinct crystalline forms, and a very effective proton transport are among many other less known features. Thus, all these extraordinary properties must be explained by the presence of specific intermolecular interactions. This distinctive feature is the hydrogen bond formed between water molecules [174].

5.1 The Water Molecule and Hydrogen Bonding

The free water molecule has a simple geometric structure where two hydrogen atoms are covalently bonded to the oxygen. In Figure 5.1, a molecular orbital energy level diagram of H_2O is shown. The water molecular orbitals are denoted according to the C_{2v} point group symmetry, with the following ground state configuration

$$(1a_1)^2(2a_1)^2(1b_2)^2(3a_1)^2(1b_1)^2$$

$1a_1$ is the localized O 1s core orbital, and the $2a_1$ is the inner valence orbital with mainly O 2s character. The outer valence consists of the strongly bonding $1b_1$ orbital, the nonbonding lone-pair orbital $1b_2$, and the $3a_1$ which has both bonding and lone-pair character. The orbital mixing is indicated in Figure 5.1 by the dashed lines. In the unoccupied valence region, the mixing of O 2p and H 1s gives the two OH anti-bonding combinations. The population of mainly bonding orbitals gives rise to the rather strong covalent intramolecular bond. The cost to break one OH bond is about 5.2 eV. Most of the electron density is centered on the oxygen atom, and in particular the lone-pair orbital gives rise to a rather strong intra-molecular dipole moment (μ~1.86 D). Geometry-wise, the covalent bond gives rise to a short OH bond length (~0.095 nm) and a near tetrahedral bond angle (104°).

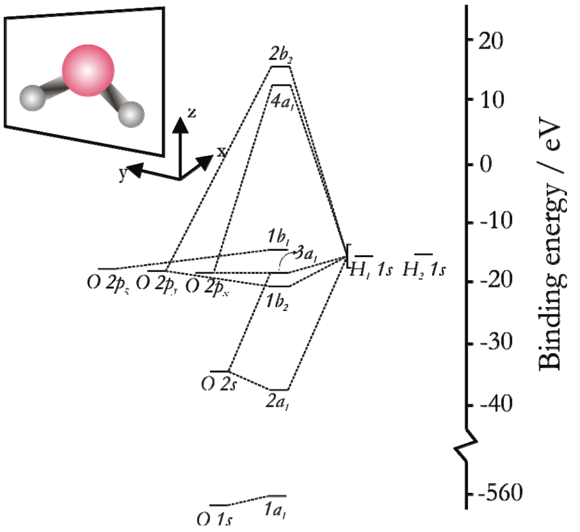

Figure 5.1 Molecular orbital energy level diagram of H_2O (adapted from [185]).

The intermolecular interaction between water molecules represents a hydrogen bond (H-bond). The H-bond strength is intermediate between covalent or ionic and Van der Waals bonding [175]. For water the intermolecular bond strength is in the order of 10 % of the intramolecular OH bond strength. The free OH group of one molecule is bonded to the lone pair side of the oxygen in another in a linear bond where the hydrogen is located along the O−O direction. The H-bond is traditionally ascribed to electrostatic interaction.

The properties of the H-bond are difficult to describe in a simple manner. The archetype of hydrogen bonding, the water dimer, has an O−O distance of ~0.295 nm. For the water trimer, this distance is significantly shorter (~0.285 nm). Via the tetramer (2.79 nm) an O−O distance close to the ice value is reached for the pentamer (0.276 nm). Clearly, the hydrogen bond strength is changed, which illustrates one of the difficulties to give a simple H-bond picture, namely the cooperativity. One approach is to calculate the bonding energies per water molecule in hydrogen bonded chains at constant O−O distances (0.284 nm) [176]. In this ab-initio study, the non-additive part of the H-bond increased by up to 16 % of the total energy, clearly demonstrating the cooperative nature of hydrogen bonded water.

The exact chemical bonding picture of the H-bond is not known. It is clear, however, that the valence electrons are subject to significant changes when hydrogen bonds form. For example, in liquid water and ice, the dipole moment increases (from 1.86 to about 2.6−3.1 D) [177] which obviously means electronic structure changes. However, whether the electronic structure changes upon hydrogen bonding are due to the internal polarization from the surrounding molecules or from a charge transfer mechanism is still a matter of debate. In most studies, the H-bond has been considered as either a pure electrostatic interaction, including internal polarization from the field of the neighboring molecules [178], or as involving charge transfer between the molecules [179], sometimes interpreted as covalent bonding [180, 181]. The controversy between the pure electrostatic and charge transfer pictures has been particularly strong [182]. The difficulty rests in the fact that the different theoretical approaches applied give varying results [183, 184] and the situation is further complicated by the lack of direct experimental evidence supporting either picture.

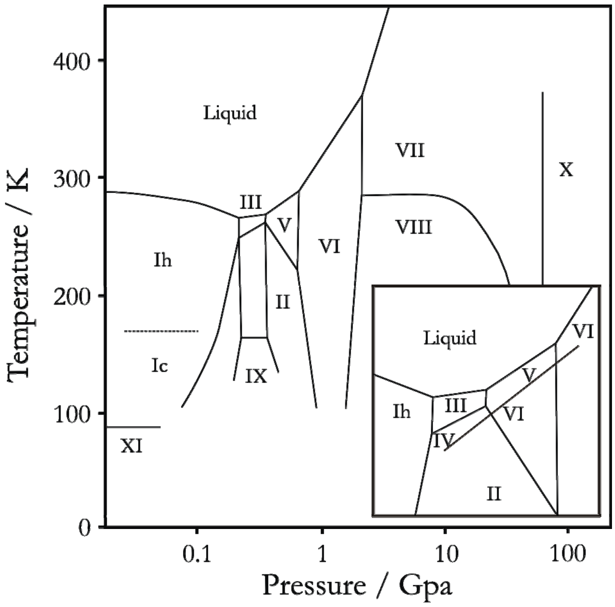

Figure 5.2 The phase diagram of water/ice. Inset: The medium pressure range showing the melting curves of metastable ices IV and XII.

5.2 Ice

The versatility of hydrogen bonds between water molecules is illustrated by the extraordinarily complex phase diagram of water. In particular, the low and high-density amorphous ice and supercooled water attracts a high scientific interest [186]. In crystalline ice, each water molecule is fully coordinated to 4 other molecules in near tetrahedral structures. Small deviations in bond angles allow for a large number of crystalline phases [187] which are depicted in Figure 5.2. Among the different phases, only the crystalline structure called hexagonal ice (ice Ih) is found in nature under normal conditions. Each water molecule is bound to four other molecules in an almost perfect tetrahedral structure, with intramolecular bond angles of ~109.5° and intermolecular O−O distances of about 0.274-0.276 nm depending on temperature. The bulk structure of hexagonal ice is often referred to as a hydrogen-bonded model system, a well characterized and understood phase. If one takes a closer look at the hexagonal geometry, it can be seen that the structure can be described by a stacking of ~0.095 nm thick bilayers separated from each other by 0.37 nm. Cubic ice (Ic) has the same bilayer structure but differs in the stacking sequence. Within the so-called Bernal-Fowler ice-rules [188], two internal hydrogen bonds can be placed in any of the four given directions. Due to entropy reasons, hexagonal ice settles into a random arrangement of hydrogen atoms, which is referred to as proton disorder. An inspection of the probability of any given arrangement in an entire crystal led Pauling to the conclusion that at the absolute zero temperature, ice Ih should have a zero-point entropy of 3.4 $\mathrm{Jmol^{-1}deg^{-1}}$ [189], in excellent agreement with experiment.

5.3 Interaction of Water with Surfaces

Surface science studies on water adsorption on solid surfaces have been reviewed by Thiel and Madey [185] and recently by Henderson [190]. In spite of a vast amount of studies reported, the adsorption and desorption behavior of water are still debated even for the systems extensively investigated for years like, for instance, Pt(111), Pd(111) and Ru(0001) [191-198]. It has been shown that water monomers form on metal surfaces at low coverage and at very low temperatures (typically < 40 K), which cluster into amorphous solid water (ASW) on heating above 60 K due to enhanced water diffusion on the surface [199, 200]. Upon further heating to or dosing at 125-135 K, a crystalline ice (CI) forms. Based on the diffraction studies it has been suggested that the CI films are cubic ice in nature which is terminated by an unreconstructed (0001) bilayer [201-203]. In the bilayer model of ice on metal surfaces, first proposed by Doering and Madey [201], the first layer consists of nearly in-plane water molecules bound to the metal surface via oxygen lone pair, while water molecules in the second layer are in plane with a surface normal. Only one H atom from the top-laying molecules is involved in formation of H-bond network to the water molecules in the first layer, another H atom is pointed from the surface (referred to as 'H-up' model). However, recent theoretical results [204, 205] suggest that this OH bond points to the metal surface ('H-down' model) leaving no dangling OH bonds protruding into the vacuum, thus explaining the non-wetting behavior of the next ice agglomerates on top of the 'hydrophobic' water bi-layer as experimentally observed by Kimmel et al. [206]. The formation of an epitaxial CI film may lead to the formation long-range ordered structures like, for example, $\sqrt{39}\times\sqrt{39}\,\mathrm{R}16.1^\circ$ on Pt(111) [191] and $\sqrt{3}\times\sqrt{3}\,\mathrm{R}30^\circ$ on Ru(0001) [201, 202]. Using scanning tunneling microscopy operating at low temperatures, cyclic water hexamers have been observed on Pt(111) [207], Cu(111) [208] and Ag(111) [209] surfaces. Based on density functional theory calculations, these hexamers have been explained as rings of nearly flat-lying water molecules which are considered as building units for the two-dimensional growth of ice on Pd(111) [210]. Very recently, Yamada et al. have reported on the self-assembling of water molecules into one-dimensional zig-zag chains on the Cu(110) surface at low coverage due to the anisotropy of the substrate [211].

Formation of the CI films on oxide surfaces has been studied to a less extent [212-215]. To date, MgO(100) seems to be the only surface on which ordered water overlayers have been observed, although different water structures have reported. Heidberg et al. [216] found a c(4×2) structure by LEED, while Goodman and co-workers [217] using MgO(100) films grown on Mo(100) reported on a p(3×2) structure. Recent studies by Ferry and co-workers have shown that there is a delicate balance between wetting and clustering behavior of water on MgO(100) which may strongly depend on the experimental conditions [218, 219]. In addition, several theoretical studies suggest that a mixed (water+hydroxyl) layer is thermodynamically more stable than water bi-layer, which implies water dissociation on MgO(100), however, this issue remains controversial [220, 221].

It is expected that oxygen terminated defect-free oxide surfaces do not dissociate water. Indeed, Tzvetkov et al. found no evidence for water dissociation on thin alumina film grown on NiAl(110) [222]. Based on work function measurements, photoelectron spectroscopy using synchrotron radiation and ultraviolet photoelectron spectroscopy, the authors suggested that isolated water molecules start to cluster at sub-monolayer coverage at around 100 K, finally forming three-dimensional ice multilayers. Also, Weiss and co-workers observed only molecular water adsorption on oxygen terminated FeO(111) films grown on Pt(111) [223]. Based on TPD and UPS results they have proposed that water first adsorbs at 100 K as monomers in upright geometry with the oxygen atom pointed toward the Fe ions underneath the top O-layer. At increasing water coverage, formation of the CI film in a 'H-up' geometry has been suggested. In contrast, Kay and co-workers [224] have found no evidence for isolated water monomers even at 30 K using TPD of N_2 and vibrational spectroscopy. The authors suggest formation of ordered ice islands wetting the FeO(111) surface at 135 K. However, no long range water ordering has been observed by LEED in both studies.

It is obvious that the epitaxial growth of ice on any substrate is favored by a small lattice mismatch between them. The O-O distance in the hexagonal ice phase is 0.275 nm (0.261 nm when projected onto the (0001) plane), that is much shorter than 0.3-0.31 nm for the close-packed FeO(111) as well as alumina film surfaces mentioned above. However, a well-ordered silica film grown on a Mo(112) single crystal exhibits a slightly distorted hexagonal lattice with an O−O distance in the top layer equal to 0.273 nm and therefore can be considered as a good substrate for the epitaxial growth of ice. The interaction of water with differently prepared silica films was previously studied by Wendt et al., who have proposed that water forms 3D clusters at 90 K even at low coverages and does not dissociate on the surface upon heating [225].

5.4 Adsorption of Water on Silica Surface and Formation of Ordered Water Overlayer

5.4.1 Desorption Kinetics of Amorphous and Crystalline Water

Thermal desorption of water has been extensively used in characterizing the interaction of water with solid surfaces, particularly in terms of monitoring reactivities, adsorption capacities, site distributions and site binding energies. The desorption properties of water have been examined primarily using temperature programmed desorption techniques [185]. The water-surface interaction has a significant impact on the desorption of water from thin ice layers. One might also expect that desorption of water from small clusters should be highly dependent on the nature of the water-surface interaction.

As has been suggested in the previous section on the desorption properties of water from solid surfaces, the interplay between water-water and water-surface interactions is manifested in many of the properties of adsorbed water. In particular, the ability of water to cluster, form structures that are registered to the host lattice or to dissociate are all linked to the energetics and dynamics of water-water versus water-surface interactions. From an energetic perspective, this interplay can be divided into three general categories: (a) water-water $\geq$ water-surface; (b) water-water $\leq$ water-surface; and (c) water-water $<<$ water-surface. The first category is the typical condition of clustering of water, such as is the case for most noble metal surfaces; the second category is a trade-off between registered molecular water and intermolecular hydrogen bonding. The third category fulfills the energetic conditions for water dissociation. One must also consider kinetic processes in these interactions. For example, systems in which water-water interactions are energetically more favorable than water-surface interactions can be isolated in metastable states where the latter do not come into play, e.g., at low temperatures. Under these conditions, the structure of molecularly adsorbed water will be considerably different than that encountered when water-water interactions are present. Therefore, ASW is also referred as a metastable phase of solid water.

Figure 5.3 (a) shows a family of TPD spectra as a function of H_2O exposure at 100 K. These spectra show a zero-order desorption kinetics of 'multilayer' water as was observed on many solid surfaces [222, 226-228]. The same kinetics is observed for D_2O adsorption, with the desorption temperature shifting by ~10 K to higher temperatures as compared to H_2O at a given water coverage. The analysis of the leading edge of these TPD spectra (see Figure 5.3 (d)) revealed desorption energies of 45 and 51.5 kJmol^{-1} for H_2O and D_2O, respectively, which are consistent with heats of sublimation reported in the literature [185, 229, 230]. No features indicating transition from monolayer to multilayer desorption have been observed by TPD (as seen on Pt(111), for example [206]), which

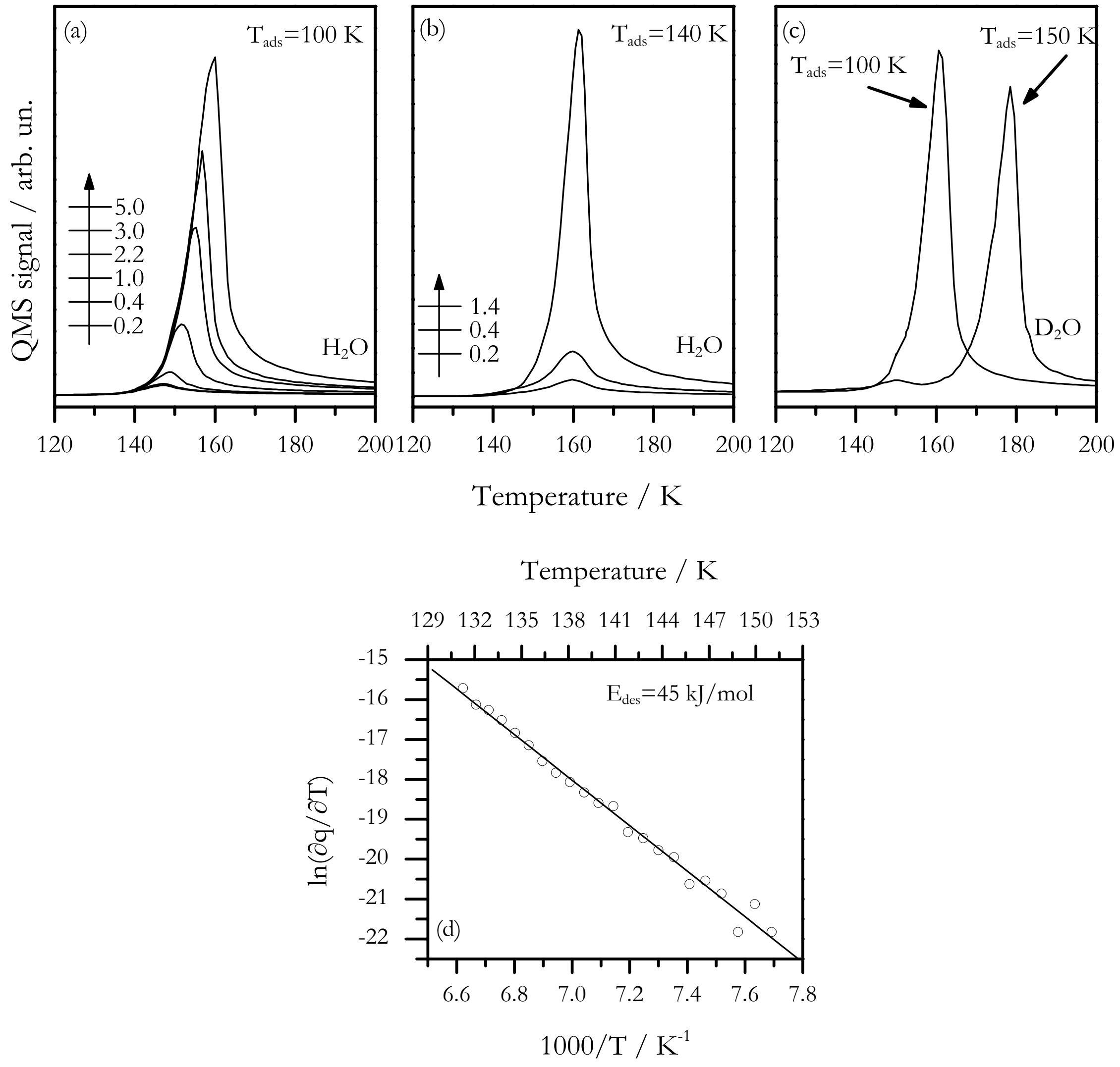

Figure 5.3 TPD spectra of H_2O adsorbed on a silica film at (a) 100 K and (b) 140 K. (c) TPD spectra of ~1 BLE D_2O adsorbed at 100 and 150 K. Heating rate was 3 Ks^{-1} for each spectrum. (d) Arrhenius plot of the amorphous H_2O desorption. The black line is a linear fit to the experimental data and corresponding slope (activation energy) is shown in the figure.

implies formation of an overlayer where the interaction with the substrate is weaker than that between the water molecules.

However, water dosing at 140 K (i.e. the edge of H_2O desorption) results in desorption with a pseudo-first order kinetics as shown in Figure 5.3 (b). The top spectrum in Figure 5.3 (b) corresponds to the highest coverage (~1.4 BLE[4]) reached under these conditions, (which in fact critically depends on the balance between the sample cooling rate and the water pumping speed since water starts to desorb at this temperature but may re-adsorb while cooling). Comparison of two sets of spectra shows that H_2O adsorbed at 140 K desorbs at temperatures ~7 K higher than water exposed at 100 K up to the same coverage. Even a larger difference ($\Delta T=\sim 18$ K) is observed for D_2O (see Figure 5.3 (c)), when adsorption at 100 K and 150 K (the edge of D_2O desorption) is compared. These

---

[4] Bilayer equivalent (BLE) refers to the amount of water adsorbed on silica film. It was calibrated with water adsorption on Pt(111), where the formation of water bilayer can be discriminated by TPD.

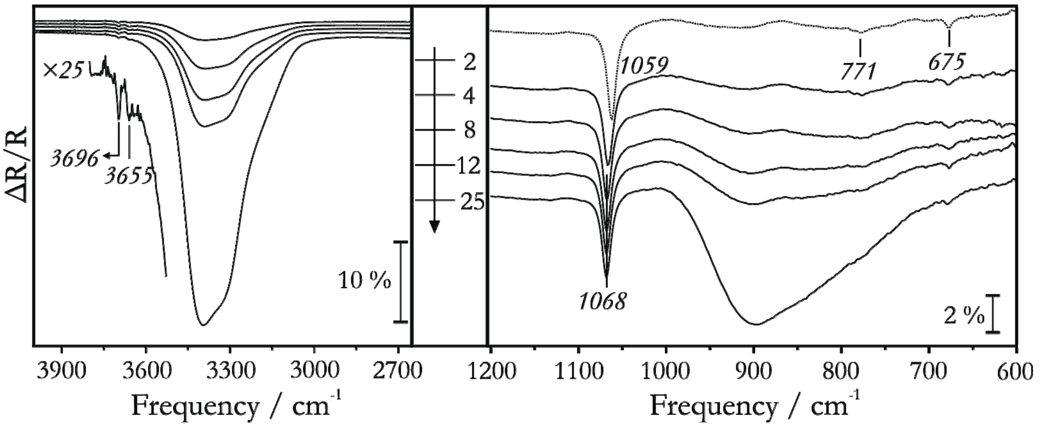

Figure 5.4 IRA spectra of H_2O adsorbed on a silica film at 100 K at increasing coverage as indicated.

findings indicate that two different structures are formed by adsorption at 100 and 140 (150) K, respectively. Figure 5.3 (c) clearly shows that the desorption signal from the 'high temperature' structure cannot comprise the high temperature tail of the TPD traces of water adsorbed at 100 K. Note also, that the TPD spectra do not reveal any feature for heating rates of 0.2-3 Ks^{-1}, which could be associated with the structural transformations upon heating in a definitive manner. Therefore, it can be concluded that the surface restructuring proceeds slower than the time scale of the TPD experiment (typically 10-20 seconds).

Interestingly, any attempts to resolve two desorption states in TPD spectra by additional adsorption at 100 K on the sample pre-exposed to H_2O at 140 K were unsuccessful as it always resulted in the same TPD spectra as for water exposed only at 100 K. This seems to indicate that the reverse transformation is kinetically limited but may be triggered by additional water adsorption.

5.4.2 Monitoring Crystallization with Vibrational Spectroscopy

Figure 5.4 shows IRA spectra of the silica film as a function of water exposure at 100 K. The infrared spectrum of water, in general, exhibits OH stretching vibration band (ν_1, ν_3) between 3000 and 3700 cm^{-1}, OH bending band (ν_2 or δ_{OH}) between 1700 and 1620 cm^{-1}, and a broad hindered rotation band (ν_r) in the 700-900 cm^{-1} region [231-234]. Besides, a fourth band, a combination band of bending vibration and hindered rotation, becomes apparent between 2250 and 2220 cm^{-1}, especially at high ice coverage (not shown). The vibrational properties of water, in many forms of crystalline ice or in a liquid phase, have been extensively studied under variety of pressure and temperature regimes. Stretching vibrational region of ice clusters is composed of the hydrogen bonded OH and free-OH bands. The free-OH band is clearly visible in the spectra of ice films and amorphous ice clusters (3690-3700 cm^{-1}) and attributed to non-hydrogen bonded dangling OH groups at the surface and periphery of the clusters [234, 235]. Hydrogen bonded OH stretching spectral region is rather broader and red-shifted as compared to the gas phase values (the frequencies of asymmetric and symmetric stretching bands of water in gas phase are 3756 and 3657 cm^{-1}, respectively [236]). The complexity of distribution of density of the states is the central reason for the variety of the different interpretations of OH stretch vibrations. For dissociative water adsorption on oxides, the frequencies of isolated OH species on the oxide surfaces are typically below 3700 cm^{-1}, for example, 3620 cm^{-1} for Cr_2O_3 [237], 3660 cm^{-1} for Fe_3O_4 [238].

The OH-stretching region of the IRA spectra, presented in the left diagram of Figure 5.4, with a broad band centered at ~3400 cm^{-1} is typical for the H-bonded ASW phase [224]. This form of non-crystalline ice is observed below ~120 K when water vapor condenses on a cold substrate. O−O inter-atomic distance between neighboring water molecules and O−O−O angle represent small deviations together with the hydrogen bonding order. In the initial stage of deposition, OH stretching band grows featureless with coverage, suggesting that at 100 K ice molecules form hydrogen bonded clusters [200]. In addition, two relatively weak signals at 3696 cm^{-1} and 3655 cm^{-1} can be detected. The band at 3696 cm^{-1} is assigned straightforwardly to the free-OH bonds on the surface of 3D ice clusters [233, 239, 240] while the band at 3655 cm^{-1} can be attributed to the isolated OH species formed on the defect sites of the silica film. Since ASW growth depends on many factors; such as surface morphology, temperature and deposition rate [241], free-OH groups may also be found in micropores possibly present inside ice clusters. Second peak at 3655 cm^{-1} is in the range of vibrational frequency of OH groups observed on metal oxides. However, this band cannot be assigned to silanol (Si−OH) groups because the frequency of these groups found in hydroxylated silica gels is much higher [242, 243]. Line defects have similar surface termination as regular silica surface and dissociation of water on these defect sites is considered to be very unlikely. As discussed in Chapter 4, the point defects (possibly silicon vacancies) are present and density of which is low. Within the first nearest neighborhood of silicon vacancies, dangling Si−O· bonds might be ideal sites for water dissociation. However, its affinity toward oxygen atoms makes molybdenum substrate questionable and saturation of Si−O· bond by substrate can not be disregarded. Besides, the free-OH groups at the periphery of ice clusters may form strained hydrogen bonding with those sites or with the regular oxygen atoms in the silica network. In addition, TPD results do not indicate any recombinative desorption peak. This band can therefore be assigned to strained OH groups weakly bonded to silica point defect sites which, in this scenario, are either molybdenum substrate accessible due to the vacancy or silicon cation not fully coordinated to 2D network of silica film.

Increase in ice coverage makes three discernable hydrogen bonded bands evolve. The band at 3390 cm^{-1} becomes sharper with two low frequency shoulders at about 3315 cm^{-1} and 3150 cm^{-1}. Sharpening the bands is an indication of extended hydrogen bonding. Since the ice overlayers are amorphous in nature at this temperature, it is difficult to make a parental assignment to unique vibrations. ASW growth has an impact on vibrational properties of silica film, too. Water adsorption at 100 K gradually shifts the main peak assigned to the Si−O−Mo stretching vibrations (1059 cm^{-1}) by ~9 cm^{-1} towards higher frequencies without significant loss of the intensity, which then stays nearly constant, although the water coverage increases as evidenced by continuous growth of the broad bands centered at ~3400 cm^{-1} and ~900 cm^{-1}.

The left panel of Figure 5.5 shows structural phase transition of ASW layers deposited at 100 to CI. Above 130 K, reshaping and red-shift are observed in OH stretching region. It is conventional to relate the changes in the shape of infrared spectra to the strength of hydrogen bonding. The shape of the OH stretching band can also be described as a central band with two distinct shoulders residing at higher and lower frequencies, similar to the bands recently assigned by Buch and Devlin [232]. Based on Ih structure, the authors propose that the central component has an asymmetric character (ν_3) and the interaction of individual dipoles with long range fields gives rise to split in ν_{LO}-ν_{TO} modes. High frequency shoulder has been interpreted as a longitudinal intermediate band involving polarizations perpendicular to the surface layer of Ih, whereas; polarizations are parallel for low frequency shoulder. The generally agreed assignment to the low frequency shoulder of CI spectrum (3140 cm^{-1} for OH) is symmetric stretching band (ν_1) oscillating in-phase [231]. Intensities of these vibrational modes depend on many factors, such as

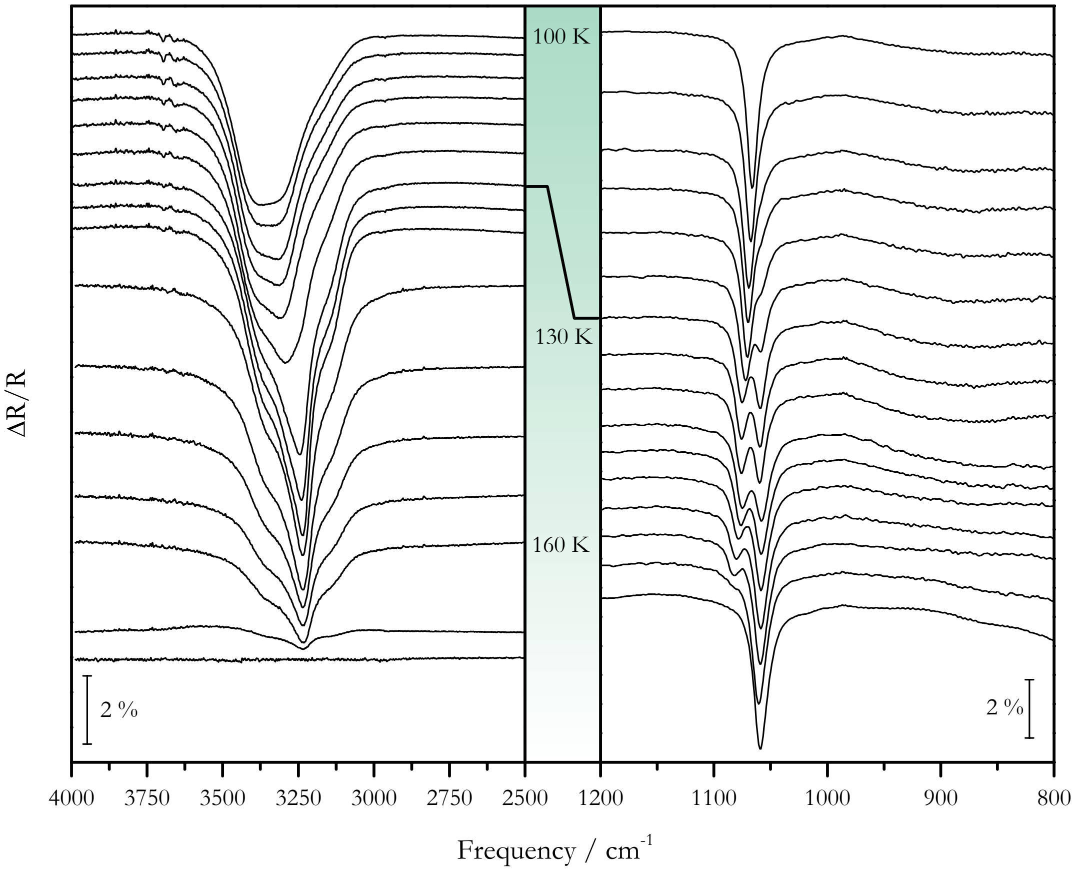

Figure 5.5 IRA spectra of 6 BLE of H_2O adsorbed on the silica film at 100 K and slowly heated up to complete desorption.

degree of crystallinity, polarity of the IR light and also spectroscopic mode. Since IRAS experiments have been carried out by using p-polarized infrared radiation at grazing incidence, interpretation OH (or OD) spectral region should be made taking optical vibrational modes into account. This section has been devoted only to observation of an ordered ice layers on silica surface and detailed interpretation of vibrational spectra and nature of bonding of water molecules on silica film will be discussed in the following section.

The formation of the more strongly bound CI layer significantly modifies the vibrational properties of the silica film, resulting in a remarkable blue-shift of the Si−O−Mo stretching frequency. On slow heating of this sample, the phonon absorption peak at 1068 cm^{-1} splits in two peaks: one peak at 1059 cm^{-1} as in the original silica film, and a high frequency peak (1076 cm^{-1} at 140 K), as shown in Figure 5.5. This splitting appears simultaneously with the spectral changes in the OH stretching region. Upon further heating, the CI film sublimates and the high frequency phonon peak vanishes while the peak at 1059 cm^{-1} from the bare silica gains the intensity. This blue shifted phonon emerges from the onset if the water is dosed at 140 K, indicating that this surface structure depends only on temperature and therefore is thermodynamically stable. The experiments with the silica film prepared with $^{36}O_2$ show the same behavior, which confirms that the effect originates from the water/silica interaction.

After crystallization is completed, CI continues to sublimate from silica surface and naturally the intensity of OH vibrational bands attenuates. At this point, OH region can give quantitative information since changes in dipole-dipole interactions between crystalline ice molecules do not influence intensity much. Divided silica phonon carries on shifting to higher frequencies. As yet, conclusions have been drawn based on structural ordering between water molecules. In a similar work done on Pt(111) surface, polar ordering (or ferroelectricity) in ice has been described as a surface induced effect, and it vanishes asymptotically when the ice layers get thicker [244]. The values of total dipole moments have been calculated for two and three puckered water bilayers [245] which may form due to lattice mismatch and compared with the values for flat layers. Results of these calculations clearly show that total dipole moment of water is higher if the overlayer is puckered. It is the O−O interatomic distance that counts for structure of Ih, which is nearly identical to that for Ic. Besides, they are both known to be the structures having lack of hydrogen order. On silica film, both OH and OD vibrational bands are much broader than the bands of hydrogen ordered ice phases (XI and XII) [246] and can not be related to ferroelectric behavior as claimed by Iedana et al. [247]. Compared with temperature regimes of proton ordered ice phases and CI formed on silica films, there is no doubt that the phonon splitting can not be taken as an indicator of changes in hydrogen order.

Above 155 K, the surface of the CI layers becomes flatter due to desorption and reorientation of hydrogen bonds. This reorientation can be understood in terms of conformation of frustrated hydrogen bonding by thermal means which is possible due to higher mobility of defects. Diffusion of hydrogen bonded molecules is restricted by their local environment and cannot take place without orienting the environment. Therefore, it is more likely that ice layers become less porous due to a kind of autocatalytic hydrogen bonding. Then, similar considerations can apply to interpretation of splitting; the polar order could be vanished due to presence of a fraction of less ordered ice molecules at the surface of clusters and divided silica phonon even shifts further to blue when disordered surface layer desorbs. Sum of the integrated intensities of divided phonon peaks is equal to that of silica film itself, so fraction of surface covered by ice can be calculated. Another reason might be the long range Coulomb interactions between water islands influencing clustering as observed on Cu(110) surface [211].

In principle, there are several factors which influence phonon spectra of thin oxide films in the presence of deposits and adsorbates as systematically studied by Frank et al. on alumina [248]. However, metal and oxide particles, deposited on thin alumina and silica films, always led to a red-shift and simultaneous broadening of the oxide phonon at increasing coverage [249, 250]. Any sorts of phonon coupling must be excluded as the vibration frequencies in water and silica film are energetically well separated. Since water is a polar molecule and has a large dipole moment, it seems plausible that the effect is caused by polarization of the water/silica interface, which influences the Si−O−Mo stretching vibration. The fact, that a much stronger phonon shift is caused by the crystalline ice, points to the formation of the ordered structures on the silica surface.

5.4.3 Photoelectron Spectroscopy

Water is a quite sensitive molecule and damaging can occur if it is exposed to high dose of electrons and photons. In order to record an O 1s XP spectrum of water the sample has to be exposed to photons with energy above the O 1s absorption threshold at about 530 eV. The generated holes from a photoemission/absorption event in the substrate or water molecules will mainly decay via an Auger mechanism emitting energetic electrons that can go through various inelastic scattering events. The inelastic scattering events in the substrate lead to a cascade of low energy secondary electrons which eventually escape from the sample through its surface. The cross section (probability) for adsorbed water molecules dissociating when exposed to these low energy electrons is very high. To make sure that water chemistry is not induced by the low energy electrons generated from the X-rays, it is of essence to minimize the electron dose per water molecule down to a

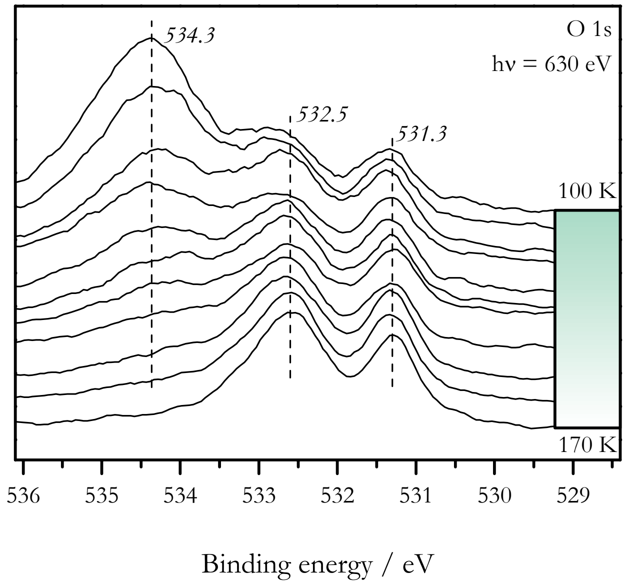

Figure 5.6 Consecutive PE-spectra of the silica film, exposed to 6 L of water at 100 K, on slow heating to 170 K. The states at 532.5 and 531.3 eV are assigned to the surface and interfacial O species in the silica film. The spectra were recorded with low acquisition time in order to prevent any photon-induced effects on the water overlayer. The spectra are offset for clarity.

level where X-ray/electron induced dissociation can not be observed. However, at the same time we need a certain photon dose to collect the number of electrons necessary to record a spectrum with reasonable statistics. For the evidently very sensitive systems studied under UHV and low temperatures, this problem is minimized by a sample scanning procedure.

Figure 5.6 shows the O 1s PE spectra of the silica film exposed to water at 100 K. Two O species at 532.5 and 531.3 eV observed on the clean film have been the O atoms in the top-most (Si−O−Si) and interface (Si−O−Mo) layers, respectively. Adsorption of 6 L of water results in a signal centered at 534.3 eV, which can be attributed to the intact water molecule [222]. It is likely that an activation barrier has to be overcome in order for dissociation to occur. This possibility can be explored by slowly increasing the temperature of the substrate and recording the O 1s spectral evolution in real time. Due to a relatively broad spectral feature of water, it is difficult to follow the crystallization process around the same temperature range in which phonon splitting is observed. Upon slow heating, this signal gradually attenuates, finally resulting in the spectrum of the clean silica surface. However, no hydroxyl species (expected at ~533.5 eV) are detected upon heating to 170 K, which is consistent with non-dissociative adsorption of water.

5.4.4 Formation of Ordered Water Layer

The TPD results clearly show that two energetically different structures are formed by adsorption at 100 and 140 K. Based on the IRAS data, these structures can be rationalized in terms of the amorphous and crystalline films formed at 100 K and 140 K, respectively. The 'high-temperature' structure is thermodynamically stable since it can be formed either by heating of the ASW film to or by water exposure directly at 140 K. However, the structural transformations are quite slow (likely, in 10^2 -seconds scale) and cannot be discriminated by TPD at the heating rates studied (0.2-3 Ks^{-1}).

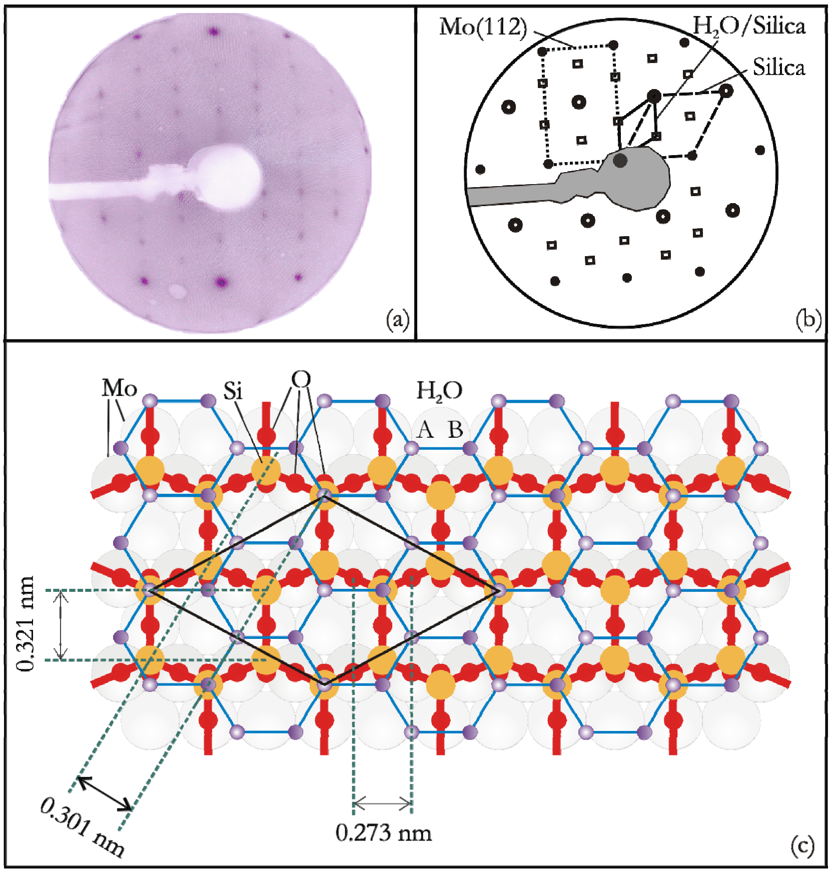

Figure 5.7 LEED pattern (negative contrast) (a) and its schematic presentation (b) developed at around 145 K during heating of the 6 BLE water, initially adsorbed at 100 K. (c) Structural model of the ice layer formed on the silica film, which exhibits a c(6×2)-Mo(112) or c(2×2)-Silica superstructure as indicated by a rhomb. A and B indicate the second- and first-layer water molecules, respectively.

Monitoring the LEED pattern while heating the water/silica sample, new diffraction spots in addition to the spots of the silica film can be observed as shown in Figure 5.7 (a). Due to water desorption, this pattern exists for a short time at temperatures very close to the maximum desorption temperature as simultaneously monitored by a mass-spectrometer. The additional experiments have proven that there are no electron induced effects; therefore the ordered structure is formed by molecular water. The analysis of the LEED patterns showed that the CI layer basically exhibits a c(6×2) structure with respect to Mo(112)-(1×1) which may coexist with a (3×2) structure, the latter exhibits relatively weak spots depending on beam energy.

Since this ordered ice layer strongly affects the Si−O−Mo stretching, it is reasonable to assume that water adsorbs on silica through the O atoms sitting above the Si^{4+} cations. Previously, Joseph et al. [223] on the FeO(111) film and Tzvetkov et al. [222] on the alumina film have suggested that, at low coverage and 100 K, the water molecules are isolated and adsorb through oxygen pointing to the metal cations (Fe^{2+} and Al^{3+}). However, as previously shown in IRA spectra, significant hydrogen bonding from the onset is observed, which favors a model consisting of a 2D network rather than that of 3D clustering.

Combining the experimental observations, a tentative model for the ordered structure of water on silica surface was depicted in Figure 5.7 (c). In this model, the position of atoms in the silica film and Mo substrate is fixed, meanwhile the distances between the water molecules are slightly varied as compared to those in the ice Ih bulk. As a starting point, a bi-layer model of adsorbed water can be adopted, although the precise (H-up vs. H-down) model cannot be determined at this stage. The distance between equivalent water molecules along the $[\bar{1}10]$ direction is 0.445 nm, which is only 1 % shorter than on the ice Ih(0001) surface (= 0.45 nm). Along the $[\bar{1}\bar{1}1]$ direction, the water-water distance projected onto the Mo surface is equal to 0.273 nm, which is longer than 0.261 nm in the ice bulk. Therefore, the ice lattice must be slightly expanded along the Mo $[\bar{1}\bar{1}1]$ direction. Alternatively, the top water layer can be relaxed inward, thus decreasing the interlayer distance between the water layers. The resulting structure consists of water molecules in a given layer which is hydrogen-bonded into hexagonal rings such that alternating molecules are raised or lowered relative to the central plane to give the proper tetrahedral bonding angles. This bilayer configuration, which consists of an upper and a lower layer, is often referred to as being puckered. Successive bilayers are then joined by the raised molecules of one bilayer hydrogen-bonded to the lowered molecules of the next. In the absence of the silica film, the ice overlayer would show a (3×1) superstructure with respect to the Mo substrate. Since the silica monolayer forms a c(2×2) structure with respect to Mo(112)-(1×1), the ice layer exhibits a c(6×2) structure when referenced to Mo(112), and a c(2×2) structure with respect to the silica surface.

5.4.5 Determination of Coverage

Adsorption of water at 100 K causes a blue-shift in Si−O−Mo asymmetric stretching band but its integral intensity does not change at all. This is actually due to coverage of water on the surface of the silica film. Here, coverage of water is not more than a couple of tens of bilayer, therefore infrared light penetrates through the water layers and be reflected from the surface of molybdenum substrate. The splitting of main silica phonon induced by crystallization is an indication of dewetting. From the intensity analysis, one may calculate fraction of silica surface covered by water. The integrated intensity is identical to that of clean silica film as silica phonon splits into two. Like other phase transition processes, a nucleation site seeds the growth of the new phase. Presumably, the surface of ice layers can still be amorphous even though the crystallization is completed in the core. This is also reflected to the vibrational spectra of water on surfaces. After complete crystallization, no spectral changes are observed.

Figure 5.8 (a) shows an OD vibrational band of fully crystallized D_2O on silica surface. The spectrum can be identified by deconvoluting it in three Gaussian peaks. Doing a quantitative analysis by integrating the peak is not always straightforward due to intensity borrowing and dipole coupling effects. However, when the crystallization is complete, relative changes can give an idea about the coverage of water layers. Relative intensities of W1, W2, and W3 are taken as a measure to estimate the completeness of the phase change. When full crystallization is achieved, frequencies of W1, W2, and W3 components do not change and the peaks attenuate with the same relative fraction during desorption. In Figure 5.8 (b), area S1 and S2 (divided silica phonon due to water restructuring) show the fraction of bare surface and the surface covered by water, respectively. In the course of desorption of CI, the intensity of divided phonon (area S2) attenuates and the frequency shifts to blue. Therefore, a plot showing the frequency shift with respect to fraction of the surface covered by water might be informative.

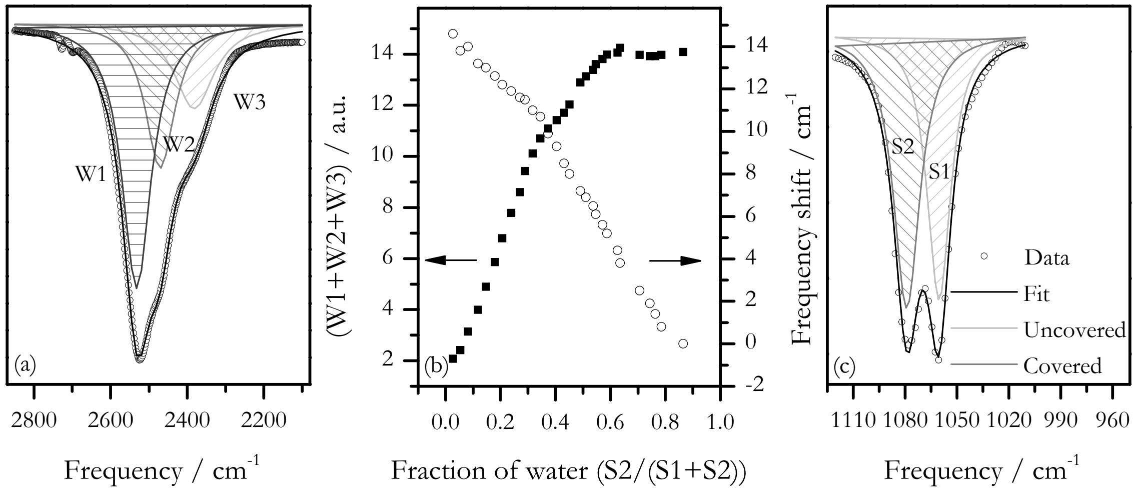

Figure 5.8 Quantitative analysis of infrared spectra. (a) Deconvoluted OD stretching region. (b) Coverage dependent frequency shift of main silica phonon. (c) Deconvoluted divided Si−O−Mo vibrational band due to crystallization of water.

Crystallization induced dewetting behavior of ice is highlighted in two different regimes. As presented in Figure 5.8 (b), polar ordering continues to evolve even the fraction of the silica surface covered by CI drops below 0.4. In this region, the structural phase change is completed, no shape changes in OD stretching bands are observed and water desorbs molecularly in CI phase. The phase change takes place between 0.4 and 0.75 where water dewets the surface faster than the dewetting rate of crystalline phase. It is very likely that amorphous water desorbs from the surface of islands until ordered phase remains. This is also supported by the disappearance of the free-OD (or OH) groups at the surface of ice islands. Sublimation rate is also smaller for CI phase; however, it does not influence frequency shift of silica phonon.

5.5 The Nature of Water Bonding to Silica Film

5.5.1 Polar Ordering Probed by IRAS

For ice I phases, even though the shape of the OH stretching band is quite typical, there are still several points to be considered; such as the spectroscopic mode and polarization of infrared light to be absorbed. The first attempt to identify the spectral features of ice has been made by Whalley [231]. Based on a hexagonal ice model, the stretching bands have been explained as symmetric (ν_1) and asymmetric (ν_3) OH stretching vibrations with dipoles oscillating in- and out-of phase. Using an ice model which includes macroscopic collective vibrations, the role of long-range field forces in frequency modification (ν_{LO}-ν_{TO} splitting); a consequence of a collective motion of dipoles as predicted by Lyddane-Sachs-Teller (LST) relation [251, 252], has also been pointed out. In addition to the field effects, the contribution of Fermi resonance owing to anharmonic interaction between a stretching fundamental mode and first overtone of HOH bending motion has been described. Not totally neglecting the influence ν_{LO}-ν_{TO} splitting, the degree coupling between the intramolecular and the intermolecular bonding has been given as a possible description to the Raman and infrared spectral changes of ice [253, 254].

Most of the infrared spectra of ice clusters that have been studied to date have been interpreted without taking polarization effects into account, because those are mostly acquired in transmission mode. P-polarized light can establish a large electric field that interacts strongly with the dipole transition in the same direction [253, 255]. For water molecules deposited on metal surfaces, only LO mode can be excited if the thickness of overlayer is smaller than the wavelength of the infrared radiation since it is the LO mode which has a transition dipole moment perpendicular to the surface plane. MSSR can be relaxed for ice films with a thickness comparable to the wavelength and contribution of TO modes into OH bands can be observed. Band shape changes due to crystallization have been reported for the thick ice films, too [234, 256, 257]. Regardless of the morphological differences, spectral changes have been attributed to the optical flatness of ice giving rice to an enhancement in reflection of infrared radiation. For aerosol ice particles, Devlin and Buch [258] have shown particles size dependent spectral modifications. Featureless spectrum of the particles smaller than 2 nm has been attributed to the lack of crystallinity. Particles larger than 2 nm have been shown to have a crystalline core but their surfaces are disordered.

Although hydrogen bonding network in ice changes dramatically with temperature and pressure, the ability of water that acts as double donor and double acceptor is universal. More specifically, in Ih lattice, oxygen atom of a water molecule is tetrahedrally coordinated to the oxygen atoms of neighboring water molecules. The arrangement of hydrogen atoms obeys Bernal-Fowler ice rules, which only take first neighboring molecules into account. However, based on a neutron scattering work, presence of another type of hydrogen bonding due to longer range polarization interaction has been described [259, 260]. The ice rule mentioned above allows protons in different orientations to place and inelastic neutron scattering studies [261] state that Ih structure is proton disordered. Proton ordered ice phases exist only at low temperatures (50-70 K) [262], and regular orientation of protons can be maintained by alkali hydroxide doping (ice XI) [263].

A comparison of vibrational bands of amorphous and crystalline H_2O and D_2O is shown in Figure 5.9. The blue-shift in Si−O−Mo stretching band caused by adsorption of H_2O and D_2O at 100 K shows no isotope dependent difference. Puzzling changes take place in silica phonon in parallel to reshapening of OD stretching band. Blue-shifted silica main phonon even shifts to higher frequencies after it is divided into two components due to dewetting. As the integral intensity ratio of ice covered regions to bare regions is ~2/3, the frequencies of divided Si−O−Mo stretching band due to H_2O and D_2O crystallization are 1078 cm^{-1} and 1084 cm^{-1}, respectively. One could suggest that the reason why the divided Si−O−Mo stretching band is shifted to the higher frequencies as D_2O crystallization occurs is because the thin silica film experiences so-called wall effect above it. This idea can be ruled out since one would expect to see same effect during growth of amorphous solid water at 100 K.

Although Rice and co-workers [253] have stated that Fermi resonance has more influence on vibrational spectrum of D_2O ice than that of H_2O ice, Devlin [258] points out that there can only be a weak influence of Fermi resonance on the high frequency shoulder of the stretching bands of water isotopes. Nevertheless, it has been considered as a second order effect as compared to intra-intermolecular interactions. As seen in Figure 5.9, stretching bands of crystalline water isotopes are similar in shape; however, full width half maximum of OD bands are somewhat smaller as compared to that of OH bands. Moreover, red-shift of the high frequency shoulder of the stretching bands (W1) which has LO character differs depending on the water isotope. The transition from the amorphous to the crystalline ice phase causes -130 cm^{-1} and -50 cm^{-1} for H_2O and D_2O, respectively. No plausible isotope dependent frequency change has been observed in W2 and W3 (ν_3 and ν_1) components.

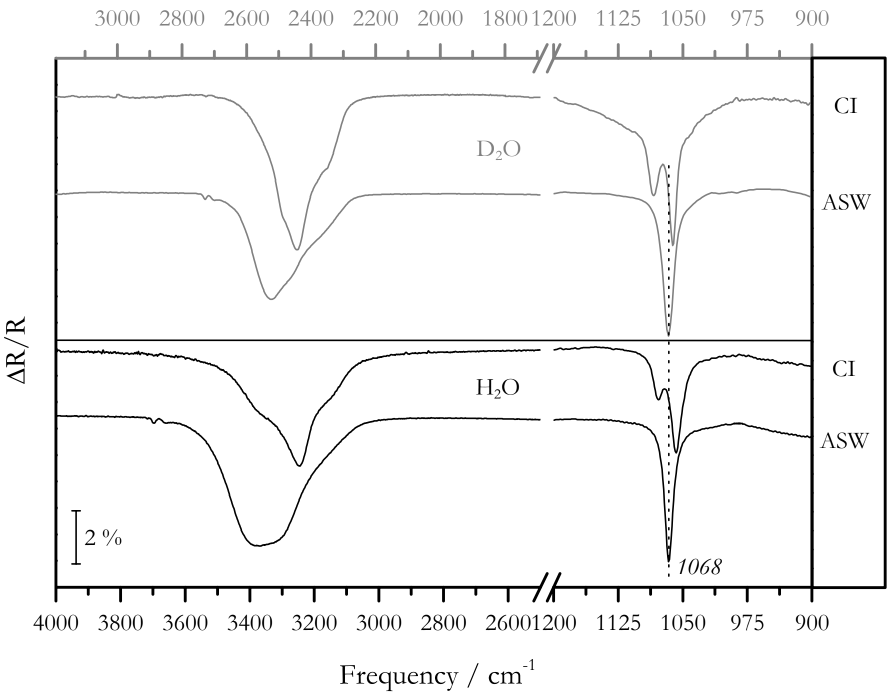

Figure 5.9 Comparison of vibrational bands of amorphous and crystalline H_2O and D_2O.

Isotope effects have been reported as small differences in work function changes due to adsorption on metal surfaces [264]. In addition to that, structural isotope effect has been observed on Ru(0001) surface due to differences in the size of the ice domains [196]. The former can not be correlated to the phonon splitting considering that it is an electron-phonon coupling, because same would be expected for ASW.

The splitting in silica main phonon is related to the change in the polar orientation of water molecules. This weak electrical polarization of thin films of ice vapor-deposited on a metal substrate is unrelated to the proton ordering expected in bulk ice at low temperatures. At the interface between ice and another material (or a vacuum) a water molecule with a component of its dipole moment directed out of the surface is not energetically equivalent to one oriented the other way, one therefore expects a small preference for one orientation over the other. The ice rules require that the resulting polarization is propagated into the bulk ice. The penetration of the polarization can only be terminated at appropriately charged protonic point defects, and the depth of penetration is therefore limited by the availability of such defects. The reason why divided silica phonon continues to blue-shift during the course of desorption is because the density of those defects becomes smaller therefore net polarization becomes dominant.

Based on these discussions, it is reasonable to think that the frequency difference in divided silica phonon caused by crystallization of water isotopes to be related to the differences in long range forces. Coupling of long range forces with vibrational mode is supposed to be the main reason of the high frequency component of OH (or OD) asymmetric stretching band. The ratio of the intensity of the central component to the intensity of the high frequency shoulder could be a measure to indicate the influence of long range forces. For totally crystalline ice phases (no observable shape change), this intensity ratio of D_2O vibrational spectra is higher as compared to that of H_2O. Since the contribution of LO modes to high frequency shoulder has been suggested, isotope effect observed in phonon splitting could be the consequence of the same behavior.

5.5.2 Electronic Structure of Amorphous and Crystalline Water

Within the three occupied valence states of water shown in Figure 5.1, the $1b_2$ and $3a_1$ states arise from bonding interactions between O and H, with the former is comprised completely of bonding character and the latter of both bonding and non-bonding character. The $1b_1$ state is comprised primarily of oxygen lone pair character, and is thus non-bonding. The $3a_1$ state possesses the symmetry of the molecule, whereas the $1b_1$ and $1b_2$ states are asymmetric about mirror planes in and normal to the molecular plane, respectively. The relative stability of these states increases with the degree of their bonding character, as one might expect. The $1b_2$ state is the lowest energy valence state, and thus is the least likely to be involved in bonding to a surface. The somewhat similar energies of the $3a_1$ and $1b_1$ states, along with their different symmetries and characters, provide an ideal opportunity for using the electronic structure of water in characterizing its adsorption properties. Energy spacing between the three valence band states of water, which can be used to describe water-surface interactions, show consistent behavior for some materials (oxides and semiconductors) but varied behavior for other materials (metals). The $1b_2$ state is a reasonably good reference for comparing the relative contributions of the other two states to adsorption. Having smaller $1b_2$-$3a_1$ difference reflects a general stabilization of the $3a_1$ state for adsorbed water on oxides relative to the gas phase. This implies that water may tend to bind to oxides via the purely non-bonding orbital on the oxygen atom.

Orientations of isolated and hydrogen bonded water molecules with respect to substrate have been studied by work function measurements and IRAS. On many metal and oxide surfaces, adsorption of water causes a reduction in work function values of the substrate and magnitude of this change has been attributed to the net dipole moment of the molecules. Binding to cationic sites of oxides results in reduction of work function [190]. It has also been pointed out that bonding nature of water to a noble metal substrate depends on d band character of the surface atoms [204]. Isotopic effects found for D_2O have been linked to a more packed overlayer, also evidenced by LEED measurements [264]. Based on UP spectra of low coverage water molecules on alumina thin film, it has been suggested that appearance of an additional state in $3a_1$ orbital can be attributed to formation of hydrogen bonded water molecules [222]. However, even at low coverage, formation of hydrogen bonding is common, especially on the surfaces like oxygen terminated oxides on which binding energy of water is relatively weaker as compared to the binding energies water adsorbed on metal surfaces. Arguments about the peak intensities of valence bands has been referenced to the formation of single and bilayers of water, but no detailed work has been reported [190]. On silica film, Goodman et al. [225] have showed a splitting $3a_1$ orbital into two for the water layers thicker than 1 L. This observation has been commented as the formation of a hydrogen bonding between water molecules. Similar conclusions have been drawn on other systems, stating that this splitting is due to co-existence of hydrogen-donor and hydrogen-acceptor water molecules [265].

The emission from the three highest occupied molecular orbitals of the water adsorbed on silica film at 100 K is shown in the left panel of Figure 5.10. Difference spectra were plotted by subtracting the clean silica spectrum in order to highlight the changes due to water adsorption. The three peaks at 7.1, 10.0, and 13.1 eV are identified with emission from water molecular orbitals $1b_1$, $3a_1$ and $1b_2$, respectively [266]. Two negative features are also observed at about 5.2 and 5.8 eV. These features coincide with the O 2p states of the silica film and appear as negative peaks in difference spectra because of nonlinear change of the inelastic background. It must be noted that inelastic background subtraction was not performed; since adsorbate related peaks observed in the 8-14 eV region preclude accurate background fitting. Bonding nature of water can be obtained by comparing the spectra of adsorbed water layers on silica film to those of the gaseous

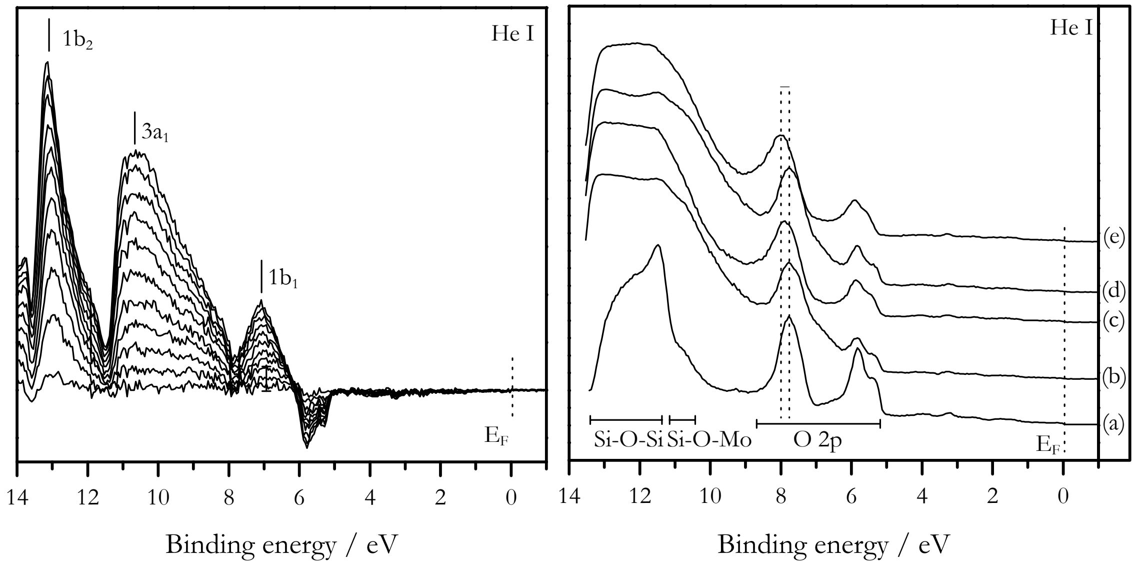

Figure 5.10 UP spectra of water adsorbed on silica film. Left panel: Growth of ASW at 100 K. Difference spectra was collected while dosing D_2O and plotted by subtracting the spectrum of clean silica surface. Each spectrum indicates 0.1 BLE water coverage increase. Right panel: Change of valence band structure of silica film due to water crystallization. Valence bands of (a) clean silica film (O-poor), (b) ~0.8 BLE AS H_2O at 100 K, (c) ~0.8 BLE AS D_2O at 100 K, (d) crystallized form of (b) at 140 K, (e) crystallized form of (c) at 150 K.

molecules [267]. In the case of dissociation, characteristic three-peak valence spectrum of adsorbed water is replaced by a two-peak spectrum identified with 1π and 3σ orbitals of adsorbed OH. In general, 1π (5-7 eV) and 3σ (9-11) states are separated by 3 to 4 eV. Typical UP spectra taken while adsorbing water at 100 K do not show any indication of OH related peaks confirming IRAS and TPD findings. In the initial stages of amorphous water growth, $1b_1$ and $1b_2$ orbitals are sharper as compared to the $3a_1$ orbital. It is clear that the electronic structure of water is modified when the density of H_2O molecules adsorbed on silica surface is increased. Increasing the water amount (~0.3 BLE) causes splitting of $3a_1$ orbital into two suggesting the formation of hydrogen bonded ice clusters.

The right panel of Figure 5.10 illustrates the UP spectra taken at a bilayer of ASW and CI. The formation of amorphous H_2O and D_2O causes attenuation in the intensities of O 2p nonbonding and Si−O bonding orbitals without showing any binding energy shift. Subtracting the clean silica spectrum from the one covered by amorphous H_2O and D_2O gives a difference spectra equivalent to the ones presented in the left panel. However, the formation of CI leads to spectral changes. First, annealing AS H_2O (D_2O) overlayers to140 K (150 K) gives rise to desorption of a small fraction of water therefore O 2p states at 5.3 and 5.8 eV gain more intensity. Similar intensity increase is also observed for the peak at 7.8 eV. Second, the binding energy of O 2p electrons increases due to formation of CI. The peak at 7.8 eV shifts to the higher energies by 0.2 eV. Similar shifts are observed for both crystalline H_2O and D_2O. In addition, they both have a shoulder at higher binding energy side. The peak at 7.8 eV seems to be wider in the case of crystalline D_2O, however it must be noted that $3a_1$ states of water might influence its width. It is difficult to comment on the changes in Si-O bonding states since they overlap with bonding orbitals of water and they are intrinsically broader.

There are several reasons which can contribute to the binding energy increase of O 2p states of the silica film upon crystallization. First, a charge transfer to water layers as a stabilizing effect can be proposed. Second, polar ordering within water layers induces a Coulomb force onto those nonbonding electrons and causes 0.2 eV shift. Third possibility is the change of interaction of water molecules at elevated temperatures. Highly probable hydrogen bonding between surface oxygen atoms of the silica film and hydrogen atoms of water molecules can give rise to redistribution of electronic states of the silica film. First probability is the least likely one within the others considered because one would expect the same effect for of ASW. Since the adsorption energy of water on silica film is relatively weak (40-50 $kJmol^{-1}$), hydrogen bonding between the ordered first water layer and additional water molecules on top is strong enough to perturb bonding behavior of water molecules to silica film. Flat lying molecules in the bottom layer have already been suggested to optimize ordered structures. Therefore, it is very likely that increase of binding energy of O 2p nonbonding electrons is related to structural changes of water molecules on silica film. Polar ordering might be accompanied by reorganization of water layer and by an enhanced hydrogen bonding interaction with surface oxygen ions. This might be the reason of high binding energy shoulder which is not observed when water is amorphous. Wider shoulder for crystalline D_2O brings the question whether there exist any isotope effect as observed in silica main phonon band splitting. At this point it is difficult to make a strong conclusion out of it and therefore theoreticians are welcome!

CHAPTER 6

CHARACTERIZATION OF VANADIUM OXIDE NANOPARTICLES

An atomic level understanding of the particle-support relation is one of the goals of heterogeneous catalysis since interaction between nanoparticles and support determine their chemical activities to a large extent. In this respect, monolayer vanadium oxide catalysts on oxide supports have attracted attention because of their properties being different than bulk vanadium oxide phases [268, 269]. This chapter deals with the characterization of vanadium oxide particles deposited on pristine and ice covered silica films.

6.1 Vanadium Oxide

The bulk vanadium oxides have been studied with many experimental and theoretical tools in an attempt to understand the interesting physical properties of these solids [270, 271]. The special chemistry of vanadium oxides results from a number of different interrelated electronic and structural factors. First, these compounds have partially filled d-orbitals which are responsible for a wide variety of electronic, magnetic and catalytic properties. Vanadium atoms can exist in different formal oxidation states which vary from two to five. The ability of vanadium atoms to possess multiple oxidation states results in easy conversion between oxides of different stoichiometry by oxidation or reduction and is believed to be an important factor for the oxide to function as catalysts in selective oxidation reactions [272].

Vanadium forms the following oxides: V_2O_5, V_6O_{13}, VO_2, V_2O_3, VO, $V_{2n}O_{5n-1}$ (which are known as the Wadsley phases) and V_nO_{5n-1} (which are known as the Magnéli phases). V_2O_5 is a diamagnetic insulator with a gap of ~2 eV. It has a distorted tetragonal pyramidal crystal structure and the V ions are in an octahedral coordination of oxygen. Formally V is 5+ and the d band is empty, although V 3d-O 2p covalent mixing results in a partial occupation of d orbitals. VO_2 is obtained by mild reduction of V_2O_5 and exhibits a rutile-like structure distorted by the presence of pairs of vanadium atoms bonded together [273]. One bond, the V=O bond, is much shorter than the others in the VO_6 units of the pentoxide structure. VO_2 displays a semiconductor-metal transition at 340 K and undergoes a crystallographic phase transition from monoclinic in the low-temperature phase to distorted rutile in the high-temperature phase. In both phases V is approximately octahedrally coordinated by oxygen. Formally V is 4+ corresponding to the valence shell configuration $3d^1$. The gap in the insulating low temperature phase amounts to ~0.5 eV. V_2O_3 has a corundum structure and is basic [273]. V_2O_3 crystallizes in the corundum phase above 170K. An insulator-metal transition occurs at 160K with a 6-7 orders of magnitude conductivity jump and a gap of 0.2-0.3 eV in the insulating phase [274, 275]. Vanadium in V_2O_3 is formally +3 with two 3d electrons per V atom. There is another phase transition in V_2O_3 at about 520K, above which the conductivity is again lower than in the metallic phase. VO has the sodium chloride crystal structure and vanadium is formally +2. Bulk vanadium monoxide has many intriguing properties that are closely related to the issue of stoichiometry. A wide range of varying oxygen concentrations is characteristic to this system: values of x between 0.8 and 1.3 have been reported for bulk VO_x [276]. Quite remarkable is the presence of a large number of both cation and anion vacancies, even for x = 1. Stoichiometric bulk VO always remains disordered; ordering of the vacancies is only reported for x values between 1.2 and 1.3 [277].

6.2 Vanadium Oxide Catalysis

The most dominant non-metallurgical use of vanadium is in catalysis. Vanadium oxide-based catalysts are used in the manufacture of important chemicals and in the reduction of environmental pollution (e.g. nitrogen oxides from flue gas of power plants) [1]. Most catalysts based on vanadium oxide consist of a vanadium oxide phase deposited on the surface of an oxide support, such as SiO_2, Al_2O_3, TiO_2 and ZrO_2. Supporting a metal oxide on the surface of another oxide was initially proposed to improve the catalytic activity of the active metal oxide phase due to a gain in surface area and mechanical strength [278]. The support is usually considered as an inert substance that provides a high surface area to carry the active metal oxide component or to improve the mechanical strength of the catalyst material. However, during the last two decades catalyst scientists have unambiguously shown that the activity and selectivity of supported metal oxide catalysts are significantly affected by the properties of the support oxide material [279]. This is generally known as the metal oxide-support effect; however, the origin and mechanism of operation are still unclear. The generally accepted theory is that the basis for the catalytic performances of supported vanadium oxides lies in the variability in geometric and electronic structure of surface vanadium oxides.

The structure of supported vanadium oxide species, often with various characterization techniques and under various conditions has been investigated. Determining their molecular structures is rather complicated, since deposition of vanadium oxide on an inorganic oxide results in a combination of various vanadium oxide species. Several structural configurations, e.g. isolated, dimeric or polymeric species; chains building up a two-dimensional wetting layers; three-dimensional vanadium oxide clusters (crystalline or amorphous) can be formed on support materials. A selection of supported vanadium oxide structures is shown in Figure 6.1. Moreover, hydration and reduction treatments profoundly change the local vanadium oxide structure. In the following paragraphs the supported vanadium oxide structures under hydrated, dehydrated, and reducing conditions will be discussed.

Many reactions can be catalyzed by supported vanadium oxide catalysts. Selective oxidation of methanol to formaldehyde [280], oxidative dehydrogenation of propane to propene [281] and selective catalytic reduction of NOx [282] are some of the examples of the reactions catalyzed by vanadium oxide supported on variety of oxide substrates. A considerable effort has been devoted to the structural characterization of these systems because there are many factors which contribute to the functionality of supported vanadium oxide catalysts; for example, dispersion, chemical state in reaction conditions,

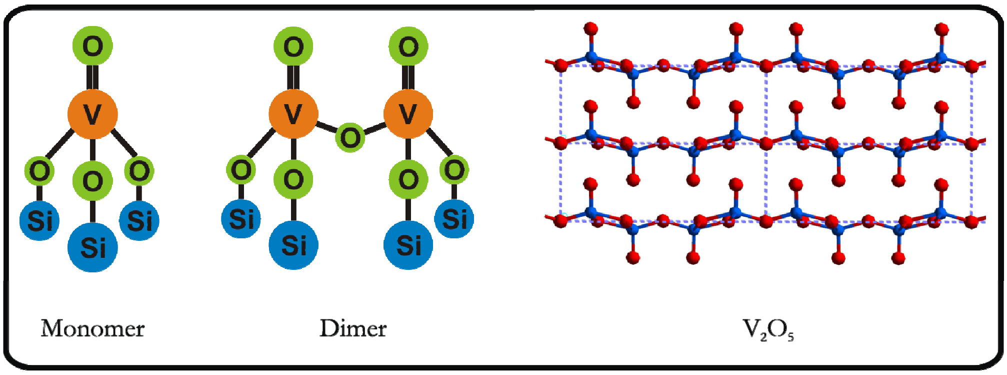

Figure 6.1 Possible structures of supported vanadium oxide species.

type of support, etc. Needles to say, the complexity of the system makes optimal catalyst design challenging.

Model systems with reduced complexity have a great potential to investigations of catalytic functionalities of vanadium oxide. Studies have been performed by utilizing different experimental approaches in order to elucidate structural characteristics of surface species and their chemical activities. The atomically flat vanadium oxide thin films have been grown on variety of low index surfaces of transition metals; such as, Cu(100) [283], Au(111) [117], $Cu_3Au(100)$ [284], and Pd(111) [285]. In addition to those, studies concerning vanadium oxide particles deposited on well defined oxide surfaces have been considered to be quite appealing owing to their resemblance to conventional mono-dispersed examples [286-288]. Several vanadium oxide deposition methods have been explored; however, those mostly do not offer the means to control the particle size distributions.

Structural and chemical properties of silica supported vanadium oxide systems have been characterized by using a range of different techniques. Raman spectroscopy has been found as a powerful tool to address issues concerning the structure of vanadium oxide, which is very much dependent on coverage [281, 289]. Although the nature of many vibrational bands have been well understood, debates still continue over the fraction of isolated and polymerized vanadium oxide species and their individual contribution into vibrational spectra. More detailed molecular orientation investigations have been performed using X-ray absorption techniques and some suggestions regarding the coordination of particles on the support have been given [290]. The structural information could also be obtained on less complex amorphous $SiO_2/Si(100)$ surfaces [291]. Use of atomic force microscopy (AFM) has helped researches to study the morphological changes of vanadium oxide layers in reaction conditions. It is also well documented that supported vanadium oxide particles undergo structural changes when dehydration treatments are performed [292].

Definition of monolayer vanadium oxide catalysis originates from spectroscopic observations [293]. It is generally believed that, on silica surfaces, polymeric vanadium oxide species begin to form at low loadings; however, monolayer catalysts are more commonly identified on more acidic supports. This is also attributed to low density of hydroxyl groups on which vanadium oxide species can anchor. The goal is to develop a method that would allow us to control both the amount and the distribution of desired vanadium oxide species over a silica surface. The strategy is to use multilayers of solid water as a reactive matrix that, to a certain extent, could mimic preparation environments of supported vanadium oxide catalysts using wet chemistry and to compare them with vanadium oxide species prepared in water free environments. This methodology has been introduced by Yan et al. [294] for the synthesis of silver nanoparticles. Later on, Song et al.

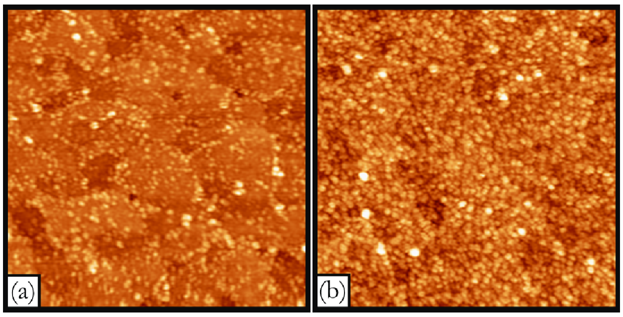

Figure 6.2 STM images (100×100 nm^2) of a model supported vanadium oxide catalyst prepared by depositing vanadium in 2×10^{-7} mbar O_2 on a pristine silica surface. The images are taken at 300 K with a tunnel current of 0.2 nA and a sample bias of 3.0 V. Silica surface is covered by (a) 0.12 MLV and (b) 0.4 MLV vanadium oxide.

[295] showed the influence of amorphous solid water layers on the stability and growth of TiO_2 crystallites on Au(111) surface and Liang and Perry [296] adopted the same approach to copper nanoparticles.

6.3 Morphologies of Vanadium Oxide Nanoparticles on Silica Film

Figure 6.2 shows STM images of a typical distribution of vanadium oxide particles deposited on pristine silica film. At room temperature, they form three-dimensional particles for all coverages studied (0.1–2.0 MLV). On a large length scale, the morphology of the silica surface supporting 0.1 MLV vanadium oxide particles can still be recognized. In comparing a low coverage STM image (Figure 6.2 (a)) with a higher coverage image (Figure 6.2 (b)), an obvious coverage dependent trend can be deduced. The particles appear as islands of heights ranging from 0.4 nm to 1.2 nm with a rather broad lateral size distribution. Notably, the continuous terrace structure fully disappears after depositing vanadium oxide more than 0.5 MLV. c(2×2) LEED pattern becomes very faint suggesting than long range order in silica film is partially lost.

Performing vanadium deposition on a silica surface covered by ASW multilayers at 100 K gives rise to differences in growth behavior of particles. Regardless of the differences between the nucleation characteristics of vanadium oxide particles on the pristine sample and the water layer assisted sample, it is clear that the vapor deposition method on former results in highly dispersed vanadium oxide particles. This is related to the strong anchoring of particles onto silica surfaces and reasons of that will be discussed later. The following sequence has previously been observed for increasing vanadium oxide loading: orthovanadate (VO_4) → pyrovanadate (V_2O_7) → metavanadate $(VO_3)_n$ → decavanadate ($V_{10}O_{28}$) → vanadium pentoxide (V_2O_5). At first glance, the topological STM images acquired at room temperature illustrate that particles mostly migrate while sublimating solid water multilayers at around 160 K and decorate the steps of the silica film at low coverage. Their population density on terraces increases with coverage as seen in Figure 6.3. Growth of low coverage of vanadium oxide results in the formation of small particles ranging from isolated particles to medium size particles, whereas interconnected agglomerates form at higher coverage.

Agglomeration is related to the nucleation procedure, which is controlled by not only vanadium-water interactions but also particle-particle interactions. Landing vanadium atoms are incorporated into the surface of water layers. Though these species display similar adsorption behavior on the pristine surface, the lateral particle-particle interactions

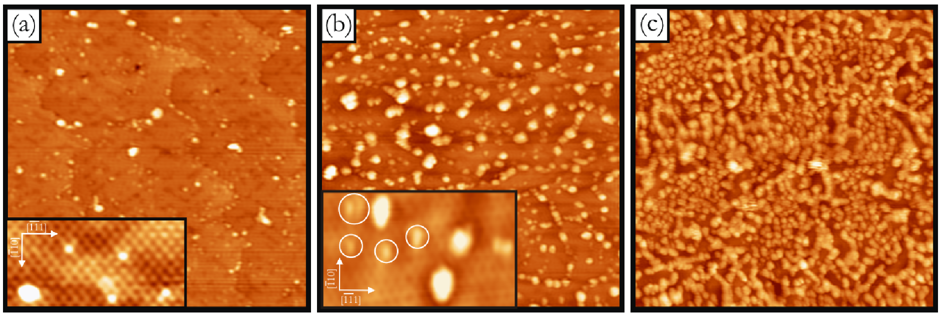

Figure 6.3 STM images (100×100 nm^2) of a model supported vanadium oxide catalyst prepared by depositing vanadium in 2×10^{-7} mbar O_2 on 3-5 ML solid water covered pristine silica surface. Many particles are nucleated at the steps on the silica surface, but many are also located on the terraces. Deposited vanadium amounts are (a) 0.035 MLV, (b) 0.15 MLV, (c) 0.5 MLV. Tunneling parameters: V_s/I = (a) +4.0 V/0.2 nA, (b) +4.0 V/0.2 nA, (c) +3.0 V/0.2 nA. Inset (a) 10×4 nm^2 - V_s/I = +1.2 V/0.3 nA, (b) 12×8 nm^2 – Vs/I = +1.0 V/0.18 nA.

might be very different. Formation of a network apparently results from adsorption-induced conformational changes and subsequent aggregation at the interface. In addition, removal of unreacted water layers via thermal desorption might have an effect in the final dispersions of the particles. Yan et al. [294] have suggested a model related to the confinement of silver particles in water droplets that form as a metastable phase of liquid water at about 150 K as proposed by Smith and Kay [297]. Supporting conclusion has been drawn by Song et al. [295] for TiO_2 nanoparticles grown on Au(111) surface in a similar way. However, recent studies discussing crystallization kinetics of amorphous solid water strongly point to the importance of crack formation within the ice layers [298]. Details of this process and its influence on particle agglomeration are not the motivation of this section and will be discussed in the following sections.

The apparent height distribution of vanadium oxide particles shown in Figure 6.3 (b) ranges between ~0.4 and ~1.5 nm. Similarly, the distribution of apparent diameters of the particles shows a broad range. With increasing coverage the density of smaller particles goes down rapidly forming larger interconnected aggregates (~1.5 nm and ~4 nm in diameter). It is possible to visualize how the oxide particles anchor to silica substrate. The inset of Figure 6.3 (a) shows an example where isolated particles locate along Si-O-Si bridging bonds in the [$\bar{1}$10] direction. Many of the isolated particles show elongated shapes derived from silica surface structures, implying a preferential [$\bar{1}$10] surface orientation (see the inset of Figure 6.3 (b)). The particles bonding to the surface are strong enough not to be dislodged by the interaction with the STM tip during scanning process. In comparing the large-scale image presented Figure 6.3 (c) with (a) and (b), it is clear that the overall morphology of silica surface, such as step edges and terraces, is not significantly changed by vanadium oxide particles.

There was no growth observed in a preferential direction rather than anchoring of particles containing less than 10 vanadium atoms. As seen in Figure 6.3 (c), the agglomeration leads to the formation of interconnected particles with the minor axis being equal to the single particle in some parts on the surfaces. Besides, isolated particles seem to be somewhat trapped within interconnected ones. It is possible that interconnected particles nucleate at the periphery of the amorphous solid water chunks at 100 K where the density of the free-OH groups is higher. This might cause the observed highly asymmetric size distribution suggesting that particles grew by Ostwald ripening rather than by coalescence at either 100 K or during the course of sublimation. Under certain

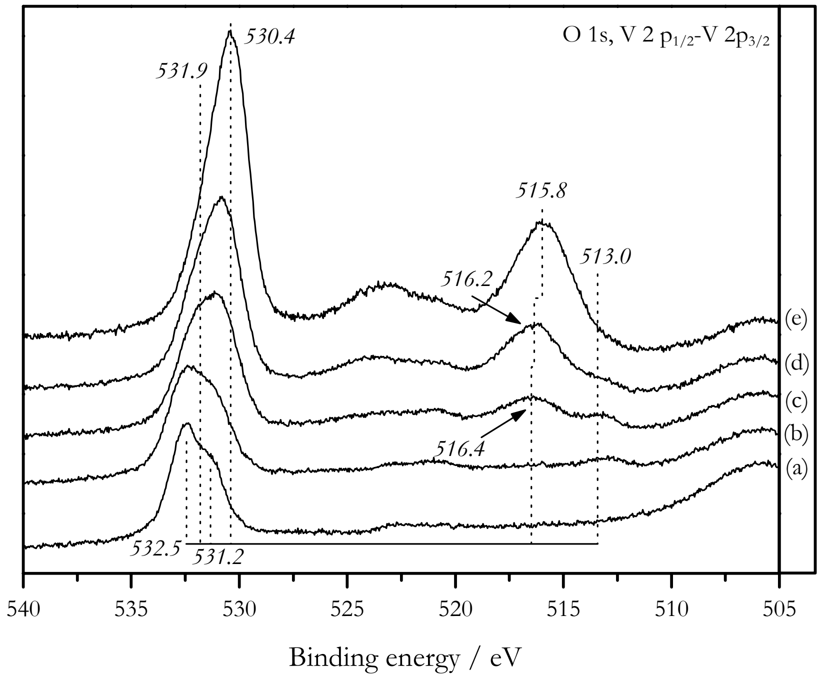

Figure 6.4 The O 1s and V 2p photoemission spectra of clean and vanadium oxide deposited Silica/Mo(112) surface. All spectra were referenced to the Fermi level of the molybdenum substrate. Deposited vanadium amounts are (a) 0, (b) 0.1, (c) 0.3, (d) 0.6, and (e) 1.0 MLV. All spectra were taken at 300 K.

circumstances, long-range repulsive barriers are known to cause separation [299]. In this case, the barrier is not strong enough to cause this separation, as observed by the disordered structure of the voids. The system is thus an amorphous solid, but it will possibly separate in smaller phases at higher attraction strength.

6.4 Oxidation States

Oxidation states of vanadium oxide are especially of interest for reactions where an oxidizing agent is absent from the gas feed. In such a case the reduced vanadium oxide species may be the catalytically active, thus information on the oxidation state and structure are required. However, a clear picture on the oxidation state and the exact structure of reduced vanadium oxide species has not been obtained so far. The reduction of supported vanadium oxide catalysts at high temperatures in the presence of e.g. CO and H_2 may lead to alter the oxidation states of vanadium from V^{5+} to V^{4+} and V^{3+}. Accordingly, the local structural modifications (i.e., VO_4, VO_5 and VO_6) take place [300, 301]. In several cases the oxidation state after reduction has been determined with temperature programmed reduction techniques (TPR), mainly with H_2-TPR [302, 303]. However, not much is known about the quantitative distribution of vanadium in different oxidation states and their exact coordination to the surface of the support. Thus, much more research efforts should be directed towards the elucidation of supported vanadium oxides under reduced conditions.

The FWHM of the V 2p states is found to increase from the (formally) d^0 system (V_2O_5) to the d^1 system (VO_2) and finally to the d^2 system (V_2O_3). This behavior can be explained by there being a growing number of available multiplet configurations in the corresponding PE final states, resulting from the coupling of the core hole to the 3d valence electrons. With a formally empty 3d shell, V_2O_5 will thus display no multiplet splitting which explains the sharpness of its core-level peaks. The effect of the multiplet splitting, in VO_2 and V_2O_3 is particularly strong in the V 3p spectra due to the large spatial overlap with the 3d shell. The V 2p spectrum is spin–orbit split into the $2p_{3/2}$ and $2p_{1/2}$ parts, separated by 7–8 eV, and this doublet is followed by the O 1s emission at 530 eV. The interaction of the core hole with the 3d valence shell not only causes a broadening of the lines but also results in satellite structures which can be found in most of the spectra. The separation from the corresponding main lines is typically 10-13 eV for VO_2 and V_2O_3. From the main-line–satellite separation in the V 2s, V 3s, and V 3p spectra the satellite positions in the V 2p spectra, where they interfere with the spin–orbit splitting and the O 1s emission can be estimated. One finds that for V_2O_5 a satellite belonging to the V $2p_{3/2}$ state and for VO_2 and V_2O_3 a satellite of the V $2p_{1/2}$ state could be expected on the high-binding-energy side of the O 1s peak. For the latter two oxides, the satellite of the V $2p_{3/2}$ state falls into the binding energy range of the V $2p_{1/2}$ state [271].

XP spectra covering O 1s and V 2p regions are shown in Figure 6.4 for vanadium oxide particles deposited on pristine silica surface under 2×10^{-7} mbar O_2 pressure. Overlapping of V $2p_{1/2}$ components with O 1s peaks produced by Al-Kα satellites due to non-monochromated X-ray source makes the analysis of the data complicated; so, only V $2p_{3/2}$ and O 1s components will be taken into account for the interpretation of the spectra.

Surface and interface oxygen ions of the silica film (532.5-531.2 eV) profoundly contribute to the O 1s region of the spectra, especially at low vanadium oxide coverage. In the initial stage of deposition, a peak centered at 513 eV dominates the spectrum and another peak appears at 516.4 eV as the coverage is increased to 0.3 MLV. Increasing the coverage progressively to 1 MLV only grows the intensity of high BE component, however its binding energy shifts to 515.8 eV, which is in the range expected for +3 state of vanadium [304]. This BE shift to the lower values is similar to the coverage dependent behavior of the V $2p_{3/2}$ states of alumina supported vanadium oxide particles [305]. The double peak feature suggests that oxide grows around a metallic or slightly oxidized core composed of less than 20 vanadium atoms. Post oxidation attempts result in modifications of the electronic structure of the silica surface and molybdenum substrate. Interpretation of XPS binding energies for small particles on oxide surfaces is complicated by final state relaxations effects, which can shift binding energies relative to the values measured for bulk materials [306]. The general trend is such that the binding energies of the core level electrons are higher for the small particles but decreases to bulk values as the sizes of the particles increase [307]. Under these circumstances, the binding energy shift shows an inverse relationship with respect to particle diameter which may be estimated by STM. Although the XPS results show a similar size dependent binding energy shift, it is worthwhile to consider other possibilities. The binding energy of V 2p electrons was not influenced by the particle size when equivalent amount of vanadium metal had been deposited on pristine silica surface at room temperature even though particles similar to vanadium oxide had been found (not shown). A high binding energy tail and appearance of the elemental silicon in Si 2p region indicate that silica film is being partially reduced by vanadium. V $2p_{3/2}$ core levels are located at binding energies of 512.4 eV consistent with the literature value of metallic vanadium [304]. If one assumes that the governing core hole screening concept is similar for both vanadium and vanadium oxide particles (which could be necessarily not true), there might be other factors influencing size dependent binding energy shift. It could also be possible that changes in the oxidation state with particle size are responsible for the observed shifts since initial state might differ.

XPS data taken at silica surface progressively covered with solid water and vanadium oxide are presented in Figure 6.5. Deposition of vanadium and solid water as a reactive layer were performed in a layer by layer manner at 100 K. Vanadium was deposited in 2×10^{-7} mbar O_2 pressure onto 3-5 layers of solid water. It is clear from the emergence of

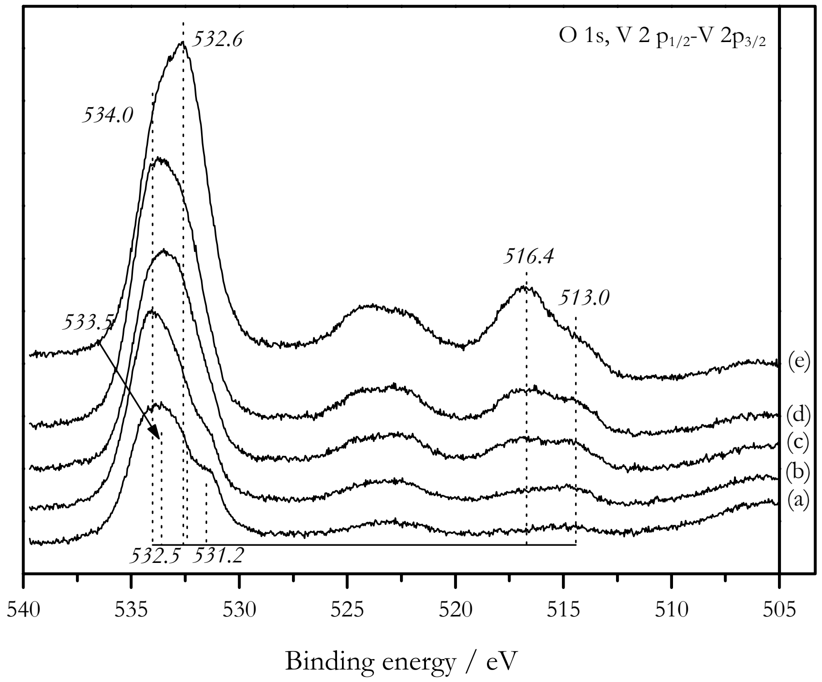

Figure 6.5 O 1s and V 2p photoemission spectra of vanadium oxide deposited on solid water covered Silica/Mo(112) surface. Deposited vanadium amounts are (a) 0.1, (b) 0.2, (c) 0.4, (d) 0.6, and (e) 1.0 MLV. All measurements were performed at 100 K.

low and high binding energy components in the V $2p_{3/2}$ spectra at low vanadium exposures that the growth of particles are similar to the behavior on the pristine surface apart from the fact that they grow at a higher oxidation state. The energy separation between those two peaks does not change with coverage as it happens for the particles on the pristine silica surface. In the initial stage of the deposition, vanadium atoms land on the solid water covered surface breaking OH bonds of water and a small portion of them gets oxidized at 100 K. For the lowest coverage (0.1 MLV), the binding energy of V $2p_{3/2}$ state is 515.0 eV, the value observed for V_2O_3 [304, 308, 309]. The asymmetric tail at the high binding energy side of the peak and the appearance of an additional peak at 516.8 eV with coverage suggest that the oxidation state of vanadium seems to be higher than the one on pristine films. However, the observation of the peak at 532.4 eV being clearly apparent for 1 MLV particles indicates that the measured binding energies cannot just be accounted by the states of vanadium oxide since it is much higher than the typical binding energies of oxygen on V_xO_y type systems. In fact, at 100 K, the resulting spectra might be slightly influenced by charging caused by water layers, which is much more severe at high vanadium oxide (and apparently solid water) coverage.

The electronic structures of vanadium oxides at low and high temperatures are not always straightforward to compare because three among all vanadium oxide phases, VO_2, V_6O_{13}, and V_2O_3, experience metal to insulator phase transitions (MIT) below phase specific critical temperatures [310, 311]. In fact, it has been reported that MIT vanishes with decreasing film thickness [312] and depends critically on doping [313] and structural crosstalk with the substrate selected [314]. Although such a phase change with small, amorphous particles is not expected, it might modify the valence band structure; therefore, more convenient comparisons regarding the asymmetry of the core level spectra are considered to be performed at the same temperature.

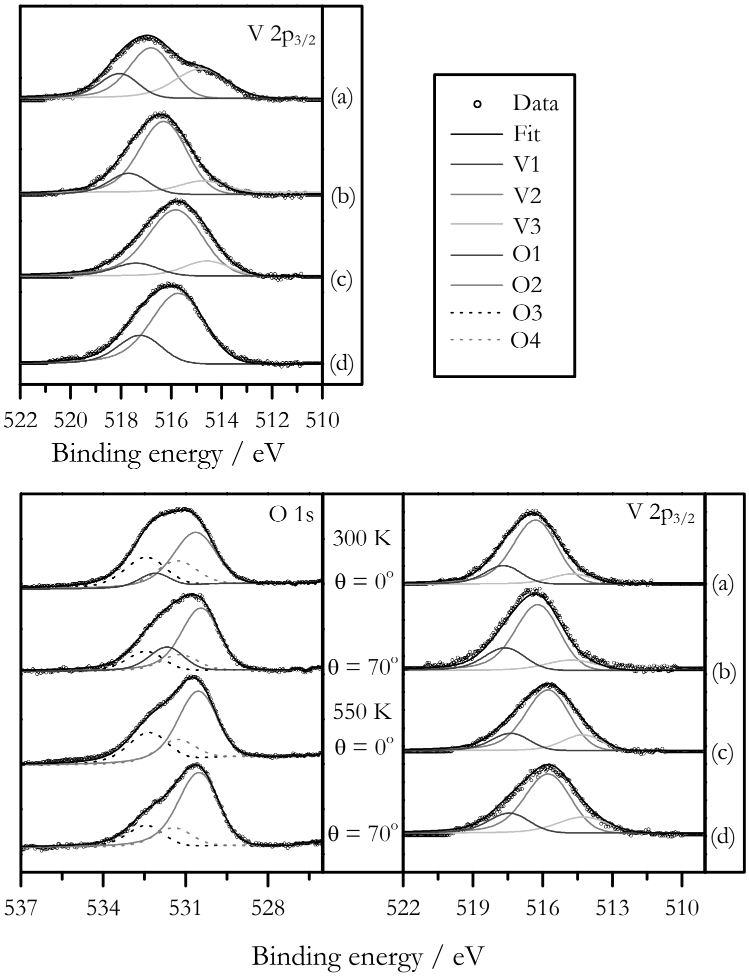

Figure 6.6 XPS and ARXPS analysis of 1 MLV vanadium oxide particles on silica. *Top panel*: Deconvoluted V $2p_{3/2}$ region of the XP spectra taken at (a) hydrated particles at 100 K (b) hydrated particles at 300 K, (c) totally dehydrated particles at 600 K (d) reoxidized particles by oxygen exposure at 600 K. *Bottom left panel*: Deconvoluted O1s region of the XP spectra taken at (a-b) hydrated and (c-d) dehydrated particles at two different electron emission angles. *Bottom right panel*: Deconvoluted V $2p_{3/2}$ region of the XP spectra taken at (a-b) partially hydrated and (c-d) dehydrated particles. Dehydration was done at 550 K. Take-off angles are indicated. Shirley background was subtracted from all spectra.

As mentioned before, water layers not interacting with particles sublimate at around 160 K. Stepwise annealing of the sample to elevated temperatures induces changes in peak shapes and in binding energies due to reorganization of the particles on silica surface. Figure 6.6 shows the comparison of V $2p_{3/2}$ and O 1s states as a function of annealing temperature and electron emission angle. The solid lines through the data points in all figures are the results of least-squares fits with a model function in which the emission lines are represented by a partial combination of Gaussian and Lorenzian profiles with a Doniach-Šunjić [20] line shape. Best fits could be obtained with Shirley background [21] for both V 2p and O 1s regions of the spectra. Here, it should be noted that an analysis of spectra by deconvoluting them into several components require detailed knowledge about the electronic structure [304]. One of the reasons of broad core level spectra corresponding to V^{4+} and V^{3+} is due to strong Coulomb interactions between the core hole and narrow 3d bands. The top panel of Figure 6.6 summarizes the changes in V $2p_{3/2}$ state depending on the treatments done. At 100 K, clearly distinguishable V $2p_{3/2}$ states can be deconvoluted into at least there peaks (V1, V2 and V3). The majority of the V2 and V3 components intermix at 300 K due to reactive interaction of the lowest BE component (V3) with water. At 300 K, V $2p_{3/2}$ peak is centered at 516.5 eV, which is within the range of reported binding energy values for V^{4+}. Annealing to 600 K gives rise to a drop in BE of the component V2 by -0.7. Post-oxidation attempts at 600 K in 1×10^{-7} O_2 pressure leads to an increase in the fraction of the component V1 suggesting that using O_2 as an oxidant might induce differences. Schoiswohl et al. [116] have attributed the high binding energy shoulder in V 2p spectra to the formation of vanadyl groups (V=O) on initially vanadium terminated $V_2O_3(0001)$ surface.

Bottom left and right panels of Figure 6.6 show the O 1s and V $2p_{3/2}$ data taken at two different take-off angles after annealing the particles to 300 K and 550 K. O3 and O4 components correspond to the surface and interface oxygen ions of the silica film, respectively. The peak at 530.4 eV (O1) is typical for V_xO_y type structures independent of the vanadium valence state. In addition to those, the O 1s spectrum involves a fourth peak (O2) at 531.7 eV, which can be attributed to hydroxyl groups. These hydroxyl groups have also been identified by XPS on many other oxide model surfaces, such as TiO_2 [315], V_2O_3 [316], and Cr_2O_3 [317]. Disappearance of O2 peak after annealing the particles to 550 K justifies this assignment since OH groups recombine and desorb as water. However, the way how these particles are grown leads to question surface and interface structures of vanadium oxide particles. Measuring O1s state with a more surface specific way reveals that hydrates are mostly at the interface region or at the periphery of the particles. However, considering the sensitivity of the technique, one can not rule out the possibility of having OH groups at the topmost layers of the particles. After removal of hydroxyl groups (dehydration) no plausible fractional change in the peak intensities is observed. Similar analysis is also performed for V $2p_{3/2}$ states. Deconvoluted V2p states offers less information due the broadness of the spectra. The relative peak intensities obtained at two different take-off angles indicate that the contribution of hydration into V1 component is more pronounced. When dehydrating the particles only a shift of -0.7 eV is observed. The measurements done at different take-off angles do not show a distinguishable behavior. Narrower full width half maximum of the V 2p core levels with increasing valence state is typical for vanadium oxide, which is also the case for our the hydrated particles. FWHM of V $2p_{3/2}$ states of hydrated samples is narrower by 0.3 eV than that of dehydrated ones, providing additional evidence that the oxidation state of hydrated samples is 4+.

6.5 Surface Termination and Vibrational Properties

Additional insights into the chemical structure of vanadium oxide particles on silica films can be derived from IRAS experiments. In precious studies, particular attention has been directed to the importance of V=O and V−O−V groups [318] as well as V−O−support bonds. Depending on the support material and loading, vanadyl stretch vibrational band can be seen in a frequency range between 1040 and 1010 cm^{-1} [290, 319, 320]. More controversial is the assignment of V−O−V (or O−V−O) and V−O−support vibrational modes. A broad band, around 920 cm^{-1}, appearing in Raman spectra by increasing the loading has been attributed to the formation of polymeric species (V−O−V chains) [320]. In addition to these, a third band at 995 cm^{-1}, which is characteristic for V_2O_5 crystallites, has been reported for high vanadium oxide loadings [321]. In a recent study on the vibrational spectra of alumina and silica supported vanadium oxide catalyst; Magg et al. [249] revised the assignment of the band around 940 cm^{-1} and suggested that, on alumina supported vanadium oxide model systems, this band can only be attributed to V−O−Al interface bonds. Similar conclusions have been drawn for the Raman band at 910 cm^{-1} obtained from the high surface area alumina supported vanadium oxide catalysts [322]. The

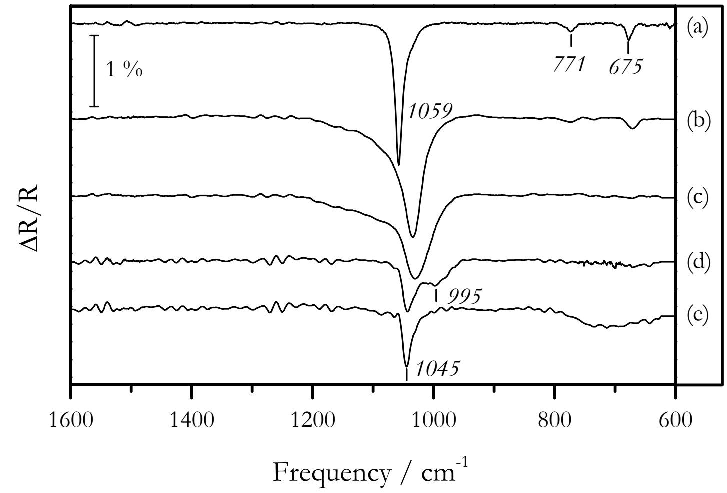

Figure 6.7 IRA spectra of vanadium oxide particles deposited on pristine silica surface at 300 K. (a) 0, (b) 0.1, (c) 0.3, (d) 0.6, and (e) 1.0 MLV vanadium is deposited in 2×10^{-7} mbar O_2.

same band has also been questioned by Keller et al. [323]. Based on an EXAFS analysis and theoretical modeling of V−O bond lengths it has been concluded that some other bonds like V−O−H or V− (O−O) should be taken into account.

Growth of vanadium oxide particles on pristine silica films induces some changes in the vibrational properties of the film. Si−O−Mo stretching band, indicative of structural order, red-shifts and broadens continuously as vanadium oxide coverage increases (Figure 6.7 (b) and (c)). An intense band appearing with increasing coverage is the band at 1046 cm^{-1}, which can be assigned to vanadyl species (Figure 6.7 (d) and (e)). Compounds which contain single V=O bonds like vanadium oxitrichloride ($V=OCl_3$) show stretching vibrational bands similar to the values presented here [324]. Coverage dependencies of the frequency of vanadyl groups have also been observed. A broad feature clearly visible at around 700 cm^{-1} is assigned to V−O−V stretching of polymeric species possibly forming with increasing coverage.

The results shown in Figure 6.7 strongly imply that attenuation and progressive red-shift in main silica phonon with increasing vanadium oxide coverage is derived mainly from the loss of long range order of silica film. Accordingly, small vibrational bands characteristic for silica films also attenuate and finally disappear even though the coverage of vanadium oxide particles is quite low. The shoulder at 995 cm^{-1}, which is in the range of the calculated frequency of in-phase V−O−Si stretching bands [249], vanishes as vanadium oxide coverage increases (Figure 6.7 (d)). This suggests that the interaction of vanadium oxide particles with the silica film is quite dramatic. It is likely that flipping the component of the SiO_4 tetrahedron which is binding the silica film to the molybdenum substrate is responsible for the successive red-shift in Si−O−Mo stretching frequency. Besides, partial incorporation of the particles into the film can not be ruled out.

Hydrated vanadium oxide particles are of certain interest because fresh technical catalysts are generally hydrated and water formed during some reactions may lead to the hydration of the catalysts [325]. Hazenkamp et al. [326] have studied the structure of silica supported vanadium oxide and claimed that, when hydrated, vanadium oxide is present as decavanadate. Based on a XANES analysis, Yoshida et al. [327] have found the coordination of vanadium to be octahedral. On the basis of NMR of vanadium oxide particles supported on titania, Nielsen et al. have concluded that vanadium is 6 coordinated with one short (V=O) and one long (V−O) axial bond [328]. Ruitenbeek et al. have come

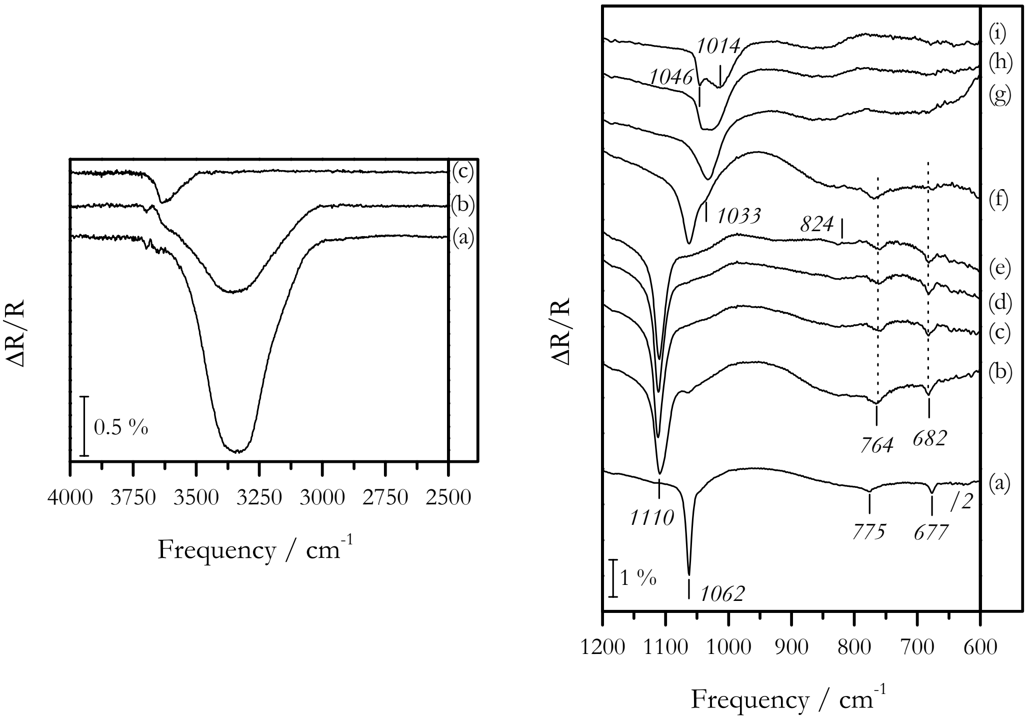

Figure 6.8 IRA spectra from hydrated and dehydrated vanadium oxide particles grown on amorphous solid water layer by layer fashion. *Left panel*: IRA spectra of OH stretch vibrational bands of (a) 5 ML amorphous solid water film on silica at 100 K, (b) after deposition of 0.4 MLV vanadium in 2×10^{-7} O_2 ambient at 100 K and (c) after sublimating unreacted solid water by annealing the sample to 300 K. *Right panel*: IRA spectra of (a) 0, (b) 0.1, (c) 0.2, (d) 0.4, (e) 0.6 MLV vanadium oxide layers grown on 3-5 ML solid water films each. Spectra were recorded at 100 K. 0.6 MLV vanadium oxide particles were annealed to 300 K (f) and to 600 K (g) in UHV. Spectra (h) and (i) were recorded after oxidizing the particles in 1×10^{-7} mbar O_2 at 300 K and at 600 K, respectively.

to the conclusion on the basis of EXAFS that for a hydrated 17.5 wt % alumina supported catalyst the vanadium is 4 coordinated with one V=O bond of 0.155 nm, one V−OH bond of 0.174 nm and two V−O bonds of 0.190 nm [329]. A similar structure has been suggested for 1.4 wt% catalysts on alumina, silica and titania by Went et al. [330]. Silversmit et al. have also used EXAFS to determine the structure of their 2.8 wt% vanadium on titania catalyst. They found a V_2O_5 resembling octahedral coordination with one short V=O bond of 0.16 nm, 4 longer V−O bonds of 0.2 nm and one long V−O bond of 0.22 nm [331].

The group of Wachs used Raman spectroscopy to determine the structure of hydrated vanadium oxide catalysts as a function of loading and support [332, 333]. The hydration process has been described for a silica supported vanadium oxide catalyst. Upon hydration the vanadium species goes through a series of stages starting with the hydrolysis of a V−O−Si bond. Addition of water is followed by the formation of chain polymers. Increase in coverage leads to the formation of 2D polymers and formation of a 2D-layered structure ($V_2O_5.nH_2O$) [334]. They have shown that the surface vanadium oxide molecular structures depend on the net pH at which the oxide surface possesses no surface charge, which is mainly determined by its composition (SiO_2, Al_2O_3, ZrO_2, TiO_2 and MgO). Under hydrated conditions, the surface of an amorphous oxide is covered by a thin water film and its hydroxyl population is subject to pH-dependent equilibria reactions.

When the vanadium oxide coverage increases two effects come into play. Firstly, the pH near the surface is lowered due to the presence of acidic vanadium oxides, and decreases with increasing vanadium oxide loading; and secondly the particle dispersion declines because it depends on the available surface area as well as the availability of surface hydroxyl groups. Both factors influence the chemistry of vanadium in the same direction; i.e., toward the formation of surface polyvanadates. However, the absence of silanol groups on the surface of silica film renders only the former process reasonable for the formation of polymeric species. Presence of high density hydroxyl groups implicates that high-surface area supports, such as alumina, will give rise to relatively less polymerized vanadium oxide species ($V_{10}O_{28}$) at high vanadium oxide loadings because more surface area is available to accommodate isolated monovanadate species.

Further evidence for the presence of hydrated particles discussed previously comes again from infrared spectroscopy. Figure 6.8 summarizes IRA spectra of hydrated and dehydrated vanadium oxide particles as well as the ones subjected to post-oxidation treatments at different temperatures. The left panel shows the OH stretching region of water adsorbed on the silica surface (a), reacted with vanadium oxide particles (b), and flashed away by annealing it to 300 K. As explained in Chapter 5, the broad peak between 3600 and 3000 cm^{-1} and small peak at 3696 cm^{-1} are typical for hydrogen bonded and free-OH groups, respectively. A relatively broad peak around ~3625 cm^{-1} appears after vanadium oxide deposition. Frequency of this band is in the range of the stretching frequency of OH groups coordinated to the vanadium oxide nanoparticles and thin films [335]. At 300 K, no unreacted water molecules remain adsorbed on silica surface, only hydrated vanadium oxide particles dominate the IRA spectra. The reason why the V−O··H stretching frequency is slightly lower at 100 K than at 300 K is because unreacted water layers at low temperature can form hydrogen bonding networks with OH groups.

In the right panel of Figure 6.8, the results of a series of surface treatments performed at 100 K (a-e) and at 300 K (f-i) are presented. The modifications in the silica vibrational bands due to the growth of hydrated vanadium oxide particles (by depositing solid water and vanadium oxide layer by layer fashion at 100 K) are quite different than the frequency shifts observed for pristine samples. The frequency of Si−O−Mo bond blue-shifts by ~50 cm^{-1} at the initial stages of the deposition and does not shift further with increasing coverage. It is also interesting to note that an opposite trend is observed as hydrated vanadium oxide is formed: the Si−O−Si stretching band red-shifts from 775 cm^{-1} to 764 cm^{-1}. This red-shift might be related to an elongation of Si−O bonds, at least in the presence of water, since it shifts back to its original frequency at 300 K. However, a number of other factors have to be taken into consideration regarding the understanding of the unexpected blue-shift in the Si−O−Mo stretching bands. First of all, the results obtained from ^{18}O labeled silica films confirm that the observed change is not related to the formation of a new bond. In addition, a similar blue-shift is observed after exposing the water layers to low energy X-rays. Test experiments showed that XPS measurements done on water layers make the Si−O−Mo stretching band blue-shift by the same amount. It is known that X-ray or softer radiation and/or low energy photoelectron can cause ordering [336] and dissociation in water layers. Petrik and Kimmel [337] have addressed this issue based on hydrogen uptake measurements and shown that the dissociation might take place both at the surface of solid water films and at the interface region between substrate and solid water films. IRA spectra do not show any traces of Si−OH groups, therefore we believe this blue-shift corresponds to dissociated water molecules which do not actually bind to the silica network. Vanadium metals impinging on water layers grown on silica have the same effect even though the deposition is performed in an oxygen ambient. In this

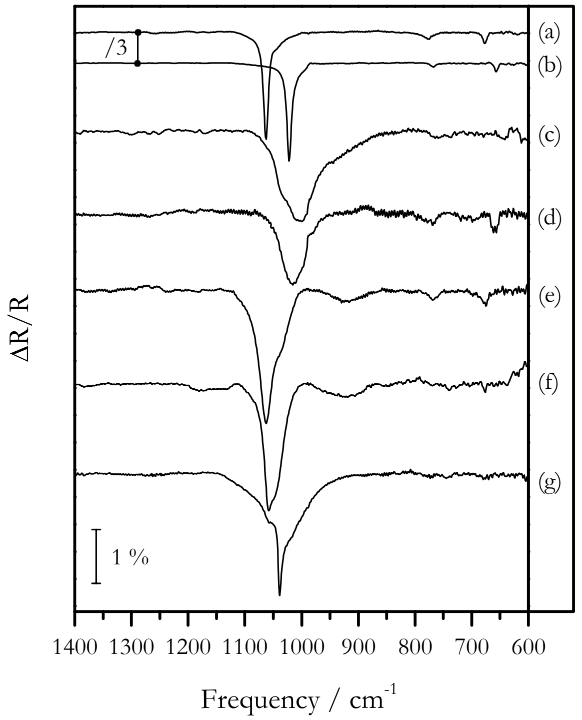

Figure 6.9 IRA spectra of hydrated vanadium oxide particles on isotopically labeled silica films. (a) silica film labeled with ^{16}O, (b) silica film labeled with ^{18}O, (c) 0.5 MLV particles deposited on silica film prepared by using ^{18}O, (d) 0.8 MLV particles deposited on silica film prepared by using ^{16}O, (e) 2 MLV particles deposited on silica film prepared by using ^{16}O, (f) after dehydrating the sample (e).

case, dissociation is expected at the surfaces of 3-5 ML water layers but penetration of electronic excitations though the film can not be ruled out.

After removing of unreacted solid water and dehydrating the particles by annealing to 300 K and 600K, a broad band at around 1033 cm^{-1} dominate the spectra as shown in the right panel of Figure 6.8. Post oxidation attempts at 300 K even broaden it further with a higher frequency shoulder which is the onset of the formation of vanadyl groups. The evolution of the band at 1046 cm^{-1} indicates that as the oxidation temperature is raised, there is a tendency to form vanadyl terminated particles. The dehydrated sites can be most easily converted to vanadyl groups by post oxidation. For all vanadium oxide coverages studied, only a broad tail is observed at around 1000 cm^{-1}, different than an apparent peak obtained on pristine films. Either V−O−Si bonds are obscured by the shoulder of the peak at 1014 cm^{-1} or by the intense H−O−H rocking bands of water.

The frequency of the vanadyl groups depends on the hydration/dehydration degree of vanadium oxide particles therefore the number of OH groups coordinated to the vanadium cations [338-340]. To elucidate the role of hydration in the formation of vanadyl groups, isotope labeling experiments were performed. Figure 6.9 shows IRA spectra of silica films prepared with ^{16}O (a), ^{18}O (b). Vanadium oxide particles were deposited on silica films covered by solid water. All spectra were recorded at 300 K after removing unreacted water layers; however, complete dehydration was not performed.

Regardless of the labeling type of silica films, a band centered around 1035 cm^{-1} is common for hydrated vanadium oxide particles. This finding suggests that the surface of vanadium oxide particles contains not only hydroxyls but a fraction of their surface is also terminated by vanadyl groups. With increasing coverage, the bands get sharper but do not blue-shift to 1046 cm^{-1} after complete dehydration. At 100 K, hydration gives rise to the formation of gel-like polymerized particles interconnected via V−OH−V bridges since no vanadyl groups are detected by IRAS. Alternatively, bands observed at frequencies lower than 1040 cm^{-1} have been proposed as vanadyl species of second or third layers of vanadium oxides [341]. The tentative conclusion from this is that phase separation during crystallization of solid water may be the reason for the formation of particles and partially dehydrated sites are converted to vanadyl groups. Re-hydration experiments also show a tendency to shift to red. Although the influence of hydration on vanadyl stretching frequency is clear, the interpretation of the broad band around 920 cm^{-1} is of importance. Care must be taken in the assignment of this band because librational modes of water molecules contribute to the spectra at the same frequency. The spectral shape of this band can be different from sample to sample because interaction of water molecules trapped in particles with the vanadium hydrate network is coverage dependent. In addition, dehydration causes a drop in the intensity of this band. Therefore, it must be related to librational mode of the water trapped inside the particles.

6.6 Effects of Dehydration and Thermal Stability

Spectroscopic fingerprints used for structural predictions do not provide sufficient information about dehydration related morphological modifications. There is still no consensus on the precise geometrical molecular structure of the different forms of vanadium oxide. Besides, it is widely accepted that dehydration treatments cause sintering of the particles as well as a loss of active surface area. Comparison of morphological modifications upon dehydration of vanadium oxide particles on silica film is therefore required for complete understandings of XP and IRA spectroscopic changes.

STM images presented in Figure 6.10 (a) and (c) are to compare the distribution of particles over the silica film before and after dehydration. Figure 6.10 (a) shows an image of an 0.5 MLV thick hydrated vanadium oxide particles. Careful examination of series of images revealed that vanadium oxide particles do not sinter on silica film through massive ripening and coalescence mechanisms [342, 343]. Instead, particles which are located on terraces shrink after annealing to 600 K and stay as separate entities (Figure 6.10 (c)). The ones which decorate steps do not seem to show morphological changes. Although we are not able to provide any STM image demonstrating the distribution of the particles at 100 K, we must note that steric interaction between particles during sublimation of unreacted water can not be ruled out. In addition to these aspects, annealing might cause partial incorporation of the particles into the silica film. Annealing experiments performed on vanadium oxide particles grown on pristine films did not show any morphological changes indicating that those particles strongly anchor onto the substrate.

As depicted in Figure 6.10 (b), H_2 and H_2O signals are detected during fast annealing experiments. H_2O formation takes place via recombination of surface OH groups in a temperature range between 400 and 600 K. Water adsorption experiments done on reduced V_2O_3 [316], TiO_2 [344], and Fe_3O_4 [213] surfaces also show molecular desorption at around 200 K and recombinative desorption of OH groups at around 500 K. The shoulder at around 400 K might indicate there is more than one type of site where OH species are attached although those are not resolvable by IRAS. The relatively high desorption signal of hydrogen indicates that there can be some hydrogen trapped within vanadium oxide particles and/or molecular hydrogen desorption results from recombination of hydrogen atoms bound to oxygen atoms of V−O−V groups. Channels in the V−O−V network might allow diffusion of the hydrogen atoms, resulting in a much higher mobility. The different dynamics might be caused by the differences in the interactions, but this also results in morphological heterogeneities as evidenced by STM. Formation of monovanadate upon dehydration has been suggested previously [290] and in

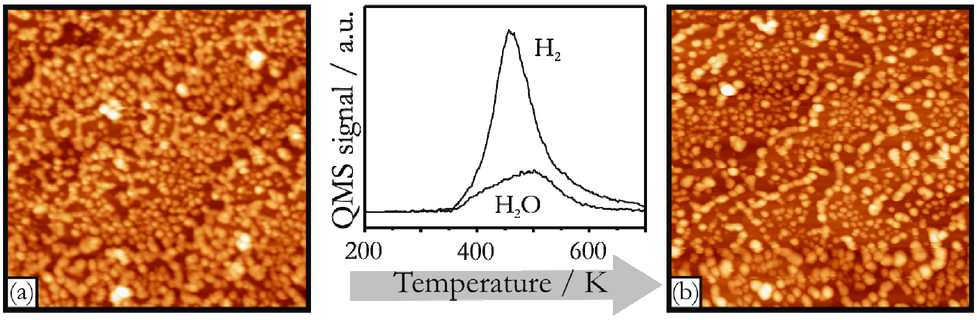

Figure 6.10 Morphologies of vanadium oxide particles at two different dehydration states. (a) STM image of hydrated vanadium oxide particles 100×100 nm^2 - V_s/I = 3.0 V/0.1 nA, (b) TPD spectra of desorbing species during dehydration process. Heating rate is 3 Ks^{-1}. (c) STM image of totally dehydrated vanadium oxide particles 100×100 nm^2 - V_s/I = 3.0 V/0.2 nA.

the light of STM results one may say that the morphological trend indicated can be attributed to less polymerized particles.

6.7 Probing Surface Sites by CO

Besides adsorption energetics of CO on different surface sites which can be extracted from temperature programmed desorption experiments, the measurements can provide quantitative information about the number of surface sites available, i.e. depending on the degree of hydration. CO adsorption studies done on totally vanadyl terminated alumina supported vanadium oxide particles highlighted the presence of defects (V^{3+}) and their coordination as judged by the frequency change of vanadyl bands [94]. Figure 6.11 (a) shows the results of CO TPD experiments performed on the particles which are subjected to the successive dehydration treatments. For each TPD experiment the same amount of CO (1 L) is adsorbed at 100 K in order to quantify the fraction of surface sites being created due to dehydration. It must be noted that CO does not adsorb on regular sites of the silica surface under these experimental conditions. A very small amount of CO uptake is observed on defective sites of the surface and contribution of which into TPD spectra is strongly eliminated by vanadium oxide particles. Temperature ramping is terminated at the point where the influence of dehydration is aimed to be monitored by CO adsorption. The results indicate that up to 300 K dehydration causes an increase in the densities of two different sites; however, above 300 K the component at 200 K saturates and only the low temperature peak (150 K) keeps on growing. When dehydration temperature is risen up to 500 K, a shoulder at 250 K evolves in the CO TPD spectra as a third component. Superposition of CO TPD spectra obtained from vanadium oxide particles dehydrated at 400 K, 500 K and 600 K shows indications of structural modifications. The reduction in particle density evidenced by STM and the increase in CO adsorption capacity upon dehydration might seem contradicting in the first place. However the XPS results presented in Figure 6.6 favor the conclusion that the particles after dehydration posses more Lewis acid sites adsorbing CO. Since the valence state of vanadium oxide particles at 300 K is in the range of 4+, the CO TPD experiments reveal that, up to 400 K, dehydration creates only two different cationic vacancies. This may involve the desorption of water trapped within the particles and/or at the interface region. Increasing dehydration temperature certainly causes reduction to 3+ valence state, as already shown in Figure 6.6.

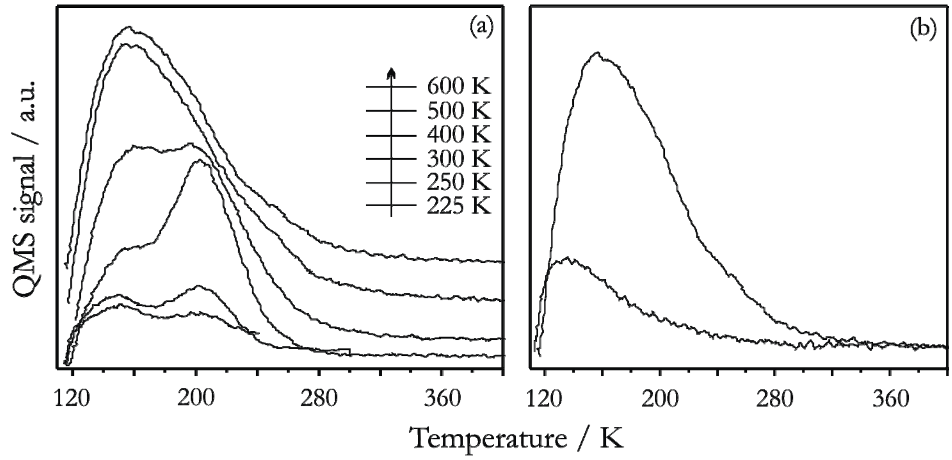

Figure 6.11 (a) CO TPD spectra taken during stepwise dehydration treatments. 1 L CO was adsorbed each time after dehydrating the vanadium oxide particles at 225, 250, 300, 400, 500 and 600 K (from bottom to top). (b) Comparison of CO TPD behaviors of dehydrated and vanadyl terminated particles.

Post oxidation of totally dehydrated samples by oxygen blocks dehydrated surface acidic sites and CO adsorption capacity drops drastically. The change in CO TPD behavior can be seen in Figure 6.11 (b). Vanadium oxide particles exposed to oxygen at 500 K appear to be totally terminated by vanadyl groups therefore CO adsorption capacity drops by 80 %. Further annealing treatments up to 700 K failed to regenerate reduced surface sites as far as the results of CO adsorption experiments are concerned.

6.8 Effect of Water Layer on the Morphology of Vanadium Oxide Particles

Crystallization and sublimation of condensed water from its amorphous phase is a natural phenomenon that can be achieved in its simplest form by waiting for the whole overlayers to sublimate. The quality and the morphologies of the resulting crystal forms depend on the rate of sublimation and several parameters including initial roughness of amorphous layers, hydrophobicity of the substrate and addition of minute quantities of an active agent such as alkaline hydroxides [345, 346]. When vanadium oxide particles are deposited on the solid water covered silica surface, the sublimation process of unreacted water becomes important. Characterization of the surface morphologies of vanadium oxide particles indicates that ice sublimation facilitates the mobility of the particles and they preferentially nucleate at the step edges at low coverage. On terraces, the particle population density increases at high coverage.

The diffusion kinetics of particles thus their degree of agglomeration is controlled by the rate of sublimation of the water layers. Figure 6.12 shows STM images of vanadium oxide particles prepared by a layer by layer fashion while varying the speed of desorption of water layers. Image (b), (d) and (f) are the close-ups of image (a), (c) and (e) where the silica surface is wetted by clusters, partially wetted by agglomerated clusters, and wetted by lamellar microstructures, respectively. Fast sublimation of water layers results in the formation of 3D particles uniformly distributed over the silica surface (see image (a) and (d)). However, slow sublimation of water layers induces significant morphological modifications depending on the amount of water. The fact that the mobility of particles is closely related to structural changes of solid water during the course of sublimation can be

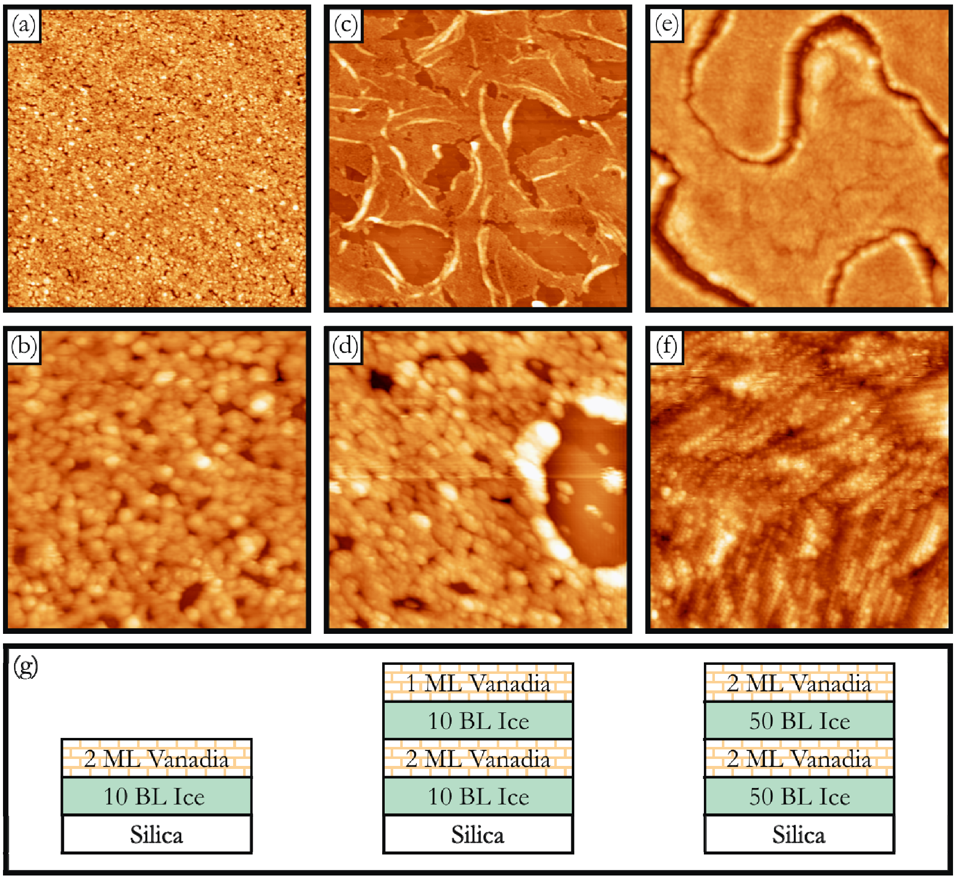

Figure 6.12 STM images of vanadium oxide prepared by varying thickness of ASW layers. (a) 200×200 nm^2 - $V_s/I = 2.0$ V/0.1 nA, (b) 40×40 nm^2 - $V_s/I = 2.0$ V/0.2 nA, (c) 400×400 nm^2 - $V_s/I = 1.8$ V/0.1 nA, (d) 50×50 nm^2 - $V_s/I = 2.0$ V/0.3 nA, (e) 400×400 nm^2 - $V_s/I = 5.0$ V/0.1 nA, (f) 30×30 nm^2 - $V_s/I = -1.0$ V/0.1 nA and (g) sketches of sample preparation methods (see also Appendix C).

justified by the observation of uncovered silica surface. It is clear that dewetting due to crystallization of ASW is the reason for partial coverage of the silica surface. Close inspection of Figure 6.12 (c) gives an initial clue about the mechanism of the dewetting process. There is a strong correlation between the amount of ice layers and vanadium oxide particles deposited on. If particles have enough freedom on ice overlayers they may form lamellar crystalline structures as shown in Figure 6.12 (e) and (f) or they may form clusters or oxide nanorods as shown in Figure 6.12 (c).

The classical theory of nucleation provides a natural explanation of why ice crystals facilitate vanadium oxide crystal nucleation: in order to grow, crystallites of the stable phase need to exceed a certain size otherwise they stay as agglomerates. Crystallites that are smaller than this critical nucleus may dissolve again, crystallites that are larger can grow to a macroscopic size. There, ASW layers may act as a seed material. The thickness o the ASW layers can greatly increase the rate at which vanadium oxide crystals nucleate. This process is qualitatively and quantitatively understood when vanadium oxide island sizes are compared on the basis of initial ASW coverage. Thicker ice layers (~50 BL) seed the formation of larger islands composed of crystalline lamellas instead of 3D agglomerates which is found on relatively thinner ice layers (~10 BL). During the phase change, the particles at the topmost layer concentrate in the space between the ice crystals and form oxide rods since the coverage of ice is not enough to form crystallites. When the sublimation rate increases, the magnitude of evaporating ahead of the phase changing

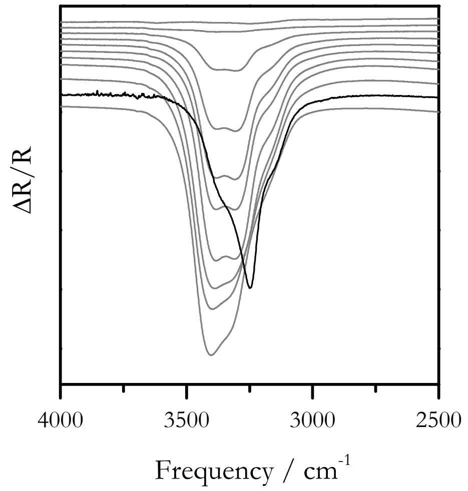

Figure 6.13 IRA spectra of OH stretching region of 100 % CI (black) and amorphous water buffer layer (gray). 2 MLV vanadium oxide was deposited onto 50 BLE ASW at 100 K in 2×10^{-7} mbar O_2. The sample was then slowly heated (in 45 min) until no unreacted water remained on the surface.

interface is increased, and as a result the radius of the ice crystals decreases and ultimately vanishes. This is the main reason of the structural differences between the samples prepared by flash sublimation and slow heating. When thick ASW layers experience phase transformation, dewetting is also accompanied by a natural crack formation and propagation within the islands. The topographic pictures show that the fractures formed do not act as a nucleation sites, instead structures resemble the surface structure of crystalline ice. Besides the assistance of sublimation kinetics of solid water, particle interactions at the interface play an important role. In the presence of attractive particle-interface interaction early stage of sublimation dramatically produces two dimensional ordered islands at the interface from which larger islands nucleate and grow. This quasi self assembly mechanism produces monolayers with exceptional order that has never been observed on silica or on any other metal substrate without thermal treatment.

An important observation in these studies is that, during crystallization of ASW, there is a critical thickness above which the suspended particles will be trapped by the evaporating ice front. Mobility of the particles triggers the formation of ordered vanadium oxide layers. Another important observation is that ice crystals exhibit strong anisotropic growth kinetics. Under slow phase transition conditions, it is possible to grow ice crystals in the form of large islands with high surface area to thickness aspect ratio. Thus, the thicker ice layers formed will have a larger surface area depending on the speed of crystallization. Under these conditions, the key question that emerges is whether the crystallization is initiated in the bulk or at the surface: if surface crystallization is favored, the particle surface will crystallize first, affecting the vanadium oxide particle morphology. Indeed, it has been proposed that the hydrogen bond rearrangement required for crystallization may occur more readily for the less coordinated water molecules at the surface [347]. On the other hand, Buch et al. have calculated that the crystalline geometry is favorable for bulk ice rather than for the surface, implying that commencement of crystallization in the bulk is more likely [348, 349]. At this point, the shape change in the vibrational spectrum characteristic to ASW crystallization may hide the fingerprints of the degree of surface crystallization. Figure 6.13 shows the IR spectral changes in the OH stretching region while ice buffer layers are desorbing from the surface. The shapes of the spectra clearly indicate that with the presence of the vanadium oxide layer 100 %

crystallization can not be accomplished. The topmost surface of the ice buffer layers is far from the crystal phase facilitating the formation of ordered vanadium oxide layers as a seed material. The ice layers are confined within vanadium oxide particles and can not form extended crystallites.

Several hypotheses regarding the nature of the formed nanoparticles and their role can be proposed: ice buffer layers are stable, amorphous species that do not directly participate in the growth of ordered vanadium oxide layers, but serve as a template during crystal growth. Alternatively, ice layers can contribute to growth and their contribution is the rate limiting so that flash sublimation of ice layers gives rise to formation of particles instead of ordered structures. As already shown in the previous sections adsorbed vanadium chemically interacts with the ice layers and gets partially oxidized. The function of ice should be therefore considered not only as a template, but also a reactive agent. V-O-V bridges can be formed by dehydration reaction as evidenced by pronounced desorption of molecular hydrogen. Thick ice layers are required because slow desorption does not lead to immediate dewetting. Particles can then gain enough mobility and form extended ordered structures.

The results show that the ice behaves as an oxidative agent, that favors vanadium oxidation up to V^{4+}, and as a buffer layer that precludes strong interaction of the V ad-atoms with the silica film. At room temperature, upon desorption of the unreacted water, nanosized particles of vanadium hydroxide containing V−OH and, to a lesser extent, V=O species, are formed. The amount of water layers is an important parameter in determining particle morphologies. The structure of silica supported vanadium oxide catalysts is determined by a calcination step and should be considered under low oxygen pressure conditions as vanadium sesquioxide nanoparticles with the V=O terminated surface.

CHAPTER 7

METHANOL ADSORPTION AND OXIDATION ON SILICA SUPPORTED VANADIUM OXIDE NANOPARTICLES

Formaldehyde is produced by the catalytic oxidation of methanol. Two chemical reaction routes produce formaldehyde:

$$CH_3OH + \tfrac{1}{2}O_2 \rightarrow H_2CO + H_2O,\ \Delta H = -159\ \text{kJ/mol}$$

$$CH_3OH \rightarrow H_2CO + H_2,\ \Delta H = +84\ \text{kJ/mol}$$

As a third route, the catalytic combustion of methanol inevitably takes place on metal catalysts. Silver catalysts have been commercialized at the beginning of the 20th century they are usually operated in oxygen lean reaction environments and at high temperature, about 1000 K [350]. The second industrial catalyst is iron-molybdate (Fe_2O_3/MoO_3), which has high activity and selectivity for the oxidation of methanol to formaldehyde. This catalyst allows for the use of lower temperatures, in the range of 600 K to 650 K, which lessens the problem of extensive oxidation. However, in spite of the intense research effort developed during the last three decades, important deactivation problems persist. For example, a wide range of other products (dimethyl ether, dimethoxymethane, methyl formate, carbon oxides, and hydrocarbons) can be obtained depending on both the redox properties and the acidity of the catalyst.

Vanadium oxide dispersed on CeO_2, TiO_2, Al_2O_3 and SiO_2 has been suggested as an alternative type of catalyst for the formaldehyde production reaction. The selectivity of this catalyst towards formaldehyde rather than combustion products can be tuned by support material [351]. There are several factors influencing the activity of the supported vanadium oxide catalysts. First, the number of active sites may be controlled by varying the loading of the active metal oxide. Second, the influence of the metal-support interaction can be monitored by changing the specific support ligand (Al, Ti, Ce, etc.) upon which the active metal oxide species is anchored (the nature of the active site can also be affected by varying the surface promoter). Surface redox sites primarily lead to the formation formaldehyde and methyl formate as the reaction products.

The dissociative adsorption of methanol on metal oxide single crystal surfaces is typically associated with the presence of cation-anion site pairs [352-356]. Methanol adsorbs on the metal cation (Lewis acid) site from the gas phase and loses a hydrogen to a neighboring oxygen anion (Lewis base), thus forming a surface hydroxyl group [355, 357], while the conjugate base anion, methoxy ($CH_3O\cdot$), binds to the cation site. An investigation by Vohs and Barteau [354] on the -O and (0001)-Zn polar faces of ZnO revealed that the zinc face of the crystal is active for methanol dissociation and oxidation, while the oxygen face is inactive. The difference in activity of these crystal faces was attributed to site-pair availability, since the zinc face exposed both zinc and oxygen ions while the oxygen face exposed only oxygen anions. For dissociation reactions to occur, it is believed that the surface cations must be coordinatively unsaturated, while the coordination of surface oxygen anions is less important.

Although these first two conditions are thought to be important for dissociative adsorption of methanol, these conditions alone are not sufficient. The surfaces of SnO_2(110) [358], CeO_2(111) [359], and TiO_2(100) [353, 360] contain acid-base site pairs and coordinatively unsaturated surface cations, yet all are nearly inactive for methanol dissociation. While the surfaces of SnO_2(110) and CeO_2(111) have been found to be inactive, reduction of the surfaces exposes cations of different coordination and oxidation states which allow for methanol dissociation. On SnO_2(110), methanol dissociation occurs preferentially at four-fold coordinated Sn^{2+} sites associated with bridging oxygen vacancies, while on CeO_2(111) the reaction occurs on four-fold coordinated Ce^{4+} oxygen deficient sites. It has been suggested that adsorption of a weaker Brønsted acid (such as methanol) is enhanced by more highly coordinatively unsaturated cation sites [355]. While this idea seems to hold for the case of CeO_2(111) and TiO_2(001), it was determined that further reduction of the active SnO_2(110) surface by removal of in-plane oxygen anions caused the surface to become again inactive for methanol dissociation. These observations demonstrate the complexity associated with generalizing the requirements for dissociative adsorption.

Methoxy is the key intermediate in the formation of all methanol decomposition products on ordered metal oxide surfaces like TiO_2 (001), Cu_2O(111) and (100), SnO_2(110), ZnO(0001), ZrO_2(100) and (110), CeO_2(111), and RuO_2(110) [352, 353, 356, 358, 359, 361], and on single crystal metal surfaces like Cu(110), Ag(110) and Ru(0001) [350, 362, 363], having been identified by XPS or high-resolution electron energy loss spectroscopy (HREELS) [356]. Temperature programmed desorption data are also suggestive of methoxy intermediates on these surfaces. Heating the surface can cause hydroxyls to react with methoxy, reforming methanol, or to react with another hydroxyl in a disproportionation to form H_2O. Another route to methanol formation from a methoxy involves rate-limiting dehydrogenation of methoxy (cleavage of a C-H bond). This reaction is distinctly apparent from the observation of simultaneous desorption of methanol and formaldehyde (CH_2O) during TPD. Decomposition of methoxy to formaldehyde releases hydrogen to the surface; this hydrogen is then free to react with another methoxy and desorbs as methanol.

Formate ($HCOO\cdot$) has been detected by XPS and TPD as a reaction intermediate in the formation of CO and CO_2 from methanol on ZnO(0001) [354]. This intermediate has also been verified by comparison of XPS spectra for adsorbed methanol and adsorbed formic acid (HCOOH) and its derivation has been described by lattice oxygen insertion into a methoxy. Formate has not been reported as a stable surface intermediate in methanol oxidation on any other metal oxide single crystal surfaces; but, it has been identified on single crystal metal surfaces [364]. Dioxymethylene (CH_2O_2) has been identified by HREELS as a reaction intermediate on ZrO_2(110), but not on ZrO_2(100). This species was also derived by lattice oxygen insertion into a methoxy. The difference in the reactivity of the (110) and (100) surfaces of ZrO_2 is attributed to surface structure. Also worth noting, coordination of oxygen anions located in different surface terminations might affect the stability of the adsorbates giving rise to various nucleophilic addition routes of oxygen during CH_2O_2 formation. On ZrO_2(110) dioxymethylene decomposes to formaldehyde

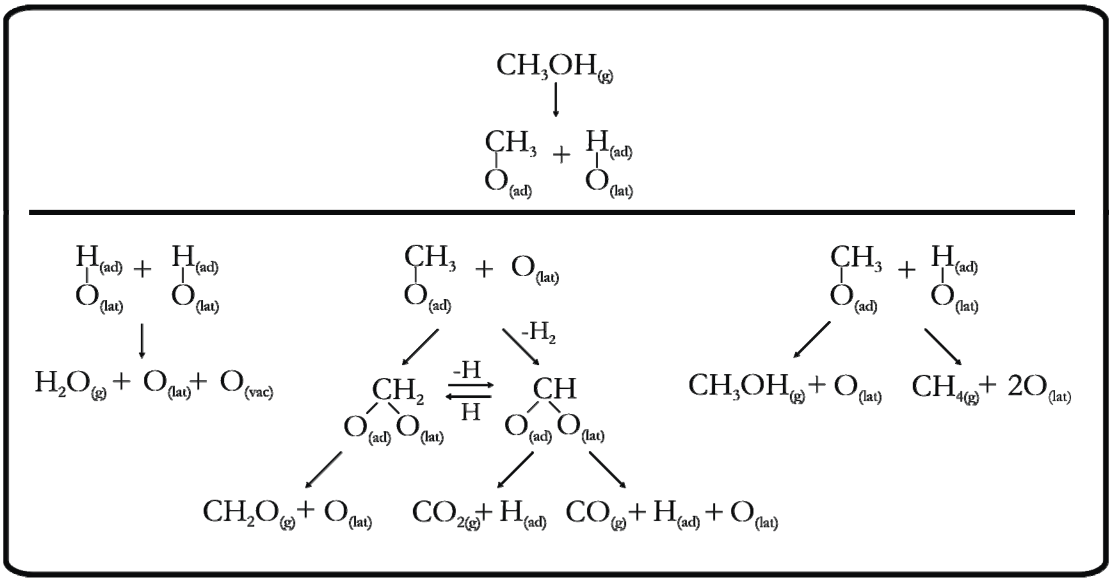

Figure 7.1 Decomposition routed of methoxy on oxide surfaces.

(CH_2O). In general, the formation of CH_2O requires a bi-functional acid-base surface that is a surface containing mildly basic oxygen species for the transfer of H^+ from a methoxy and weaker acidic cation sites for the desorption of the product [365].

Formaldehyde has been observed as a reaction product during thermal desorption on TiO_2(001), ZnO(0001), Cu_2O(100) and (111), SnO_2(110), ZrO_2(110), CeO_2(111), and RuO_2(110). For the case of TiO_2(001) studied by Kim and Barteau [353], the formations of formaldehyde and dimethyl ether (CH_3OCH_3) on faceted surfaces have been attributed to the presence of 5-coordinate Ti^{4+} cations. This is the only case where CH_3OCH_3 was observed during methanol oxidation on a metal oxide single crystal surface. Methane (CH_4) has also been observed as a product during thermal desorption experiments on {011} and {114}-faceted TiO_2(001), reduced TiO_2(001), ZrO_2(100), and ZrO_2(110) [366] surfaces. In these instances, CH_4 formation was attributed to the reaction of a methoxy with an adsorbed hydrogen atom. For TiO_2, deoxygenation of methoxy to CH_4 occurred at oxygen-deficient Ti cations, and hence cleavage of the C-O bond led to reoxidation of the surface [353, 360]. The same reaction occurs on ZrO_2 but it has been reported that oxygen produced in this manner is either incorporated into the lattice or reacted with adsorbed hydrogen to form water. Non-selective oxidation products (CO and CO_2) are frequently encountered in studies of alcohol oxidation. CO is a reaction product in thermal desorption from ZrO_2(100) and (110), and oxygen deficient TiO_2(001); while CO and CO_2 have both been identified as reaction products from ZnO(0001), Cu_2O(100) and (111), and RuO_2(110). On ZnO(0001), CO is formed via two separate reaction pathways: methoxy dehydrogenation and formate decomposition. CO_2 is strictly derived from decomposition of a formate on this surface. Reaction of methanol on supported vanadium oxide powders show a methoxy formed upon dissociative adsorption of methanol, indicating an adsorption process similar to that seen on many metal oxide single crystal surfaces [288, 367, 368]. On hydrated V_2O_5/silica-alumina-titania-ceria, methanol is thought to adsorb and react with hydroxyl groups to form methoxy and hydrogen gas [320]. Reduced, oxidized, and hydrated vanadium oxide surfaces all produce CO and CO_2 [369]. Ethylene ($CH_2{=}CH_2$) and acetylene ($CH{\equiv}CH$) were detected as reaction products during methanol thermal desorption experiments on hydroxylated Cr_2O_3(1012) surfaces, but the reaction mechanisms for these products were not described [370]. Dimethyl ether has also been identified as a reaction product from Cr_2O_3 in thermal desorption from reduced and

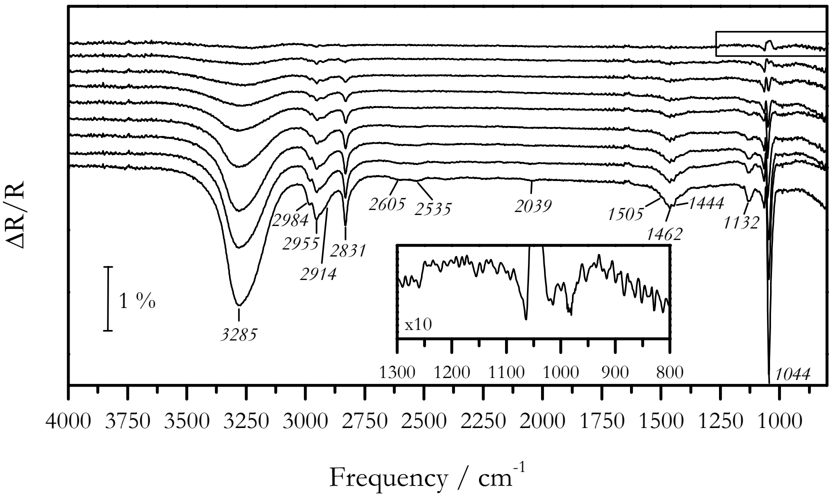

Figure 7.2 IRA spectra of methanol multilayer adsorbed on vanadyl terminated particles (0.8 MLV) at 100 K. Each spectrum represents the increase in methanol coverage by 0.4 L.

hydroxylated Cr_2O_3 surfaces [370, 371]. The suggested mechanisms for this product differed between sources; one listing a dehydration reaction of two methanol molecules [371], while the other suggests a coupling reaction of two methoxys [370] as the reaction pathway.

These possible reaction routes observed on various oxide surfaces are summarized in Figure 7.1. The idea behind comparing several oxide systems is to show the apparent fact that on most of the oxide systems methanol reacts to give methoxy if the surface is not totally oxygen terminated. Availability of the anion-cation site pairs with proper coordination is the key for the activity of the surfaces towards methanol.

7.1 Adsorption of Methanol on Vanadyl Terminated Particles

The exposure dependent data shown in Figure 7.2 highlights a number of interesting features during the development of the adsorbed layer at 100 K and formation of multilayer with increasing exposure. The intense band at 2955 cm^{-1} in the CH stretching region is assigned to the asymmetric stretch of the methyl group ($\nu_a(CH_3)$). It probably overlaps the overtone of the asymmetric methyl deformation, which is enhanced by Fermi resonance with the symmetric stretch of the methyl group ($2\delta_s(CH_3)$) [372]. This broad peak may well envelop other modes, particularly on the low frequency side at 2914 cm^{-1}. The Fermi resonances actually result in both frequency shifts, as a result of repulsion between the modes involved, as well as intensity redistribution from fundamentals to overtone modes. The intensity redistribution often makes the intensity of the overtones comparable with that of the fundamental modes. A necessary condition for Fermi resonances to occur is that the overtone and the fundamental mode frequencies are close to degenerate and that the modes exhibit the same symmetry. For surface adsorbates it follows that all dipole active fundamental modes may interact with the first overtone of any fundamental mode. Moreover, a number of combination bands become detectable in the frequency range between 2500 and 2700 cm^{-1}. The peak at 2605 cm^{-1} is attributed to $\delta_a(CH_3)+\varrho(CH_3)$. For the adsorbed methanol multilayer, the weak peak at 1505 cm^{-1} is assigned to OH bending mode, $\delta(COH)$. Table 7.1 summarizes observed IR peaks of methanol adsorbed on vanadyl terminated particles and their assignments.

The most intense mode of methanol multilayers is the CO stretch, which provides a useful starting point for examination of the coverage dependent behavior. At the lowest exposure of 0.4 L, the band at 985 cm^{-1} is observed. This ν(CO) can be attributed to a chemically different adsorption site. At 0.8 L a peak at 990 cm^{-1} dominates the spectrum, with a weaker feature at 985 cm^{-1}. In addition to those, a third but positive peak can be also seen in the spectra at 1046 cm^{-1}. This feature is related with the interaction of the adsorbed methanol with vanadyl species and appears as a positive peak since the spectra related to adsorption of methanol are referenced to the clean vanadyl terminated surface. With increasing exposure, a band at 990 cm^{-1} continues to dominate, and a new feature emerges at 1044 cm^{-1}. With further exposure, the peak at 1044 cm^{-1} gradually grows in intensity due to formation of methanol multilayer.

Table 7.1 IR frequencies and mode assignments of methanol adsorbed on silica supported vanadyl terminated particles.

Assignment	Frequency (cm^{-1})
ν(OH)	3285
$\nu_a(CH_3)$	2955
$\nu_s(CH_3)$	2831
$\delta_a(CH_3)+\varrho(CH_3)$	2605
2ν(CO)	2030
$\delta_a(CH_3)$	1462
$\delta_s(CH_3)$	1444
$\varrho(CH_3)$	1132
ν(CO)	1044

The distinction between species is also clearly illustrated in the behavior of the OH stretching band. The broad band centered at ~3250 cm^{-1} is first observed at 0.4 L and is assigned to chemisorbed methanol. The growth of a second broad band at about 3285 cm^{-1} is correlated with the development of the additional condensed layer of methanol. As previously observed for condensed methanol phases [373] the OH stretch is red-shifted by 366 cm^{-1} from the gas phase frequency [374] to 3285 cm^{-1} due to strong intermolecular hydrogen bonding. These effects are typical for the hydrogen-bonded systems such as water and ice as described in detail in Chapter 5. While hydrogen bonding within the methanol multilayer is not surprising, it is interesting that even at the lowest exposures (<0.2 L), the broad OH stretching peak appears. Similar to the ASW growth on the clean silica, this could be due to the formation of hydrogen bonded methanol islands at low coverage. During the subsequent growth of the multilayer no new feature develops, but the ν(OH) peak gets sharper. In the CH stretching region, at the lowest exposure, a sharp feature at 2955 cm^{-1} is observed. In the exposure range above 0.8 L, this band grows together with a weak band appearing at 2831 cm^{-1}, which is assigned to the symmetric stretch of the methyl group ($\nu_s(CH_3)$). At 0.8 L, a third peak appears, which is well resolved on the high frequency shoulder of the central CH stretching peak at 2984 cm^{-1} and correlated with the appearance of the OH stretch of chemisorbed methanol. The high frequency shoulder is attributed to $\nu'_s(CH_3)$ mode. The 's' and 'a' indicate whether the mode is symmetric or asymmetric with the molecular plane defined by the HCOH atoms while the prime indicates asymmetry about the C_3 axis of the methyl group. The broad peaks at 1462 and 1444 cm^{-1} can be attributed to the overlapping asymmetric and symmetric bending modes ($\delta_a(CH_3)$ and $\delta_s(CH_3)$), respectively. When $\delta_s(CH_3)$ exceeds 1400 cm^{-1} there is a strong Fermi resonance perturbation between $\nu_s(CH_3)$ and $\delta_s(CH_3)$ [372]. The weak

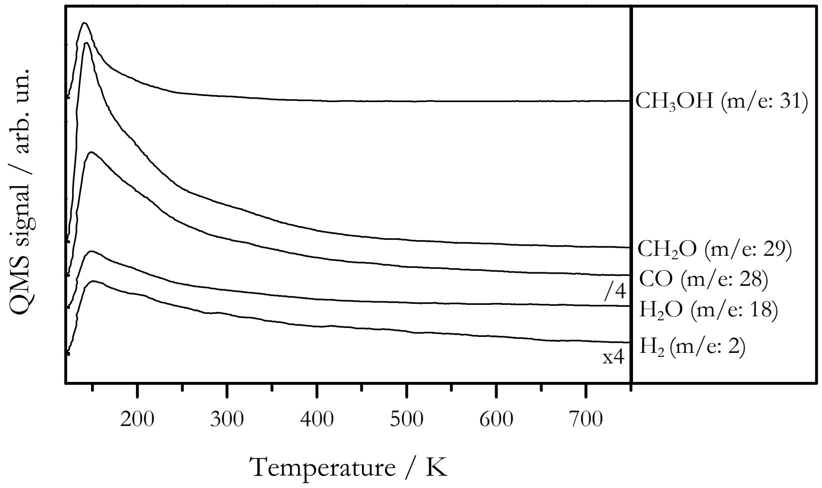

Figure 7.3 TPD data for 0.8 MLV vanadyl terminated particles exposed to 2 L CH_3OH at 100 K. Heating rate was 3 Ks^{-1}. Spectra have been offset for clarity.

bands appearing at 2039 cm^{-1} and at 1132 cm^{-1} are the first overtone of ν(CO) and methyl rocking modes ($\varrho(CH_3)$) with some contribution of the in-plane C-O-H deformation, respectively [375]. All these findings indicate that the interaction of methanol with vanadyl terminated particles and silica film is quite weak. No information about the dissociative adsorption and methoxy formation is obtained. One may consider the ν(CO) band around 985 cm^{-1} as an evidence for stronger interaction. Vanadyl groups are influenced by the presence of adsorbed methanol and they fully recover after desorption.

Warming methanol multilayer to 130 K results in a dramatic loss of intensity of the multilayer features, due to desorption (not shown). Basically, all peaks related to methanol attenuate gradually without a major change[5] and all methanol layers desorb below 250 K. Representative data for a single TPD experiment are presented in Figure 7.3. The main masses evident in these spectra are H_2, H_2O, CO, CH_2O, and CH_3OH, which are basically the fragmentation pattern of CH_3OH. In agreement with IRAS findings, only molecular desorption of methanol is observed and there is no evidence for the desorption of any oxidation products. The peak at 140 K is attributed to the desorption of methanol multilayer and the additional weak feature seen in TPD spectra at around 200 K might be associated with the desorption of chemisorbed species which are also identified by IRA especially at low methanol coverage.

7.2 Adsorption of Methanol on Dehydrated Vanadium Oxide Particles

A key step to fully understand the catalytic working mechanism is a profound knowledge of the surface structure of the particles. Hydration can also be of interest for a better understanding of catalytic performances. H_2O for instance, is formed during some oxidation reactions which may lead to a partial hydration of the catalyst surface. The extent of catalyst dehydration is known to influence the molecular structure of vanadium oxides and it was already shown that the surface of the vanadium oxide particles prepared by reactive solid water assisted method is terminated by hydroxyl groups together with vanadyl

---

[5] Methanol, similar to ASW, experiences a phase transition at around 110-120 K. Small changes in the shape of the peaks can be observed.

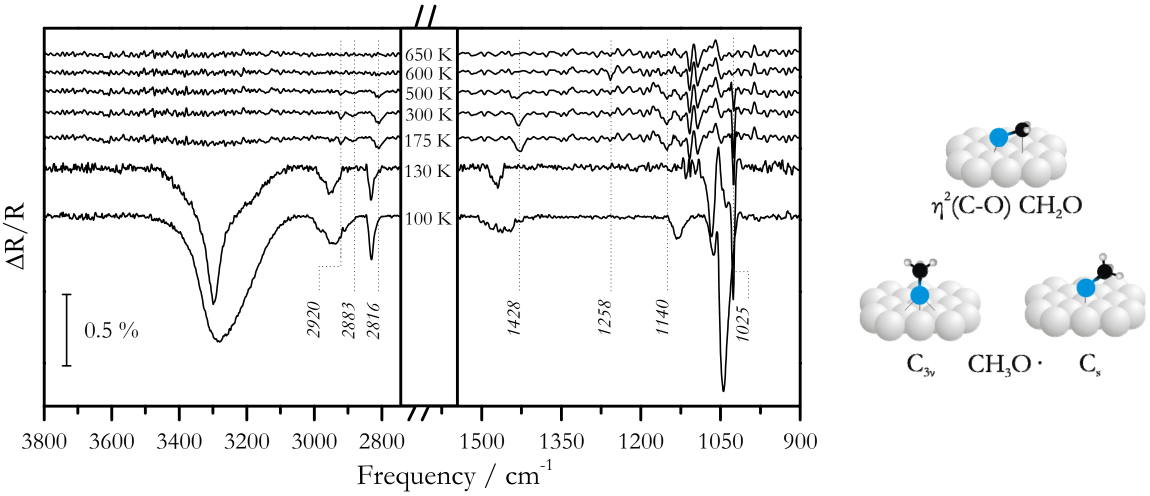

Figure 7.4 IRA spectra as a function of annealing temperature following a 2 L methanol exposure to dehydrated vanadium oxide nanoparticles supported by silica film.

species. Annealing to 600 K leads to total dehydration. CO adsorption experiments initially showed the creation of cationic surface sites upon dehydration and their interaction with methanol can also be important due to the fact that fully vanadyl terminated particles are found to be basically not active towards methanol oxidation reactions.

The study of methanol adsorption on dehydrated vanadium oxide particles permits a direct comparison of the interaction of this molecule with the particles totally terminated by vanadyl groups. Figure 7.4 shows a series of spectra as a function of annealing temperature following a 2 L CH_3OH exposure to the 0.6 MLV dehydrated vanadium oxide particles at 100 K. It is known that if a submonolayer methoxy forms first, the presence of second and higher multilayer of methanol might well obscure the spectral features of the methoxy species. Low diffusivity of methanol molecules over the silica surface below 120 K may lead to the formation of hydrogen bonded methanol clusters before they dissociate on the vanadium oxide particles. This difficulty is overcome by adsorbing methanol molecules that wet the whole surface and removing the multilayer by thermal desorption. The adsorption experiments show that the IRA spectrum for the 2 L exposure of methanol is in a good agreement with the spectra of a condensed layer of methanol obtained on vanadyl terminated particles at 100 K (see Figure 7.2). Features which can be assigned to methoxy were not observed at low methanol exposure at 100 K. The most pronounced changes with annealing are evident between 120 and 140 K. Within this temperature range multilayer crystallizes and spectral changes can be observed. Except for small frequency shifts due to weak surface perturbation IRA spectra indicate nondissociative molecular adsorption. In general, both the symmetric and asymmetric vibrational modes are observed, consistent with a bonding configuration where the molecules are in a hydrogen bonded environment.

Further annealing to 175 K leads to attenuation of all peaks associated with desorption of methanol multilayer. The broad OH stretching band of methanol almost disappears and intensities and frequencies of all symmetric-asymmetric stretching and bending modes of CH_3 slightly change. These results clearly indicate that methanol is converted to different surface species, i.e. methoxy. On most oxide surfaces, methoxy species form by cleavage of O-H bond of methanol and adsorbs via its oxygen end [376]. The peak that can barely be seen at ~3620 cm^{-1} after annealing to 175 K can be attributed to the surface V-OH groups, however its appearance at the noise level and weak influence on the frequency of vanadyl groups makes this assignment unclear. The assignment of the peak at 2816 cm^{-1} to the symmetric CH_3 stretch is straightforward, and its presence might be compatible with both a C_s and C_{3v} local symmetry form. In a C_s geometry or lower, the $\nu_s(CH_3)$ mode would be affected by the proximity of the surface, which explains the lower frequency of this band. The methoxy in a C_{3v} local symmetry simply lacks the $\nu_a(CH_3)$ bands near 3000 cm^{-1}, and compared to the molecular methanol spectra, the $\nu_s(CH_3)$, $2\delta_a(CH_3)$ and $2\delta_s(CH_3)$ bands are shifted to the lower frequencies by 40, 39, and 50 cm^{-1}, respectively [375]. However, the band at 2949 cm^{-1} can more reasonably be assigned to the $\nu_a(CH_3)$ of a slightly tilted methoxy (C_s symmetry) [377]. Even though the presence of some methanol on the surface can not be totally ruled out, the relatively low intensity of the symmetric stretching mode is also more consistent with this geometry. In addition, it must be noted that the particles are actually amorphous and bonding symmetries different than perfect C_{3v} geometry are expected. The persistence of a feature at 1140 cm^{-1} ($\varrho(CH_3)$), a weak feature at 1428 cm^{-1} ($\delta_s(CH_3)$) and a shoulder on the high frequency side of the mode at 2915 cm^{-1} are all consistent with the presence of tilted methoxy species. When methoxy is in upright position, $\nu_s(CH_3)$ is particularly expected to be the strongest band in this region [375]. It is generally agreed that the weak band at 2885 cm^{-1} is the $2\delta_s(CH_3)$ overtone that has gained intensity via a Fermi resonance from $\nu_s(CH_3)$. The main controversy lies in the assignment of the band at 2921 cm^{-1}, which has been in various cases attributed to a $2\delta_a(CH_3)$ overtone, which has also borrowed intensity from $\nu_s(CH_3)$ [377, 378], or one component of the asymmetric methyl stretch [379-381]. With the help of the experiments performed with methanol isotopomers, this peak has been attributed to $2\delta_a(CH_3)$. Moreover, the extent of this symmetry reduction due to tilting is dependent on the orientation of the C-O bond relative to the surface, the nature of the adsorption site, and the strength of the surface-adsorbate interaction [382]. As a general trend, the frequency of the $\nu(CO)$ mode decreases as the interaction with the surface gets stronger, e.g., $\nu(CO)$ is at ~1036 cm^{-1} for Cu(111) [377] and at ~1048 cm^{-1} for Ag(111) [375]. After annealing to 300 K, it becomes apparent that $\nu(CO)$ is in fact red-shifted to 1030 cm^{-1}, suggesting that the oxygen is bonded to the surface cationic sites. A strong metal-oxygen bonding can be responsible for weakening the C-O bond, with the consequent shift of the $\nu(CO)$ mode to lower frequencies [383]. $\nu(OH)$ bands vanish at 300 K and no change in the intensities of methoxy related peaks is observed after annealing the sample to 500 K.

At 600 K, the amount of methoxy decreases, but a surprising weak feature develops at ~1260 cm^{-1}, which must be assigned to different species. At this temperature, methoxy may be decomposing to a new species or recombining with H_{ad} to desorb as methanol. Taking into account the HREELS results obtained by Mitchell et al. [384] on hydrogenation of CO over-layers on Ru(0001), the band at 1262 cm^{-1} is tentatively assigned to the $\nu(CO)$ mode of bridging formaldehyde [η^2(C,O)-H_2CO], formed upon dehydrogenation. In this geometry, the C-O bond would not be oriented parallel to the surface. The proposed bonding structures for the methoxy and η^2-formaldehyde geometries are schematized in the right panel of Figure 7.4. The frequency observed for the CO stretching mode of η^2(C,O)-H_2CO is slightly lower as compared to modes observed on metal surfaces [385]. Those small differences in vibrational energies can be attributed to the influence of steric effects which may perturb the vibrational coupling between molecules as a function of coverage and the extent of electron donation into the d states of the cationic sites and back-donation into nonbonding π^* orbital of adsorbed H_2CO. After annealing to 650 K, no additional features are observed and either all methoxy species are converted to formaldehyde, or they recombine with surface hydrogen and desorb as molecular methanol. Besides, CO is not detected on the surface at any step of the measurements. No carbon accumulation is detected by XPS. Also, no additional vanadyl groups forms after exposing the particles to methanol. This demonstrates that methanol reacting on dehydrated surface partially populated with V=O species does not leave behind any terminal oxygen. At this point, TPD experiments following methanol adsorption might be useful to identify the desorbing products after adsorbing methanol on dehydrated vanadium oxide particles.

TPD data recorded following exposure of dehydrated particles to various CH_3OH exposures provide more insight into the species formed the decomposition process which occurs as a result of heating. A typical set of TPD spectra following adsorption of 1 L CH_3OH at 100 K on vanadium oxide particles is displayed in Figure 7.5 (a). H_2 and CO production are measured by measuring the yields of their molecular ions at m/e: 2 and m/e: 28, respectively. Meanwhile, formaldehyde is monitored using its major cracking fragment, CHO^+, at m/e: 29, instead of its molecular ion CH_2O^+ at m/e: 30, due to a higher abundance of the CHO^+ fragment in the mass spectral cracking pattern of formaldehyde. The production of formaldehyde is further verified by comparing the integrated peak intensity ratio of CHO^+/CH_3O^+ (m/e: 29/31). In addition to the multilayer desorption peak at 140 K, three desorption states can be evidenced by groups of peaks at different temperatures. The lower temperature states include two CH_3OH peaks coincident at 200 and 325 K, respectively. The higher temperature state consists of a weak additional CH_3OH peak at 610 K, and a new CH_2O peak at 610 K, a CH_4 peak at 620 K, a H_2 peak at 615 K, a CO peak at 610 K and trace amounts of CO_2 and H_2O peaks at 620 K and 632 K, respectively. Other molecules which were measured but not detected include CH_3OCH_3, C_2H_4, C_2H_6, and $HCOOCH_3$. Low temperature features are cracking pattern of CH_3OH (i.e. m/e: 31, 29, 28, 18) that are carefully verified by methanol thermal desorption experiments on the clean silica surface. However, within the features desorbing at low temperatures, H_2O contains a small additional feature, which can be considered as desorption of water. For comparison, water adsorption experiments were performed. The TPD spectrum of water involves mainly two desorbing features, a relatively intense peak at 185 K and a broad peak centered at 415 K, respectively. Dehydrated particles can be re-hydrated by water adsorption, however less hydroxyl groups are obtained as compared to the hydroxyl amounts of freshly hydrated particles due to the morphological changes after annealing to elevated temperatures. The high temperature peak agrees with the dehydration behavior of the particles leading to water desorption along a recombination pathway. The low temperature peak can either be attributed to the desorption of molecular water or recombinative desorption from neighboring V–O–V regular sites. The latter route might be responsible for the feature obtained in methanol TPD experiments. The coverage dependent TPD behavior of methanol desorbing from dehydrated particles is illustrated in Figure 7.5 (b) to highlight the fraction of formaldehyde being formed. For the lowest dose, two desorption features centered at 360 K and 620 K are observed. Both features shift down to lower temperatures with increasing doses indicating a second order desorption process. As mentioned earlier, this low temperature feature is mainly due to the cracking pattern of methanol and it is difficult to extract any information about desorption of formaldehyde as a dehydrogenation product. However, proper analysis of the data while subtracting the contribution of cracking components of methanol[6] corroborates that the high temperature peak is certainly related to the formation of formaldehyde. Between 0.3 and 0.5 L, a third peak starts to dominate the spectra at 200 K. With doses grater than about 1 L, a first desorption feature appears as a shoulder at about 140 K, and grows without saturation for increasingly higher doses, confirming the characteristics of multilayer adsorption.

Starting with the vanadyl terminated particles on which no methanol dissociation is observed, it is reasonable to consider that the activity of methanol dissociation increases as

---

[6] TPD spectra here were presented without subtracting cracking components of methanol. At especially high methanol doses at 100 K, pumping speed plays a crucial role for different m/e values.

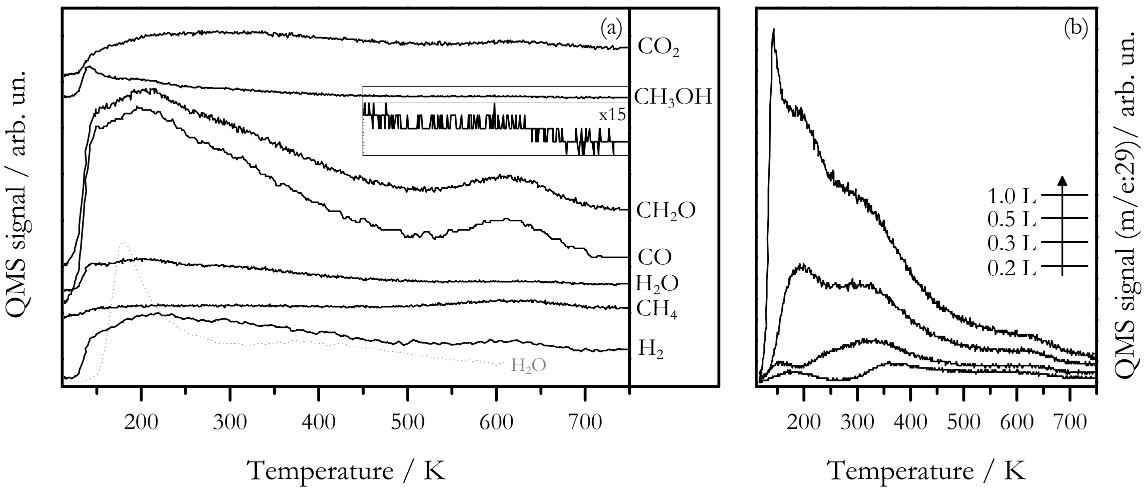

Figure 7.5 (a) TPD spectra following adsorption of methanol (1 L) at 100 K on 1 MLV dehydrated vanadium oxide nanoparticles (solid lines). Dotted line represents a TPD spectrum of water following dosing 100 L of H_2O at 160 K (above multilayer desorption temperature) (b) Formaldehyde desorption following successive adsorption of methanol at 100 K. Initial coverages are indicated in the figure. Heating rate was 3 Ks^{-1}.

the particles are dehydrated, exposing more cationic vanadium and anioic oxygen sites. The dehydration step itself provides this condition as given below:

$$2(VO_x\text{-}OH) \rightarrow 2VO_{x+½}+H_2O$$

The major question to be asked is weather oxygen anions are to be converted to vanadyl groups or to bridge neighboring vanadium cations or they simply stay as chemisorbed species. Even though the temperature to get to fully dehydrated state is high enough to form vanadyl groups, no evidence was found in IRA and XP spectroscopic investigations (see Chapter 6). Instead, it is more likely that after dehydration the number of nonstoichiometric oxygen species increases together with the creation of more cationic sites for methoxy formation. Coverage dependent TPD spectra show that methanol directly dissociates and form methoxy at low coverage. A fraction of methoxy desorbs as methanol via recombining with surface hydrogen at 415 K. The remaining is stable up to 550 K on the dehydrated particles and dehydrogenates to formaldehyde. The high temperature formaldehyde peak does not grow with coverage indicating that the surface is already fully saturated with methoxy after dosing 0.5 L methanol at 100 K.

TPD spectra point out that nonselective decomposition competes with selective dehydrogenation of CH_3OH over the dehydrated particles. The presence of CO_2 formed during methoxy reaction, coupled with H_2 evolution with a peak at 610 K, indicates that nonselective decomposition of methoxy occurs around this temperature. Subsequently, a large fraction of methoxy partially dehydrogenate to formaldehyde, giving rise to the CH_2O peak observed during TPD.

$$CH_3O_{(ad)} \rightarrow CH_2O_{(ad)}+H_{(ad)}$$

$$CH_2O_{(ad)} \rightarrow CH_2O_{(g)}$$

$$H_{(ad)} \rightarrow ½H_{2(g)}$$

$$2H_{(ad)}+O_{(lat)} \rightarrow H_2O_{(g)}$$

In competition, formaldehyde from partial dehydrogenation of methoxy may also undergo rapid elimination to CO directly or via forming a formate surface intermediate.

Once formed, $H_{(a)}$ desorbs rapidly as H_2 and H_2O, contributing to the weak hydrogen and water peaks observed during TPD. Since hydrogen which id present in

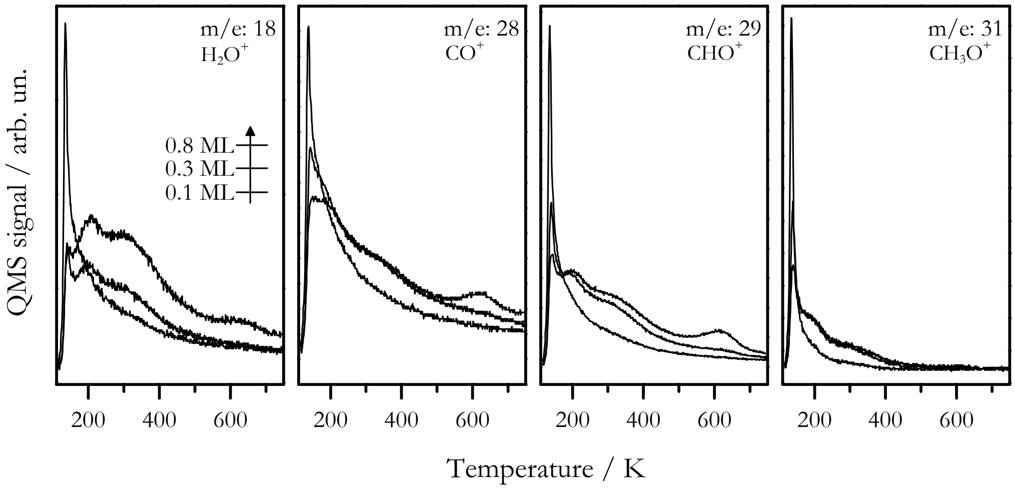

Figure 7.6 TPD spectra of H_2O, CO, CH_2O and CH_3OH following 0.5 L methanol adsorption on 0.1, 0.3 and 0.8 MLV dehydrated particles at 100 K. Heating rate was 3 Ks^{-1}.

hydrated particles desorbs at ~450 K, the production of H_2 from methoxy at 615 K is concluded to be due to dehydrogenation pathway. The identification of surface methoxy by IRAS, the absence of ^{18}O incorporation into CH_2O on the isotopically labeled surface, and the concomitant evolution of H_2 with these oxygenates strongly indicate that CH_2O and CO both originate from a dehydrogenation pathway of methanol. The correspondence in peak temperatures and profiles for CH_2O and CO provides further evidence for a common intermediate for both products. This is consistent with a methoxy precursor to CH_2O and CO. Indeed, numerous studies on methanol reactions over clean metal [386, 387] and oxide [367, 388, 389] surfaces identify methoxy as the primary intermediate to formaldehyde. The possibility that a formate intermediate may also be formed cannot be discounted. While oxidation of methoxy to surface formate occurs readily on oxide [390] the decomposition of HCOO· generally proceeds via dehydrogenation to form CO_2 and H_2 and/or dehydration to CO and H_2O [391, 392]. Desorption of trace amounts of CO_2 and H_2O at 620 and 632 K during methanol TPD might support the idea that surface formate is being formed on the dehydrated particles even though it could not be detected by IRAS. Another hypothesis for the reaction intermediate is the formation of dioxymethylene on oxide surfaces. Such a surface intermediate is similar to the report of Abee et al. that CO_2 adsorbs on the nearly-stoichiometric Cr_2O_3 surface as a bidentate carbonate [393]. Both adsorbed species require a cation-anion site-pair with molecular oxygen bound to a surface cation site, with nucleophilic attack of surface lattice oxygen on an electron deficient carbon center. The lattice oxygen left behind after CH_4 desorption might either recombine with hydrogen atoms and desorb as water or interact with the neighboring intermediate species leading to the desorbing CO_2 molecules.

The concept of structural sensitivity has been used to describe reactions on supported vanadium oxide catalysts whose rates depend on particle size, surface termination and orientations of the crystallographic planes in the presence of large particles. While the structure of the vanadium oxide is largely invariant on a wide range of oxide supports [332, 394, 395], the activity of vanadium oxide, as measured by the turnover frequency for the oxidation of methanol to formaldehyde, is strongly influenced by the support and varies by several orders of magnitude [396]. Bulk silica is an interesting support for vanadium oxide and somewhat distinct from other commonly used oxide supports such as TiO_2, CeO_2, etc. For very low loadings, the structure of vanadium oxide on bulk silica is very similar to that on other oxides whereas the formation of crystallites on silica occurs well below monolayer coverage, and two dimensional polyvanadate species are not readily formed [292, 397]. The reactivity of dispersed vanadium oxide on silica is substantially less than that for the vanadium oxide on the other reducible supports. On the silica film surface, a somewhat similar trend is observed as the coverage of vanadium oxide in increased. Three dimensional particles form at very low coverages and their lateral sizes get larger with deposited vanadium amount. Recalling the fact that fresh hydrated particles contain some vanadyl groups at 300 K and an increased number of V–O–V species is expected for larger particles; one may expect a size dependent performance of those catalysts. Figure 7.6 shows sequential changes in TPD spectra of H_2O, CO, CH_2O and CH_3OH following 0.5 L methanol adsorption on dehydrated vanadium oxide particles (0.1, 0.3 and 0.8 MLV). The desorption behavior is qualitatively consistent with the results shown in Figure 7.5 (a) for all coverages above 0.2 MLV. On 0.1 MLV vanadium oxide particles, formaldehyde is not detected, probably due to the detection limit of the mass spectrometer. The formaldehyde yield increased with the particle coverage and no size dependent activity and selectivity modifications are observed. Comparing the relative intensities of the desorbing products, a small difference is found for the low temperature water desorption peak and can be attributed to an increase of basic sites with coverage. Availability of more sites for hydrogen obtained after dissociation of methanol is not unexpected, it can be cross related to desorption of more water.

7.3 Influence of Surface Oxygen on Formaldehyde Formation

The reactivity of methanol on surfaces can be modified by the presence of pre- or co-adsorbed atoms. These species effect the electronic potentials and therefore, charge transfer coupling in the vicinity [398], including the rearrangement of substrate atoms. These may involve first and second layers of the coordination shell. Depending on the adsorbate-substrate bond strength this reconstruction may result in a global effect and/or introduce certain surface disordering. On single crystal surfaces, it has been shown that induced nonlocal effects may result in change of the work function [399]. The average distance between first and second next neighboring atoms can also be altered [400]. The extent of the latter depends on the local flexibility of the surface atoms, on the nature of adsorbed atom, and on coverage. Finally a blocking effect may be expected, as adsorbed atomic species reduce the number of available active sites for adsorption, either by competing with the same site or by repulsive interaction with the neighboring adsorbate [5].

The strong influence of the oxygen to methanol ratio in determining the methanol conversions and formaldehyde yields has also been observed under conventional catalytic conditions. Although oxygen is essential for efficient production of formaldehyde form methanol; an excess of oxygen will further oxidize it to carbon dioxide and water. The interaction of hydroxyl end of a methanol molecule with surface oxygen is also critical and the amount of surface oxygen atoms and their coordination are expected to influence the catalytic activity since the adsorbed O induces a continuous increase in the work function with increasing coverage, resulting from a withdrawal of electron density from the surface. Even though methoxy is the common surface intermediate on almost all surfaces, methoxy-substrate and oxygen-substrate bond strengths play a crucial role in terms of selectivity.

The left panel of Figure 7.7 compares high temperature formaldehyde formation depending on the state of the vanadium oxide particles at the same coverage (0.8 MLV) following the same amount of methanol exposure (1 L) at 100 K. The spectra are offset for clarity. Spectrum (a) is obtained following methanol exposure to dehydrated particles and (b) shows increase of high temperature formaldehyde peak after predosing oxygen to the

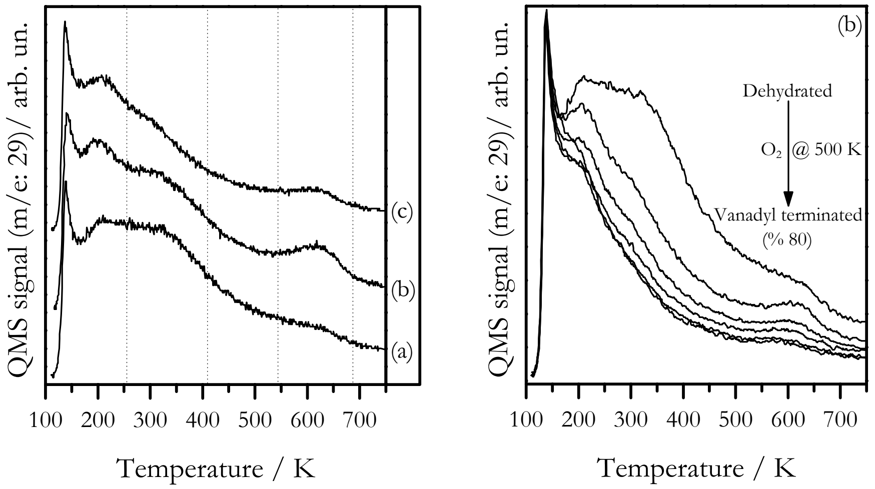

Figure 7.7 Effect of predosed oxygen on formaldehyde formation. *Left panel*: TPD spectra of formaldehyde following 0.5 L methanol adsorption on 0.6 MLV (a) dehydrated, (b) oxygen predosed (25 L at 300 K) and (c) oxygen predosed (25 L at 500 K) vanadium oxide particles. *Right panel*: TPD spectra of formaldehyde following 0.5 L methanol adsorption on 0.6 MLV dehydrated (top) and 5, 25, 50 and 300 L oxygen predosed (from second from the top to bottom) vanadium oxide particles at 500 K. Heating rate was 3 Ks^{-1}.

dehydrated surface at 300 K. In contrast to the increase in formaldehyde yield at 610 K, no change is detected in low temperature region suggesting that molecular and recombinative desorption channels are still open. However, dosing the same amount of oxygen on the surface (b) at 500 K induces an irreversible partial blocking in the formaldehyde formation channel. Moreover, the low temperature recombinative desorption peak loses most of its intensity due to the formation of vanadyl groups, which reduces the number of available acidic sites created after dehydration. The right panel of Figure 7.7 shows more systematically the loss of active sites required to stabilize methoxy. Dosing oxygen at 500 K gradually reduces both low and high temperature uptakes as opposed to oxygen dosing done at 300 K. Above 500 K, dosing oxygen at any extent ends up with the appearance of vanadyl groups inhibiting the activity of the particles towards methoxy formation and therefore formaldehyde production.

Thermal desorption data for the reactions of methanol all show CH_3OH, CH_2O, CO, CO_2, and CH_4 desorbing in the same high temperature range; signifying that the reaction might go through several reaction intermediates. When these vanadium oxide particles are modified with oxygen, formaldehyde (from partial dehydrogenation of methoxy) is stabilized on the surface, and its subsequent decomposition to CO is partially inhibited, giving rise to the evolution of gaseous CH_2O [401]. Remarkable differences in activity toward formaldehyde are observed between the vanadyl terminated, dehydrated and the O-modified vanadium oxide particles on silica film surfaces. The lack of activity of the vanadyl terminated particles is attributed to unavailability of acid-base site pairs required for methoxy formation. Methanol reactivity over the O-modified dehydrated particles and dehydrated particles is also markedly different. Taken together with these findings on three sample conditions (effect of hydration was not discussed here due to its inactive behavior), all these studies demonstrate that changes in local geometric structure can significantly affect the activity of model oxidation catalysts toward methanol reaction. The inhomogeneous distribution of oxygen on the O-covered particles may also play a role in its increased activity toward methanol reaction. Methanol conversion to methoxy is known to occur primarily at open high-coordination sites on oxide and oxidized metal surfaces [358, 402]. Thus, it is quite likely that vacancies are present at high-coordination sites on the O-covered dehydrated surface, which may promote CH_3OH reaction. It has been argued that presence of peroxo (O_2^-) species can influence the activity of the vanadium oxide surfaces [403]. However, those peroxo species might be present only if particles are exposed to molecular oxygen at low temperatures (i.e. 100 K) and having them on the surface at 300 K is not expected. Oxygen might play a very crucial role as a stabilizing agent for methoxy and other possible surface intermediates like formate or dioxomethylene. Considering the Lewis-base function of the surface oxygen anions, one would expect that unsaturated bridging oxygen anions (since no additional vanadyl species are observed) on the dehydrated particles to be more reactive than the vanadyl groups. The difference in ability of these particles to dissociate methanol is attributable primarily to the availability of surface vanadium cations with slightly modified coordination. The limited reactivity observed on vanadyl terminated particles can thus be explained by the lack of highly coordinated vanadium cations. High temperature desorption peaks are all reaction limited and the rate of high temperature methanol desorption is limited by hydrogen amount. TPD results indicate that no hydrogen desorption is observed above 450 K; so the source of hydrogen is the methoxy itself. β-hydride elimination from methoxy occurs over the entire high temperature range. The hydrogenation of methoxy to methane then requires two conditions; namely, a formation of an intermediate and a combination of hydrogen with this intermediate. The same condition is required for the formation of carbon monoxide and carbon dioxide. The interaction of the oxygen of methoxy with vanadium cation site and nucleophilic attack on the carbon center by neighboring unsaturated oxygen anion may yield dioxymethylene and this intermediate can be stabilized by an additional oxygen dose on the dehydrated particles. Dehydrogenation of this intermediate may be the sources of all oxidation products and the formation of formate as an intermediate is less likely since it could not be detected by IRAS and no desorption of formic acid was observed.

CHAPTER 8

SUMMARY AND OUTLOOK

The investigations on vanadium oxide supported on SiO_2, Al_2O_3, TiO_2, CeO_2, etc. have revealed that the geometric and electronic structures of vanadium oxides are the fundamental basis for the catalytic performance. There is a general consensus that structural and reactivity characteristics of vanadium oxide are modified with respect to bulk vanadium oxide by interaction with the oxide support surface and that this specific oxide–oxide interaction leads to a spreading of vanadium oxide over the support surface to form a thin monolayer film. However, catalytic functionalities of these monolayer catalysts are complicated. At this point, the model systems offer advantages owing to less structural complexity while addressing important issues of supported catalysts such as the role of support and particle size effects. The work over the last two decades has demonstrated that atomic-level surface science techniques can provide fundamental insights into the physics and chemistry of the oxide surfaces by enabling the synthesis of metal and metal oxide clusters on oxide films. Even though growth methods of oxide thin films are pretty much established, several issues have remained unsolved, for example, crystal structures, surface terminations, defects and their role in reactivity and nucleation of deposited particles, etc. The whole thesis has been structured in such a way that in each chapter some of these issues are discussed on a sample system that is mostly related to silicon dioxide thin films.

One driving force for performing research on crystalline silica is the wide range of its applications and the expectation that insight into surface properties on the fundamental level will help to improve the understanding of catalytic reactions. Therefore, a detailed knowledge about chemical properties of the surface of silica at the atomic level is required in order to envision better catalysts. Growth of crystalline silica films on metal substrates is not trivial due to the fact that single crystallinity requires some critical conditions such as good lattice matching with the metal substrate and necessity of high temperature treatments. These prerequisites leave many of the candidate metals out as a substrate material for silica thin films. (112) terminated molybdenum has already been shown to be a good surface of choice owing to both similarities between the surface interatomic distances of molybdenum atoms and the lattice parameters of bulk silica crystals and high melting point. Silica film preparation methods involve oxidation steps at elevated temperatures; it is therefore required to take a closer look at the interaction of oxygen with the clean molybdenum surface.

Being an early transition metal with a strong affinity towards oxygen, a thin oxide layers, most generally MoO_2 and MoO_3, can easily be formed on molybdenum surfaces. The initial stage is generally assumed to proceed via the formation of chemisorbed oxygen layers followed by nucleation and growth of two dimensional oxide islands. On a Mo(112) surface, following the saturation state of chemisorbed oxygen, a unique surface oxide forms with a commensurate periodic structure. It was found that Mo(112)-p(2×3)-O, which was thought to be a structure associated with chemisorbed oxygen, turned out to be the oxide layer with one dimensional periodicity. As judged by LEED and STM studies, stripes belonging to the oxide layer propagate in a dimensional fashion. Besides, oxygen induces mass transport at the surface and the periodic structure is broken due to a high density of domain boundaries. IRAS conclusively shows that the surface is terminated by Mo=O groups, the fingerprints of which can also be observed in high resolution photoemission spectra. In addition to surface oxygen, rich Mo 3d spectra indicate the presence of subsurface oxygen. This specific surface oxide is a potential candidate as a model system for selective alcohol oxidation reactions, where the local structure of metal oxide is important.

Atomic structure of the thin crystalline silica film on a Mo(112) substrate were determined based on the excellent agreement between experimental findings and DFT calculations. The film consists of a two dimensional network of corner sharing SiO_4 tetrahedra, with one oxygen atom from each tetrahedron bonding to Mo atoms of the protruding rows on the Mo(112) surface. The other three oxygen atoms form Si−O−Si bonds with the neighboring tetrahedra. With a proper control of oxygen amount during film preparation, the unit cell can be enriched in terms of oxygen content. The film is one layer thin and any attempt to build up additional ordered layers results in the formation of particles and loss of long range order. Difference in coordination of surface and interface oxygen ions makes them distinguishable by means of spectroscopic approaches based on measurements of the binding energies of core level electrons. The ratio of the O 1s peak intensities of surface oxygen ions to interface ones and the appearance of a third component with the addition of extra oxygen atoms into the unit cell confirm a 2D network model as a building block of the silica films. Thanks to the structural order in the film, the valance band spectra are quite structured clearly resolving Si−O bonding and O nonbonding states. The Si−O−Mo bond has a strong dipole along the surface normal therefore the stretching frequency of which dominates the IRA spectra of the film. The behavior of Si−O−Mo stretching frequency together with Si−O−Si bending modes in the presence of adsorbates and particles help to understand their interaction level. While the enrichment of the unit cell with oxygen atoms is only modifying Si−O−Mo stretching vibrational mode, exchanging surface atoms causes energy shifts in all vibrational modes. A part of the stress created by the lattice misfit between the substrate and the epitaxial layer can relax by the creation of so called antiphase domain boundaries. They are characterized by a phase shift vector which describes the displacement of the sublattice site at the boundary. Therefore, the APDs subdivide the superstructure into domains. The origin of antiphase domain boundaries is closely connected to the surface morphology of the underlying molybdenum oxide (buffer) layer which acts as a template. As compared to those extended line defects, the number of point defects remains minor. That is why it is quite difficult to get spectroscopic evidence for their existence but, STM results indicates that there are very few defect sites which can be attributed to silicon vacancies.

One of the motivations of this thesis was to extend the quite limited knowledge of the interaction of water with oxygen-terminated silica surfaces. Certainly, the interplay between the local electronic and vibrational structures of silica film and adsorbed water can provide more insight with the nature of their interaction. Defects, i.e. vacancies, domain boundaries, steps, corners, are the sufficient sites to cause water dissociation on silica thin films. However, it has been shown that water adsorbs molecularly on the surface of silica film at 100 K. On the basis of TPD, IRAS, UPS, and XPS results, the following picture has been proposed for the adsorption and growth of water layers: In the initial stages of water adsorption the individual molecules are weakly bound to the surface. As increasing exposure, the isolated water molecules start to condense into hydrogen-bonded clusters. The presence of the latter is deduced from the UPS data which show the splitting of the feature due to emission from the $3a_1$ orbital of water. In contrast to adsorption at 100 K, water exposure at 140 K follows a pseudo-first order desorption kinetics and results in a strong blue shift of the silica phonon. Even larger effects have been observed for D_2O adsorption. The results suggest that water forms three-dimensional, amorphous ice clusters at 100 K but two-dimensional crystalline ice at 140 K. This ice layer is in a good epitaxial relationship with the silica substrate, leading to a c(2x2) structure with respect to the silica surface as observed by LEED. The detailed structure of the epitaxial ice layer needs further investigations including theoretical calculations.

In our present day knowledge monolayer catalysts are a few layers of e.g. vanadium oxides on another oxide substrate, but the morphology, atomic structure, and chemical composition of these oxide-on-oxide overlayers are largely unknown. The necessity of a detailed elucidation of their structures at the atomic level and the knowledge of the atomic structure of the silica film put us into the position to study the nucleation and growth of vanadium oxide nanoparticles on flat well characterized silica surfaces. Using well ordered silica systems as a support, vanadium oxide particles in hydrated and dehydrated state have been investigated in a great detail. On hydrophobic silica surface, vanadium oxide forms three dimensional particles and their interaction with the substrate is quite strong. Based on an XPS analysis, it was shown that the nature of vanadium oxidation is not uniform and as a result, not all particles have the same valence state. Particles contain predominantly V^{3+}; however, some metallic component contained at the core of the particles can not be ruled out. IRA spectra indicate that vanadyl termination is becoming dominant with increasing the coverage. The applicability of solid water as a reactive layer for vanadium oxide particles to characterize their hydrated state has been successfully demonstrated. The nucleation behavior of oxide particles grown on amorphous solid water multilayers was found to be different as compared to the examples on pristine silica surface even though the formation three dimensional particles was observed in both cases. At low coverage, isolated and dimeric species were present, however their tendency to form 3D particles were severe. Removal of unreacted solid water layers influenced dramatically the anchoring pathways of the particles. Completely hydrated particles did not contain any vanadyl species, however, on partially dehydrated samples, V−OH and V=O species turned out to be coexisting. At room temperature, the oxidation state of the partially dehydrated samples was in the range of 4+ and complete dehydration caused reduction. The reduced vanadium sites which are potentially important for reactions were quantitatively probed by CO during dehydration and it was shown that converting reduced sites to V=O by post oxidation reduced dramatically the number of sites available for CO. Annealing treatments done for dehydrating the particles did not cause ripening; instead, shrinkage in particle size was observed.

The interest in adsorption studies on supported vanadium oxide nanoparticles is driven by the relevance of these oxides in the field of heterogeneous catalysis. Although vanadium oxides are amongst the most important materials in oxide catalysis, the molecular level characterization of the elementary steps of methanol oxidation reactions and their selectivity towards formaldehyde are not or only poorly understood. In this context the value of model studies on atomically defined surfaces is well recognized and adsorption and reaction studies on supported vanadium oxide surfaces might lead to a deeper understanding. Activities of vanadyl terminated, dehydrated and oxygen modified submonolayer vanadium oxide particles towards methanol oxidation reactions were compared via methanol adsorption studies. Methanol TPD and IRAS experiments conclusively demonstrated that methanol weakly interacted with the silica film itself and vanadyl terminated particles supported by silica film and desorbs molecularly without inducing changes at the particles. On dehydrated particles prepared by the assistance of ice, dissociation of methanol takes place with O-H bond breaking and one dissociation product, i.e. methoxy, is stable on the surface up to 550 K and other one, i.e. hydrogen, adsorbs on basic sites and desorbs as water via a recombination channel. Stable methoxy also decomposes through two competing pathways above 600 K. Partial dehydrogenation takes place to evolve gaseous formaldehyde in one route and rapid hydrogen elimination causes carbon monoxide and carbon dioxide formation in the second route. Formation of methane suggests the availability of different reaction intermediates which can play an important role in those dehydrogenation routes. Dioxymethylene is proposed to be the reactive intermediate, the stability of which can be improved by uncoordinated oxygen sites. Exposing dehydrated particles to molecular oxygen at room temperature was found to increase the formaldehyde yield as well as other oxidation products. Increasing oxygen exposure temperature dramatically reduced the activities of the dehydrated particles leading to gradual formation of vanadyl groups.

This study has selectively dealt with a number of topics having to do with thin silica film and its interaction with water and deposited vanadium oxide particles, emphasizing recent improvements in surface characterization. Full understanding of properties of the silica films grown on a Mo(112) substrate enables detailed predictions about their interaction with water and vanadium oxide particles. The electronic properties of this monolayer film is very much like bulk silica, therefore it is an excellent support as a model system. The only drawback might be its thickness since penetration of deposited particles through the film is quite probable at elevated temperatures. It is likely that rapid growth of research in this field will continue as high pressure techniques are adapted and new materials with unique properties are introduced.

APPENDIX A

SYMBOLS

ϕ	Work function
τ	Life-time of the core hole
σ	Photoelectron cross-section
ν_a	Asymmetric stretching vibration
δa	Bending vibration
Γ	FWHM of life time broadening
ν_s	Symmetric stretching vibration
h	Planck constant
m_e	Electron mass
ψ	Wave function
λ	Wavelength
μ	Dipole moment
ϱ	Rocking mode

APPENDIX B

ABBREVIATIONS

Å	Angstrom
AFM	Atomic force microscopy
APDB	Antiphase domain boundary
ARXPS	Angle resolved X-ray photoelectron spectroscopy
bcc	Body centered cubic
BL	Bilayer
BLE	Bilayer equivalent
$CH\equiv CH$	Acetylene
$CH_2=CH_2$	Ethylene
CH_2O	Formaldehyde
CH_2O_2	Dioxymethylene
CH_3OCH_3	Dimethyl ether
CH_3OH	Methanol
CH_4	Methane
CI	Crystalline ice
CO	Carbon monoxide
CO_2	Carbon dioxide
CVD	Chemical vapor deposition
D	Debye
DFT	Density functional theory
DS	Doniach and Ŝunjić
E_b	Binding energy
E_F	Fermi level
E_{kin}	Kinetic energy
E_p	Energy of the primary electron beam (LEED)
ESR	Electron spin resonance
FC	Frank-Condon
fcc	Face centered cubic
fs	Femto second
FWHM	Full width at half maximum
HCOO	Formate
HCOOH	Formic acid
hcp	Hexagonal closed packed
HREELS	High resolution electron energy loss spectroscopy
Ic	Cubic ice I

IC	Integrated circuit
Ih	Hexagonal ice I
IP	Ionization potential
IRAS	Infrared reflection absorption spectroscopy
LDOS	Local density of states
LEED	Low energy diffraction
LO	Longitudinal optical
LST	Lyddane-Sachs-Teller
MBE	Molecular beam epitaxy
MCT	Mercury-cadmium-telluride
MIT	Metal insulator phase transition
ML	Monolayer
MOSFET	Metal-oxide-semiconductor field effect transistor
MSSR	Metal surface selection rule
nA	Nano Ampere
NBO	Non-bridging oxygen
pA	pico Ampere
PVD	Physical vapor deposition
QMS	Quadrupole mass spectrometer
SCLS	Surface core level shift
STM	Scanning tunneling microscopy
TDS	Thermal desorption spectroscopy
TM	Transition metal
TO	Transverse optical
TPD	Temperature programmed desorption
UPS	Ultraviolet photoelectron spectroscopy
V_s	Sample voltage
XPS	X-ray photoelectron spectroscopy

APPENDIX C

SAMPLE PREPARATION

Experiments were performed in two separate ultra high vacuum chambers with base pressures better than 2×10^{-10} mbar. X-ray photoelectron spectroscopy, infrared reflection absorption spectroscopy and scanning tunneling microscopy experiments were performed in one multipurpose chamber which allowed sample transfer without subjecting it to air. Temperature programmed desorption experiments were performed in another one equipped with a quadruple mass spectrometer and low energy electron diffraction / Auger electron spectroscopy optics. High temperature flashes in order to clean sample and heating treatments during silica film preparations were done by electron bombardment from a thoriated tungsten filament placed close to backside of the Mo(112) crystal (Matek). Temperatures were measured by tungsten-rhenium (W-5%Re/W-26%Re) thermocouples spot-weld at the rim of the samples. Silicon and vanadium deposition were performed by electron beam evaporation from silicon and vanadium (Goodfellow) rods. During evaporation, the sample was kept on the same potential as the Si and V rods in order to prevent ions from being accelerated towards the surface. Oxygen (Linde Gas 99.9995%) was dosed by backfilling the chamber with high precision leak valves.

The XPS binding energies were calibrated relative to the Fermi edge of the clean Mo crystal (zero on the binding energy scale). XPS is performed using Al Kα (hν=1486.6 eV) and Mg Kα (hν=1253.6 eV) sources for V 2p - O 1s and Si 2p spectral ranges, respectively. All UPS measurements were performed using He I (hν=21.2 eV) as excitation energy. All STM (Omicron) images were recorded at room temperature in a constant current mode and the bias voltage is given relative to the sample (positive bias for empty state imaging). The infrared spectroscopic data was acquired using a Bruker IFS 66v/S spectrometer in reflection mode at 2 and 4 cm^{-1} resolution with p-polarized light at 84° grazing angle of incidence. A liquid N_2 cooled MCT (mercury-cadmium-telluride) was used as a detector. Each spectrum was collected by taking the average of 1000-4000 scans depending on desired precision of the experiment. A sketch of the experimental setup can be seen in Figure C.1. TPD experiments were performed by placing the sample 1 cm away from the head of QMS in order to avoid background contributions. The temperature and linear heating rate were precisely controlled by the feedback system (Schlichting Phys. Instrum.) The PES measurements were performed using the synchrotron facilities at BESSY II in Berlin (beamline UE52-PGM1). The spectra were recorded with a Scienta R4000 analyzer at normal and grazing electron emission.

Mo(112) crystals were cleaned by repeated oxidation (in 1×10^{-6} mbar O_2 at 800 K) annealing cycles (at 2300 K in UHV) until surface carbon contamination goes beyond detection limit of XPS or AES. Oxygen dosage was done to form molybdenum surface oxide by backfilling the chamber. No oxide formation was observed at the temperatures below 600 K independent of the oxygen amount. Formation of molybdenum surface oxide was followed in-situ by LEED while keeping oxygen partial pressure constant at 5×10^{-9} mbar at 850 K. Since phase diagram of O/Mo(112) system is quite rich, care has to be taken not to have more than one phases on the surface. p(1×2) is a quite stable phase below 700 K and p(1×2)→p(1×3) transition is observed above it. The temperature range between 600 and 700 K seem to be important since the onset of oxide formation in O_2 pressures below 1×10^{-6} mbar resides in this range. Formation of Mo(112) p(1×3)-O phase is triggered by increase of oxygen amount on the surface and heat of oxygen adsorption leads to buckling of top layers. Mo(112) p(2×3)-O phase was prepared by exposing clean surface to O_2 for 10 min in 5×10^{-8} mbar at a temperature of 850 K. The surface begins to form facets and ultimately bulk-like oxide layers if the temperature is increased above 1000 K.

Silica films were prepared by depositing 1.2 ML silicon in 5×10^{-8} mbar O_2 pressure at 900 K. Deposition rate of silicon was 0.07 ML/min and calibrated by XPS. So-called reactive deposition of silicon in O_2 ambient requires optimization of deposition rate to control amount of oxygen in the unit cell. Faster deposition rates even at lower temperatures are possible; however, under those conditions the post oxidation step might be necessary. While deposition is being made molybdenum surface is also being covered by oxygen and lack of surface oxygen might give rise to presence of silicon not fully oxidized. Besides, prior to depositing silicon, the clean molybdenum surface is exposed to 5×10^{-8} mbar O_2 for 5 min at the same temperature. UHV annealing at 1250 K for 5 min results in formation of well ordered oxygen poor silica films. Incorporation of additional oxygen into the unit cell to form oxygen rich films requires annealing to the same temperatures in 5×10^{-7} mbar O_2 pressures for maximum 5 min. The amount of oxygen can be controlled by changing the dosing time. Annealing the film to the temperatures above 1250 K results in evaporation of part of the film leaving oxygen covered patches behind and the film is completely removed above 1450 K.

Water (H_2O and D_2O), methanol and carbon monoxide were exposed to the surface using a directional gas doser inside the IRAS cell and TPD chamber. Calibration of water dosage was done by adsorption on Pt(111), where the formation of water bilayer can be discriminated by TPD. Before use, doubly ionized H_2O, D_2O (Isotec, 99.96 %) and CH_3OH (Merck, <99.99 %) were cleaned by several freeze-pump-thaw cycles. Cleanness was check mass spectrometer by filling the chamber with their vapor in TPD machine or IRAS by forming condense multilayers on clean silica surface, which shows no activity towards those molecules.

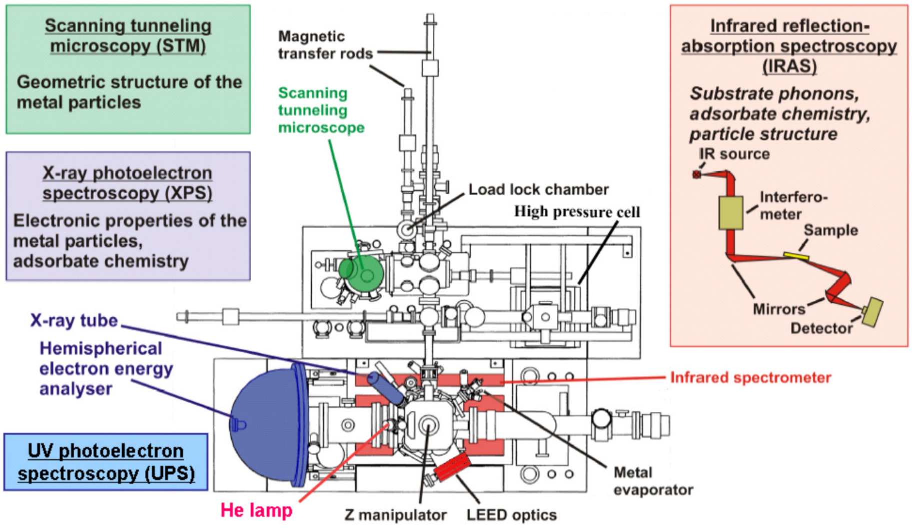
Scanning tunneling microscopy (STM)
Geometric structure of the metal particles
X-ray photoelectron spectroscopy (XPS)
Electronic properties of the metal particles, adsorbate chemistry
X-ray tube
Hemispherical electron energy analyser
UV photoelectron spectroscopy (UPS)
He lamp
Magnetic transfer rods
Scanning tunneling microscope
Load lock chamber
High pressure cell
Infrared reflection-absorption spectroscopy (IRAS)
Substrate phonons, adsorbate chemistry, particle structure
IR source
Interfero-meter
Sample
Mirrors
Detector
Infrared spectrometer
Metal evaporator
Z manipulator
LEED optics

Figure C.1 Schematic illustration of the UHV system (MEGA machine).

Vanadium was deposited on pristine silica films in 2×10^{-7} mbar O_2 pressure at 300 K. Evaporation rate was 0.035 ML/s calibrated by quartz crystal microbalance and XPS. For consistency, we use monolayer (MLV) expression referring to number of vanadium atoms calculated on the basis of interlayer distance between V(110) surface and correlating it to microbalance, XPS and STM calibrations. Post oxidation treatments were performed in the same way.

CURRICULUM VITAE

Sarp Kaya
15.09.1977
in Ankara, Türkei

	Schulbildung
1988-1995	Ankara Deneme Schule, in Ankara, Türkei
	Hochschulbildung
10/1995 – 06/2000	Studium Chemieingenieurwesen, an der Technische Universität des Nahen Ostens (Middle East Technical University), in Ankara, Türkei
06/2000 – 08/2002	Forschungstätigkeit (Diplomarbeit), an der Technische Universität des Nahen Ostens (Middle East Technical University), in Ankara, Türkei in der Arbeitsgruppe von Frau Prof. Dr. Deniz Üner Titel: CO Oxidation on Alumina Supported Pd-Pt Mono- and Bimetallic Catalysts: Temperature Hysteresis
10/2000 – 10/2001	Forschungstätigkeit, Kale Porcelain Company, in Istanbul, Türkei Thema: Preparation and loading of alumina washcoat over domestic honeycomb ceramic
09/2002 - 06/2003	Wissenschaftlicher Mitarbeiter, Sabanci Universität, in Istanbul, Türkei
	Promotion
07/2003 -	Forschungstätigkeit am Fritz-Haber-Institut der Max-Planck-Gesellschaft, Berlin, in der Arbeitsgruppe von Herrn Prof. Dr. Hans-Joachim Freund Titel der Dissertation: Structural and Catalytic Investigations on Vanadium Oxide Nanoparticles Supported on Silica Films Grown on a Mo(112) Substrate

PUBLICATIONS

[1] CO adsorption study of V/SiO_2: the low vanadium coverage regime,
B. Immaraporn; N. Magg; S. Kaya; J. Wang; M. Baumer; H. J. Freund, *Chemical Physics Letters,* 392, 127 (2004)

[2] Atomic structure of a thin silica film on a Mo(112) substrate: A two-dimensional network of SiO_4 tetrahedra
J. Weissenrieder; S. Kaya; J. L. Lu; H. J. Gao; S. Shaikhutdinov; H. J. Freund; M. Sierka; T. K. Todorova; J. Sauer, *Physical Review Letters,* 95, 076103 (2005)

[3] Formation of one-dimensional crystalline silica on a metal substrate
J. L. Lu; S. Kaya; J. Weissenrieder; T. K. Todorova; M. Sierka; J. Sauer; H. J. Gao; S. Shaikhutdinov; H. J. Freund, *Surface Science,* 600, L164 (2006)

[4] Atomic structure of a thin silica film on a Mo(112) substrate: A combined experimental and theoretical study T. K. Todorova;
M. Sierka; J. Sauer; S. Kaya; J. Weissenrieder; J. L. Lu; H. J. Gao; S. Shaikhutdinov; H. J. Freund, *Physical Review B,* 73, 165414 (2006)

[5] Low temperature CO induced growth of Pd supported on a monolayer silica film
J. L. Lu; S. Kaya; J. Weissenrieder; H. J. Gao; S. Shaikhutdinov; H. J. Freund, *Surface Science,* 600, L153 (2006)

[6] Interplay between theory and experiment in the quest for silica with reduced dimensionality grown on a Mo(112) surface
M. Sierka; T. K. Todorova; S. Kaya; D. Stacchiola; J. Weissenrieder; J. Lu; H. Gao; S. Shaikhutdinov; H. J. Freund; J. Sauer, *Chemical Physics Letters,* 424, 115 (2006)

[7] Vanadium oxide surfaces and supported vanadium oxide nanoparticles
S. Guimond; M. Abu Haija; S. Kaya; J. Lu; J. Weissenrieder; S. Shaikhutdinov; H. Kuhlenbeck; H. J. Freund; J. Dobler; J. Sauer, *Topics in Catalysis,* 38, 117 (2006)

[8] Synthesis and Structure of an Ultrathin Aluminosilicate Film
D. Stacchiola, S. Kaya, J. Weissenrieder, H. Kuhlenbeck, S. Shaikhutdinov, H.-J. Freund, M. Sierka, T. Kumanova Todorova, J. Sauer, *Angewandte Chemie International Edition*, 45, 7636 (2006)

[9] Synthese und Struktur eines ultradünnen Alumino-Silikatfilms
D. Stacchiola, S. Kaya, J. Weissenrieder, H. Kuhlenbeck, S. Shaikhutdinov, H.-J. Freund, M. Sierka, T. K. Todorova, J. Sauer, *Angew. Chem.*, 118, 7798 (2006)

[10] Formation of an ordered ice layer on a thin silica film.
S. Kaya, J. Weissenrieder, D. Stacchiola, S. Shaikhutdinov, H.-J. Freund, *Journal of Physical Chemistry C*, 111, 759 (2007)

[11] Characterization of Vanadium Oxide Nanoparticles on Well-ordered Silica Films
S. Kaya, Y. Sun, J. Weissenrieder, D. Stacchiola, S. Shaikhutdinov, H.-J. Freund, *Journal of Physical Chemistry C*, 111, 5337 (2007)

[12] Oxygen Adsorption on Mo(112) Surface Studied by Ab Initio Genetic Algorithm and Experiment
M. Sierka, T. K. Todorova, J. Sauer, S. Kaya, D. Stacchiola, J. Weissenrieder, S. Shaikhutdinov, H.-J. Freund, *J. Chem. Phys.* (accepted)

[13] A thin silica film on a Mo(11 2) substrate: a critical review.
S. Kaya, D. Stacchiola, J. Weissenrieder, T. K. Todorova, S. Shaikhutdinov, M. Sierka, J. Sauer , H.-J. Freund (submitted)

BIBLIOGRAPHY

[1] G. Ertl, H. Knoezinger and J. Weitkamp, *Handbook of heterogeneous catalysis*, Wiley-VCH, Weinheim (1997).

[2] J. A. Moulijn, P. W. N. M. v. Leeuwen and R. A. v. Santen, *Catalysis : an integrated approach to homogeneous, heterogeneous and industrial catalysis*, Elsevier, Amsterdam; New York (1993).

[3] G. C. Bond, *Heterogeneous catalysis : principles and applications*, Oxford chemistry series; 34, Clarendon Press, Oxford Oxfordshire; New York, ed. 2nd (1986).

[4] P. L. J. Gunter, J. W. Niemantsverdriet, F. H. Ribeiro and G. A. Somorjai, *Catal. Rev.-Sci. Eng.* 39, 77-168 (1997).

[5] G. A. Somorjai, *Introduction to surface chemistry and catalysis*, Wiley, New York (1994).

[6] G. K. Wertheim, *Z. Phys. D-Atoms Mol. Clusters* 12, 319-326 (1989).

[7] M. Valden, X. Lai and D. W. Goodman, *Science* 281, 1647-1650 (1998).

[8] V. E. Henrich and P. A. Cox, *The surface science of metal oxides*, Cambridge University Press, Cambridge; New York (1994).

[9] C. R. Henry, *Surf. Sci. Rep.* 31, 235-325 (1998).

[10] C. T. Campbell, *Surf. Sci. Rep.* 27, 1-111 (1997).

[11] M. Baumer and H. J. Freund, *Prog. Surf. Sci.* 61, 127-198 (1999).

[12] D. W. Goodman, *Surf. Rev. Lett.* 2, 9-24 (1995).

[13] S. A. Chambers, *Surf. Sci. Rep.* 39, 105-180 (2000).

[14] A. Zangwill, *Physics at surfaces*, Cambridge University Press, Cambridge Cambridgeshire; New York (1988).

[15] C. S. Fadley, *Basic Concepts of X-ray Photoelectron Spectroscopy.* C. R. Brundle and A. D. Baker, Electron Spectroscopy: Theory, Techniques and Applications, London (1978).

[16] J. Stöhr, *NEXAFS spectroscopy*, Springer series in surface sciences ; 25, Springer-Verlag, Berlin ; New York (1992).

[17] S. Hufner and G. K. Wertheim, *Phys. Rev. B* 11, 678-683 (1975).

[18] W. Bambynek, C. D. Swift, Craseman.B, H. U. Frend, P. V. Rao, R. E. Price, H. Mark and R. W. Fink, *Rev. Mod. Phys.* 44, 716 (1972).

[19] P. H. Citrin, G. K. Wertheim and Y. Baer, *Phys. Rev. B* 16, 4256-4282 (1977).

[20] S. Doniach and M. Sunjic, *J. Phys. C* 3, 285 (1970).

[21] D. A. Shirley, *Phys. Rev. B* 5, 4709 (1972).

[22] J. F. Moulder and J. Chastain, *Handbook of x-ray photoelectron spectroscopy : a reference book of standard spectra for identification and interpretation of XPS data*, Physical Electronics Division Perkin-Elmer Corp., Eden Prairie, Minn. (1992).

[23] D. P. Woodruff and T. A. Delchar, *Modern techniques of surface science*, Cambridge solid state science series, Cambridge University Press, Cambridge; New York, ed. 2nd (1994).

[24] L. J. Clarke, *Surface crystallography : an introduction to low energy electron diffraction*, Wiley, Chichester West Sussex; New York (1985).

[25] G. Binnig, H. Rohrer, C. Gerber and E. Weibel, *Phys. Rev. Lett.* 49, 57-61 (1982).

[26] G. Binnig, H. Rohrer, C. Gerber and E. Weibel, *Phys. Rev. Lett.* 50, 120-123 (1983).

[27] R. Wiesendanger, *Scanning probe microscopy and spectroscopy: methods and applications*, Cambridge University Press, Cambridge England (1994).

[28] J. Tersoff and D. R. Hamann, *Phys. Rev. B* 31, 805-813 (1985).

[29] J. K. Gimzewski and R. Moller, *Phys. Rev. B* 36, 1284-1287 (1987).

[30] R. G. Greenler, *J. Chem. Phys.* 44, 310 (1966).

[31] R. G. Greenler, *J. Chem. Phys.* 50, 1963 (1969).

[32] Y. J. Chabal, *Surf. Sci. Rep.* 8, 211-357 (1988).

[33] D. L. Allara and J. D. Swalen, *J. Phys. Chem.* 86, 2700-2704 (1982).

[34] I. Chorkendorff and J. W. Niemantsverdriet, *Concepts of modern catalysis and kinetics*, Wiley-VCH, Weinheim Germany (2003).

[35] R. I. Masel, *Principles of adsorption and reaction on solid surfaces*, Wiley series in chemical engineering, Wiley, New York (1996).

[36] I. Langmuir, *Phys. Rev.* 8, 149-176 (1916).

[37] L. A. Petermann, *Thermal Desorption Kinetics of Chemisorbed Gases*, Progress in Surface Science, Pergamon Press, Oxford, vol. 1 (1972).

[38] D. A. King, *Surf. Sci.* 47, 384-402 (1975).

[39] D. Menzel, *Thermal Desorption.* R. Vanselow and R. Howe, Chemistry and Physics of Solid Surfaces, Springer, Berlin, vol. IV (1982).

[40] K. Christmann, *Introduction to Surface Physical Chemistry*, Topics in Physical Chemistry, Steinkopff, Springer-Verlag, Darmstadt, New York, vol. 1 (1991).

[41] A. M. Dejong and J. W. Niemantsverdriet, *Surf. Sci.* 233, 355-365 (1990).

[42] P. A. Redhead, *Vacuum* 12, 203 (1962).

[43] E. Habenschaden and J. Kuppers, *Surf. Sci.* 138, L147-L150 (1984).

[44] J. K. Norskov, *Rep. Prog. Phys.* 53, 1253-1295 (1990).

[45] U. Starke, M. A. Vanhove and G. A. Somorjai, *Prog. Surf. Sci.* 46, 305-319 (1994).

[46] H. Conrad, G. Ertl, J. Kuppers and E. E. Latta, *Surf. Sci.* 65, 245-260 (1977).

[47] M. V. Ganduglia-Pirovano, M. Scheffler, A. Baraldi, S. Lizzit, G. Comelli, G. Paolucci and R. Rosei, *Phys. Rev. B* 6320 (2001).

[48] L. Kohler, G. Kresse, M. Schmid, E. Lundgren, J. Gustafson, A. Mikkelsen, M. Borg, J. Yuhara, J. N. Andersen, M. Marsman and P. Varga, *Phys. Rev. Lett.* 93, 266103 (2004).

[49] Y. D. Kim, S. Wendt, S. Schwegmann, H. Over and G. Ertl, *Surf. Sci.* 418, 267-272 (1998).

[50] C. Stampfl, S. Schwegmann, H. Over, M. Scheffler and G. Ertl, *Phys. Rev. Lett.* 77, 3371-3374 (1996).

[51] G. Kleinle, J. Wintterlin, G. Ertl, R. J. Behm, F. Jona and W. Moritz, *Surf. Sci.* 225, 171-183 (1990).

[52] M. Bader, A. Puschmann, C. Ocal and J. Haase, *Phys. Rev. Lett.* 57, 3273-3276 (1986).

[53] S. R. Parkin, H. C. Zeng, M. Y. Zhou and K. A. R. Mitchell, *Phys. Rev. B* 41, 5432-5435 (1990).

[54] L. Becker, S. Aminpirooz, A. Schmalz, B. Hillert, M. Pedio and J. Haase, *Phys. Rev. B* 44, 13655-13659 (1991).

[55] J. Sokolov, F. Jona and P. M. Marcus, *Europhys. Lett.* 1, 401-408 (1986).

[56] A. Bottcher and H. Niehus, *Phys. Rev. B* 60, 14396-14404 (1999).

[57] C. I. Carlisle, T. Fujimoto, W. S. Sim and D. A. King, *Surf. Sci.* 470, 15-31 (2000).

[58] E. Lundgren, G. Kresse, C. Klein, M. Borg, J. N. Andersen, M. De Santis, Y. Gauthier, C. Konvicka, M. Schmid and P. Varga, *Phys. Rev. Lett.* 88, 246103 (2002).

[59] W. Liu, K. C. Wong and K. A. R. Mitchell, *Surf. Sci.* 339, 151-158 (1995).

[60] J. Trost, H. Brune, J. Wintterlin, R. J. Behm and G. Ertl, *J. Chem. Phys.* 108, 1740-1747 (1998).

[61] G. Ketteler, D. F. Ogletree, H. Bluhm, H. J. Liu, E. L. D. Hebenstreit and M. Salmeron, *J. Am. Chem. Soc.* 127, 18269-18273 (2005).

[62] J. Gustafson, A. Mikkelsen, M. Borg, E. Lundgren, L. Kohler, G. Kresse, M. Schmid, P. Varga, J. Yuhara, X. Torrelles, C. Quiros and J. N. Andersen, *Phys. Rev. Lett.* 92, 126102 (2004).

[63] M. Saidy, O. L. Warren, P. A. Thiel and K. A. R. Mitchell, *Surf. Sci.* 494, L799-L804 (2001).

[64] K. Reuter and M. Scheffler, *Phys. Rev. Lett.* 90, 046103 (2003).

[65] J. Schnadt, A. Michaelides, J. Knudsen, R. T. Vang, K. Reuter, E. Laegsgaard, M. Scheffler and F. Besenbacher, *Phys. Rev. Lett.* 96, 146101 (2006).

[66] M. Todorova, K. Reuter and M. Scheffler, *Phys. Rev. B* 71, 195403 (2005).

[67] E. Bauer and T. Engel, *Surf. Sci.* 71, 695-718 (1978).

[68] E. Bauer, H. Poppa and Y. Viswanath, *Surf. Sci.* 58, 517-549 (1976).

[69] E. Bauer and H. Poppa, *Surf. Sci.* 88, 31-64 (1979).

[70] E. I. Ko and R. J. Madix, *Surf. Sci.* 109, 221-238 (1981).

[71] T. McAvoy, J. Zhang, C. Waldfried, D. N. McIlroy, P. A. Dowben, O. Zeybek, T. Bertrams and S. D. Barrett, *Eur. Phys. J. B* 14, 747-755 (2000).

[72] T. Sasaki, Y. Goto, R. Tero, K. Fukui and Y. Iwasawa, *Surf. Sci.* 502, 136-143 (2002).

[73] A. K. Santra, B. K. Min and D. W. Goodman, *Surf. Sci.* 513, L441-L444 (2002).

[74] K. Fukui, T. Aruga and Y. Iwasawa, *Surf. Sci.* 281, 241-252 (1993).

[75] T. Schroeder, J. B. Giorgi, A. Hammoudeh, N. Magg, M. Baumer and H. J. Freund, *Phys. Rev. B* 65, 115411 (2002).

[76] A. Kiejna and R. M. Nieminen, *J. Chem. Phys.* 122, 044712 (2005).

[77] T. Schroeder, J. Zegenhagen, N. Magg, B. Immaraporn and H. J. Freund, *Surf. Sci.* 552, 85-97 (2004).

[78] S. Y. Quek, M. M. Biener, J. Biener, C. M. Friend and E. Kaxiras, *Surf. Sci.* 577, L71-L77 (2005).

[79] M. Cavalleri, K. Hermann, S. Guimond, Y. Romanyshyn, H. Kuhlenbeck and H. J. Freund, *Catal. Today*, (accepted) (2007).

[80] J. Gustafson, A. Resta, A. Mikkelsen, R. Westerstrom, J. N. Andersen, E. Lundgren, J. Weissenrieder, M. Schmid, P. Varga, N. Kasper, X. Torrelles, S. Ferrer, F. Mittendorfer and G. Kresse, *Phys. Rev. B* 74, 035401 (2006).

[81] J. G. Wang, W. X. Li, M. Borg, J. Gustafson, A. Mikkelsen, T. M. Pedersen, E. Lundgren, J. Weissenrieder, J. Klikovits, M. Schmid, B. Hammer and J. N. Andersen, *Phys. Rev. Lett.* 95, 256102 (2005).

[82] T. Aruga, K. Tateno, K. Fukui and Y. Iwasawa, *Surf. Sci.* 324, 17-24 (1995).

[83] M. Sierka, T. K. Todorova, J. Sauer, S. Kaya, D. Stacchiola, J. Weissenrieder, S. Shaikhutdinov and H. J. Freund, *J. Chem. Phys.*, (accepted) (2007).

[84] F. C. Nart, S. Kelling and C. M. Friend, *J. Phys. Chem. B* 104, 3212-3218 (2000).

[85] G. K. Wertheim and P. H. Citrin, *Phys. Rev. B* 38, 7820-7823 (1988).

[86] T. Jirsak, M. Kuhn and J. A. Rodriguez, *Surf. Sci.* 457, 254-266 (2000).

[87] G. H. Smudde and P. C. Stair, *Surf. Sci.* 317, 65-72 (1994).

[88] M. Sing, R. Neudert, H. von Lips, M. S. Golden, M. Knupfer, J. Fink, R. Claessen, J. Mucke, H. Schmitt, S. Hufner, B. Lommel, W. Assmus, C. Jung and C. Hellwig, *Phys. Rev. B* 60, 8559-8568 (1999).

[89] G. Mestl and T. K. K. Srinivasan, *Catal. Rev.-Sci. Eng.* 40, 451-570 (1998).

[90] J. Kroger, S. Lehwald and H. Ibach, *Phys. Rev. B* 55, 10895-10904 (1997).

[91] P. K. Stefanov and T. S. Marinova, *Surf. Sci.* 200, 26-34 (1988).

[92] F. M. Hoffmann, *Surf. Sci. Rep.* 3, 107 (1983).

[93] M. L. Colaianni, J. G. Chen, W. H. Weinberg and J. T. Yates, *J. Am. Chem. Soc.* 114, 3735-3743 (1992).

[94] N. Magg, J. B. Giorgi, A. Hammoudeh, T. Schroeder, M. Baumer and H. J. Freund, *J. Phys. Chem. B* 107, 9003-9010 (2003).

[95] B. Chakraborty, S. Holloway and J. K. Norskov, *Surf. Sci.* 152, 660-683 (1985).

[96] V. D. Borman, E. P. Gusev, Y. N. Devyatko, V. N. Tronin and V. I. Troyan, *Surf. Sci.* 301, L239-L244 (1994).

[97] R. L. Mozzi and B. E. Warren, *J. Appl. Crystallogr.* 2, 164 (1969).

[98] J. Silva, D. G. Pinatti, C. E. Anderson and M. L. Rudee, *Philosophical Magazine* 31, 713-717 (1975).

[99] F. R. Boyd and J. L. England, *J Geophys. Res.* 65, 749-756 (1960).

[100] S. T. Pantelides and W. A. Harrison, *Phys. Rev. B* 13, 2667-2691 (1976).

[101] P. Balta and E. Balta, *Introduction to the Physical Chemistry of the Vitreous State*, vol. Tunbridge Wells: Abacus (1976).

[102] R. N. Nucho and A. Madhukar, *Phys. Rev. B* 21, 1576-1588 (1980).

[103] W. H. Zachariasen, *J. Am. Chem. Soc.* 54, 3841-3851 (1932).

[104] J. T. Randall, H. P. Rooksby and B. S. Cooper, *Z. Kristall.* 75, 196-214 (1930).

[105] A. C. Wright and R. N. Sinclair, *The Physics of* SiO_2*, and its Interfaces.* S. T. Pantelides, Pergamon, New York (1978).

[106] J. H. Konnert and D. E. Appleman, *Acta Crystallogr. Sect. B-Struct. Commun.* 34, 391-403 (1978).

[107] R. W. G. Wyckoff, *Crystal structures*, Interscience Publishers, New York,, ed. 2d (1963).

[108] S. C. Street, C. Xu and D. W. Goodman, *Annu. Rev. Phys. Chem.* 48, 43-68 (1997).

[109] H. J. Freund, H. Kuhlenbeck and V. Staemmler, *Rep. Prog. Phys.* 59, 283-347 (1996).

[110] R. P. Blum, D. Ahlbehrendt and H. Niehus, *Surf. Sci.* 396, 176-188 (1998).

[111] R. M. Jaeger, H. Kuhlenbeck, H. J. Freund, M. Wuttig, W. Hoffmann, R. Franchy and H. Ibach, *Surf. Sci.* 259, 235-252 (1991).

[112] H. Graupner, L. Hammer, K. Heinz and D. M. Zehner, *Surf. Sci.* 380, 335-351 (1997).

[113] G. Schmitz, P. Gassmann and R. Franchy, *Surf. Sci.* 397, 339-345 (1998).

[114] R. Franchy, *Surf. Sci. Rep.* 38, 199-294 (2000).

[115] J. Schoiswohl, G. Kresse, S. Surnev, M. Sock, M. G. Ramsey and F. P. Netzer, *Phys. Rev. Lett.* 92, 206103 (2004).

[116] J. Schoiswohl, M. Sock, S. Surnev, M. G. Ramsey, F. P. Netzer, G. Kresse and J. N. Andersen, *Surf. Sci.* 555, 101-117 (2004).

[117] A. C. Dupuis, M. Abu Haija, B. Richter, H. Kuhlenbeck and H. J. Freund, *Surf. Sci.* 539, 99-112 (2003).

[118] S. Valeri, S. Altieri, U. del Pennino, A. di Bona, P. Luches and A. Rota, *Phys. Rev. B* 65, 245410 (2002).

[119] M. Sterrer, E. Fischbach, T. Risse and H. J. Freund, *Phys. Rev. Lett.* 94, 186101 (2005).

[120] S. K. Shaikhutdinov, Y. Joseph, C. Kuhrs, W. Ranke and W. Weiss, *Faraday Discuss.*, 363-380 (1999).

[121] G. Kresse, M. Schmid, E. Napetschnig, M. Shishkin, L. Kohler and P. Varga, *Science* 308, 1440-1442 (2005).

[122] C. T. Campbell, *Phys. Rev. Lett.* 96, 066106 (2006).

[123] M. M. Atalla, E. Tannenbaum and E. J. Scheibner, *Bell Sys. Tech. J* 38, 749-783 (1959).

[124] A. G. Revesz, *Phys. Status Solidi* 19, 193 (1967).

[125] L. Young, *Anodic oxide films*, Academic Press, London, New York, (1961).

[126] J. W. He, X. Xu, J. S. Corneille and D. W. Goodman, *Surf. Sci.* 279, 119-126 (1992).

[127] X. P. Xu and D. W. Goodman, *Appl. Phys. Lett.* 61, 774-776 (1992).

[128] T. Schroeder, J. B. Giorgi, M. Baumer and H. J. Freund, *Phys. Rev. B* 66, 165422 (2002).

[129] M. S. Chen, A. K. Santra and D. W. Goodman, *Phys. Rev. B* 69, 155404 (2004).
[130] D. Ricci and G. Pacchioni, *Phys. Rev. B* 69, 161307 (2004).
[131] T. Schroeder, M. Adelt, B. Richter, M. Naschitzki, M. Baumer and H. J. Freund, *Surf. Rev. Lett.* 7, 7-14 (2000).
[132] T. Schroeder, M. Adelt, B. Richter, M. Naschitzki, M. Baumer and H. J. Freund, *Microelectron. Reliab.* 40, 841-844 (2000).
[133] J. L. Lu, S. Kaya, J. Weissenrieder, T. K. Todorova, M. Sierka, J. Sauer, S. W. Gao, S. Shaikhutdinov and H. J. Freund, *Surf. Sci.* 600, L164-L168 (2006).
[134] P. Reinig, F. Fenske, W. Fuhs, A. Schopke and B. Selle, *Appl. Surf. Sci.* 210, 301-306 (2003).
[135] M. P. Soriaga, *Thin films : preparation, characterization, applications*, Kluwer Academic/Plenum Publishers, New York (2002).
[136] R. Wiesendanger and H. J. Güntherodt, *Scanning tunneling microscopy III: theory of STM and related scanning probe methods*, Springer series in surface sciences; 29, Springer-Verlag, Berlin; New York (1993).
[137] J. Libuda, F. Winkelmann, M. Baumer, H. J. Freund, T. Bertrams, H. Neddermeyer and K. Muller, *Surf. Sci.* 318, 61-73 (1994).
[138] I. Sebastian and H. Neddermeyer, *Surf. Sci.* 454, 771-777 (2000).
[139] A. Rosenhahn, J. Schneider, J. Kandler, C. Becker and K. Wandelt, *Surf. Sci.* 435, 705-710 (1999).
[140] U. Martinez, L. Giordano and G. Pacchioni, *J. Phys. Chem. B* 110, 17015-17023 (2006).
[141] G. Hollinger and F. J. Himpsel, *J. Vac. Sci. Technol. A-Vac. Surf. Films* 1, 640-645 (1983).
[142] T. H. Distefano and D. E. Eastman, *Phys. Rev. Lett.* 27, 1560 (1971).
[143] B. Fischer, R. A. Pollak, T. H. Distefano and W. D. Grobman, *Phys. Rev. B* 15, 3193-3199 (1977).
[144] C. Senemaud, Costalim.Mt, J. A. Roger and A. Cachard, *Chem. Phys. Lett.* 26, 431-433 (1974).
[145] S. Wendt, E. Ozensoy, T. Wei, M. Frerichs, Y. Cai, M. S. Chen and D. W. Goodman, *Phys. Rev. B* 72, 115409 (2005).
[146] G. Pacchioni and G. Ierano, *Phys. Rev. B* 57, 818-832 (1998).
[147] B. O. Seraphin, *Optical properties of solids: new developments*, North-Holland Pub. Co., American Elsevier Pub. Co., Amsterdam, New York (1976).
[148] W. A. Pliskin, *J Vac. Sci. Tech.* 14, 1064-1081 (1977).
[149] R. Ruppin and R. Englman, *Rep. Prog. Phys.* 33, 149 (1970).
[150] B. K. Ridley, O. Aldossary, N. C. Constantinou and M. Babiker, *Phys. Rev. B* 50, 11701-11709 (1994).
[151] C. T. Kirk, *Phys. Rev. B* 38, 1255-1273 (1988).
[152] L. Giordano, D. Ricci, G. Pacchioni and P. Ugliengo, *Surf. Sci.* 584, 225-236 (2005).
[153] F. Liebau, *Structural chemistry of silicates: structure, bonding, and classification*, Springer-Verlag, Berlin; New York (1985).
[154] J. Weissenrieder, S. Kaya, J. L. Lu, H. J. Gao, S. Shaikhutdinov, H. J. Freund, M. Sierka, T. K. Todorova and J. Sauer, *Phys. Rev. Lett.* 95, 076103 (2005).
[155] M. Sierka, T. K. Todorova, S. Kaya, D. Stacchiola, J. Weissenrieder, J. Lu, H. Gao, S. Shaikhutdinov, H. J. Freund and J. Sauer, *Chem. Phys. Lett.* 424, 115-119 (2006).
[156] M. S. Chen and D. W. Goodman, *Surf. Sci.* 600, L255-L259 (2006).
[157] T. Schroeder, A. Hammoudeh, M. Pykavy, N. Magg, M. Adelt, M. Baumer and H. J. Freund, *Solid-State Electron.* 45, 1471-1478 (2001).
[158] B. K. Min, W. T. Wallace, A. K. Santra and D. W. Goodman, *J. Phys. Chem. B* 108, 16339-16343 (2004).

[159] Y. D. Kim, T. Wei and D. W. Goodman, *Langmuir* 19, 354-357 (2003).

[160] W. L. Warren, E. H. Poindexter, M. Offenberg and W. Mullerwarmuth, *J. Electrochem. Soc.* 139, 872-880 (1992).

[161] R. A. Weeks, *J. Appl. Phys.* 27, 1376-1381 (1956).

[162] D. L. Griscom and E. J. Friebele, *Phys. Rev. B* 34, 7524-7533 (1986).

[163] K. C. Snyder and W. B. Fowler, *Phys. Rev. B* 48, 13238-13243 (1993).

[164] Z. Y. Lu, C. J. Nicklaw, D. M. Fleetwood, R. D. Schrimpf and S. T. Pantelides, *Phys. Rev. Lett.* 89, 285505 (2002).

[165] R. A. B. Devine and J. Arndt, *Phys. Rev. B* 35, 9376-9379 (1987).

[166] R. A. B. Devine and J. Arndt, *Phys. Rev. B* 39, 5132-5138 (1989).

[167] M. E. Zvanut, F. J. Feigl, W. B. Fowler, J. K. Rudra, P. J. Caplan, E. H. Poindexter and J. D. Zook, *Appl. Phys. Lett.* 54, 2118-2120 (1989).

[168] S. Wendt, Y. D. Kim and D. W. Goodman, *Prog. Surf. Sci.* 74, 141-159 (2003).

[169] O. Bikondoa, C. L. Pang, R. Ithnin, C. A. Muryn, H. Onishi and G. Thornton, *Nat. Mater.* 5, 189-192 (2006).

[170] A. Zecchina, D. Scarano, S. Bordiga, G. Ricchiardi, G. Spoto and F. Geobaldo, *Catal. Today* 27, 403-435 (1996).

[171] C. H. Cho, S. Singh and G. W. Robinson, *Faraday Discuss.* 103, 19-27 (1996).

[172] F. Franks, *Water : a matrix of life*, RSC paperbacks, Royal Society of Chemistry, Cambridge, ed. 2nd (2000).

[173] D. S. Eisenberg and W. Kauzmann, *The structure and properties of water*, Oxford University Press, New York, (1969).

[174] L. Pauling, *The nature of the chemical bond and the structure of molecules and crystals; an introduction to modern structural chemistry*, Cornell University Press, Ithaca, N.Y., ed. 3d (1960).

[175] K. Muller-Dethlefs and P. Hobza, *Chem. Rev.* 100, 143-167 (2000).

[176] L. Ojamae and K. Hermansson, *J. Phys. Chem.* 98, 4271-4282 (1994).

[177] P. L. Silvestrelli and M. Parrinello, *Phys. Rev. Lett.* 82, 5415-5415 (1999).

[178] A. D. Buckingham, P. W. Fowler and J. M. Hutson, *Chem. Rev.* 88, 963-988 (1988).

[179] A. E. Reed, L. A. Curtiss and F. Weinhold, *Chem. Rev.* 88, 899-926 (1988).

[180] R. L. Fulton and P. Perhacs, *J. Phys. Chem. A* 102, 9001-9020 (1998).

[181] J. J. Dannenberg, L. Haskamp and A. Masunov, *J. Phys. Chem. A* 103, 7083-7086 (1999).

[182] A. J. Stone, A. D. Buckingham and P. W. Fowler, *J. Chem. Phys.* 107, 1030-1031 (1997).

[183] P. L. Silvestrelli and M. Parrinello, *J. Chem. Phys.* 111, 3572-3580 (1999).

[184] T. K. Ghanty, V. N. Staroverov, P. R. Koren and E. R. Davidson, *J. Am. Chem. Soc.* 122, 1210-1214 (2000).

[185] P. A. Thiel and T. E. Madey, *Surf. Sci. Rep.* 7, 211-385 (1987).

[186] O. Mishima and H. E. Stanley, *Nature* 396, 329-335 (1998).

[187] R. Ludwig, *Angew. Chem.-Int. Edit.* 40, 1809-1827 (2001).

[188] J. D. Bernal and R. H. Fowler, *J. Chem. Phys.* 1, 515-548 (1933).

[189] L. Pauling, *J. Am. Chem. Soc.* 57, 2680-2684 (1935).

[190] M. A. Henderson, *Surf. Sci. Rep.* 46, 5-308 (2002).

[191] S. Haq, J. Harnett and A. Hodgson, *Surf. Sci.* 505, 171-182 (2002).

[192] H. Ogasawara, B. Brena, D. Nordlund, M. Nyberg, A. Pelmenschikov, L. G. M. Pettersson and A. Nilsson, *Phys. Rev. Lett.* 89, 276102 (2002).

[193] M. Morgenstern, T. Michely and G. Comsa, *Phys. Rev. Lett.* 77, 703-706 (1996).

[194] C. Clay, S. Haq and A. Hodgson, *Phys. Rev. Lett.* 92, 046102 (2004).

[195] T. Mitsui, M. K. Rose, E. Fomin, D. F. Ogletree and M. Salmeron, *Science* 297, 1850-1852 (2002).

[196] G. Held and D. Menzel, *Phys. Rev. Lett.* 74, 4221-4224 (1995).

[197] P. J. Feibelman, *Science* 295, 99-102 (2002).

[198] J. Weissenrieder, A. Mikkelsen, J. N. Andersen, P. J. Feibelman and G. Held, *Phys. Rev. Lett.* 93, 196102 (2004).

[199] S. Andersson, C. Nyberg and C. G. Tengstal, *Chem. Phys. Lett.* 104, 305-310 (1984).

[200] S. Yamamoto, A. Beniya, K. Mukai, Y. Yamashita and J. Yoshinobu, *J. Phys. Chem. B* 109, 5816-5823 (2005).

[201] D. L. Doering and T. E. Madey, *Surf. Sci.* 123, 305-337 (1982).

[202] G. Held and D. Menzel, *Surf. Sci.* 316, 92-102 (1994).

[203] A. Glebov, A. P. Graham, A. Menzel and J. P. Toennies, *J. Chem. Phys.* 106, 9382-9385 (1997).

[204] A. Michaelides, A. Alavi and D. A. King, *Phys. Rev. B* 69, 113404 (2004).

[205] A. Michaelides and P. Hu, *J. Chem. Phys.* 114, 513-519 (2001).

[206] G. A. Kimmel, N. G. Petrik, Z. Dohnalek and B. D. Kay, *Phys. Rev. Lett.* 95, 166102 (2005).

[207] M. Morgenstern, J. Muller, T. Michely and G. Comsa, *Z. Phys. Chemie-Int. J. Res. Phys. Chem. Chem. Phys.* 198, 43-72 (1997).

[208] K. Morgenstern and K. H. Rieder, *J. Chem. Phys.* 116, 5746-5752 (2002).

[209] K. Morgenstern and J. Nieminen, *Phys. Rev. Lett.* 88, 066102 (2002).

[210] J. Cerda, A. Michaelides, M. L. Bocquet, P. J. Feibelman, T. Mitsui, M. Rose, E. Fomin and M. Salmeron, *Phys. Rev. Lett.* 93, 116101 (2004).

[211] T. Yamada, S. Tamamori, H. Okuyama and T. Aruga, *Phys. Rev. Lett.* 96, 036105 (2006).

[212] M. J. Stirniman, C. Huang, R. S. Smith, S. A. Joyce and B. D. Kay, *J. Chem. Phys.* 105, 1295-1298 (1996).

[213] U. Leist, W. Ranke and K. Al-Shamery, *Phys. Chem. Chem. Phys.* 5, 2435-2441 (2003).

[214] J. J. Yang and E. G. Wang, *Phys. Rev. B* 73, 035406 (2006).

[215] M. Abu Haija, S. Guimond, A. Uhl, H. Kuhlenbeck and H. J. Freund, *Surf. Sci.* 600, 1040-1047 (2006).

[216] J. Heidberg, B. Redlich and D. Wetter, *Ber. Bunsen-Ges. Phys. Chem. Chem. Phys.* 99, 1333-1337 (1995).

[217] C. Xu and D. W. Goodman, *Chem. Phys. Lett.* 265, 341-346 (1997).

[218] D. Ferry, A. Glebov, V. Senz, J. Suzanne, J. P. Toennies and H. Weiss, *J. Chem. Phys.* 105, 1697-1701 (1996).

[219] D. Ferry, S. Picaud, P. N. M. Hoang, C. Girardet, L. Giordano, B. Demirdjian and J. Suzanne, *Surf. Sci.* 409, 101-116 (1998).

[220] L. Giordano, J. Goniakowski and J. Suzanne, *Phys. Rev. Lett.* 81, 1271-1273 (1998).

[221] Y. Wang and T. N. Truong, *J. Phys. Chem. B* 108, 3289-3294 (2004).

[222] G. Tzvetkov, Y. Zubavichus, G. Koller, T. Schmidt, C. Heske, E. Umbach, M. Grunze, M. G. Ramsey and F. P. Netzer, *Surf. Sci.* 543, 131-140 (2003).

[223] Y. Joseph, W. Ranke and W. Weiss, *J. Phys. Chem. B* 104, 3224-3236 (2000).

[224] J. L. Daschbach, Z. Dohnalek, S. R. Liu, R. S. Smith and B. D. Kay, *J. Phys. Chem. B* 109, 10362-10370 (2005).

[225] S. Wendt, M. Frerichs, T. Wei, M. S. Chen, V. Kempter and D. W. Goodman, *Surf. Sci.* 565, 107-120 (2004).

[226] R. S. Smith, C. Huang, E. K. L. Wong and B. D. Kay, *Surf. Sci.* 367, L13-L18 (1996).

[227] C. Clay, S. Haq and A. Hodgson, *Chem. Phys. Lett.* 388, 89-93 (2004).

[228] E. Ozensoy, J. Szanyi and C. H. F. Peden, *J. Phys. Chem. B* 109, 3431-3436 (2005).

[229] R. J. Speedy, P. G. Debenedetti, R. S. Smith, C. Huang and B. D. Kay, *J. Chem. Phys.* 105, 240-244 (1996).

[230] D. R. Haynes, N. J. Tro and S. M. George, *J. Phys. Chem.* 96, 8502-8509 (1992).
[231] E. Whalley, *Can. J. Chem.-Rev. Can. Chim.* 55, 3429-3441 (1977).
[232] V. Buch and J. P. Devlin, *J. Chem. Phys.* 110, 3437-3443 (1999).
[233] A. B. Horn, M. A. Chesters, M. R. S. McCoustra and J. R. Sodeau, *J. Chem. Soc.-Faraday Trans.* 88, 1077-1078 (1992).
[234] B. Mate, A. Medialdea, M. A. Moreno, R. Escribano and V. J. Herrero, *J. Phys. Chem. B* 107, 11098-11108 (2003).
[235] H. Ogasawara, J. Yoshinobu and M. Kawai, *Chem. Phys. Lett.* 231, 188-192 (1994).
[236] F. Bensebaa and T. H. Ellis, *Prog. Surf. Sci.* 50, 173-185 (1995).
[237] D. Cappus, C. Xu, D. Ehrlich, B. Dillmann, C. A. Ventrice, K. Alshamery, H. Kuhlenbeck and H. J. Freund, *Chem. Phys.* 177, 533-546 (1993).
[238] C. Lemire, R. Meyer, V. E. Henrich, S. Shaikhutdinov and H. J. Freund, *Surf. Sci.* 572, 103-114 (2004).
[239] B. W. Callen, K. Griffiths and P. R. Norton, *Surf. Sci.* 261, L44-L48 (1992).
[240] B. Rowland, M. Fisher and J. P. Devlin, *J. Chem. Phys.* 95, 1378-1384 (1991).
[241] G. A. Kimmel, K. P. Stevenson, Z. Dohnalek, R. S. Smith and B. D. Kay, *J. Chem. Phys.* 114, 5284-5294 (2001).
[242] B. A. Morrow and A. J. McFarlan, *J. Phys. Chem.* 96, 1395-1400 (1992).
[243] F. Boccuzzi, S. Coluccia, G. Ghiotti, C. Morterra and A. Zecchina, *J. Phys. Chem.* 82, 1298-1303 (1978).
[244] X. C. Su, L. Lianos, Y. R. Shen and G. A. Somorjai, *Phys. Rev. Lett.* 80, 1533-1536 (1998).
[245] V. Buch, P. Sandler and J. Sadlej, *J. Phys. Chem. B* 102, 8641-8653 (1998).
[246] C. Knight, S. J. Singer, J. L. Kuo, T. K. Hirsch, L. Ojamae and M. L. Klein, *Phys. Rev. E* 73 (2006).
[247] M. J. Iedema, M. J. Dresser, D. L. Doering, J. B. Rowland, W. P. Hess, A. A. Tsekouras and J. P. Cowin, *J. Phys. Chem. B* 102, 9203-9214 (1998).
[248] M. Frank, K. Wolter, N. Magg, M. Heemeier, R. Kuhnemuth, M. Baumer and H. J. Freund, *Surf. Sci.* 492, 270-284 (2001).
[249] N. Magg, B. Immaraporn, J. B. Giorgi, T. Schroeder, M. Baumer, J. Dobler, Z. L. Wu, E. Kondratenko, M. Cherian, M. Baerns, P. C. Stair, J. Sauer and H. J. Freund, *J. Catal.* 226, 88-100 (2004).
[250] J. L. Lu, S. Kaya, J. Weissenrieder, H. J. Gao, S. Shaikhutdinov and H. J. Freund, *Surf. Sci.* 600, L153-L157 (2006).
[251] M. Born and K. Huang, *Dynamical theory of crystal lattices*, International series of monographs on physics, Clarendon Press, Oxford, (1954).
[252] A. S. Barker, *Phys. Rev. B* 12, 4071-4084 (1975).
[253] S. A. Rice, M. S. Bergren, A. C. Belch and G. Nielson, *J. Phys. Chem.* 87, 4295-4308 (1983).
[254] M. G. Sceats, M. Stavola and S. A. Rice, *J. Chem. Phys.* 71, 983-990 (1979).
[255] L. Schriver-Mazzuoli, A. Schriver and A. Hallou, *J. Mol. Struct.* 554, 289-300 (2000).
[256] P. Jenniskens, S. F. Banham, D. F. Blake and M. R. S. McCoustra, *J. Chem. Phys.* 107, 1232-1241 (1997).
[257] A. B. Horn, S. F. Banham and M. R. S. McCoustra, *J. Chem. Soc.-Faraday Trans.* 91, 4005-4008 (1995).
[258] J. P. Devlin, C. Joyce and V. Buch, *J. Phys. Chem. A* 104, 1974-1977 (2000).
[259] J. C. Li and D. K. Ross, *Nature* 365, 327-329 (1993).
[260] M. I. Heggie, C. D. Latham, S. C. P. Maynard and R. Jones, *Chem. Phys. Lett.* 249, 485-490 (1996).
[261] J. C. Li and D. K. Ross, *J. Phys.-Condes. Matter* 6, 10823-10837 (1994).
[262] O. Dengel, U. Eckener, H. Plitz and N. Riehl, *Phys. Lett.* 9, 291-292 (1964).

[263] S. M. Jackson and R. W. Whitworth, *J. Chem. Phys.* 103, 7647-7648 (1995).
[264] G. Held and D. Menzel, *Surf. Sci.* 327, 301-320 (1995).
[265] D. Schmeisser, F. J. Himpsel, G. Hollinger and B. Reihl, *Phys. Rev. B* 27, 3279-3286 (1983).
[266] A. Nilsson, H. Ogasawara, M. Cavalleri, D. Nordlund, M. Nyberg, P. Wernet and L. G. M. Pettersson, *J. Chem. Phys.* 122, 154505 (2005).
[267] J. W. Rabalais, T. P. Debies, J. L. Berkosky, J. T. J. Huang and F. O. Ellison, *J. Chem. Phys.* 61, 516-528 (1974).
[268] N. Tsuda, *Electronic conduction in oxides*, Springer series in solid-state sciences, 94, Springer, Berlin ; New York, ed. 3rd rev. and enl. (2000).
[269] C. N. R. Rao and B. Raveau, *Transition metal oxides*, VCH, New York (1995).
[270] I. Pollini, A. Mosser and J. C. Parlebas, *Phys. Rep.-Rev. Sec. Phys. Lett.* 355, 1-72 (2001).
[271] R. Zimmermann, R. Claessen, F. Reinert, P. Steiner and S. Hufner, *J. Phys.-Condes. Matter* 10, 5697-5716 (1998).
[272] J. Haber, M. Witko and R. Tokarz, *Appl. Catal. A-Gen.* 157, 3-22 (1997).
[273] I. L. Botto, M. B. Vassallo, E. J. Baran and G. Minelli, *Mater. Chem. Phys.* 50, 267-270 (1997).
[274] O. Muller, J. P. Urbach, E. Goering, T. Weber, R. Barth, H. Schuler, M. Klemm, S. Horn and M. L. denBoer, *Phys. Rev. B* 56, 15056-15061 (1997).
[275] T. Schmitt, L. C. Duda, M. Matsubara, M. Mattesini, M. Klemm, A. Augustsson, J. H. Guo, T. Uozumi, S. Horn, R. Ahuja, A. Kotani and J. Nordgren, *Phys. Rev. B* 69 (2004).
[276] M. D. Banus, T. B. Reed and A. J. Strauss, *Phys. Rev. B* 5, 2775 (1972).
[277] M. Morinaga and J. B. Cohen, *Acta Crystallogr. Sect. A* 35, 745-756 (1979).
[278] C. N. Satterfield, *Heterogeneous catalysis in practice*, McGraw-Hill chemical engineering series, McGraw-Hill, New York (1980).
[279] L. J. Burcham and I. E. Wachs, *Catal. Today* 49, 467-484 (1999).
[280] G. Deo and I. E. Wachs, *J. Catal.* 146, 323-334 (1994).
[281] A. Khodakov, B. Olthof, A. T. Bell and E. Iglesia, *J. Catal.* 181, 205-216 (1999).
[282] G. C. Bond and S. F. Tahir, *Appl. Catal.* 71, 1-31 (1991).
[283] K. Kishi, K. Hirai and T. Yamamoto, *Surf. Sci.* 290, 309-318 (1993).
[284] H. Niehus, R. P. Blum and D. Ahlbehrendt, *Surf. Rev. Lett.* 10, 353-359 (2003).
[285] S. Surnev, L. Vitali, M. G. Ramsey, F. P. Netzer, G. Kresse and J. Hafner, *Phys. Rev. B* 61, 13945-13954 (2000).
[286] M. Sambi, G. Sangiovanni, G. Granozzi and F. Parmigiani, *Phys. Rev. B* 55, 7850-7858 (1997).
[287] S. Agnoli, M. Sambi, G. Granozzi, C. Castellarin-Cudia, S. Surnev, M. G. Ramsey and F. P. Netzer, *Surf. Sci.* 562, 150-156 (2004).
[288] G. S. Wong, M. R. Concepcion and J. M. Vohs, *Surf. Sci.* 526, 211-218 (2003).
[289] I. E. Wachs, J. M. Jehng, G. Deo, B. M. Weckhuysen, V. V. Guliants and J. B. Benziger, *Catal. Today* 32, 47-55 (1996).
[290] B. Olthof, A. Khodakov, A. T. Bell and E. Iglesia, *J. Phys. Chem. B* 104, 1516-1528 (2000).
[291] C. Schild, J. Engweiler, J. Nickl, A. Baiker, M. Hund, M. Kilo and A. Wokaun, *Catal. Lett.* 25, 179-189 (1994).
[292] S. B. Xie, E. Iglesia and A. T. Bell, *Langmuir* 16, 7162-7167 (2000).
[293] R. J. Lad, *Surf. Rev. Lett.* 2, 109-126 (1995).
[294] X. M. Yan, J. Ni, M. Robbins, H. J. Park, W. Zhao and J. M. White, *J. Nanopart. Res.* 4, 525-533 (2002).
[295] D. Song, J. Hrbek and R. Osgood, *Nano Lett.* 5, 1327-1332 (2005).
[296] G. Liang and S. S. Perry, *Surf. Sci.* 594, 132-140 (2005).

[297] R. S. Smith and B. D. Kay, *Nature* 398, 788-791 (1999).
[298] S. M. McClure, D. J. Safarik, T. M. Truskett and C. B. Mullins, *J. Phys. Chem. B* 110, 11033-11036 (2006).
[299] R. P. Sear, S. W. Chung, G. Markovich, W. M. Gelbart and J. R. Heath, *Phys. Rev. E* 59, R6255-R6258 (1999).
[300] M. E. Harlin, V. M. Niemi and A. O. I. Krause, *J. Catal.* 195, 67-78 (2000).
[301] M. E. Harlin, V. M. Niemi, A. O. I. Krause and B. M. Weckhuysen, *J. Catal.* 203, 242-252 (2001).
[302] M. M. Koranne, J. G. Goodwin and G. Marcelin, *J. Catal.* 148, 369-377 (1994).
[303] S. T. Oyama, *J. Catal.* 128, 210-217 (1991).
[304] G. A. Sawatzky and D. Post, *Phys. Rev. B* 20, 1546-1555 (1979).
[305] N. Magg, J. B. Giorgi, T. Schroeder, M. Baumer and H. J. Freund, *J. Phys. Chem. B* 106, 8756-8761 (2002).
[306] Y. Takasu, R. Unwin, B. Tesche, A. M. Bradshaw and M. Grunze, *Surf. Sci.* 77, 219-232 (1978).
[307] G. K. Wertheim and S. B. Dicenzo, *Phys. Rev. B* 37, 844-847 (1988).
[308] M. Demeter, M. Neumann and W. Reichelt, *Surf. Sci.* 454, 41-44 (2000).
[309] S. Surnev, M. G. Ramsey and F. P. Netzer, *Prog. Surf. Sci.* 73, 117-165 (2003).
[310] S. A. Carter, J. Yang, T. F. Rosenbaum, J. Spalek and J. M. Honig, *Phys. Rev. B* 43, 607-614 (1991).
[311] S. Shin, S. Suga, M. Taniguchi, M. Fujisawa, H. Kanzaki, A. Fujimori, H. Daimon, Y. Ueda, K. Kosuge and S. Kachi, *Phys. Rev. B* 41, 4993-5009 (1990).
[312] Q. Luo, Q. L. Guo and E. G. Wang, *Appl. Phys. Lett.* 84, 2337-2339 (2004).
[313] D. S. Toledano, P. Metcalf and V. E. Henrich, *Surf. Sci.* 449, 19-30 (2000).
[314] H. Schuler, S. Klimm, G. Weissmann, C. Renner and S. Horn, *Thin Solid Films* 299, 119-124 (1997).
[315] L. Q. Wang, D. R. Baer, M. H. Engelhard and A. N. Shultz, *Surf. Sci.* 344, 237-250 (1995).
[316] J. Schoiswohl, G. Tzvetkov, F. Pfuner, M. G. Ramsey, S. Surnev and F. P. Netzer, *Phys. Chem. Chem. Phys.* 8, 1614-1623 (2006).
[317] V. Maurice, S. Cadot and P. Marcus, *Surf. Sci.* 471, 43-58 (2001).
[318] K. R. Asmis, M. Brummer, C. Kaposta, G. Santambrogio, G. von Helden, G. Meijer, K. Rademann and L. Woste, *Phys. Chem. Chem. Phys.* 4, 1101-1104 (2002).
[319] N. Das, H. Eckert, H. C. Hu, I. E. Wachs, J. F. Walzer and F. J. Feher, *J. Phys. Chem.* 97, 8240-8243 (1993).
[320] L. J. Burcham, G. T. Deo, X. T. Gao and I. E. Wachs, *Top. Catal.* 11, 85-100 (2000).
[321] E. V. Kondratenko, M. Cherian, M. Baerns, D. S. Su, R. Schlogl, X. Wang and I. E. Wachs, *J. Catal.* 234, 131-142 (2005).
[322] Z. L. Wu, H. S. Kim, P. C. Stair, S. Rugmini and S. D. Jackson, *J. Phys. Chem. B* 109, 2793-2800 (2005).
[323] D. E. Keller, F. M. F. de Groot, D. C. Koningsberger and B. M. Weekhuysen, *J. Phys. Chem. B* 109, 10223-10233 (2005).
[324] F. A. Miller and L. R. Cousins, *J. Chem. Phys.* 26, 329-321 (1957).
[325] J. M. Jehng, G. Deo, B. M. Weckhuysen and I. E. Wachs, *J. Mol. Catal. A-Chem.* 110, 41-54 (1996).
[326] M. F. Hazenkamp and G. Blasse, *J. Phys. Chem.* 96, 3442-3446 (1992).
[327] S. Yoshida, T. Tanaka, T. Hanada, T. Hiraiwa, H. Kanai and T. Funabiki, *Catal. Lett.* 12, 277-286 (1992).
[328] U. G. Nielsen, N. Y. Topsoe, M. Brorson, J. Skibsted and H. J. Jakobsen, *J. Am. Chem. Soc.* 126, 4926-4933 (2004).

[329] M. Ruitenbeek, A. J. van Dillen, F. M. F. de Groot, I. E. Wachs, J. W. Geus and D. C. Koningsberger, *Top. Catal.* 10, 241-254 (2000).

[330] G. T. Went, L. J. Leu and A. T. Bell, *J. Catal.* 134, 479-491 (1992).

[331] G. Silversmit, J. A. van Bokhoven, H. Poelman, A. M. J. van der Eerden, G. B. Marin, M. F. Reyniers and R. De Gryse, *Appl. Catal. A-Gen.* 285, 151-162 (2005).

[332] G. Deo, I. E. Wachs and J. Haber, *Crit. Rev. Surf. Chem.* 4, 141-187 (1994).

[333] M. A. Banares and I. E. Wachs, *J. Raman Spectrosc.* 33, 359-380 (2002).

[334] X. T. Gao, S. R. Bare, B. M. Weckhuysen and I. E. Wachs, *J. Phys. Chem. B* 102, 10842-10852 (1998).

[335] N. Uchida and S. Kittaka, *J. Phys. Chem.* 98, 2129-2133 (1994).

[336] D. Chakarov and B. Kasemo, *Phys. Rev. Lett.* 81, 5181-5184 (1998).

[337] N. G. Petrik and G. A. Kimmel, *Phys. Rev. Lett.* 90, 166102 (2003).

[338] P. Concepcion, B. M. Reddy and H. Knozinger, *PCCP Phys. Chem. Chem. Phys.* 1, 3031-3037 (1999).

[339] C. B. Wang, G. Deo and I. E. Wachs, *J. Catal.* 178, 640-648 (1998).

[340] G. Busca, G. Ramis and V. Lorenzelli, *J. Mol. Catal.* 50, 231-240 (1989).

[341] H. Miyata, M. Kohno, T. Ono, T. Ohno and F. Hatayama, *J. Mol. Catal.* 63, 181-191 (1990).

[342] L. Lietti, I. Nova, G. Ramis, L. Dall'Acqua, G. Busca, E. Giamello, P. Forzatti and F. Bregani, *J. Catal.* 187, 419-435 (1999).

[343] C. H. Bartholomew, *Appl. Catal. A-Gen.* 212, 17-60 (2001).

[344] M. A. Henderson, *Langmuir* 12, 5093-5098 (1996).

[345] Z. Dohnalek, R. L. Ciolli, G. A. Kimmel, K. P. Stevenson, R. S. Smith and B. D. Kay, *J. Chem. Phys.* 110, 5489-5492 (1999).

[346] A. H. C. Neto, P. Pujol and E. Fradkin, *Phys. Rev. B* 74, 024302 (2006).

[347] P. Lofgren, P. Ahlstrom, D. V. Chakarov, J. Lausmaa and B. Kasemo, *Surf. Sci.* 367, L19-L25 (1996).

[348] V. Buch, L. Delzeit, C. Blackledge and J. P. Devlin, *J. Phys. Chem.* 100, 3732-3744 (1996).

[349] B. Rowland, N. S. Kadagathur, J. P. Devlin, V. Buch, T. Feldman and M. J. Wojcik, *J. Chem. Phys.* 102, 8328-8341 (1995).

[350] I. E. Wachs and R. J. Madix, *Surf. Sci.* 76, 531-558 (1978).

[351] I. E. Wachs, *Catal. Today* 100, 79-94 (2005).

[352] M. A. Barteau, *Chem. Rev.* 96, 1413-1430 (1996).

[353] K. S. Kim and M. A. Barteau, *Surf. Sci.* 223, 13-32 (1989).

[354] J. M. Vohs and M. A. Barteau, *Surf. Sci.* 176, 91-114 (1986).

[355] X. D. Peng and M. A. Barteau, *Langmuir* 7, 1426-1431 (1991).

[356] P. A. Dilara and J. M. Vohs, *Surf. Sci.* 321, 8-18 (1994).

[357] H. Onishi, T. Aruga, C. Egawa and Y. Iwasawa, *Surf. Sci.* 193, 33-46 (1988).

[358] V. A. Gercher, D. F. Cox and J. M. Themlin, *Surf. Sci.* 306, 279-293 (1994).

[359] R. M. Ferrizz, G. S. Wong, T. Egami and J. M. Vohs, *Langmuir* 17, 2464-2470 (2001).

[360] L. Q. Wang, K. F. Ferris, J. P. Winokur, A. N. Shultz, D. R. Baer and M. H. Engelhard, *J. Vac. Sci. Technol. A-Vac. Surf. Films* 16, 3034-3040 (1998).

[361] D. F. Cox and K. H. Schulz, *J. Vac. Sci. Technol. A-Vac. Surf. Films* 8, 2599-2604 (1990).

[362] C. Ammon, A. Bayer, G. Held, B. Richter, T. Schmidt and H. P. Steinruck, *Surf. Sci.* 507, 845-850 (2002).

[363] R. B. Barros, A. R. Garcia and L. M. Iharco, *Surf. Sci.* 600, 2425-2433 (2006).

[364] M. Endo, T. Matsumoto, J. Kubota, K. Domen and C. Hirose, *J. Phys. Chem. B* 104, 4916-4922 (2000).

[365] J. M. Tatibouet, *Appl. Catal. A-Gen.* 148, 213-252 (1997).

[366] P. A. Dilara and J. M. Vohs, *J. Phys. Chem.* 97, 12919-12923 (1993).

[367] Q. G. Wang and R. J. Madix, *Surf. Sci.* 496, 51-63 (2002).

[368] I. E. Wachs, G. Deo, M. V. Juskelis and B. M. Weckhuysen, *Methanol oxidation over supported vanadium oxide catalysts: New fundamental insights about oxidation reactions over metal oxide catalysts from transient and steady state kinetics*, vol. 109 (1997).

[369] J. M. Vohs, T. Feng and G. S. Wong, *Catal. Today* 85, 303-309 (2003).

[370] S. Kittaka, T. Umezu, H. Ogawa, H. Maegawa and T. Takenaka, *Langmuir* 14, 832-838 (1998).

[371] K. Yamashita, S. Naito and K. Tamaru, *J. Catal.* 94, 353-359 (1985).

[372] P. Uvdal and A. D. MacKerell, *Surf. Sci.* 393, 141-149 (1997).

[373] M. Falk and E. Whalley, *J. Chem. Phys.* 34, 1554-& (1961).

[374] A. Serralla, R. Meyer and H. H. Gunthard, *J. Mol. Spectrosc.* 52, 94-129 (1974).

[375] W. S. Sim, P. Gardner and D. A. King, *J. Phys. Chem.* 99, 16002-16010 (1995).

[376] H. E. Sanders, P. Gardner and D. A. King, *Surf. Sci.* 333, 1496-1502 (1995).

[377] M. A. Chesters and E. M. McCash, *Spectroc. Acta Pt. A-Molec. Biomolec. Spectr.* 43, 1625-1630 (1987).

[378] P. Uvdal, M. K. Weldon and C. M. Friend, *Phys. Rev. B* 50, 12258-12261 (1994).

[379] R. Zenobi, J. Z. Xu, J. T. Yates, B. N. J. Persson and A. I. Volokitin, *Chem. Phys. Lett.* 208, 414-419 (1993).

[380] R. Ryberg, *Phys. Rev. B* 31, 2545-2547 (1985).

[381] H. E. Dastoor, P. Gardner and D. A. King, *Chem. Phys. Lett.* 209, 493-498 (1993).

[382] N. V. Richardson and N. Sheppard, *Vibrational Spectroscopy of Molecules on Surfaces*. J. T. Yates and T. E. Madey, Plenum, New York (1987).

[383] M. Nakamura and M. Ito, *Chem. Phys. Lett.* 325, 293-298 (2000).

[384] W. J. Mitchell, J. Xie, T. A. Jachimowski and W. H. Weinberg, *J. Am. Chem. Soc.* 117, 2606-2617 (1995).

[385] A. B. Anton, J. E. Parmeter and W. H. Weinberg, *J. Am. Chem. Soc.* 108, 1823-1833 (1986).

[386] R. B. Barros, A. R. Garcia and L. M. Ilharco, *J. Phys. Chem. B* 105, 11186-11193 (2001).

[387] A. K. Chen and R. Masel, *Surf. Sci.* 343, 17-23 (1995).

[388] G. S. Wong, D. D. Kragten and J. M. Vohs, *J. Phys. Chem. B* 105, 1366-1373 (2001).

[389] G. Busca, *Catal. Today* 27, 457-496 (1996).

[390] J. F. Edwards and G. L. Schrader, *J. Phys. Chem.* 89, 782-788 (1985).

[391] A. W. Grant, J. H. Larsen, C. A. Perez, S. Lehto, M. Schmal and C. T. Campbell, *J. Phys. Chem. B* 105, 9273-9279 (2001).

[392] C. Houtman and M. A. Barteau, *Surf. Sci.* 248, 57-76 (1991).

[393] M. W. Abee, S. C. York and D. F. Cox, *J. Phys. Chem. B* 105, 7755-7761 (2001).

[394] G. T. Went, S. T. Oyama and A. T. Bell, *J. Phys. Chem.* 94, 4240-4246 (1990).

[395] H. Eckert and I. E. Wachs, *J. Phys. Chem.* 93, 6796-6805 (1989).

[396] L. J. Burcham, L. E. Briand and I. E. Wachs, *Langmuir* 17, 6164-6174 (2001).

[397] I. E. Wachs, *Catal. Today* 27, 437-455 (1996).

[398] M. Casagrande, S. Lacombe, L. Guillemot and V. A. Esaulov, *Surf. Sci.* 445, L29-L35 (2000).

[399] E. R. Behringer, D. R. Andersson, B. H. Cooper and J. B. Marston, *Phys. Rev. B* 54, 14765-14779 (1996).

[400] D. Menzel, *Surf. Rev. Lett.* 4, 1283-1289 (1997).

[401] J. Wang, M. A. Deangelis, D. Zaikos, M. Setiadi and R. I. Masel, *Surf. Sci.* 318, 307-320 (1994).

[402] K. T. Queeney, C. R. Arumainayagam, A. Balaji and C. M. Friend, *Surf. Sci.* 418, L31-L38 (1998).

[403] M. Abu Haija, S. Guimond, Y. Romanyshyn, A. Uhl, H. Kuhlenbeck, T. K. Todorova, M. V. Ganduglia-Pirovano, J. Dobler, J. Sauer and H. J. Freund, *Surf. Sci.* 600, 1497-1503 (2006).

ERKLÄRUNG

Hiermit erkläre ich, dass ich die vorliegende Arbeit selbständig und nur unter Verwendung der angegebenen Literatur und Hilfsmittel angefertigt habe.

Berlin, 10. Juni 2007